Interparticle Coupling Effect on the Surface Plasmon Resonance of Gold Nanoparticles: From Theory to Applications

Sujit Kumar Ghosh[†] and Tarasankar Pal*[,§]

Department of Chemistry, Raidighi College, Raidighi-743383, South 24-Parganas, India, and Department of Chemistry, Indian Institute of Technology, Kharagpur-721302, India

Received November 3, 2006

Contents

---

* Corresponding author E-mail: tpal@chem.iitkgp.ernet.in.
[†] Raidighi College.
[§] Indian Institute of Technology.

10.1021/cr0680282 CCC: $65.00

Dr. Sujit Kumar Ghosh has been graduated as Doctor of Philosophy working with Professor Tarasankar Pal at Indian Institute of Technology, Kharagpur. His doctoral research encompasses the optical, electronic, and catalytic aspects of metal nanoparticles. He was a postdoctoral fellow with Professor Naoki Toshima at Tokyo University of Science at Yamaguchi, Japan. Presently, he is appointed as a Lecturer in Chemistry at Raidighi College, South 24-Parganas, India. His current research interest involves studying the optical properties of nanoscale assemblies and the photophysical properties of molecular probes on the surface of nanoscale materials.

Professor Tarasankar Pal obtained his Ph.D. degree in Chemistry from Burdwan University. In 1984, he was appointed as a faculty member in the Department of Chemistry, Indian Institute of Technology, Kharagpur. He worked as a visiting scientist at Oak Ridge National Laboratory with Prof. Tuan Vo-Dinh. He has also served as a visiting Professor in the University of Kent at Canterbury, University of Paris-sud, Tokyo University of Science at Shinjuku-ku, and Georgia Institute of Technology. Prof. Pal has received numerous national and international awards including R & D-100 Award, U.S.A., CRSI medal, and Royal Society-INSA Fellowship. Dr. Pal is a reviewer for ACS, RSC, Elsevier, and several other nanoscience journal publishers and an editorial board member of ChemTracts in Inorganic Chemistry. Recently, he has received D.Sc. degree in Chemistry from Visva-Bharati University. His research interests include syntheses and catalytic and spectroscopic applications of metal and semiconductor nanoparticle assemblies including surface-enhanced Raman scattering (SERS) studies and analytical and environmental chemistry.

1. General Introduction

Nanoscience and nanotechnology are recent revolutionary developments of science and engineering that are evolving at a very fast pace. They are driven by the desire to fabricate materials with novel and improved properties that are likely to impact virtually all areas of physical and chemical sciences, biological sciences, health sciences, and other interdisciplinary fields of science and engineering. Particles with sizes in the size range of 1−100 nm are called nanoparticles, whether they are dispersed in gaseous, liquid, or solid media. Nanoparticles are a number of atoms or molecules bonded together (these particles usually contain 10^6 atoms or fewer) and are intermediate in size between individual atoms and aggregates large enough to be called bulk material.[1,2] Because the nanoparticles are larger than individual atoms and molecules but are smaller than the bulk solid, materials in the nanometer size regime show behavior that is intermediate between that of a macroscopic solid and that of an atomic or molecular system. There are three major factors that are responsible for these differences: high surface-to-volume ratio,[2−5] quantum size effect,[6] and electrodynamic interactions.[7] Metallic nanoparticles possess unique optical, electronic, chemical, and magnetic properties that are strikingly different from those of the individual atoms as well as their bulk counterparts. Nanometer-scale metal particles exhibit optical properties of great aesthetic, technological, and intellectual value.[8] Colloidal solutions of the noble metals, namely, copper, silver, and gold, show characteristic colors that have received considerable attention from researchers.

The interesting colors observed in gold sols have led to extensive study of their optical spectroscopic properties in an effort to correlate their behavior under different microenvironmental conditions.[9−25] Although the extraction of gold started in the 5th millennium B.C. in Bulgaria, “soluble” gold appeared around the 5th century B.C. in Egypt and China.[26] Andreas Cassius’s (1605−1673) preparation of the “Purple of Cassius” was widely used as a pigment in enamel, chinaware and silk fabric as well as in glass. Johann Kunckel’s (1630−1703) perfected the age-old technique of making ruby-colored stained glass. The Lycurgus cup (4th century A.D.), which can be seen at the British Museum, is a striking example of the early (artistic) use of metal nanoparticles embedded in glass: the vessel appears green in daylight (reflected light), but red when it is illuminated from the inside (transmitted light). Paracelsus described the preparation of potable gold, which was believed to have remarkable medicinal properties. Until the Middle Ages, the soluble gold was used to disclose fabulous curative powers for various diseases, such as venereal problems, dysentery, epilepsy, and tumors, and for diagnosis of syphilis. Thus, the remarkable features exhibited by colloidal gold have been utilized for centuries. But the scientific research on gold sol started with Michael Faraday.[27] A sample of gold colloid prepared by Faraday is still on display in the Royal Institution.[28] Faraday reported the formation of a deep red solution of colloidal gold by reduction of an aqueous solution of chloroaurate ($AuCl_4^-$) using phosphorus in CS_2 (a two-phase system). He investigated the optical properties of thin films prepared from dried colloidal solutions and observed reversible color changes (from bluish-purple to green) of the films upon mechanical compression. The term “colloid” (from the French, *colle*) was coined shortly thereafter by Graham, in 1861. Although, Faraday’s best known contributions were in electromagnetism, he posed the central problem of small particle optics in a marvelous paper that constituted a Bakerian lecture.[27] This paper is a respository of experiments with thin metal films, metal island films, aerosols, hydrosols, and gels, which are mainly carried out with gold but also with silver, platinum, copper, tin, iron, lead, zinc, palladium, aluminum, rhodium, iridium, mercury, and arsenic. Faraday’s purpose in exploring colloidal phenomena followed his concerns with the interaction between light and matter. Faraday reasoned that there might be some value in observing the action of light on material particles, which, in turn, were also small compared with the wavelength of light. Gold came to his mind because samples could be prepared with particles that were much smaller than the wavelength “and because known phenomena appeared to indicate that a mere variation in the size of its particles gives rise to a variety of colors". Despite Faraday's appreciation that it was the interaction of light with particles of different morphologies that gave rise to the color, the notion that these phenomena were due to intrinsic color persisted. In 1908, Gustav Mie came forward to explain the red color of the gold nanoparticles in solution[29] by solving Maxwell's equations.[30−31] It is to be remembered that Rayleigh solved the problem for a sphere smaller than the wavelength of light; Mie made a solution to the problem for a sphere of a size comparable to the wavelength.[32−34]

Metal nanoparticles, especially gold, have attracted considerable attention recently because of their many interesting properties and potential technological applications.[35−43] The optical properties of isolated gold nanoparticles have been extensively studied.[44−46] Bulk gold has a familiar yellow color, caused by a reduction in reflectivity for light at the end of the spectrum.[22] Whenever gold is subdivided into smaller and smaller particles, the ratio of the radius to the wavelength becomes important, and when the particle is smaller than the wavelength, the Rayleigh approximation (i.e., no retardation) holds and the mathematics becomes simple.[32] Mie has shown that plasmon excitation is present when the radius is large compared with the wavelength of light, and in that case, the retardation effect should be included to get the correct results. When the particles of gold are small enough, their color is ruby red, due to their strong absorption of green light at about 520 nm, corresponding to the frequency at which a plasmon resonance occurs with the gold. Actually, many other metals display this type of spectrally selective resonance, too, but in general the resonance frequency lies in the visible range, in the near ultraviolet. Furthermore, gold is one of the very few metals noble enough to survive as a nanoparticle under atmospheric conditions. This serendipitous combination of properties has encouraged its application in a diverse range of niche applications.

Characteristically, noble metal nanoparticles exhibit a strong absorption band in the visible region, and this is indeed a small particle effect, since they are absent in the individual atom as well as in the bulk.[44,46] The physical origin of the light absorption by metal nanoparticles is the coherent oscillation of the conduction band electrons induced by the interacting electromagnetic field. The electromagnetic surface waves can propagate along the interface between conducting materials and a dielectric over a broad range of frequencies, ranging from dc and radio frequencies up to the visible.[47] The oscillation modes comprise an electromagnetic field coupled to the oscillations of conduction electrons and are called surface plasmons. These are characterized by strong field enhancement at the interface, while the electric field vector decays exponentially away from the surface (in the nanometer range).[48−50] When the dimensions of the conductor are reduced, boundary and surface effects become very important, and for this reason, the optical properties of small metal nanoparticles are dominated by collective oscillation of conduction electrons.[51−53] An absorption band results when the incident photon frequency is resonant with the collective oscillation of the conduction band electrons and is known as the surface plasmon resonance (SPR). For many metals, such as, Pb, In, Hg, Sn, and Cd, the plasma frequency lies in the UV part of the spectrum and nanoparticles do not display strong color effects. Such small metal particles are also readily oxidized making surface plasmon experiments difficult. The coinage metals are exceptional. First, they are nobler and form air-stable colloids. Second, due to d−d band transitions, the plasma frequency lies in the visible part of the spectrum. Third, at the plasmon frequency the imaginary part of the dielectric constant is very small, and this is why the near-field effect is so high that makes the plasmon excitation very interesting. Hence, surface plasmon experiments are most commonly carried out with Cu, Ag, and Au. The resonance frequency of this SPR is strongly dependent upon the size, shape, interparticle interactions, dielectric properties, and local environment of the nanoparticle.[54−59] The oscillation frequency is critically determined by four factors: the density of electrons, the effective electron mass, and the shape, and the size of the charge distribution. Real time monitoring of the optical properties of a system of metallic nanoparticles needs to take following parameters into consideration: presence of a supporting substrate or stabilizing ligand shell, a solvent layer on the top of the particles, and electromagnetic interactions between the particles that are close enough in the ensemble to influence the optical properties.[60−67]

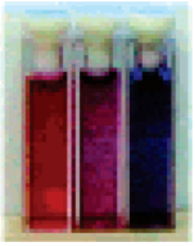

Figure 1. Color change in gold nanoparticle aggregates.

In the past two decades, the unusual size-dependent electronic properties of small metal particles have motivated a large number of workers concerned with the simulated optical properties, preparation, and characterization of a wide range of new clusters.[29,68−73] The engineering of materials and devices on the nanoscale is of greater current interest in electronics and optics than the engineering of either individual molecules or macroscopic solids.[74,75] Confinement and quantization of conduction electrons within a small volume enhance the optical and electronic conductance properties of materials composed of nanocrystals.[76−79] When the dimension of the nanoparticles becomes smaller than the wavelength of the exciting light, energy can be confined in the small spatial regions through the local excitation of surface plasmon resonances. The enhanced fields in these regions are used in a wide range of applications including optical energy transport[80,81] and chemical and biological sensors,[82−86] surface-enhanced Raman scattering (SERS),[55,56,87−100] near-field scanning optical microscopy,[101−104] and nanoscale optical devices.[105,106] It was predicted that the electromagnetic field enhancement may be very large when two resonant particles are brought close to each other and most of the energy is located between the particles.[107]

It is now known that the intrinsic properties of metal nanoparticles are mainly governed by their size, shape, composition, crystallinity, and structure. In principle, one could control any one of these parameters to fine-tune the properties of these nanoparticles. If such tiny particles are allowed to coalesce in a controlled fashion, their color can be systematically varied[108−110] from pink through violet to blue as shown in Figure 1. This phenomenon has been invoked as a colorimetric indicator in home pregnancy tests[111] and for testing for specific genetic sequences.[112] Well-defined, ordered solids prepared from tailored nanocrystallite building blocks provide opportunities for optimizing properties of materials and offer possibilities for observing interesting, new, and potentially useful collective physical phenomena. This is due to a change in their absorption spectrum upon aggregation, caused by increase of the absorbance of the red wavelength of light. The dimension of the particles in the nanometer size regime makes them ideal candidates for nanoengineering of surfaces and the fabrication of functional nanostructures.[113−119] They have been widely used in photography, catalysis, biological labeling, photonics, optoelectronics, information storage, surface-enhanced Raman scattering, and formulation of magnetic ferrofluids.[120] Also, interesting nonlinear optical effects are possible using gold nanoparticles and their aggregates, which may find application some day in optoelectronic circuitry.[121]

Several techniques have been developed for directing the self-assembly of nanocrystals into ordered aggregates or quantum dot superlattices.[122−132] Self-assembly of nanoparticles has been of tremendous interest to science and technology because it provides effective building blocks for physical, chemical, and biological applications. These assemblies present some very exciting possibilities. In principle, interparticle separations, particle size, and particle stoichiometry may be individually manipulated to produce macroscopic solids. This is similar to the well-known case of a one-dimensional quantum-dot superlattice that might be engineered to exhibit unique physical properties. Whereas attention is focused primarily on the assembly of macroscopic crystals and films of dense cluster matter, there is also interest in developing methods for assembling small controlled aggregates of nanoparticles. Due to the spherical symmetry and uniform reactivity of individual nanoparticle surfaces, the synthesis of small controlled nanoparticle assemblies is a significant challenge. When metal nanoparticles are placed in close proximity to one another, the interparticle coupling effect becomes very important and Mie's theory developed for isolated particles fails to account for the optical absorption spectrum. However, effective medium theories, dating back to 1904, predicted by Maxwell Garnett have been successfully applied to this problem to account for the optical absorbance behavior of an assembly of metal nanoparticles.[133] The color change that follows from aggregation of gold nanoparticles has been used commercially to provide sensitive biochemical assays[112,134] and has been demonstrated in the form of coatings on glass.[135,136] The properties of regularly packed aggregates have different and rather variable optical properties.[137] If these properties can be controlled, then there might, for example, be applications for the clusters as novel pigments or in spectrally selective coatings for solar glazing.[136] Such materials could be important constituents of tunnel resonant resistors[138] in novel microelectronic devices. These properties, in particular local electric field enhancements, enable applications such as single molecule detection using surface-enhanced Raman scattering[100,139] and the synthesis of composite materials exhibiting an enhanced nonlinear optical response.[140] In addition, resonant energy transfer between closely spaced metal nanoparticles enables transport of electromagnetic energy at length scales below the diffraction limit.[141] The self-assembly of nanoparticles into dense arrays, crystals, and Langmuir−Blodgett films yields materials with novel physical properties arising from interactions between nanoparticles.[142−144] Particle−particle interactions also regulate the linear and nonlinear optical properties of nanoparticles embedded in matrices or assembled into thin films at a high volume fraction.[145,146] Currently, there is great motivation to exploit the unique properties of these materials in electronic and optical device applications.[147−156]

In this review, we discuss the varieties in synthetic strategies and characterization of nanoscale gold particles assembled into an aggregate structure. Due to the explosion of the publications in this field in recent times, we could not cover all the published work, but rather a description of the methods is presented. Theoretical and experimental aspects of the optical properties of gold nanoparticles in a close-packed assembly have been elegantly explored. The stabilization phenomenon of the gold particles in making well-defined and organized assembly has been accounted in the light of Derjaguin−Laudau−Verwey−Overbeck (DLVO) theory, and varieties of examples have been cited in an effort to correlate the stability aspects under different microenvironmental conditions. The kinetics of the aggregation process from isolated gold particles has been explored and the effects of various physical parameters on the aggregation process are documented. The conditions for the reversibility of the aggregation process have been elucidated. The ultrafast electronic relaxation and coherent vibrational oscillation of strongly interacting gold nanoparticles measured by femtosecond laser spectroscopy is reported. The influence of an intense laser pulse on nanoparticle aggregation has been discussed. Finally, a number of real-time applications of nanoscale gold assembly have been realized from theoretical perspectives. Therefore, the aim of this present review is to survey the assembling strategies for nanostructured materials and to derive a general protocol with the basic understanding of the colloid and surface chemistry, to accumulate the results of their optical properties in a variety of microenvironmental conditions and their correlations with the effective medium theory predicted for nanoscale building blocks, and finally, to open up new insights by multidisciplinary approaches to their numerous possible applications from theoretical perspectives. The review will help the readers to understand the physical and chemical know-how to this inherently fascinating and highly rewarding field of investigations of advanced materials. The reader should also be aware of the extensive and pertinent work published by researchers in the same or marginally different disciplines. We feel that the outlook of self-assembled nanostructured materials is bright in the present scenario of research involving materials in the nanometer size regime. Therefore, we are confident that in the next few years there will be an explosive growth of chemical research focused upon self-assembled nanostructured materials.

2. Optical Properties of Metal Clusters in a Close-Packed Assembly: Interparticle Coupling Effect on the Surface Plasmon Resonance

2.1. Cluster Size Effect

Particles with sizes in the range of 1−100 nm are called nanoparticles, and these particles usually comprise of a large number of atoms or molecules bonded together. Thus, the nanoparticles can also be defined as a number of unspecified objects gathered together or growing together, containing number of atoms $3 < N < 10^7$ (considering a dimer as a molecule).[1,2] These particles may be distributed in free space or in gaseous, liquid, or solid embedding substances or may

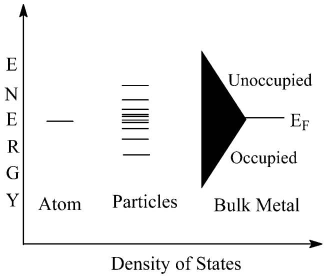

Figure 2. Energy levels in metal particles.

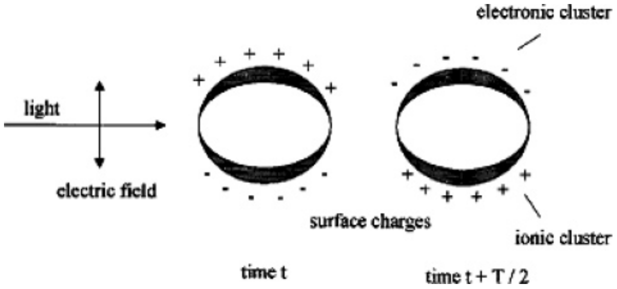

Figure 3. Schematic presentation of the creation of surface plasmon in metallic nanoparticles due to the interaction of electromagnetic radiation with the metal sphere. A dipole is induced, which oscillates in phase with the electric field of the incoming light.

be covered by shells or deposited on substrate materials. In general, all the possible components, covering shell or embedding medium, may be a metal, a semiconductor, or a dielectric, leaving open a large number of combinations. Interest in metallic nanoparticles has increased recently because of the possibility to artificially tailor novel materials with extraordinary properties. The material properties of these smaller sized particles are very interesting and cover a wide range depending upon the number of surface atoms. There are two different size effects in this specific size regime: intrinsic size effects and extrinsic size effects. Intrinsic size effects concern specific changes in volume and surface material properties. Experimentally, they deal with electronic and structural properties, namely, ionization potentials, binding energies, chemical reactivity, crystallographic structure, melting temperatures, and optical properties of metal clusters that depend upon the particle size and geometry. As the size of the particle becomes larger and larger, the energy levels continue to split and finally merge into the quasi-continuous band structure for the bulk solid. The energy level spacing of metal is shown in Figure 2. The extraordinary spectra arising due to the discretion (quantization) of electron energy levels are known as quantum size effects. For small sizes, the optical functions become size-dependent, whereas for larger ones, the electrodynamic theory can be applied using bulk optical constants, and this is known as extrinsic size effect.

2.2. Creation of Surface Plasmon Oscillation in Metal Nanoparticles

In Figure 3, a schematic presentation of the creation of a surface plasmon oscillation is shown. The electric field of an incoming light wave induces a polarization of the (free) conduction electrons with respect to the much heavier ionic core of a spherical nanoparticle. The positive charges in the particle are assumed to be immobile and the negative charges, that is, the conduction electrons, move under the influence of external fields. Therefore, a displacement of the negative charges from the positive ones occurs when the metallic nanoparticle is placed in an electric field, that is, there results a net charge difference at the nanoparticle boundaries. This, in turn, gives rise to a linear restoring force to the system. As a consequence, a dipolar oscillation of the electrons is created (with a particular time period), and this is known as the surface plasmon oscillation. The collective oscillation of the electrons is also sometimes denoted as the “dipole particle plasmon resonance” to differ from plasmon excitations that occur in bulk metal surfaces. The surface plasmon resonance is the coherent excitation of all the “free” electrons within the conduction band, leading to an in-phase oscillation.[157] It is to be noted that plasmons also exist in the bulk and at the surface of large chunks of material.[158−161] However, because of a mismatch between the plasmon dispersion relation and that of the photon, the plasmons cannot be excited by ordinary plane-wavelength light. The speciality of the small particles is that momentum conservation is no longer required and the plasmons can be excited by ordinary light. In small clusters, the surface and the bulk plasmon are coupled, and the charge density varies everywhere in the particle.[52,53,107] The multipolar resonances exist for individual nanoparticles and can be excited. The only difference between multipolar plasmons and dipolar plasmons is the shape of the surface charge distribution on the nanoparticle surface. The term “surface” stems from the fact that although all electrons are oscillating with respect to positive-ion background, the main effect producing the restoring force is the surface polarization. The surface, thus, plays a very important role for the observation of surface plasmon resonance because it alters the boundary condition for the polarizability of the metal and, therefore, shifts the resonance to optical frequencies. Thus, the conduction electrons in a spherical cluster act like an oscillator system. In the bulk material, the Drude frequency is not excited by light, and in this sense, the conduction electrons in the bulk behave like a relaxator system.

2.3. Optical Properties of Isolated Metal Nanoparticles: The Mie Theory

The general solution of the diffraction problem of a single sphere of arbitrary material within the framework of electrodynamics was first given by Mie in 1908.[29] It was the color variation of colloidal gold with particle size that motivated Mie to apply the general theory of light extinction to small particles. He applied Maxwell’s equations with appropriate boundary conditions in spherical coordinates using multipole expansions of the incoming electric and magnetic fields and offered an exact electrodynamic calculation of the interaction of light with spherical metallic nanoparticles. The theory describes the extinction (absorption and scattering) of spherical particles of arbitrary sizes. In reality, there are 11 geometries for which Maxwell equations and the boundary conditions are separable and can be solved analytically. Exact solutions are possible for an infinite cylinder, ellipsoids, two spheres, a sphere and a plane, a parallelepiped, spherical shells, etc.[52,56,57,89,90,162−166] However, most standard colloidal preparations yield particles that are approximately spherical, and most of the optical methods for characterizing nanoparticle spectra probe a large ensemble of these particles. This leads to results that can be modeled reasonably well using Mie theory.

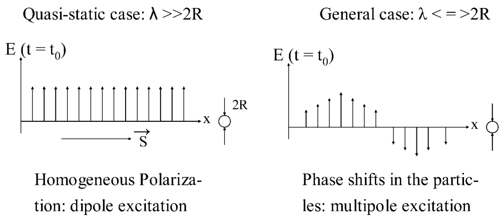

Figure 4. The interaction of light with clusters can be described in a simple way if $\lambda \gg 2R$, that is, in the quasistatic regime. In the general case, phase shifts of the electromagnetic wave in the particles complicate the optical response.

2.3.1. Assumptions of Mie Theory

The main assumption of Mie's theory is that the particle and its surrounding medium are each homogeneous and describable by their bulk optical dielectric functions.[167,168] The boundary is defined by the electron density, which is assumed to have a sharp discontinuity at the surface of the particle at radius R. The particle size and the optical materials function of the particle and of the surrounding medium were employed as the input parameters. To relate the dipole plasmon frequency of a metal nanoparticle to the dielectric constant, we consider the interaction of light with a spherical particle that is much smaller than the wavelength of light ($2R \ll \lambda$), where R is the radius of the particle. Under these circumstances, the electric field of light can be taken to be constant, and the interaction is governed by electrostatics rather than electrodynamics. This is often called the quasistatic approximation, because the wavelength-dependent dielectric constant of the metal particle, ϵ, and of the surrounding medium, ϵ_m, is used in a similar fashion to those of other electrostatic theories. In the quasistatic regime, phase shifts, that is, retardation effects, of the electrodynamic field over the cluster diameter are negligible. A simplified picture of the interaction of light with metallic nanoparticles is presented in Figure 4. If $2R > \lambda$, the optical effect of light scattering becomes effective, and the quasistatic approximation no longer holds.

2.3.2. Quasistatic Response of a Spherical Metal Nanoparticle to an Electric Field

The assumption of the quasistatic approximation enables the understanding of the optical response of metallic nanoparticles to an electric field. Let us denote the electric field of the incident electromagnetic wave by the vector $\mathbf{E}_0$. Under the influence of externally applied electric field, $\mathbf{E}_0$, of the incident electromagnetic field, the electric field inside the particle, $\mathbf{E}_i$, is given by

$$\mathbf{E}_{\mathrm{i}} = \mathbf{E}_0 \frac{3\epsilon_{\mathrm{m}}}{\epsilon + 2\epsilon_{\mathrm{m}}} \tag{1}$$

where, ϵ_m is the dielectric constant of the surrounding medium. In this approximation, excitations due to the magnetic field do not occur.

The electromagnetic field surrounding the particle can be obtained by solving Laplace's equation (the fundamental equation of electrostatics), $\nabla^2\varphi = 0$, where φ is the electric potential and the field $\mathbf{E}_0$ is related to φ by $\mathbf{E}_0 = -\nabla\varphi$, using the two boundary conditions (i) that φ is continuous at the sphere surface and (ii) that the normal component of the electric displacement, D, is also continuous, where $D = \epsilon_m\mathbf{E}_0$.

The influence of an electromagnetic field on a spherical metal nanoparticle surface causes polarization of the charges of the particle free conduction electrons, and using the boundary conditions, we can calculate the resulting polarization of the sphere as a whole. The induced dipole field, that is, the induced dipole moment that results from the polarization of the conduction electron density, $p = \epsilon_m\alpha\mathbf{E}_0$, where the static polarizability of the sphere, α, can be obtained by the solution of Laplace's equation and is given by

$$\alpha = 4\pi\epsilon_0 R^3 \frac{\epsilon - \epsilon_{\mathrm{m}}}{\epsilon + 2\epsilon_{\mathrm{m}}} \tag{2}$$

where ϵ is the dielectric function of the metallic nanoparticle.

The value of ϵ for metal particles is obtained by taking into account the contribution of its real and imaginary parts and is given by

$$\epsilon = \epsilon_1(\omega) + i\epsilon_2(\omega) = (n + i\kappa)^2 \tag{3}$$

in which n is the index of refraction and κ is related to light absorption. Usually, ϵ_m is taken as a real constant throughout the visible, and it is possible to find a resonance frequency. Under this condition, eq 4 is modified to the relation

$$[\epsilon_1(\omega) + 2\epsilon_{\mathrm{m}}]^2 + [\epsilon_2(\omega)]^2 = \text{minimum} \tag{4}$$

The wavelength of this plasma resonance is, therefore, given by the wavelength dependence of $\epsilon_1(\omega)$, that is, when the condition of $\epsilon_m = -2\epsilon_s$ is fulfilled, the local field at the particle is enhanced. The optical material functions are the quantities that determine not only the position but also the shape of these resonances. The width and height of the resonance are determined by the $\epsilon_2(\omega)$ value at this wavelength. Furthermore, the plasmon peak width is also related to the dielectric constant of the surrounding environment.[169−171] The change in the dielectric medium in which nanoparticles are immersed affects the spectral position of the plasmon resonance in that increasing the dielectric function of the surrounding medium causes the plasmon resonance position to shift to longer wavelengths.[172,173] Thus, the resonance properties depend on the properties of the particles and those of the medium because they polarize each other and the charge density has to adjust not only to the incident fields but also to the fields caused by polarization.

2.3.3. External Size Effect of Metal Nanoparticles on the Optical Response

Optical properties of isolated colloidal particles and, in particular, their dependence on particle size effect[171,174] have been intensively investigated through Mie scattering theory.[175,176] In particular, the Mie theory is a mathematical−physical description of the scattering of electromagnetic radiation by spherical particles immersed in a continuous medium.[74,75,177−183] The Mie scattering solution begins with macroscopic Maxwell equations. Using the complex representation of the electric field, $\mathbf{E}$, and auxiliary magnetic field, $\mathbf{H}$, the Maxwell equations assume the form

$$\nabla\cdot\mathbf{E} = 0 \tag{5}$$

$$\nabla\cdot\mathbf{H} = 0 \tag{6}$$

$$\nabla \times \mathbf{E} = i\omega\mu\mathbf{H} \tag{7}$$

$$\nabla \times \mathbf{H} = -i\omega\epsilon\mathbf{E} \tag{8}$$

The configuration of an incident electromagnetic field with two components, the electric field, $\mathbf{E}$, and the magnetic field, $\mathbf{H}$, can be described by the Helmholtz's equation as[74,75]

$$\nabla^2\mathbf{E} + k^2\mathbf{E} = 0 \tag{9}$$

$$\nabla^2\mathbf{H} + k^2\mathbf{H} = 0 \tag{10}$$

in which k is the wavenumber defined as

$$k^2 \equiv \omega^2\epsilon\mu \tag{11}$$

The series for **E** and **H**, which were used for the scattering amplitude functions, may be inserted into the appropriate integrals, and carrying out the integration term by term, we obtain the extinction and scattering coefficients as[74,75]

$$\sigma_{\text{ext}} = \frac{2}{x^2}\sum_{n=1}^{\infty}(2n+1)[\text{Re}(a_n + b_n)] \tag{12}$$

$$\sigma_{\text{sca}} = \frac{2}{x^2}\sum_{n=1}^{\infty}(2n+1)(|a_n|^2 + |b_n|^2) \tag{13}$$

$$\sigma_{\text{abs}} = \sigma_{\text{ext}} - \sigma_{\text{sca}} \tag{14}$$

in which the size parameter, x, is given by

$$x = \frac{2\pi R n_{\text{m}}}{\omega} \tag{15}$$

where R is the radius of the particle, n_{m} is the refractive index of the medium, ω is the wavelength of the incident light *in vacuo*, and a_n and b_n are the scattering coefficients, which may be expressed in terms of the Ricatti−Bessel expressions:[1]

$$a_n = \frac{m\psi_n(mx)\psi_n'(x) - \psi_n(y)\psi_n'(mx)}{m\psi_n(mx)\xi_n'(x) - \xi_n(x)\psi_n'(mx)} \tag{16}$$

$$b_n = \frac{\psi_n(mx)\psi_n'(x) - m\psi_n(y)\psi_n'(mx)}{\psi_n(mx)\xi_n'(x) - m\xi_n(x)\psi_n'(mx)} \tag{17}$$

in which $\psi_n(x)$ and $\zeta_n(x)$ are Ricatti−Bessel cylindrical functions and $m = n/n_{\text{m}}$, where n is the complex refractive index of the particle and n_{m} is the real refractive index of the surrounding medium. The prime indicates differentiation with respect to the argument in parentheses. In these expressions, n is the summation index of the partial waves as illustrated in Figure 5; $n = 1$ corresponds to the dipole oscillation, while $n = 2$ is associated with the quadrupole oscillation, and so on.

The effect of particle size on the peak resonant wavelength results from two different mechanisms depending on the particle size range. In the limit of $2R \ll \lambda$ (where R is the radius of the particles and λ is the wavelength of the light in media), only the electric dipole term contributes significantly to the extinction cross-section.[79,184−186] The Mie theory, then, reduces to the following relationship:

$$\sigma_{\text{ext}} = 9\frac{\omega}{c}\epsilon_{\text{m}}^{3/2}V\frac{\epsilon_2(\omega)}{[\epsilon_1(\omega) + 2\epsilon_{\text{m}}]^2 + [\epsilon_2(\omega)]^2} \tag{18}$$

where $V = (4\pi/3)R^3$ is the volume of the spherical particle, ω is the angular frequency of the exciting light, c is the velocity of light, and ϵ_{m} and $\epsilon(\omega) = \epsilon_1(\omega) + i\epsilon_2(\omega)$ are the dielectric functions of the surrounding medium and the material itself, respectively. While the first is assumed to be frequency independent, the latter is complex and is a function of energy. The resonance condition is fulfilled when $\epsilon_1(\omega) = -2\epsilon_{\text{m}}$ if ϵ_2 is small or weakly dependent on ω.

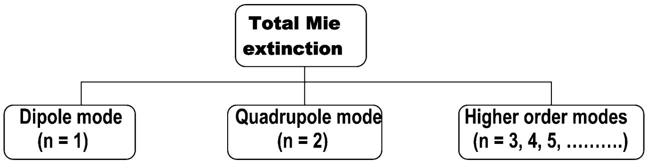

Figure 5. Scheme for decomposing the total Mie extinction spectra in dipolar, quadrupolar, and higher-order modes.

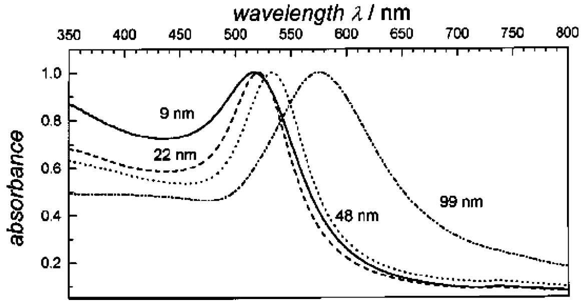

Figure 6. Surface plasmon resonance of 22, 48, and 99 nm spherical gold nanoparticles. Reprinted with permission from ref 46. Copyright 1999 American Chemical Society.

The UV−visible absorption spectra of a fairly dilute dispersion of colloidal particles can be calculated from the "Mie theory".[29] The absorbance, A of a colloidal solution containing N particles per unit volume is given by

$$A = (N\sigma_{\text{abs}}L/\ln 10) \tag{19}$$

where σ_{abs} and L are the absorption cross-section and the optical path length, respectively. The number of particles per unit volume, N, is easily determined from the number of moles of gold ions before reduction with the reducing agent, assuming that all the gold ions are reduced and form nanoparticles. The size of the nanoparticles, as determined from the magnified transmission electron microscopy images and the density of bulk fcc gold (59 atoms nm^{-3}) then gives the aggregation number in each particle: $N_{\text{Au}} = (59\ \text{nm}^{-3})(\pi/6)(D_{\text{MS}})^3$ where D_{MS} is the mean diameter of the particles. Then, the number of moles of gold nanoparticles in solution are calculated, which is in the nanomolar range for 20 nm particles.

The above equations have been used extensively to explain the absorption spectra of small metallic nanoparticles in a qualitative as well as quantitative manner.[1,186] However, for larger nanoparticles (greater than about 20 nm in the case of gold) where the dipole approximation is no longer valid, the dipole resonance depends explicitly on the particle size because x is a function of the particle radius R. The larger the particles become, the more important the higher order modes are because the light can no longer polarize the nanoparticles homogeneously. As a consequence, retardation effects of the electromagnetic field across the particle can cause huge shifts and broadening of the surface plasmon resonances. These higher order modes peak at lower energies, and therefore, the plasmon band red shifts with increasing particle size.[79,184−186] This is illustrated in Figure 6, and the results are in accordance with Mie theory. Because the optical absorption spectra depend directly on the size of the nanoparticles, this is regarded as an extrinsic size effect.

Metals are denoted as free-electron metals if most of the electronic and optical properties are due to the conduction electrons alone. Examples are the alkali metals, magnesium, aluminum, and, to some extent, also the noble metals. These metals have completely filled valence bands and partially filled conduction bands. Their linear response to the electromagnetic wave is described by the dielectric function, $\epsilon(\omega)$. Thus, for free-electron metals, $\epsilon(\omega)$ is governed mainly by the transitions within the conduction band, whereas in other metals, substantial contribution of interband transitions from lower-lying bands into the conduction band or from the conduction band into higher occupied levels are present. The noble metals constitute the special monovalent metals, which show both types of transitions. The likely origin of these effects can be ascertained to by considering the elementary facts of the electronic structure of the gold nanoparticles. Noble metal atoms, namely, Cu, Ag, or Au, have completely filled 3d, 4d, and 5d shells and just one electron in the 4s, 5s, and 6s bands, respectively. The interband transitions occur within the broad conduction band (derived mainly from Au $6s^1p$ hybridized atomic orbitals), which onset at zero frequency (or above the Kubo gap in small particles).[187] The high polarizability of the $5d^{10}$ cores (equivalent to the dielectric constant near 10) gives rise to a second effect: its intensity is dominated by the interband transitions and its location is modified strongly by the polarizable Au^+ ion cores. As a matter of fact, the influence of electrons, which undergo interband transitions, gives an additive complex contribution, $\chi^{IB} = \chi_1^{IB} + i\chi_2^{IB}$, to the susceptibility. The complex dielectric function incorporating all optical material properties around the visible region is given by

$$\epsilon(\omega) = 1 + \chi^{IB}(\omega) + \chi^{DS}(\omega) \tag{20}$$

The first step in obtaining the size dependence for metal particles is the decomposition of the dielectric function into two terms: an interband contribution (IB), accounting for the response of 5d electrons, and a free electron contribution (Drude, D) from the electrodynamics of the nearly free conduction electrons:[188]

$$\epsilon_1(\omega) = \epsilon_{1IB}(\omega) + \epsilon_{1D}(\omega), \quad \epsilon_2(\omega) = \epsilon_{2IB}(\omega) + \epsilon_{2D}(\omega) \tag{21}$$

where

$$\epsilon_{1D}(\omega) = 1 - \frac{{\omega_P}^2}{\omega^2 + {\omega_0}^2}, \quad \epsilon_{2D}(\omega) = \frac{{\omega_P}^2\omega_0}{\omega(\omega^2 + {\omega_0}^2)} \tag{22}$$

Here, ω_p is the frequency of the plasma oscillation of free electrons expressed in terms of the free electron density (N), the electron charge (e), and effective mass (m):

$$ {\omega_p}^2 = \pi N e^2/m \tag{23}$$

which corresponds energetically to 8.89 eV for gold.[189] The term ω_0, usually on the order of hundredths of an electronvolt, stands for the frequency of inelastic collisions (electron−phonon coupling, defects, impurities) of free electrons within the metal.

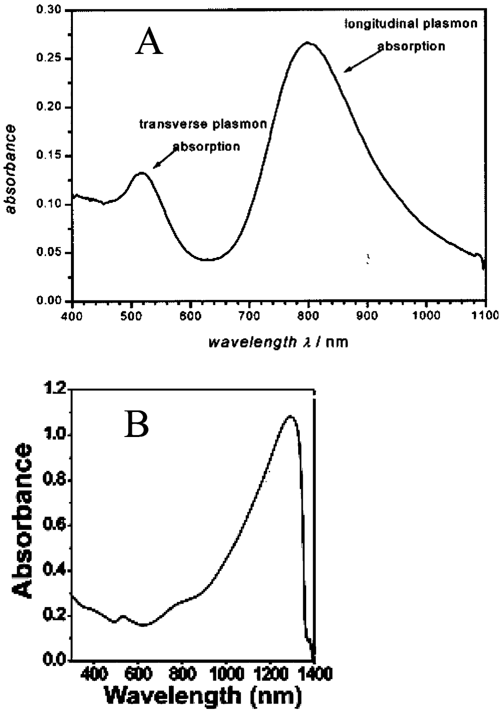

Figure 7. The effect of particle shape on the absorption spectrum of the colloidal gold (A) nanorods and (B) nanoprisms. Reprinted with permission from ref 46 (panel A) and ref 67 (panel B). Copyright 1999 and 2005 American Chemical Society.

To introduce size effects, one assumes that as the size of the particle diminishes, the rate of scattering from the particle surface (ω_s) begins to greatly exceed the bulk scattering rate (ω_0). The surface scattering rate is expressed in terms of the Fermi velocity ($v_F = 1.4 \times 10^8$ cm/s for gold) and particle radius:[188,190]

$$\omega_s = Z v_F/R \tag{24}$$

This expression can be interpreted as a limitation of the *mean free path* of the free electrons by the particle dimensions. The proportionality factor, Z, is on the order of unity assuming the scattering to be isotropic. The size evolution of the optical absorption spectrum shows that the onset of absorption is sharper for larger particles than for smaller particles.

2.3.4. Deviation of the Particle Shape from Sphericity

The surface plasmon oscillation in metallic nanoparticles is modified if the nanoparticle shapes deviate from sphericity.[191−202] The shape-dependent radiative properties of metallic particles can be treated by the Gans modification of Mie theory. This theory predicts that the shift in the surface plasmon resonance occurs when the particles deviate from spherical geometry. In this circumstance, the longitudinal and transverse dipole polarizability no longer produce equivalent resonances. Consequently, two plasma resonances appear: a broadened and red-shifted longitudinal plasmon resonance and a transverse plasmon resonance. According to Gans, for gold nanorods, the plasmon absorption splits into two bands[186,191−195] corresponding to the oscillation of the free electrons along and perpendicular to the long axis of the rods.[191,201] The transverse mode shows a resonance at about 520 nm, which is co-incident with the plasmon band of spherical particles,[199] while the resonance of the longitudinal mode is red-shifted and strongly depends on the aspect ratio (defined as the ratio of the length to width of the rod) of the nanorods. An absorption spectrum of colloidal gold nanorods (with aspect ratio 4.1) clearly showing the presence of two absorption maxima is shown in Figure 7A. Orendorff et al.[203]

have reported the unique shape-dependent plasmon resonance of gold nanoparticles, which covers a wide range of the visible spectrum. Using polarized light microscopy, the observed plasmon resonance from gold nanorods (aspect ratio 16) is observed to depend on the orientation of the rods.

The nanoshell is of considerable current interest in the field of plasmonics as it imparts highly tunable plasmon resonances.[204] In striking contrast to the plasmon resonance of gold nanorods, which exhibit a dependence on the aspect ratio, the plasmon resonance of a nanoshell happens to be a sensitive function of the nanoparticle's inner and outer shell dimensions. The nanoshell plasmon resonances result from the interaction between the essentially fixed-frequency plasmon response of a sphere and that of a cavity.[205] The sphere and cavity plasmons are electromagnetic excitations at the outer and inner interfaces of the metal shell, respectively. The strength of the interaction between the sphere and cavity plasmons is controlled by the thickness of the shell layer.[206]

The galvanic replacement reaction between a Ag template and $HAuCl_4$ in aqueous solution transforms 30−200 nm Ag nanocubes into Au nanoboxes and nanocages (nanoboxes with porous walls).[207] By controlling the molar ratio of Ag to $HAuCl_4$, the extinction peak of resultant structures can be continuously tuned from the blue (400 nm) to the near-IR (1200 nm) region of the electromagnetic spectrum. These hollow Au nanostructures are characterized by extraordinarily large cross-sections for both absorption and scattering. The absorption cross-section is more than 5 orders of magnitude larger than those of conventional organic dyes. It has been found that the magnitudes of both scattering and absorption cross-sections of Au nanocages can be tailored by controlling their dimensions, as well as the thickness and porosity of the wall. This novel class of hollow nanostructures is expected to find application both in optical imaging in early stage tumor detection and as a therapeutic agent for photothermal cancer treatment.[208]

Millstone et al.[67] measured for the first time a UV−vis−NIR spectrum of the purified gold nanoprisms with an average edge length of 144 ± 30 nm (Figure 7B). An in-plane dipole band with $\lambda_{max} \approx 1300$ nm is observed in both spectra, as is a quadrupole band occurring at $\lambda_{max} \approx 800$ nm. The asymmetry of the experimental dipole resonance peak at ~1300 nm is due to the truncation of the peak by the absorbance of water in the IR region. The optical spectrum of the nanoprisms exhibits a distinct dipole resonance at 532 nm as observed in isotropic spherical structures in addition to weaker higher order resonances. It has been noted that the resonance bands, either of gold or of silver, red shift with increase in edge length and sharpness and decrease in thickness. Jin et al.[209] noted that during the photoinduced conversion of silver nanospheres to nanoprisms, a decrease in intensity of the characteristic surface plasmon band in the ultraviolet−visible spectroscopy for the spherical particles at $\lambda_{max} = 400$ nm with a concomitant growth of three new bands of $\lambda_{max} = 335$ nm (weak), 470 nm (medium), and 670 nm (strong). After 70 h, the band at 400 nm completely disappeared indicating the complete morphological transformation of nanospheres to nanoprisms. Theoretical calculations coupled with experimental observations allow for the assignment of the nanoprism plasmon bands and for the first identification of two distinct quadrupole plasmon resonances for a nanoparticle.

2.3.5. Limitations of Mie Theory

The size dependence of the optical spectra of large clusters in an extrinsic cluster size effect is governed only by the dimension of the particle with respect to the wavelength of light. Mie attempted to calculate the optical response of large isolated, that is, single, metal particles following classical electrodynamics. This model gives a qualitative account of the variation of the optical properties with the size or the surrounding medium. This model is imperfect, because the matrix effect and polydispersity are not taken into account even for isolated particles. Moreover, it is assumed that the individual particles are non-interacting and separated from one another. Therefore, the electric field created around the particle by the excitation of surface plasmon resonance is not felt by the other surrounding particles. In general, when the particle size ($2R$) is small enough (assumed to be spherical in shape) compared with the wavelength of light λ ($2R < \lambda$), and also the particle concentration is very low, an absorption peak would result due to the excitation of dipole plasma mode ($n = 1$), and the optical extinction spectra can be described well by Mie theory.[1,29,74,75,210] Thus, although the Mie theory is valid for spheres of any size, the limitation of the theory is that the dielectric constant of a small particle is different from that of the bulk,[211] and the Maxwell equations themselves break down at points very close to the border.[212−216]

2.4. While the Metallic Particles in the Colloidal Solution Are Not Isolated: Maxwell Garnett Effective Medium Theory

In recent years, there is abundant literature covering the science and technology of gold nanoparticles, particularly with respect to their optical properties.[217−220] Much of the interest has been focused on the plasmon resonance of dilute suspensions of spherical particles, which have a red-purple color reflected by a broad absorption peak centered at ca. 520 nm. The surface plasmon oscillation in metallic nanoparticles is drastically changed if the particles are densely packed in the reaction medium so that the individual particles are electronically coupled to each other. It has been seen theoretically and experimentally that when the individual spherical gold particles come into close proximity to one another, electromagnetic coupling of clusters becomes effective for cluster−cluster distances smaller than five times the cluster radius ($d \leq 5R$, where, d is the center-to-center distance and R is the radius of the particles) and may lead to complicated extinction spectra depending on the size and shape of the formed cluster aggregate by a splitting of single cluster resonance.[79,107,221−224] As a consequence, their plasmon resonance is red-shifted by up to 300 nm, causing the color in transmission to become blue.[225−228] This effect is negligible if $d > 5R$ but becomes increasingly important at smaller distances.[229] Aggregation causes a coupling of the gold nanoparticle's plasma modes, which results in a red shift and broadening of the longitudinal plasma resonance in the optical spectrum.[230] The wavelength at which absorption due to dipole−dipole interactions occurs may be varied from 520 nm (effectively isolated particles) through 750 nm (particles that are separated by only 0.5 nm), and the resulting spectra are a composite of the conventional plasmon resonance due to single spherical particles and the new peak due to particle−particle interactions.[231−236] Since the interparticle coupling is stronger than the coupling within the surrounding medium, the Mie's theory developed for very dilute solutions

Table 1. Definition of Sample Topologies

case A/case B	case C	case D
separated single particles in full statistical disorder (parameter, filling factor f): (A) small f ($f < 10^{-3}$); (B) larger f ($f > 10^{-3}$)	aggregates of more or less closely connected particles; aggregates well separated, (small aggregate filling factor); no aggregate−aggregate interactions	general case: more or less dense aggregates plus single particles, both in various packing, including all kinds of collective interaction effects

and isolated particles fails to describe the optical absorption spectrum. However, the effective-medium theories, dating back to 1904, predicted by J. C. Maxwell Garnett[133] have been successfully applied to this problem to account for the optical absorbance behavior of the metal nanoparticles present in a closely packed assembly. The Maxwell Garnett theory is strictly valid in the quasistatic limit ($2R \ll \lambda$) along with very small interparticle distances but can be generalized to various shapes of the particles.

The Maxwell Garnett theory is an effective-medium theory.[133,234,237−239] The optical properties of the small particles are mainly determined by two contributions: the properties of the particles acting as well-isolated individuals and the collective properties of the whole ensemble. Only in the case of well-separated particles in optically thin samples, the response of an N-particle system is equal to N-fold of the individual. But, in an ensemble of large number of particles, the isolated-particle approximation breaks down and the electromagnetic interactions between the particles play a determining role to offer a satisfactory description of the surface plasmon oscillation.[240] While the isolated metal clusters are characterized by their material properties, the characteristic lengths, the geometrical shapes, and so forth, the aggregated clusters are characterized by their correlation length of spatial order, filling factors, details of the structure of geometric ordering, etc. Therefore, to model the influence of interparticle coupling, an explicit knowledge of the statistical variation of the positions and pairwise distances of all particles is to be taken into consideration. The convenient approach is to consider a statistical average over a large number of aggregates and the averaged volume fraction, f, of separated clusters in the sample, that is, the *filling factor* is introduced to describe the topology as

$$f = \frac{V_{\text{cluster}}}{V_{\text{sample}}} \tag{25}$$

Assuming the aggregate to be spherical, a simple functional form of the filling factor can be given by

$$f = \frac{NR^3}{r^3} \tag{26}$$

where r is the radius of the spherical aggregate. Thus, the more the topology differs from the statistically homogeneous isotropic cluster distribution, the more this filling factor has the character of only a rough average. Figure 8 shows topological realizations of metal clusters that can arise depending on the synthetic condition, and the averaged volume fraction of such topologies are illustrated in Table 1.

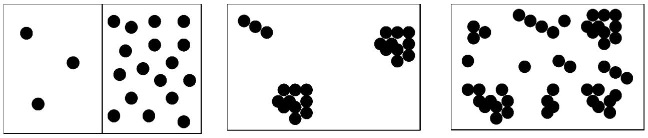

Figure 8. Topological realizations of cluster matter.

2.4.1. Assumptions of Effective-Medium Model

There are only a very few special examples where all building units and building blocks of a sample have well-defined parameters and, in particular, all the characterizing parameters vary from individual to individual. Therefore, the large number of particles and their aggregates in macroscopic samples have to be treated satisfactorily. To evade this complicacy, the following points are presupposed in order to be restricted to a simplified model system: (i) the particle sizes are strictly limited to the quasistatic regime so that the scattering of light by the particles becomes ineffective; (ii) particle shapes can be approximated by a sphere, instead of realistic nonspherical shapes; (iii) easily treatable geometries of the nanoscale assemblies can be selected; (iv) the number of different chemical structural constituents may be reduced to their minima, that is, one for nanostructured matter and two for matrix matter, while the interfaces are not regarded as additional constituents, that is, the influence of proximity effects of the sample surface is neglected; and (v) a linear response to the external electromagnetic field is assumed so that the tunneling processes between the neighboring nanoparticles can be disregarded.

2.4.2. Quasistatic Response of Aggregates of Metal Spheres to an Electric Field: The Effective-Medium Theory

Let us select one polarizable particle in the sample. The dielectric function of this particle is the sum of all contributions to the electrical polarization including retarded electrodynamics in the neighboring particles. For the selected particle, the surrounding appears to be homogeneous only on a scale larger than the length of spatial correlations, while the closely neighboring particles contributing to the effective local field individually by their scattering fields and their spatial arrangements have to be considered in detail. The local field, originally introduced by Lorentz as the field at an atom, is now assumed to act on the particle as a whole. Extending the concepts of the Lorentz sphere to a system consisting of nanoscale metal particles allows us to give analytical expressions for the interaction fields at a given particle summed over all other ($N_{\text{sa}} - 1$) particles of the sample. The proper size of this sphere is still an open question; obviously, in a nanoparticle system it depends on the details of topology, that is, the filling factor. The polarization of this sphere is calculated, as typical of the Lorentz−Lorenz concept, in the quasistatic approximation.

Applying the Lorentz theory of dielectric properties to nanoparticles (Figure 9), one can write the effective electric field at the position of a given particle as the Lorentz local field,

$$E_{\text{local}} = E_0 + E_{\text{d}} + E_{\text{s}} + E_{\text{near}} \tag{27}$$

where E_0 is the external field, E_{d} is the field due to charges at the external surface, E_{s} is the field due to polarization charges around the sphere, and E_{near} is the field due to dipoles

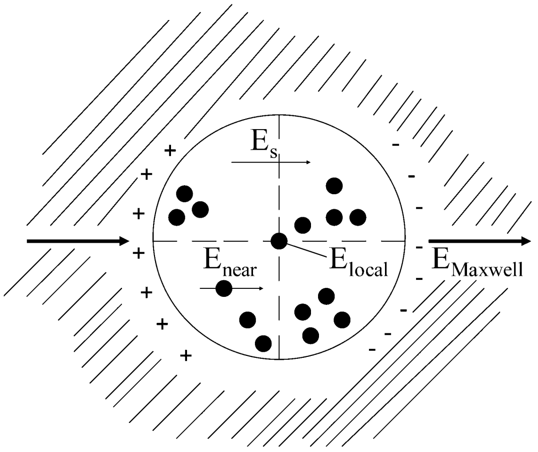

Figure 9. The Lorentz sphere concept applied to cluster matter. The sign of the charges corresponds to an empty sphere in the dielectric surrounding.

inside the sphere. The above equation can also be written as

$$E_{\text{local}} = E_{\text{Maxwell}} + E_{\text{s}} + E_{\text{near}} \tag{28}$$

where E_{Maxwell} is the incident field (i.e., the average field, simply denoted as E) in the matrix, that is, the external field plus the field from polarization charges at the surface of the Lorentz sphere. The dielectric function, ϵ_m, of the material in which the particles are embedded is assumed to be real. Influence of the proximity of the sample surfaces is neglected here. The local field, originally introduced by Lorentz as the field at an atom, is now assumed to act on the particle as a whole.

To find out how the plasmons are affected by the crystal field in a system of touching spheres of colloidal particles, a new embedding method has been employed to solve Maxwell's equations. At low filling fractions, the interaction between the spheres can be considered within the Maxwell Garnett approximation. In the case of statistically distributed single particles with filling factor $f > 10^{-3}$ collective properties become important. Under such situation, $E_{\text{near}} = 0$ since the scattering fields of all the particles within the Lorentz sphere cancel by interference at the sphere center, but the field due to polarization charges around the sphere, E_s, is taken into consideration and is given by

$$E_s = \int_0^{\pi} \left(\frac{P\cos\theta}{R^2}\right) \cos\theta\,(2R^2 \sin\theta)\,d\theta = \frac{4\pi}{3}P \tag{29}$$

Thus, the local field, E_{local}, is related to the average field (E) and polarization (P) as

$$E_{\text{local}} = E + 4\pi P/3 \tag{30}$$

The local field can be used to evaluate the dipole moment (μ) and the polarization (P) of an atom or a particle. The dipole moment of an atom or particle can be expressed in the form

$$\mu = \alpha E_{\text{local}} \tag{31}$$

and the polarization (P) in the form

$$P = \sum_i N_i \mu_i = \sum_i N_i \alpha_i E_{\text{local}}(i) \tag{32}$$

where N_i and α_i are the number density and the polarizability of the ith particle species. Putting the value of E_{local} in eq 32, we get

$$P = \sum_i N_i \mu_i = \sum_i N_i \alpha_i \left(E + \frac{4\pi}{3}P\right) \tag{33}$$

Then, the susceptibility (χ) is defined by

$$\chi = \frac{P}{E} = \frac{\sum_i N_i \alpha_i}{1 - \frac{4\pi}{3}\sum_i N_i \alpha_i} \tag{34}$$

The polarizability of a spherical particle with permittivity ϵ and radius R is defined as

$$\alpha = \frac{\epsilon - \epsilon_m}{\epsilon + 2\epsilon_m} R^3 \tag{35}$$

If the *quasistatic approximation* is fulfilled, the system may be replaced by an *effective medium*. An effective medium acts approximately like homogeneous material and can be described by the *effective dielectric function*, $\epsilon_{\text{eff}} = \epsilon_{1,\text{eff}} + i\epsilon_{2,\text{eff}}$, of the whole composite sample. The effective dielectric function, ϵ_{eff}, expresses the linear response of the whole sample to the external field in terms of dielectric function or polarizabilities of the particles and matrix material and of suitably chosen topology parameters. The effective dielectric function can be defined as some physical property that remains invariant upon replacement of the inhomogeneous sample by the corresponding effective medium. The Clausius−Mossotti relation describes the link between the macroscopic observable ϵ_{eff} and microscopic parameter α as

$$\frac{\epsilon_{\text{eff}} - \epsilon_m}{\epsilon_{\text{eff}} + 2\epsilon_m} = \frac{4\pi}{3}\sum_i N_i \frac{\epsilon - \epsilon_m}{\epsilon + 2\epsilon_m} R^3 \tag{36}$$

Introducing the volume fraction of the inclusion, that is, the filling factor (f), eq 36 can also be expressed as

$$\frac{\epsilon_{\text{eff}} - \epsilon_m}{\epsilon_{\text{eff}} + 2\epsilon_m} = f\frac{\epsilon - \epsilon_m}{\epsilon + 2\epsilon_m} \tag{37}$$

and is a popular version of Lorentz−Lorenz formula. Frequently, eq 37 is changed into the form

$$\epsilon_{\text{eff}} = \epsilon_m \frac{1 + 2f\Lambda}{1 - f\Lambda} \tag{38}$$

where

$$\Lambda = \frac{1}{\epsilon_m}\frac{\epsilon - \epsilon_m}{\epsilon + 2\epsilon_m} = \frac{\alpha}{3\epsilon_0 \epsilon_m V} \tag{39}$$

When dealing with a material composed of two equivalent inclusions, the Maxwell Garnett formula is changed into the form

$$\frac{\epsilon_{\text{eff}} - \epsilon_m}{\epsilon_{\text{eff}} + 2\epsilon_m} = f_1\frac{\epsilon_1 - \epsilon_m}{\epsilon_1 + 2\epsilon_m} + f_2\frac{\epsilon_2 - \epsilon_m}{\epsilon_2 + 2\epsilon_m} \tag{40}$$

Collective effects like those globally included in eq 38 are caused by the homogeneous polarization of the Lorentz sphere and do not exhibit explicit dependencies on individual particle properties like the particle positions and sizes. Equation 38 holds under quasistatic conditions; hence the particle size enters only implicitly if $\alpha_i(\omega)$ develops some size dependence due to quantum size effects. If the particles are atoms, eq 36 is named after Clausius and Mossotti, but in case of nanoparticles, eq 38 is called the Maxwell Garnett formula.

There is only one resonance at $\epsilon = -2\epsilon_m$ corresponding to the surface plasmon resonance at $\omega = \omega_p/(1 + 2\epsilon_m)^{1/2}$ of an isolated metal particle. The absorption spectrum is, then, given explicitly by the absorption constant, $\gamma_a(\omega)$,

$$\gamma_a(\omega) = \frac{\omega}{n_r c}\mathrm{Im}\{\epsilon_{\mathrm{eff}}\} = \frac{4\pi k}{\lambda} = \frac{2\omega}{c}\sqrt{-\frac{\epsilon_{1,\mathrm{eff}}{}^2}{2} + \frac{\sqrt{\epsilon_{1,\mathrm{eff}}{}^2 + \epsilon_{2,\mathrm{eff}}{}^2}}{2}} \quad (41)$$

The derivation of Maxwell Garnett is based on the assumption of homogeneous fields within and outside the nanoparticles and limited to low filling factors, f. However, the obtained formulas for ϵ_{eff} are commonly applied beyond this latter limit, justified by experiment. The Maxwell Garnett theory is only valid for dilute ensembles of particles, which interact through the far-field. If the particles are close enough for their near-field to interact, the theory breaks down. Modern calculations[241−243] have abandoned Maxwell Garnett and solve the Maxwell equation for the ensemble, including thus the near-field interactions between the particles.

2.4.3. Explicit Particle Methods

In the Maxwell Garnett approach, we have seen that a simpler description of nanoparticle aggregates may be achieved by invoking effective-medium approximations, wherein the aggregate is replaced by an effective object that has a uniform dielectric constant. As long as the aggregate density is sufficiently low and the polarizability per particle is not too high, satisfactory results could be obtained to explain the optical spectra of aggregated clusters. However, if the particle density is not too high and the particles are spherical, then a simpler theoretical approach based on *coupled multipoles* is often possible.[117,234] This makes it feasible to study aggregates with a few hundred particles. If the particle sizes are sufficiently small, then *coupled dipole* versions of this approach may be adequate. In this case, it may be possible to study as many as 10^5 particles by representing the aggregate structure on a lattice and using Fourier transformation methods to perform dipole sums. Such calculations are functionally identical to DDA calculations in which one represents each particle by a single dipole (discussed in section 2.4.4).

The behavior of light incident on a macroscopic target is governed by Maxwell's equation for the electric and magnetic vector fields. The general framework for modeling the optical response of a collection of spheres involves self-consistent solution of the response of each particle to the incident field and the scattered fields of the other particles. Spherical particles of nonmagnetic materials with sizes much smaller than the wavelength of light respond primarily to the electric dipole component of the local field unless the higher multipole components of the local field are very large. For isotropic materials, the frequency-dependent dipole polarizability α_1 of the spheres is determined by the electric dipole scattering coefficient according to the expression[218]

$$\alpha_1 = r^3\frac{3i}{2(kr)^3}a_1 \quad (42)$$

where r is the sphere radius, $k = m_0(2\pi/\lambda)$ is the magnitude of the wave vector in a dielectric medium with real refractive index m_0 and a_1 is a function of the size parameter kr and relative metal index of refraction $m = \sqrt{\epsilon}/m_0$.

The response of a dielectric aggregate of small nonmagnetic nanospheres to electromagnetic radiation can be determined by self-consistent solution of the electric dipole polarizations, P_i, of each sphere in the superposed field of the incident light and the dipole fields of the other particles. Thus, the coupled nanosphere problem can be formulated with one dipole per particle instead of many. For a given dipole at position r_i,

$$P_i = \alpha_i E_{\mathrm{loc}}(r_i) \quad (43)$$

where $E_{\mathrm{loc}}(r_i)$ is the sum of the incident plane wave, $E_{\mathrm{inc},i} = E_0 \exp(ikr_i - i\omega t)$, and the retarded fields

$$-\mathbf{A}_{ij}\cdot\mathbf{P}_j = \frac{\exp(i\mathbf{k}\cdot r_{ij})}{r_{ij}{}^3}\left[\mathbf{k}^2 r_{ij} \times (r_{ij} \times \mathbf{P}_j) + \frac{(1 - i\mathbf{k}r_{ij})}{r_{ij}{}^2} \times \{(r_{ij}{}^2\cdot\mathbf{P}_j) - 3r_{ij}(r_{ij}\cdot\mathbf{P}_j)\}\right] \quad (j \neq i) \quad (44)$$

of the other $N - 1$ dipoles, and $\mathbf{R}$ is a polarizability tensor with elements $\alpha_{kl} = \delta_{kl}\cdot\alpha_1$. Use of the retarded field expression eliminates the need for explicit modeling of the time dependence of the fields and polarizations. Thus,

$$(\alpha^{-1})\mathbf{P}_i + \sum_{j\neq i}\mathbf{A}_{ij}\cdot\mathbf{P}_j = \mathbf{E}_{\mathrm{inc},i} \quad (45)$$

The N linear complex equations for three-vectors $\mathbf{P}_j$ and $\mathbf{E}_{\mathrm{inc},i}$ can be formulated as a single $3N$-dimensional matrix equation, where $\mathbf{P}$ and $\mathbf{E}_{\mathrm{inc}}$ are $3N$ vectors and $\mathbf{A}$ is a $3N \times 3N$ symmetric matrix constructed from the 3×3 interparticle interaction matrices $\mathbf{A}_{ij}$, with additional terms, $\alpha_1{}^{-1}$, along the diagonal. Higher multipole couplings could also be included. However, for aggregates composed of fairly uniformly packed small spheres separated by distances that are substantial relative to the particle diameter, those do not need to be included.

2.4.4. Discrete Dipole Approximation (DDA)

The description of aggregates of nanoparticles presents a number of additional complications compared with single particles, but in some cases, great simplifications are possible, depending on the number and density of nanoparticles in the aggregates. If the aggregates have only a few particles, then it may be possible to solve Maxwell's equations explicitly using the DDA approach, with each particle in the aggregate represented by polarizable elements that are coupled together to determine the overall polarization response.[234] This approach has the advantage of allowing one to describe aggregates wherein the particles have arbitrary shapes, sizes, compositions, and geometrical arrangements (touching and partially coalescing). The disadvantage is that the number of elements needed to describe an aggregate is often very large even for 10 coupled particles.

There are now several approaches available for describing nonspherical particles, but the majority of recent applications to isolated particles have been done using the finite element discrete dipole approximation (DDA) theory. The DDA methods divide the particle into a large number of polarizable cubes. The induced dipole polarizations in these cubes are determined self-consistently, and then properties like the extinction cross-section are determined using the induced polarizations. The discrete dipole approximation was originally proposed by Purcell and Pennypacker in 1973.[123] However, it has only become an important computational tool in the past decade due to the work of Draine, Flatau, and Goodman,[200,201] and its application to chemical problems was introduced by Schatz and Van Duyne.[172] This method circumvents the imposition of difficult boundary conditions in the light scattering calculations by dividing the particle into elements and allowing the elements to interact only through dipole−dipole interactions. In this approach, it is assumed that the particle is represented by a cubic array of N point dipoles with polarizabilities denoted as α_i and centers at position r_i. The interaction of each dipole with a local electric field, $\mathbf{E}_{\mathrm{loc}}$ will induce a polarization given by (omitting frequency factors, $e^{i\omega t}$) eq 43. For isolated particles, $\mathbf{E}_{\mathrm{loc}}$ is the sum of the incident field, $\mathbf{E}_{\mathrm{inc}}$ and the dipole field, $\mathbf{E}_{\mathrm{dip}}$ (arising from all other dipoles in the particle), as

$$\mathbf{E}_{\mathrm{loc}}(r_i) = \mathbf{E}_{\mathrm{loc},i} = \mathbf{E}_{\mathrm{inc},i} + \mathbf{E}_{\mathrm{dip},i} = \mathbf{E}_0 \exp(i\mathbf{k}\cdot r_i) - \sum_{j\neq i} \mathbf{A}_{ij}\cdot\mathbf{P}_j \quad (46)$$

where $\mathbf{E}_0$ and $\mathbf{k}$ are the amplitude and wave vector of the incident wave, respectively. The interaction matrix $\mathbf{A}$ has the form

$$\mathbf{A}_{ij}\cdot\mathbf{P}_j = \frac{\exp(i\mathbf{k}\cdot r_{ij})}{r_{ij}^{\;3}}\Bigg[\mathbf{k}^2 r_{ij} \times (r_{ij} \times \mathbf{P}_j) + \frac{(1 - i\mathbf{k}r_{ij})}{r_{ij}^{\;2}} \times \{(r_{ij}^{\;2}\mathbf{P}_j) - 3r_{ij}(r_{ij}.\mathbf{P}_j)\}\Bigg] \quad (j \neq i) \quad (47)$$

where $\mathbf{k} = \omega/c$. Substituting eqs 46 and 47 into eq 43 and rearranging terms, we generate an equation of the form

$$\mathbf{A}'\cdot\mathbf{P} = \mathbf{E} \quad (48)$$

where $\mathbf{A}'$ is a matrix that is built out of the matrix $\mathbf{A}$ from eq 47. For a system with N total dipoles, $\mathbf{E}$ and $\mathbf{P}$ are $3N$-dimensional vectors and $\mathbf{A}'$ is a $3N \times 3N$ matrix. Solving this set of $3N$ complex linear equations allows the polarization vector $\mathbf{P}$ to be obtained, and consequently the optical properties, such as the extinction cross-section, to be calculated. The explicit expression for the extinction cross-section is

$$C_{\mathrm{ext}} = \frac{4\pi k}{|\mathbf{E}_0|^2}\sum_{j=i}^{N} (\mathbf{E}^*_{\mathrm{loc},j}\cdot\mathbf{P}_j) \quad (49)$$

To solve this system of $3N$ complex linear equations, an adaptation of an approach developed by Draine and Flatau[200] can be used in which they have developed a program that utilizes fast Fourier transform methods to perform the sum over dipole fields in eq 46 and complex conjugate gradient techniques to solve eq 48. The polarizabilities, α_i, are related to the dielectric constant, ϵ, of the particle by an expression (lattice dispersion relationship) from Draine and Goodman.[201] This expression forces the optical response of a bulk dipole lattice to match that of bulk material once the calculation is converged with respect to the dipole density. Although this does not guarantee that DDA will give exact results for finite size particles, comparisons with exact analytical solutions for spherical particles (i.e., Mie theory) show that accurate results (typically within 5% of the correct extinction cross-section) are always obtained provided that the calculation is converged.

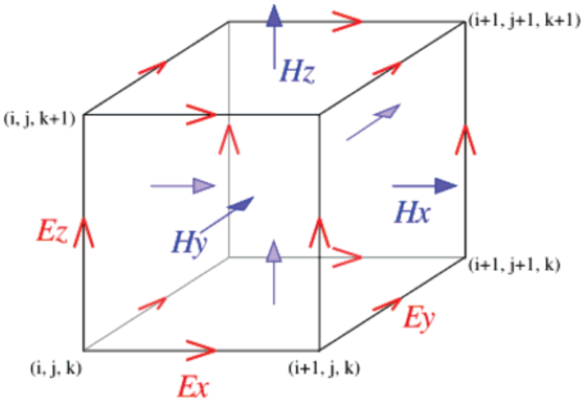

Figure 10. Illustration of a standard Yee lattice used for FDTD, in which different field components use different locations in a grid. Visualized as a cubic voxel, the electric field components correspond to the edges of the cube and the magnetic field components to the faces. The sign of the charges corresponds to an empty sphere in the dielectric surrounding.

2.4.5. Finite-Difference Time-Domain (FDTD) Method

Finite-difference time-domain (FDTD) method is a popular computational electrodynamics modeling technique that is easy to understand and implement in software packaging. The FDTD method belongs to the general class of grid-based differential time-domain numerical modeling methods. Since it is a time-domain method, solutions can cover a wide frequency range with a single simulation run. Maxwell's equations are modified to central-difference equations, discretized, and implemented in software. The equations are solved in a leapfrog manner: the electric field is solved at a given instant of time, then the magnetic field is solved at the next instant, and the process is repeated over time and again. The basic FDTD space grid and time-stepping algorithm trace back to a seminal 1966 paper by Kane Yee[244] and its corresponding "FDTD" acronym was originated by Allen Taflove in 1980.[245] Since about 1990, FDTD techniques have emerged as a primary means to computationally model many scientific and engineering problems dealing with electromagnetic wave interactions with material structures. Current FDTD modeling applications range from near-DC through microwaves to visible light and are widely used to simulate the expected performance of photonic crystals, nanoplasmonics, solitons, and biophotonics.

The method is an explicit time-marching algorithm used to solve Maxwell's curl equations on a discretized spatial grid.[246] When Maxwell's differential equations are examined, it can be seen that the change in the **E**-field in time (the time derivative) is dependent on the change in the **H**-field across space (the curl) as shown in Figure 10. This results in the basic FDTD time-stepping relation that, at any point in space, the updated value of the **E**-field in time is dependent on the stored value of the **E**-field and the numerical curl of the local distribution of the **H**-field in space. The **H**-field is time-stepped in a similar manner. At any point in space, the updated value of the **H**-field in time is dependent on the stored value of the **H**-field and the numerical curl of the local distribution of the **E**-field in space. Iterating the **E**-field and **H**-field updates results in a marching-in-time process wherein sampled data analogues of the continuous electromagnetic waves under consideration propagate in a numerical grid stored in the computer memory. There are certain advantages of using FDTD for simulating photonic crystal and nanophotonic devices: the algorithm is rigorous; it can handle dispersive materials including metals and the simulation in time domain.

2.4.6. Isotropic vs Anisotropic Colloidal Assemblies

During the last 5 years, much attention has been focused toward the synthesis, characterization, and application of functional nanoassemblies based on anisotropic metal nanoparticles. The properties of anisotropic nanoparticles have raised tremendous interest, not only because deviation from the spherical geometry leads to much larger variations in physical and chemical properties than those derived from changes in particle size (in particular for metal nanoparticles) but also because of the high degree of sophistication that such geometries offer from the point of view of the creation of nanostructured materials that can be useful for a large number of applications. For example, linear nanoarrays based on metal nanoparticles[247−249] offer a huge potential applications not only in microelectronics[250] but also in photonics, since the use of metal nanoparticle chains for wave guiding via surface plasmons has been predicted.[251−256] For analytical application of such systems, it is important not only to be able to manipulate the interparticle interactions on the nanoscale but also to understand their optical response in the cases of the various geometries arising due to the synthetic condition. In the calculation of optical response of an aggregate of small spherical particles, several approximations are often made as discussed in section 2.4.1. These include, for example, the quasistatic approximation, the neglect of high-*n* multipolar polarizabilities, restriction to highly symmetric geometrical arrangement of spherical particles, and the use of a local dielectric function. The second approach is to consider the particle aggregate as a homogeneous sphere with a suitably chosen average dielectric function. But models considering an aggregate by an equivalent homogeneous sphere have major deficiencies. Aggregates actually have irregular shapes, and their “surfaces” are extremely rough. Furthermore, the distribution of the particles is inhomogeneous and correlated in such a way that the validity of the average dielectric function is questionable. Under such situations, it will be convenient to consider a statistical average over a large number of aggregates with irregular shapes and to make the corrections of the deficiencies of the homogeneous sphere model. However if the aggregate is nonspherical, then the solution to Maxwell’s equations can be just as difficult, in principle, as that for a nonspherical single particle. Although generating a numerical solution is conceptually straightforward, because of the complex shape of the particles of interest, and their complex environment, doing this can be difficult. However, a great deal of effort has been put into developing numerical methods. In fact, since the classical electrodynamics problem is also relevant to radar and medical imaging, the literature on numerical methods is enormous. However, there are some important challenges and simplifications associated with metal nanoparticles that limit the applicability of methods used to study problems with much longer wavelengths and length scale.

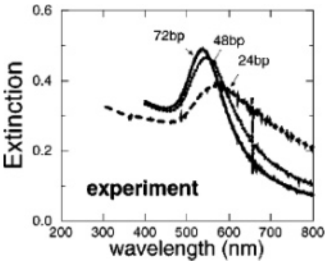

Figure 11. Comparison between experimental and theoretical extinction spectra for DNA-linked 16 nm gold particles, showing results for 24, 48, and 72 base-pair duplexes. Calculated extinction is the extinction cross section normalized by the Au volume [units of (μm)$^{-1}$]; Au volume fractions are 0.07, 0.12, and 0.24 for 72, 48, and 24 base pairs, respectively. Reprinted with permission from ref 234. Copyright 2001 Elsevier.

A comparison has been made by Schatz between measured and calculated extinction spectra for DNA-linked gold nanoparticle aggregates, where the aggregate has been modeled as being spherical. The measured spectra are from recent measurements from the Mirkin group.[115] The aggregates are composed of 16 nm gold particles linked with three different lengths of DNA, namely, 24-, 48-, and 72-mer DNA linkers (will be discussed in section 3.1.1.2), along with 16 nm gold particles, while it has been demonstrated that the length of DNA controls the mean distance between the particles and that the particle density is consistent with arrangement of the particles on a body-centered cubic lattice. If it is assumed that the aggregates have a spherical shape with a diameter of 300 nm, then the effective-medium theory yields the extinction spectra shown in Figure 11. This figure shows that effective medium theory is able to describe the red shifting and broadening of the plasmon resonance that occurs as the aggregate linkers vary from 72 base pairs, where the particles are spaced by 20 nm, to 24 base-pairs, where the particles are spaced by 7 nm. Recently, it has been demonstrated[31] that the EMT results in Figure 12 are almost identical to what is obtained from coupled dipole calculations on the same aggregates. This validates the use of effective-medium theory for this calculation.

Now let us see the influence of aggregate shape on extinction spectra. In recent work,[31] the DDA method was used to calculate spectra of aggregates of 13 nm Au particles linked by 24-mer DNA and having a Au volume fraction of 0.155. Spectra of aggregates having 5:1 oblate and prolate spheroidal shapes are shown in Figure 12. These aggregates have the same volume as a spherical aggregate whose diameter is 234 nm, and for comparison, the spectrum of the spherical aggregate has been included. In this case, the spectra have been averaged over orientation of the polarization and propagation axes of the incident light relative to the principal axis of the spheroidal aggregates. It is clear from the figure that while the ellipsoidal aggregates have slightly higher extinctions in the UV than the spherical one and they have plasmon bands that are slightly less red-shifted and less broadened, the spectra are remarkably similar. From this, it can be concluded that the comparisons in Figure 11 are not sensitive to the aggregate shape used in the calculation.

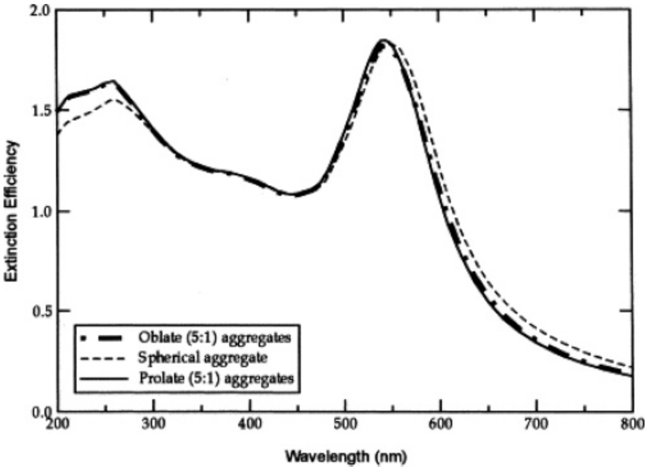

Figure 12. Extinction spectra of DNA-linked gold nanoparticle aggregates in water: orientational averages of spectra of ellipsoidal aggregates. The spectra are similar, indicating that spectra of ensembles of randomly oriented equivolume ellipsoidal aggregates are aggregate shape independent. Reprinted with permission from ref 234. Copyright 2001 Elsevier.

3. Synthetic Strategies in Making Nanoscale Gold Assemblies

The ability to engineer materials at the nanoscale level is crucial in the development of new technologies.[257−259] Studies of metal nanoparticles continue to reveal fundamental information regarding the size-, shape-, and medium-dependent optical and electronic behaviors of nanoscopic materials.[260−266] Among the many attributes of nanoparticle scaffolds is their ability to be synthetically manipulated in terms of size and surface functionality, often exhibiting intrinsic functionality such as magnetism, photoluminescence, or catalytic activity. The assembly of nanoparticles provides opportunities for exploring the fine-tunable interparticle spatial and macromolecular properties in many areas of nanoparticle structured technologies.[113] This utility can be extended through noncovalent assembly methods that possess the ability to regulate spacing and structure in the resulting nanocomposite systems. Directed self-assembly of nanometer-sized building blocks using noncovalent interactions (e.g., hydrogen bonding, acid−base proton transfer, and electrostatic forces) has been proven as an effective way to create tailored nanomaterials.[267−269] Some of the existing assembly strategies also involve layer-by-layer,[270] DNA,[271] polymeric recognition,[272] and mediator templating[115,273,274] of molecularly capped nanoparticles. Much of this research has involved characterization of collective properties of disordered and crystalline two-dimensional (2D) and three-dimensional (3D) arrangements of clusters.[275−277] Optical absorption and electron hopping in these nanoparticles are strongly dependent on the distance and medium between particles. The synthetic strategies in making nanoscale gold assemblies can be categorized into two major approaches: *in situ* formation of nanoscale gold aggregates and the induced aggregation among already formed gold particles. These two strategies with recent citations (we have only cited the variation in synthetic methodologies based on some recent publications) are discussed in detail as follows.

3.1. *In Situ* Formation of Nanoscale Gold Aggregates

3.1.1. Biologically Programmed Nanoparticle Assembly

3.1.1.1. Antigen−Antibody Interactions. In recent years, there has been growing interest among chemists to incorporate complementary receptor−substrate sites into the molecule and to attach complementary receptor−substrate sites to the surface of metal nanoparticles.[278] The highly specific recognition properties of antibodies and antigens make them excellent candidates for the programmed assembly of nanoparticles in solution. Indeed, the versatility of using preformed nanoparticles in association with antigen−antibody engineering should make it possible to assemble a wide range of nanoparticle-based structures with specific cross-linked structures, compositions, and macroscopic structures (Scheme 1).

Streptavidin−biotin binding is an ideal model for protein−substrate nanocrystal assembly because the complex has one of the largest free energies of association known for noncovalent binding of a protein and small ligand in aqueous solution ($K_a > 10^{14}$ M^{-1}). Moreover, there exist a range of readily accessible analogues with K_a values of 10^0−10^{15} M^{-1} that are extremely stable over a wide range of temperature and pH. In principle, reversible cross-linking of biotinylated nanoparticles should occur because the tetrameric structure of streptavidin provides a connecting unit for three-dimensional aggregation (Figure 13).

The use of streptavidin−biotin recognition motif in nanocrystal aggregation has been reported by Mann et al.[278] Gold nanocrystals were functionalized by chemisorption of a disulfide biotin analogue (DSBA) and then cross-linked by multisite binding on subsequent addition of protein, streptavidin (Figure 13). The assembly of gold nanocrystals was monitored using dynamic light scattering, which yields an average hydrodynamic radius of all particles in solution. Addition of streptavidin gave a rapid increase in the average hydrodynamic radius that obeyed the expected power law ($P < 0.0001$) for diffusion-limited aggregation. Aggregation was also monitored by a red to purple color change in the sol that was attributed to the distant-dependent optical properties of gold nanoparticles. Transmission electron microscopy (TEM) images showed that the unmodified gold nanocrystals were present mostly as single particles, whereas the biotin-coated particles underwent aggregation following addition of streptavidin. Subsequently, the nanocrystals were invariably separated from each other by approximately 5 nm, consistent with the separation expected for streptavidin cross-linking. The results indicate that aqueous dispersions of gold nanocrystals possessing a narrow size distribution can be readily modified by chemisorption of DSBA and subsequently assembled by molecular recognition.

3.1.1.2. Modification by Proteins and Oligonucleotides. Since 1996, DNA and its synthetically programmable sequence recognition properties have been utilized to assemble nanoparticles functionalized with oligonucleotides into preconceived architectures the origin of which may be traced to the method (Scheme 2) reported by Mirkin et al.[115] These strategies[82,116,279−283] and off-shoots of them that rely on protein−receptor interactions can be used to generate a wide range of architectures with many unusual and, in some cases, useful chemical and physical properties.[284−287] Since proteins and certain protein receptors can be functionalized with oligonucleotides, one, in principle, could immobilize

Scheme 1. Schematic Representation Showing the Formation of an Idealized Ordered Structure Using Surface-Attached Antibodies and Artificial Antigens for Cross-linking of Gold Nanoparticles[a]

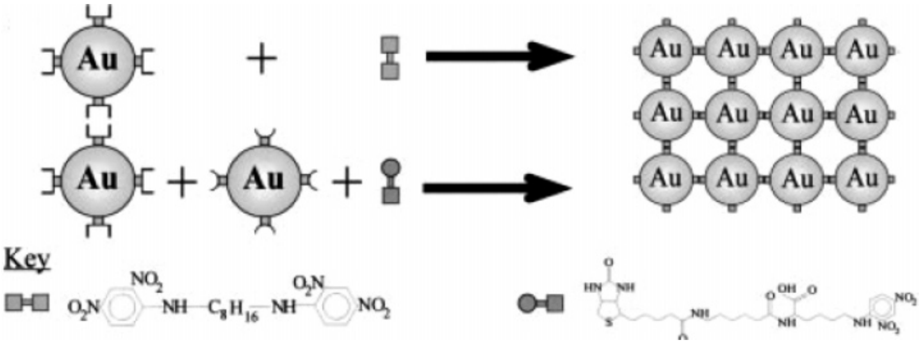

[a] Reprinted with permission from ref 278. Copyright 2000 Wiley-VCH.

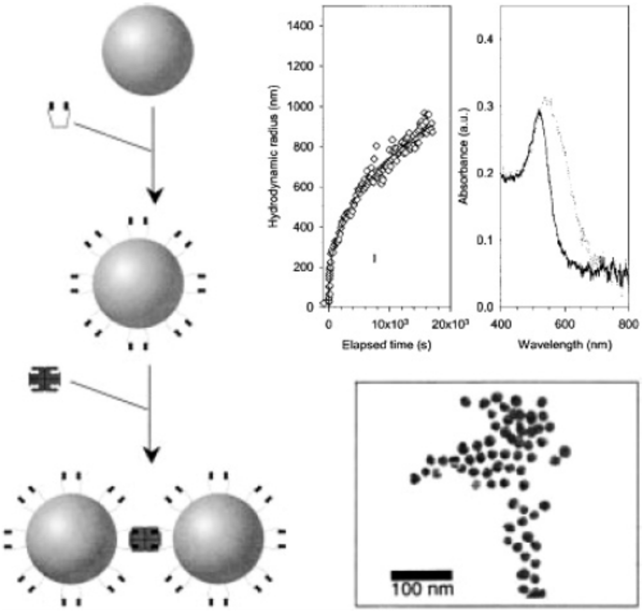

Figure 13. The streptavidin−biotin-programmed aggregation of gold nanocrystals was monitored by dynamic light scattering and the resulting aggregates imaged by transmission electron microscopy. Reprinted with permission from ref 278. Copyright 2000 Wiley-VCH.

such molecules onto oligonucleotide-modified nanoparticles and generate a new class of hybrid particles that exhibit the high stability of the oligonucleotide-modified particles with molecular recognition properties that are dictated by the surface-immobilized protein or receptor rather than DNA. Alternatively, one could functionalize a protein that has multiple receptor binding sites with receptor-modified oligonucleotides so that the protein−receptor complex could be used as one of the building blocks, in place of one of the inorganic nanoparticles. Particles with surface-adsorbed proteins have played an important role in immunochemistry, and the development of stable protein−particle conjugates where the protein does not directly interact with the nanoparticle surface could lead to improved nanoparticle probes for histochemical studies and immunoassays.

Letsinger and colleagues[288] have reported a method to synthesize a nanoparticle/protein assembly utilizing 13 nm gold particles, streptavidin, and biotinylated oligonucleotide to explore these hypotheses and some of the physical and chemical properties of the resulting new bioinorganic materials. The nanoparticle−protein assembly relies on three building blocks: streptavidin complexed to four biotinylated oligonucleotides (**1**-STV), oligonucleotide-modified gold

Scheme 2. Schematic Representation of DNA-Directed Assembly of Gold Nanoparticles and Streptavidin[a]

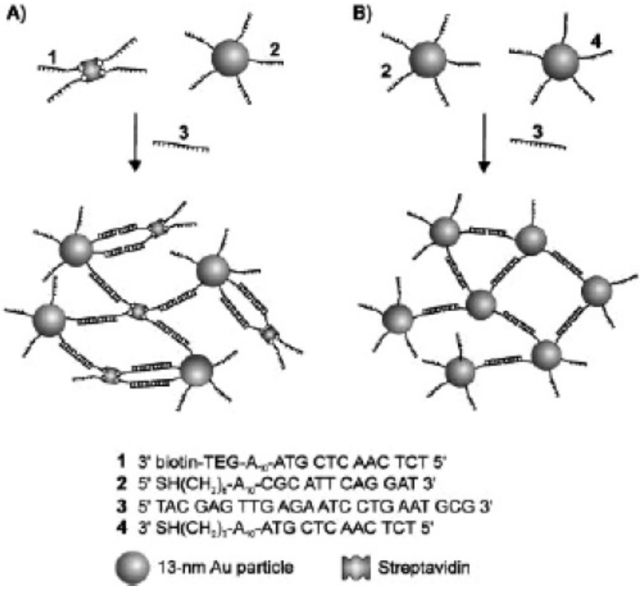

[a] (A) Assembly of oligonucleotide-functionalized streptavidin and gold nanoparticles (Au−STV assembly). (B) Assembly of oligonucleotide-functionalized Au nanoparticles (Au−Au assembly). Please note that **1** and **4** have the same DNA sequence. Reprinted with permission from ref 288. Copyright 2001 Wiley-VCH.

nanoparticles (**2**-Au), and a linker oligonucleotide (**3**) that has one-half of its sequence complementary to **1** and the other half complementary to **2** (Scheme 2). In a typical experiment, linker DNA (**3**) was introduced to a mixture of **2**-Au in 0.3 M phosphate-buffered saline. Aggregates with similar properties could be formed by both methods, but premixing **3** and **1**-STV facilitates aggregate formation. Since a 13-nm gold particle is substantially larger than streptavidin,[284−287] a 1:20 molar ratio of gold nanoparticle to streptavidin was used to favor the formation of an extended polymeric structure rather than small aggregates comprised of a few nanoparticles or a structure consisting of a single gold nanoparticle functionalized with a hybridized layer of streptavidin.

It was seen that when **1**-STV, **2**-Au, and **3** were mixed at room temperature, no significant particle aggregation took place, even after 3 days, as evidenced by an unperturbed UV−vis spectrum of the solution. However, raising the temperature of the solution (53 °C) to a few degrees below the melting temperature of the DNA interconnects resulted in the growth of micrometer-sized aggregates (Figure 14A)

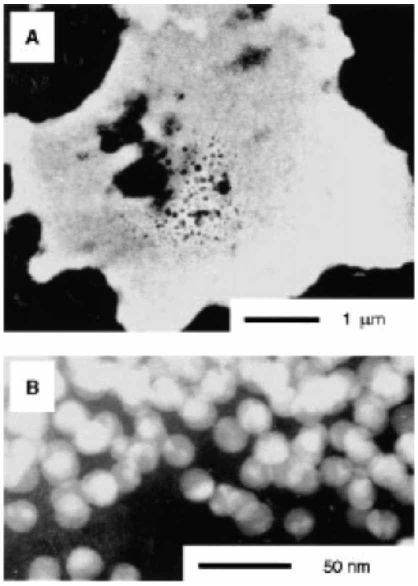

Figure 14. TEM images of 24-mer DNA-linked aggregates of gold nanoparticles and streptavidin: (A) low-magnification image showing an entire aggregate; (B) high-magnification image of a portion of the aggregate. Reprinted with permission from ref 288. Copyright 2001 Wiley-VCH.

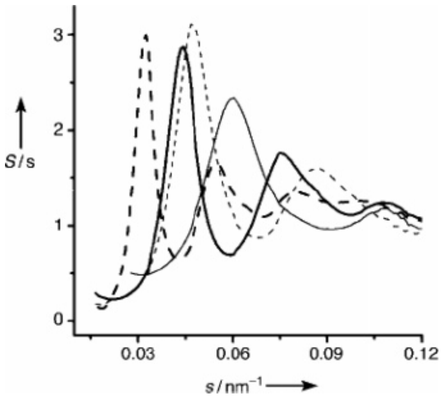

Figure 15. Structure factors of the DNA-linked Au−STV and Au−Au assemblies (—, 24-mer-linked, − − −, 48-mer-linked) —from SAXS patterns. Reprinted with permission from ref 288. Copyright 2001 Wiley-VCH.

and the characteristic red shift and dampening of the gold surface plasmon resonance associated with particle assembly.[115] The transmission electron micrograph (Figure 14B) shows that the particles within the aggregates retain their physical shape prior to and after annealing, which indicates the stabilizing action of surface oligonucleotide layer.

Small-angle X-ray scattering (SAXS)[282,288−290] data were collected for aggregates formed from the gold nanoparticles and streptavidin building blocks (**1**-STV, **2**-Au) and two different lengths of DNA-linker (24-mer (**3**) and 48-mer), and the results were compared with those for aggregates based on a Au−Au assembly with the same linking oligonucleotides (**2**-Au, **4**-Au, 24-mer linker (**3**), 48-mer linker; Figure 15). The aggregates linked by DNA showed relatively well-defined diffraction peaks, and the Au−STV aggregates exhibited diffraction peaks at smaller *s* values than the Au−Au aggregates formed from the same linker. This observation suggests a larger interparticle distance between the gold centers in the Au−STV system. Furthermore, the diffraction peaks shifted to smaller angles when 48-mer DNA was used as a linker instead of the 24-mer for both the Au−Au and Au−STV assemblies (Figure 15).

The pair distance distribution function (PDDF), $g(r)$, has been calculated from the SAXS patterns as

$$g(r) = 1 + (1/2\pi^2\rho r)\int q(S(q) - 1)\sin(qr)\,\mathrm{d}q \quad (50)$$

where $g(r)$ gives the probability of finding a second particle as a function of distance r from a chosen particle, $q = 4\pi/\lambda \sin(\theta)$, and ρ is the particle number density.[288,289] The nearest neighbor interparticle Au−Au distances (center-to-center distance) obtained from the PDDFs are 19.3, 25.4, 28.7, and 40.0 nm for the 24-mer linked Au−STV and 48-mer Au−STV assemblies, respectively. A comparison of the interparticle distances for the Au−STV system and the Au−Au system clearly shows that the Au−STV assembly has the Au nanoparticle/streptavidin periodicity and that the two components (Au nanoparticle and streptavidin) are well separated by rigid DNA duplex linkers.[291,292]

3.1.2. Organic Ligand Modified Nanoparticle Building Blocks

3.1.2.1. Thiols and Their Derivatives. For the precise control of nanoscale architecture and component miniaturization, most existing approaches explore the strong affinity of thiols to gold (monolayer-capping via two-phase synthesis,[293] place-exchanging,[113] stepwise assembling,[270−272] etc.) and disulfides,[294] thioethers,[295] thioacetate groups,[296] and tetradentate thioether ligands[297] have recently been used to mediate the formation of spherical or related assemblies of gold nanoparticles. Although many preparation methods for gold nanoparticles have been described,[113,293,298] a challenge persists to prepare well-defined, controlled assemblies in one-, two-, and three-dimensions.[299] One dimensional assemblies are a "Holy Grail" in nanoparticle science because of their anticipated transport (optical and electrical) properties.[300−302] Several approaches have been described in the literature for the synthesis of 1D assemblies of gold nanocrystals, namely, DNA-template[303,304] and polymer-template[305] methods and combinations of scanning tunneling microscopy based chemistry and nanoparticle self-assembly.[306,307]

Recently, a synthetic strategy was described for the 1D assembly of gold nanoparticles on surfaces.[308] Scheme 3 provides a schematic overview of the overall process. An electron beam is used to write patterns on an ultrathin film of Au(I) thiolate materials, and subsequent pyrolysis of the patterns allows for gold nanoparticle growth upon removal of the organic material. The combination of such precursor materials with the electron beam lithography technique provides a flexible and rapid method for producing a 1D array of gold nanoparticles. This template-free technique allows one to obtain size-selective, controllable, and defect-free assemblies on a large scale.

Briefly, the Au(I) thiolate complexes are synthesized using readily available precursors following the adaptation of a published route.[309] The thiols used to prepare the Au(I) thiolates are thiocholesterol and polystyrenethiol (PS19-SH; 19 units of styrene), yielding Au(I) thiocholesterol and Au(I) PS19, respectively. After development, organometallic lines with widths as narrow as 15 nm are obtained (Figure 16A) when the center-to-center distance between two consecutive e-beam spots is small (e.g., 2.5 nm) and effective overlap of the exposure spots is possible. Subsequent pyrolysis (450 °C) of this organometallic line in a mixed atmosphere of

Scheme 3. Schematic Representation of the Fabrication Method[a]

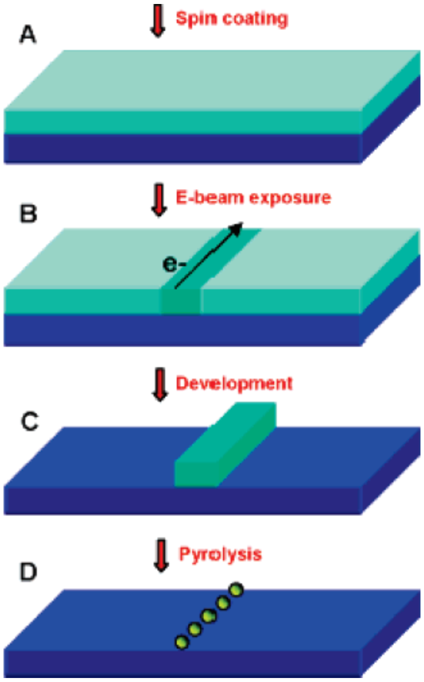

[a] (A) A thin film of Au(I) thiolate is spin-coated on a substrate. (B) The thin film is partially exposed to a focused electron beam. The resulting exposed region is outlined in darker blue. (C) Upon development in an organic solvent, the unexposed areas are dissolved away and only the beam-exposed organogold pattern remains on the substrate. (D) After pyrolysis, a 1-D gold nanoparticle array appears on the substrate. Reprinted with permission from ref 308. Copyright 2006 American Chemical Society.

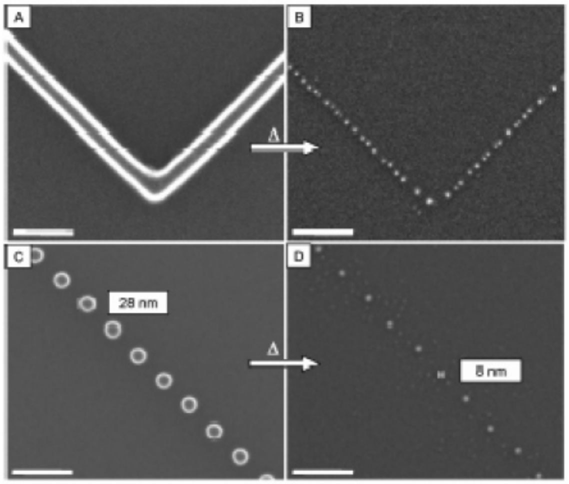

Figure 16. FEG−SEM images of Au(I)-PS19 patterns written with an e-beam spot center-to-center distance of 2.5 (A) and 60 nm (C) on p-doped Si and of the corresponding gold nanoparticle arrays after pyrolysis (B, D). Scale bars in panels A−D = 100 nm. Reprinted with permission from ref 308. Copyright 2006 American Chemical Society.

oxygen and nitrogen yields a 1D line of single gold nanoparticles (Figure 16B). When the center-to-center distance of the e-beam spot exposure is increased to larger values (for example, to 60 nm), 1D assemblies of cylinders of the organometallic material are obtained after the development step (Figure 16C). Following pyrolysis, 1D lines of 8 nm diameter gold nanoparticles separated by 60 nm are observed (Figure 16D). Assuming a spherical shape of the nanoparticle, the nominal volume of gold present in a given organogold nanocylinder corresponds to the gold volume in a nanoparticle after pyrolysis of the nanocylinder.

Scheme 4. Phenylacetylene Oligomers I and II (PA I, II)[a]

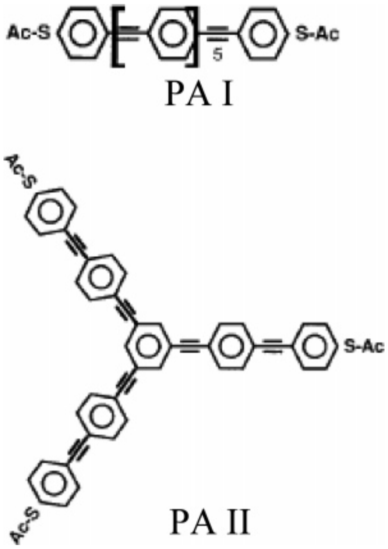

[a] Reprinted with permission from ref 319. Copyright 1999 Wiley-VCH.

3.1.2.2. Amines and Their Derivatives. The fundamental and applied advances related to extended cluster networks have been formulated by many authors to examine the properties of more discrete assemblies of nanoclusters (dimers, trimers etc.) so that the effects of local symmetry on collective particle properties could be assessed.[310−318] Feldheim and co-workers[319] attempted to synthesize phenylacetylene (PA)-bridged (PA **I, II**; as shown in Scheme 4) gold nanoparticle dimers and trimers from solution. Phenylacetylene oligomers **I** and **II** were chosen as basic linker repeat units, which provide conformational rigidity and a variety of geometries (e.g., linear, bent, trigonal planar, tetrahedral)[320] without significant solubility problems and serve as potential wire candidates for molecular electronic devices. Indeed, it was found that the array symmetry does influence the optical properties in accord with the theoretical predictions.

Gold nanoparticles were synthesized using the citrate reduction method reported by Natan and co-workers.[321] The strategy for formation of gold nanoparticle dimers and trimers involves producing a locally high concentration of the gold sol with respect to the PA linkers. Phenylacetylene-bridged gold nanoparticle dimer formation was followed with time by visible spectroscopy (Figure 17). The shift in plasmon absorption band (525 to 535 nm) was ascribed to an increase in particle aspect ratio upon dimer formation.[223] Moreover, a large oscillator strength is expected for longitudinal plasmon modes, consistent with the absorbance increase observed over time (inset in Figure 17). In contrast to these relatively subtle shifts in plasmon energy, when an excess of PA linkers was added rapidly to a solution of nanoparticles, a broad band was observed centered at ca. 580 nm. This band could be attributed to the cross-linking of particles into large agglomerates. When similar particle linking experiments were performed with the trisubstituted thioester PA **II**, shifts in the plasmon band were not observed. This result is not surprising considering that, although the trimers are larger than the gold monomers, the change in particle aspect ratio upon trimer formation is not substantial. Figure 18 shows the TEM images of well-spaced gold dimers and trimers in which the edge−edge distance was estimated as

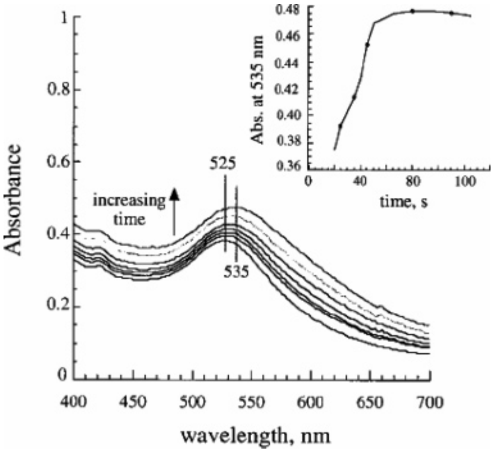

Figure 17. UV−vis spectra of a solution of PA linker I and ca. 12 nm diameter gold particles. Inset shows the absorbance at 535 nm vs time. Reprinted with permission from ref 319. Copyright 1999 Wiley-VCH.

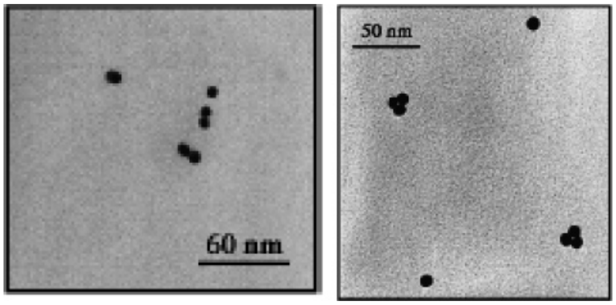

Figure 18. TEM images of (A) PA I bridged gold nanoparticle dimers and (B) PA II bridged gold nanoparticle trimers. Reprinted with permission from ref 319. Copyright 1999 Wiley-VCH.

5 nm, close to the value of a seven phenyl unit PA oligomer. The structures have been proven to be useful in assessing electronic communication between nanoscopic metal spheres arranged in well-defined symmetries.

3.1.2.3. Fullerenes. Since the discovery of C_{60} ([C_{60}]-fullerene), there has been a tremendous amount of research focused on the synthesis of C_{60}-based organic or inorganic nanocomposites including C_{60} thin films.[322−325] Fullerene (C_{60})-capped nanoparticles have recently begun to attract interests of materials researchers.[294,296,318,326,327] Chemically modified C_{60} has been used to covalently attach C_{60} to solid surfaces and polymeric organic and inorganic matrices,[322−325] and they have exhibited new optical and electronic responses.[113] Examples include van der Waals interaction based assembly of unfunctionalized C_{60} and gold nanoparticles,[326] covalent layer-by-layer assembly of C_{60}-capped nanoparticles,[327] and electrostatically linked C_{60} derivatives to CdTe nanoparticles.[296,318] The well designed assembly of C_{60}-linked nanoparticles on solid surfaces provides a tremendous opportunity for several device applications.[328−332]

The ability to assemble C_{60} nanoparticles into 3D architectures with tunable interparticle chemistry has been recently realized. The method adopted by Shon et al.[333] for the synthesis of C_{60}-linked gold nanoparticles is as follows. The 4-aminothiophenoxide/hexanethiolate-protected gold nanoparticles were synthesized using the modified Brust reaction followed by ligand place-exchange reaction of hexanethiolate-protected gold nanoparticles with 4-aminothiophenol.[334] Unmodified C_{60} was reacted with 4-aminothiophenoxide/hexanethiolate-protected gold nanoparticles in toluene via amination reaction to generate C_{60}-linked gold nanoparticles.[335] Two different methods were used to prepare C_{60}/nanoparticle multilayer films (Scheme 5). First, the functionalized glass slides were alternately soaked in the toluene solution containing C_{60}-linked gold nanoparticles and ethanol solution containing ethylene diamine for at least 24 h for the layer-by-layer growth of nanoparticle films (method 1). Second, the reactive slides were alternately soaked in the toluene solutions containing unmodified C_{60} and 4-aminothiophenoxide/hexanethiolate-protected gold nanoparticles (method 2). The amination reaction of C_{60} facilitated self-assembly of nanoparticles on the glass surfaces for both assembly methods.[336]

Scheme 5. C_{60}/Nanoparticle Multilayer Films[a]

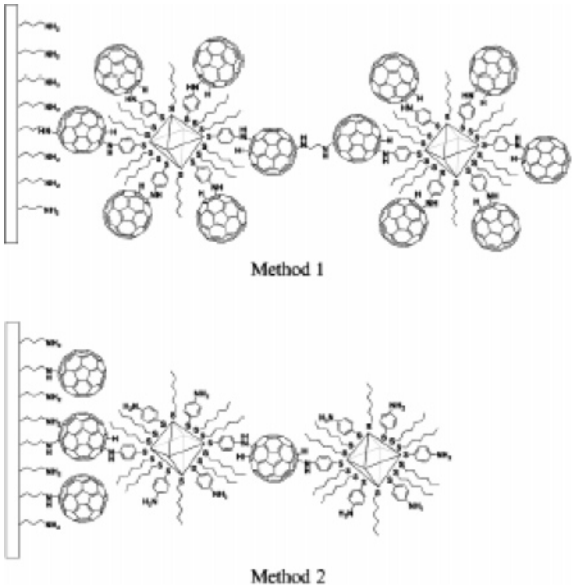

[a] Reprinted with permission from ref 333. Copyright 2002 The Royal Society of Chemistry.

The C_{60}-functionalized gold nanoparticles and 4-aminothiophenoxide/hexanethiolate-protected gold nanoparticles were characterized by UV−vis spectroscopy and transmission electron microscopy. The average diameter of 4-aminothiophenoxide/hexanethiolate-protected gold nanoparticles was 2 nm. Although monolayer-protected gold nanoparticles with this small size fail to exhibit the sharp absorption peak corresponding to the surface plasmon band of gold, the broad absorption at 520 nm could be observed for gold nanoparticle assembly. There was a slight increase and red shift of the gold surface plasmon band of C_{60}-linked gold nanoparticles. This might indicate a decrease in spacing (due to interaction between C_{60} units) between the gold nanoparticles. The UV−vis spectra of nanoparticle multilayer films, which were grown layer-by-layer on the modified glass surface, showed that the surface plasmon band of gold at 580 nm gradually became more evident as successive layers were added to the films (Figure 19). This plasmon band enhancement (and shift from ∼520 nm) suggests that nanoparticle cores approach one another through interactions between C_{60} and amine moieties. TEM images of C_{60}-linked gold nanoparticles also showed the presence of C_{60}-induced small aggregates of nanoparticles upon evaporation of solvents (Figure 20).

In a recent communication, Zhong et al.[337] have reported a novel strategy by exploring the chemically tunable multifunctional interactions between negatively charged groups on gold nanoparticles and positively charged piperazinyl

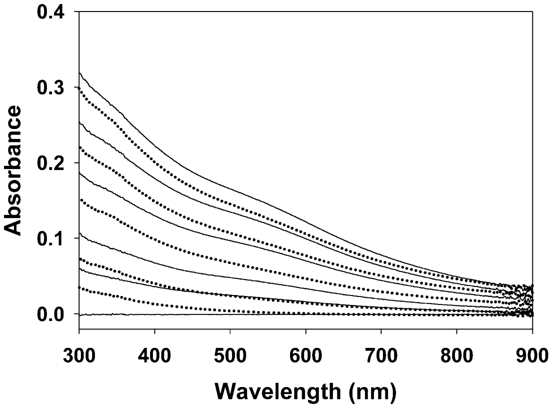

Figure 19. UV−vis absorption spectra of the layer-by-layer assemblies (up to five layers): the dotted lines represent UV−vis spectra obtained after immersion in toluene solution containing C_{60}, and the solid lines represent UV−vis spectra obtained after immersion in toluene solution containing 4-aminothiophenoxide/hexanethiolate-protected gold nanoparticles. Reprinted with permission from ref 333. Copyright 2002 The Royal Society of Chemistry.

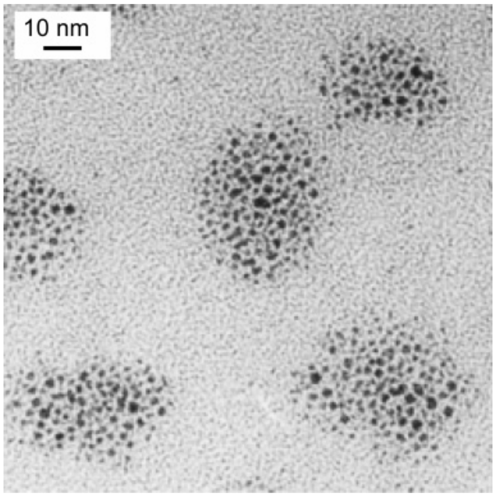

Figure 20. TEM images of C_{60}-induced small aggregates of 4-aminothiophenoxide/hexanethiolate-protected gold nanoparticles. Reprinted with permission from ref 333. Copyright 2002 The Royal Society of Chemistry.

Scheme 6. Schematic Illustration of MPF-Mediated Assembly of Nanoparticles[a]

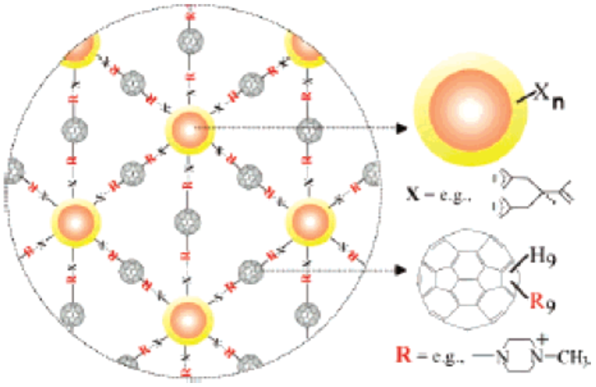

[a] Reprinted with permission from ref 336. Copyright 2005 American Chemical Society.

groups on 1-(4-methyl)piperazinyl fullerene (MPF) (Scheme 6). The multifunctionalized fullerene is used to assemble citrate-capped gold nanoparticles in aqueous solution, and more importantly, it provides electrostatic interaction between the negatively charged nanoparticles and the positively charged fullerenes. In addition to the design of functional nanomaterials (e.g., controlled drug delivery and optical sensing), an important driving force for the fullerene−nanoparticle combination is to harvest the unique electron or energy transfer properties that cannot be obtained with individual gold nanoparticles or fullerenes. Direct evidence comes from the exploration of the photophysical properties in self-organization of porphyrin (donor) and fullerene (acceptor) units by clusterization with gold nanoparticles for organic solar cells.[338] The self-assembly of gold nanoparticles as the central nanocore and appended fullerene moieties as the photoreceptive shell is also demonstrated for a photoactive antenna system.[339] The exploration of these properties expands the well-documented photochemical properties of porphyrinfullerene dyads.[339]

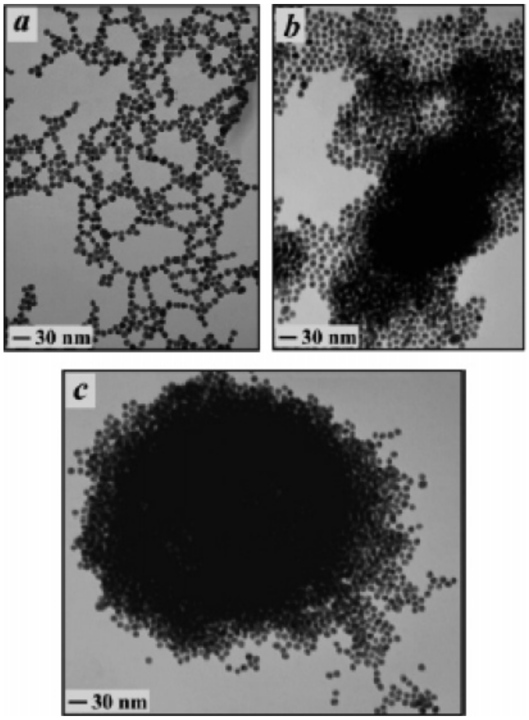

Figure 21. TEM images for (a) Au_{nm} nanoparticles and MPF−Au_{nm} assemblies obtained at (b) $r \approx 4390$ and (c) $r \approx 7440$. Reprinted with permission from ref 337. Copyright 2005 American Chemical Society.

The number of piperazinyl groups on MPF is synthetically or chemically controllable, which can be considered as an ideal building block for defining the interparticle spatial or chemical properties. Citrate-capped gold nanoparticles[340] with average particle size of 11.5 ± 0.6 nm were used as nanoscale building units. The MPF-mediated assemblies of gold nanoparticles were sampled after adding MPF into an aqueous solution of gold nanoparticles and were examined using TEM (Figure 21). In contrast to the relatively scattered 2D fractal morphology for gold nanoparticles (panel a), the observation of highly clustered features with arrays or ensembles of gold nanoparticles for the MPF-mediated assembly (panel b) indicates 3D interparticle linking. The MPF-to-gold nanoparticle molar ratio ($r = [\mathrm{MPF}]/[\mathrm{Au}_{nm}] \approx 1$) translates to ~0.01 piperazinyl groups anchored on fullerene per citrate group capped on gold particles and since the negative charges are 2 orders of magnitude higher than the positive charges on MPF, it is not a simple surface neutralization effect that is responsible for the interparticle assembly.

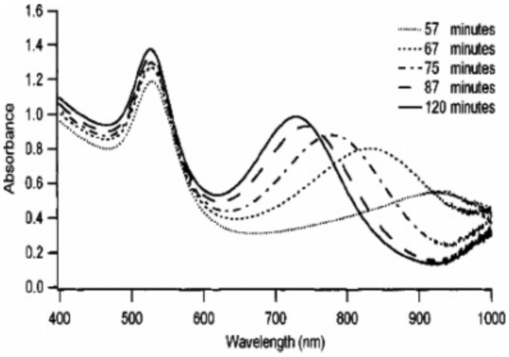

Figure 22. The evolution of the optical absorption spectrum following method C. The second peak shifts from ∼920 to ∼720 nm, while the first remains relatively constant at ∼540 nm. Reprinted with permission from ref 341. Copyright 2002 American Chemical Society.

The size of the assembly was found to increase with the MPF-to-gold nanoparticle molar ratio and assembling time. For $r = 7440$ (panel c), the resulting highly clustered 3D ensemble of gold nanoparticles exhibits a large spherical shape. The fact that there were hardly any free nanoparticles or fractal morphologies being spotted for the MPF-gold nanoparticle samples (panels b and c) was indicative of the interparticle linkages of particles by the multifunctional MPF, which was substantiated by the analysis of the interparticle distance. The edge-to-edge interparticle distance determined from the interconnected gold nanoparticles in the TEM image (panel a) yielded an average value of 1.14 ± 0.20 nm.

3.1.3. Self-Assembly Generated by Inorganic Ligands

3.1.3.1. By Sulfide Coordination. The reduction of $HAuCl_4$ by Na_2S has been reported to produce Au_2S/Au core/shell structures in which gold nanoparticles are present in the form of an aggregate.[341] Zhang et al. performed the reduction of $HAuCl_4$ by Na_2S using methods similar to those of Zhou et al. and presented extensive experimental evidence to demonstrate that the explanation for the observed near-IR absorption is the result of the formation of gold nanoparticle aggregates.[342−344]

Gold nanoparticles were prepared by a variety of methods based on literature methods.[342,345] After approximately 1 h of the preparation of nanoparticles, UV−vis spectrum (Figure 22) shows that the transverse and longitudinal plasma resonances can be seen clearly at ∼520 and ∼920 nm, respectively. Ten minutes later both plasma resonances are blue-shifted. The transverse plasmon shifted to approximately ∼520 nm, and the longitudinal plasmon shifted to approximately ∼825 nm. After 2 h, the transverse plasmon remained at ∼520 nm while the longitudinal plasmon blue-shifted further to ∼720 nm. Both resonances grew in intensity as the reaction progressed; the transverse plasmon remained more intense than the longitudinal plasmon. The TEM data, in general, shows that the methods produce particles with a large particle distribution (for example, Figure 23). Therefore, the optical absorption spectrum is consistent with that seen in gold aggregates and the electron microscopy data suggest that the aggregation process occurred by the coating of Au nanoparticles with S followed by the clustering of the coated particles.

3.1.3.2. Electrostatic Self-Assembly. Polyhedral oligomeric silsesquioxanes (POSS), such as, octaammonium POSS (OA-POSS, Scheme 7) are cubic-shaped molecules that contain an inorganic siloxane core (6 Å^3) surrounded by eight functional organic groups.[346−348] The POSS core units are stable under a variety of conditions, and the nature of the organic groups dictates the solution and solid-state chemical properties and functionalization of these POSS units.[349−355]

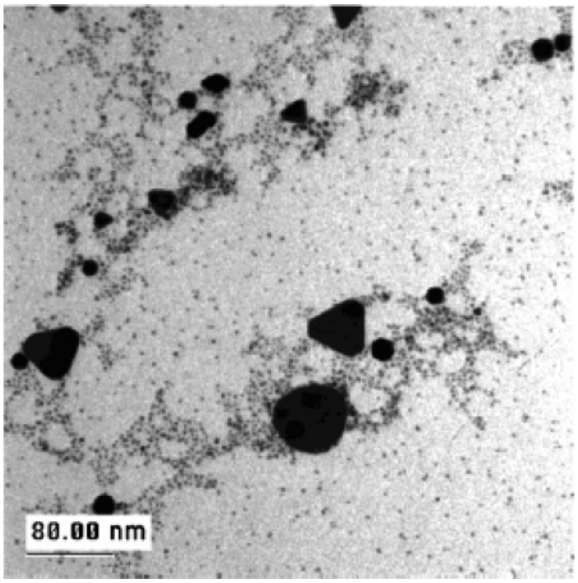

Figure 23. TEM micrograph of gold nanoparticles prepared by method C. The TEM sample was prepared 2 h after the reaction had begun. Reprinted with permission from ref 341. Copyright 2002 American Chemical Society.

Carrol et al.[356] reported the preparation of ordered networks of electrostatically assembled POSS/Au nanoparticles. Carboxylic acid-functionalized nanoparticles (MMPCs) of varying size (1.5 and 6.8 nm) were assembled with octaammonium POSS units resulting in well-ordered, extended structures. The 1.5 nm gold particles used in this experiment (**MMPC1**) were prepared through Brust−Schiffrin[16] methodology. Subsequent, Murray place exchange reaction[357] of mercaptoundecanoic acid into the octanethiol-functionalized gold nanoparticles resulted in ca. 50% acid coverage. The larger 6.8 nm gold particles (**MMPC2**) were prepared by heat treatment method. Samples of electrostatically coupled nanocomposites were prepared from solutions of MMPCs (1.5 and 6.8 nm) into a solution of octa-ammonium POSS. The quarternary ammonium functionalities on the POSS units act as electrostatic cross-linking agents as is shown in Scheme 7. The 1.5 nm particles began to assemble within 2 min as the solution become visibly turbid, indicative of an aggregation process. The 6.8 nm particles assembled more slowly, precipitating fully after 48 h. Obviously, very few POSS molecules are needed to link two 1.5 nm gold particles together given their relative similarity in size. In contrast, an increased number of POSS units (6−10) are needed to cross-link the 6.8 nm particles; the steric and entropic demands of reorganization process for larger particles are evidenced by the slower assembly times.

The SPR of **MMPC2** was monitored by UV−vis spectroscopy before, during, and after the formation of the assembly to investigate the effect of POSS spacing on the optical properties of the gold nanoparticles under investigation. A kinetic experiment was performed measuring the SPR shifts during the aggregation process (Figure 24). Over time, the size of the aggregates in solution becomes increasingly large causing a red shift (Figure 24A) in SPR due to an increase in scattering, which is in good agreement with Mie

Scheme 7. Schematic Illustration Showing (Top) Octa-ammonium Polyhedral Oligomeric Silsesquioxane (OA-POSS) and (Bottom) the Electrostatic Self-Assembly between the (A) 1.5 nm Core (ca. 4 nm with Monolayer) MMPC 1, (B) 6.8 nm Core (ca. 9 nm with Monolayer) MMPC 2 with OA-POSS (ca. 1 Nm), and (C) Control MMPC 1 Precipitated from Hexanes Assembled through Acid−Acid Dimerization[a]

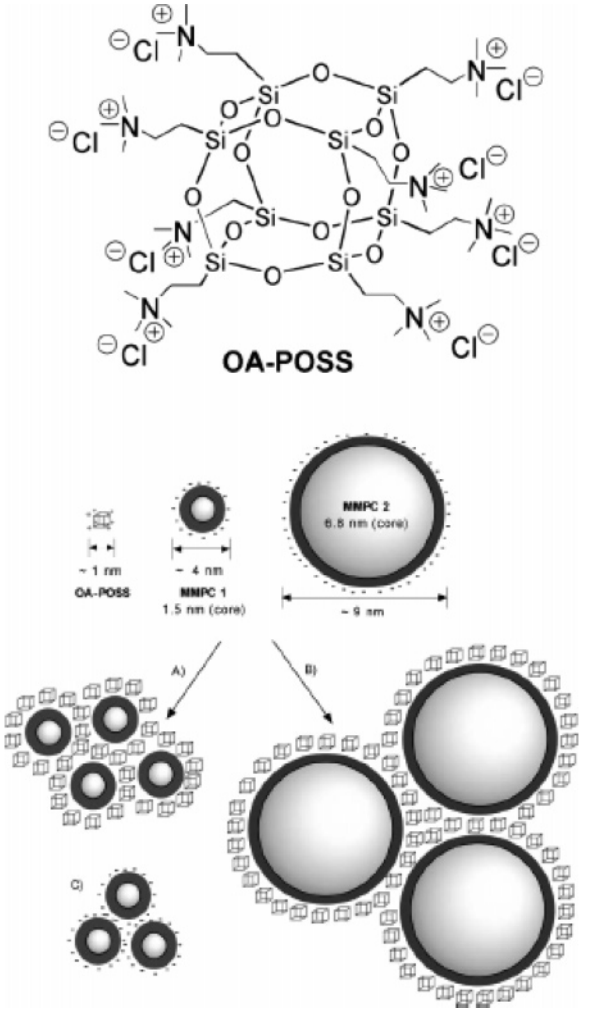

[a] Reprinted with permission from ref 356. Copyright 2004 The Royal Society of Chemistry.

theory.[21,63,82] As precipitation continued over the next several days, the intensity of the SPR band continued to decrease while shifting to longer wavelengths, finally becoming stable at 541 nm. The UV−vis spectrum taken of the aggregates in the solid state reveals a characteristic blue shift to lower wavelengths (Figure 24B). This shift occurs because as two nanoparticles are brought close together, they have a strong dipole−dipole interaction shifting the SPR band to higher wavelengths. As the interparticle spacing between the nanoparticles is increased using POSS units, dipole−dipole interactions are weakened resulting in a blue shift in the SPR band in the UV−vis spectrum.[358,359]

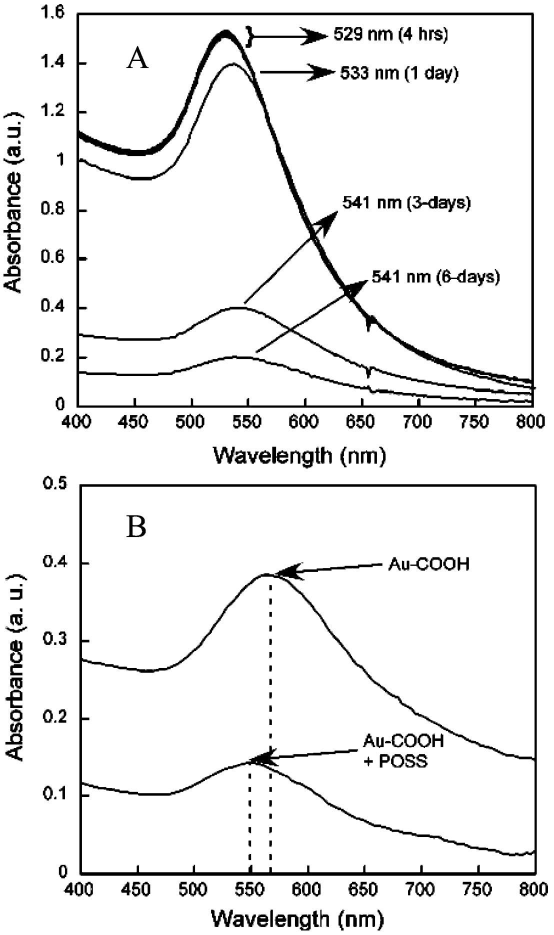

Figure 24. (A) UV/vis spectrum of OA-POSS/MMPC 2 in solution (MeOH) showing a time-dependent red shift in the SPR band of the Au nanoparticles and (B) UV/vis spectrum of OA-POSS/MMPC 2 aggregates and control MMPC 2 (alone) on Mylar films showing a blue shift in the SPR band of the Au nanoparticles. Reprinted with permission from ref 356. Copyright 2004 The Royal Society of Chemistry.

Small-angle X-ray scattering studies were performed to quantify the interparticle spacing within the POSS/Au aggregates. Control 1.5 nm particles **MMPC1** (the nanoparticle alone) exhibited one distinct peak at 1.91*q*, revealing an average interparticle spacing of ca. 3.2 nm (Figure 25A). The value is consisted with the expected interparticle spacing for 1.5 nm gold nanoparticles separated only by their monolayers.[360] Upon assembly with **OA-POSS**, a decrease in the principle *q* spacing to 0.145 is observed correlating to an interparticle spacing of 4.3 nm. This 1.1 nm increase in interparticle spacing is consistent with the average diameter observed for one octa-ammonium POSS unit (ca. 1 nm). This result suggests that only a single layer of POSS is required in order to assemble the nanoparticles, consistent with the cross-linking assembly represented in Scheme 7. The shoulder observed at 0.275*q* can be indicative of some degree of medium-range ordering in these hybrid aggregates. SAXS studies of control **MMPC2** (alone) reveal the presence of one distinct peak at 0.0857*q*, which correlates to a 7.32 nm interparticle spacing between nanoparticles (Figure 25B). This distance agrees well with the projected interparticle spacing between 6.8 nm core Au nanoparticles with an acid-functionalized monolayer. Upon assembly with POSS, the major peak shifts to a lower *q* value of 0.0738 corresponding to an interparticle distance of 8.51 nm. This 1.2 nm increase in interparticle spacing is similar to the 1.1 nm increase in spacing observed with the 1.5 nm particles as a result of electrostatic assembly of one layer of POSS on the periphery of the nanoparticle monolayer. Thus, electrostatic self-assembly can be used to create inorganic/organic nanoscale hybrids with novel architectures.

3.1.3.3. On Silica Substrates. Colloidal aggregates of gold with controlled size and interparticle spacing were synthesized on silica nanoparticle substrates.[361] The distance

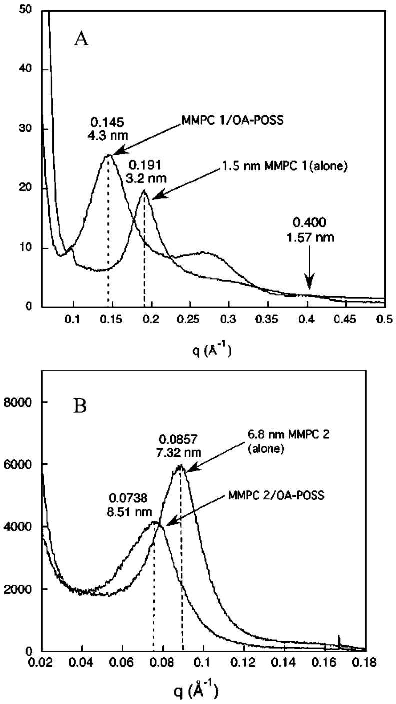

Figure 25. SAXS plots of (A) MMPC 1 and (B) MMPC 2 alone and in aggregates assembled with OA-POSS units. Reprinted with permission from ref 356. Copyright 2004 The Royal Society of Chemistry.

between aggregated gold nanoparticles was primarily controlled by a molecular linker, 4-aminobenzenethiol, which can attach to the surface of gold nanoparticles via either its amine or its thiol functional group and covalently attach the constituent nanoparticles to each other.[362] Short molecular linkers were used so that the interparticle spacing would be small compared with the mean nanoparticle radius.

The silica nanoparticle substrates used in this experiment, the surfaces of which were terminated with amine groups, were grown using the Stöber method.[363,364] Citrate-stabilized gold nanoparticles can be bound to substrates via amine groups;[365] mixing of gold nanoparticles with the functionalized silica nanoparticles resulted in immobilization of a dilute coverage of gold nanoparticles onto the silica nanoparticle surfaces.[366] Upon addition of 4-aminobenzenethiol to a solution of “gold-decorated” silica nanoparticles, one functional group reacted with the immobilized gold nanoparticles while the other functional group was extended outward from the nanoparticles (due necessarily to the rigid nature of the intervening aromatic moiety). After centrifuging and redispersing several times to remove any excess linker molecule, additional gold nanoparticles were added to the solution. These gold nanoparticles were allowed to react with the extended functional group, generating structures in which gold nanoparticles were attached to each other via the rigid molecular linker. The UV−vis extinction spectrum of the solution of linked nanostructures exhibited a markedly different appearance (Figure 26A). This double-peaked spectrum consists of two broad resonances with maxima at 513 and 604 nm (dashed lines). The emergence of the long wavelength peak is consistent with theoretical predictions in the optical spectrum due to plasmon−plasmon interactions between the gold nanoparticles. The second peak is relatively broad because its position is dependent on both the number of the coupled nanoparticles and their relative position with respect to each other and to the incident light. TEM images show that structure of linked gold nanoparticles was prevalent (Figure 26B). After 2 weeks, the observed UV−visible spectrum was only slightly broadened. The spectrum showed no further change over another 8 weeks (Figure 26A, dotted line) indicating the remarkable stability of the final assembled nanostructures.

3.1.4. Surfactant-Mediated Nanoparticle Aggregates

Surfactants, surface-active agents, or detergents are amphiphilic, organic, or organometallic compounds that form association colloids or micelles in solution.[367] Amphiphilic substances, or amphiphiles, are molecules possessing distinct regions of hydrophobic or hydrophilic moieties. Depending on the chemical structure of the hydrophilic moiety bound to the hydrophobic portion, the surfactants may be classified as cationic, anionic, nonionic, or zwitterionic. When the surfactant concentration exceeds the critical micelle concentration (cmc), micelles are formed as aggregates of surfactant molecules. In normal micelles, the hydrophobic hydrocarbon chains of the surfactants are oriented toward the interior of the micelle and the hydrophilic groups of the surfactants are in contact with the surrounding aqueous medium. On the other hand, reverse micelles are formed in nonaqueous media where the hydrophilic headgroups are directed toward the core of the micelles and the hydrophobic groups are directed outward. In both cases, the micelles exist only as a small amount of solubilized hydrophobic or hydrophilic material as illustrated in Figure 27. As the surfactant concentration increases further, micelles can be deformed and can change into different shapes, which makes it possible to synthesize different nanoparticle shapes.

3.1.4.1. Monomeric Surfactant. Self-assembly approaches are becoming increasingly important for the

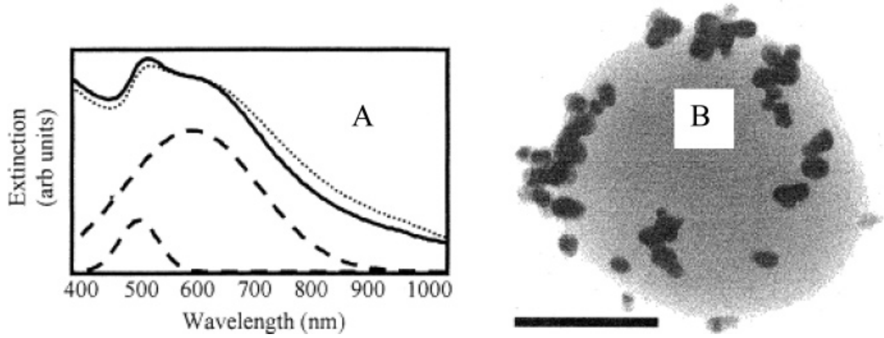

Figure 26. (A) UV−visible extinction spectrum of the aggregates of gold nanoparticles on the silica nanoparticle surfaces (solid line) and Gaussian fits to the two peaks (dashed lines) and (B) TEM image of linked gold nanoparticles. The scale bar is 50 nm. Reprinted with permission from ref 361. Copyright 1999 Elsevier.

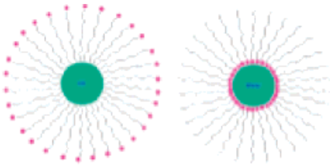

Figure 27. Normal micelle and reverse micelle structures.

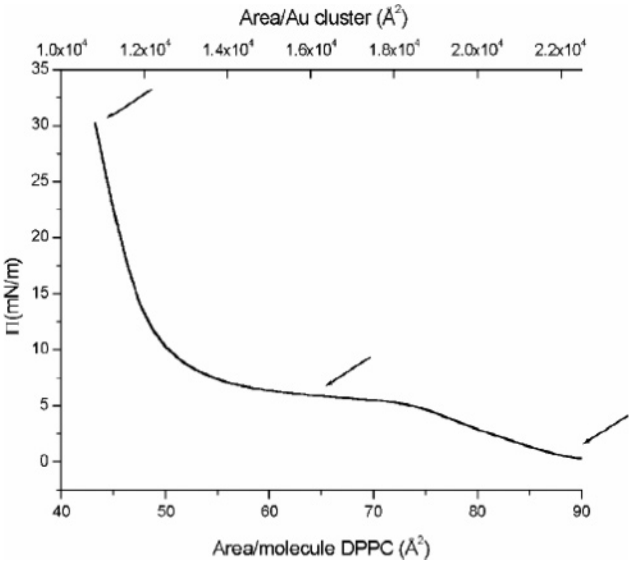

Figure 28. Compression isotherm of a LB film containing 99.56 mol % DPPC and 0.04 mol % dodecanethiol-capped gold nanoparticles. The arrows indicates points of transfer of the film onto a solid substrate (amorphous carbon or mica). The curve is shown as a function of the area available to a DPPC molecule and area available to a nanoparticle assuming that the complete area is available of either of the compounds. Reprinted with permission from ref 368. Copyright 2002 Wiley-VCH.

controlled fabrication of 1D, 2D, and 3D architectures as mentioned in section 3.1.2.1. It is demonstrated that the morphology of these nanostructures can, to some extent, be controlled by adjusting the parameters that affect the self-assembly process. Experiments have shown that dodecanethiol-capped gold nanoparticles of 1.5−3 nm diameters self-assemble in water in the presence of surfactants into a maze of continuous gold nanowires, resembling a molecular electronic circuit board.[368]

Dodecanethiolate-capped gold nanoparticles of 1.5−3 nm diameter were prepared according to a well-established two-phase liquid/liquid reduction route.[16] Partially hydroxyl-functionalized particles were obtained by Murray's ligand place exchange route.[369] Dodecanethiol-capped gold particles and 11-mercapto-1-undecanol were mixed in chloroform, and particles containing the ligand shell were isolated by precipitation and washing with ethanol. Langmuir films were obtained from chloroform solution containing mixtures of gold nanoparticles and dipalmitoylphosphatidylcholine (DPPC) on the water surface in the Langmuir trough. Compression isotherms were measured for gold nanoparticle/DPPC mixtures at different surface pressures in order to monitor the process of nanostructure formation. Figure 28 shows a typical compression isotherm for such DPPC systems containing 0.44 mol % of gold nanoparticles. The isotherm is completely dominated by the properties of the DPPC surfactant. The presence of gold nanoparticles has no significant effect apart from the particles' proportional contribution to the total surface area covered. Langmuir−Blodgett films were transferred by horizontal lifting onto continuous amorphous carbon for inspection by TEM. Samples were taken at three different points of the compression isotherm as indicated by the arrows in Figure 28. The progressive compression of hydrophobic dodecanethiol-capped particles into narrower lines accompanied by sintering into quasi-1D metallic nanoscale wires is shown by TEM in Figure 29A−C.

This unidirectional sintering of the particles, which is accompanied by packing into a maze-like structure, is due to a template effect of the surfactant at the molecular level. This model is based on template effect hypothesis that the amphiphilic DPPC molecules energetically prefer to occupy the entire water surface, while the hydrophobic gold particles, if left alone on the water surface, form close-packed 2D hexagonal rafts floating on the water surface.[370] If a mixture of these two compounds is placed on the water surface, the resulting morphology of the monolayer is an energetical compromise of the two packing motifs. Thus, it can be concluded that the complexity of the surfactant phase behavior may be utilized to regulate the formation of structures on the micrometer scale, while their molecular structure can influence the assembly process on the nanometer length scale.

Fabrication of fractal structure from metallic nanoparticles is specially important due to their novel physicochemical properties.[371−379] Wang and colleagues[380] have found that as-synthesized cetyltrimethylammonium bromide-capped gold nanoparticles can aggregate rapidly into fractals after spreading their chloroform solution on water surfaces. In principle, chloroauric acid, $HAuCl_4$ can be transferred into organic solvent by virtue of ion-pair extraction,[381−383] and subsequent reduction by sodium borohydride generated stable gold nanoparticles. The resulting ruby solution was stored in the dark at 4 °C. The colloidal solutions were very stable and show no sign of precipitation even after 1 year. When CTAB-capped gold nanoparticles were spread on the surface of pure water in the Langmuir−Blodgett (LB) trough, a blue-colored discontinuous film was formed immediately after, which is an indication of extensive nanoparticle aggregation. In fact, the formation of aggregates can be explained very well by

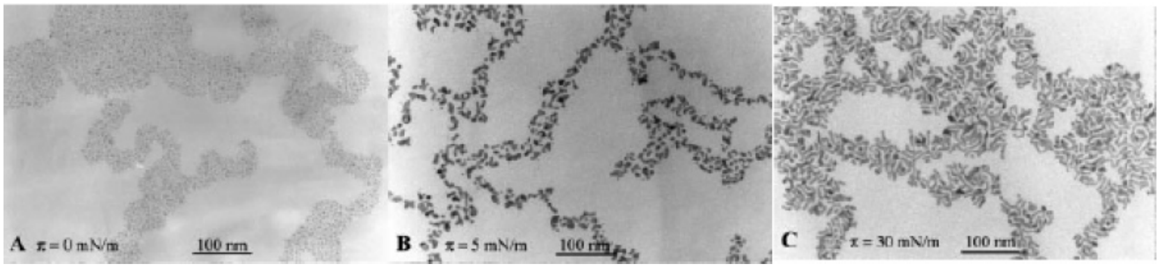

Figure 29. TEM images of the transferred LB films onto amorphous carbon substrates at a surface pressure of (A) 0, (B) 5, and (C) 30 mN m^{-1}. Reprinted with permission from ref 368. Copyright 2002 Wiley-VCH.

the recently developed integral equation theory of solvent-induced potential of mean force between two passivated nanoparticles.[384−386] The CTAB-capped gold nanoparticles are solvophilic with respect to choroform and solvophobic with respect to water and air. The drying of the choroform would force the nanoparticles into a solvophobic environment (air/water interface), therefore enhancing the solvophobic attractive forces between the nanoparticles. Because the contact between hydrophobic gold nanoparticles and water surfaces is incompatible, the nanoparticles are highly movable. Thus, aggregation happened rapidly by the strong solvophobic attractions.

The efficient sticking upon contact might come from the limited stability of the CTAB-capped gold nanoparticles at the air/water interface. It is known that the capping interactions between CTAB molecules and gold nanoparticles are electrostatic.[368,387] In chloroform, the CTAB-capped gold nanoparticles are in an extremely stable dynamic state. This is not the case at the air/water interface. The CTAB molecules can form monolayers by adsorbing on water surfaces or dive into water to form reverse micelles at the air/water interface. The chloroform evaporation forces hydrophobic nanoparticles to accumulate locally, and strong drying-mediated collision would result in dislocation of the capping CTAB molecules from the gold surfaces by adsorbing on water surfaces and diving into water. The removal of the capping of CTAB molecules renders the gold nanoparticles partially unprotected; as a result, the gold nanoparticles have to fuse into larger structures to lower the surface-to-volume ratio to decrease the surface energy.[290,368,388] The dispersion attractions among gold nanoparticles act as driving factors for the fusing process, whereas the nanoparticle surface bound CTAB molecules counteract this fusing process because it has to overcome the electrostatic repulsion between positively charged CTAB and withdraw hydrophobic alkyl chains. When the driving and counteracting interactions are balanced, the nanoparticles stop fusing. Besides the efficient sticking interactions, incompatible contact between hydrophobic nanoparticles and the water interface might also play a role for the formation of fractals. This incompatible contact enables nanoparticles to diffuse at will on water surfaces. This might be another precondition of growth of nanoparticles into fractal aggregates.[389−391]

The transfer efficiency of fractal aggregates from the air/water interface onto a solid surface is critically dependent on surface pressures. Figure 30 shows UV−vis absorbance spectra of transferred nanoparticle films on a glass slide at different surface pressures. The maximum of surface plasmon resonant bands for these transferred nanoparticle films are all located at 620 to ∼720 nm and the increase in surface pressure evidently strengthened the absorbance intensity. Compared with the resonant peak of gold nanoparticles in chloroform solution (∼527 nm, dashed line in Figure 30), all the resonant peaks in the LB films shift significantly to red. The red shift widening of surface plasmon bands demonstrate extensive aggregation of gold nanoparticles. The elevated surface pressure did not result in a further red shift and widening in the surface plasmon band indicating that the interior structure of the aggregate (for example, particle-to-particle distance) does not change with increased surface pressure, rather increases only the local particle density. Due to weak interactions between nanoparticle surfaces and CTAB ligands, dampening of surface plasmon absorbance intensity occurs. Therefore, a fractal-like arrangement of strong surface plasmon polaritons (SPPs) would be expected, which confines the optical energy around nanoparticle chains.[392] Thus, the reported method might result in applications, such as, nanoscale optical devices relying on SPPs or surface-enhanced Raman scattering from strong local electromagnetic fields.

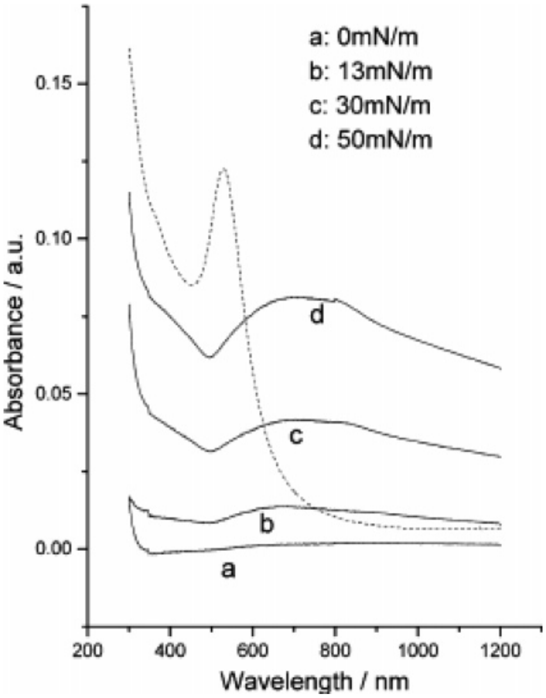

Figure 30. UV−vis absorbance spectra of transferred nanoparticle films on glass at different surface pressures. The dashed line corresponds to the spectrum of unaggregated nanoparticles in chloroform, whose intensity is reduced by 12 times for clear comparison. Reprinted with permission from ref 380. Copyright 2005 American Chemical Society.

3.1.4.2. Micelles. Aggregates of metallic nanoparticles can be prepared by reducing metal salts in micelles. Our group has exploited the UV-photoactivation technique to produce gold nanoparticle aggregates with almost uniform interparticle spacing in cetyltrimethylammonium chloride (CTAC) micelles.[393] The method produces an aggregate structure containing gold particles in the ∼3−5 nm size range in the presence of citrate in an alkaline pH (8−12) at room temperature. Absorbance measurement of the resulting blue solution showed the appearance of a broad band at ∼650 nm. The particles remained stable for months together in a vacuum desiccator if isolated from the reaction mixture by centrifugation. Citrate has been widely used to produce gold sols of variable size[394] from boiling aqueous $HAuCl_4$ solution. Different types of surfactants were used to achieve monodisperse gold nanoparticle aggregates.

Figure 31A shows the development of absorption spectra during the evolution of gold nanoparticles. Before irradiation, the reaction mixture does not show any characteristic absorption band (trace a). After 5 min of irradiation, an absorption band develops with maximum at around 600 nm (trace b) that can be ascribed to the surface plasmon resonance of the gold nanoparticles. This arises from the collective oscillation of the free conduction band electrons that are induced by the incident electromagnetic radiation. As the time of irradiation increases, the absorption maximum gradually red shifts (for example, trace c) and finally becomes stable at ∼650 nm (trace d) corresponding to the blue sol.

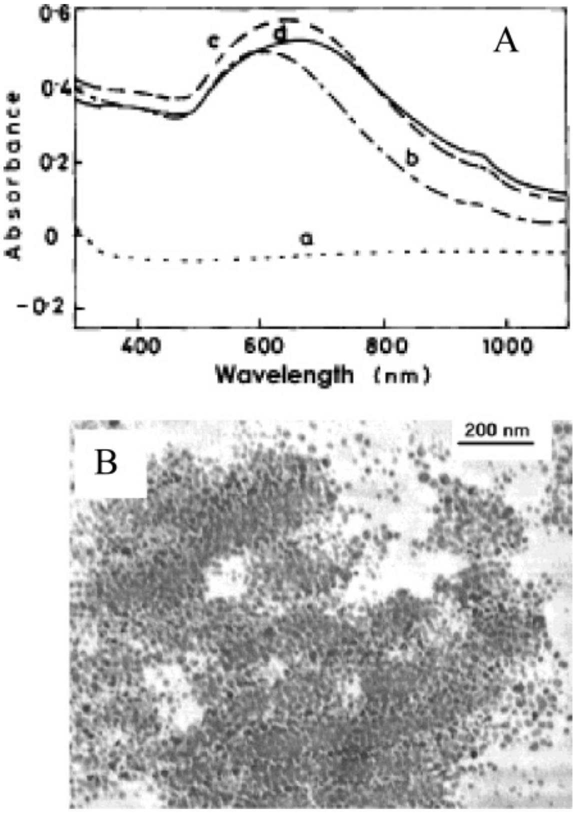

Figure 31. (A) Evolution of UV−visible spectra during the formation of gold nanoparticle aggregates and (B) TEM images of the gold nanoparticle aggregates. Conditions: [$HAuCl_4$] = 0.23 mM; [$C_{16}TAC$] = 4.5 mM; [sodium citrate] = 2.3 mM; [NaOH] = 4.5 mM. Irradiation times: (a) 0, (b) 5, (c) 10, and (d) 15 min. The irradiation was carried out with a 200 W UV light. Reprinted with permission from ref 393. Copyright 2004 American Chemical Society.

Scheme 8. Schematic Presentation of Gold Nanoparticle Aggregates with CTAC and Negatively Charged Citrate Ions[a]

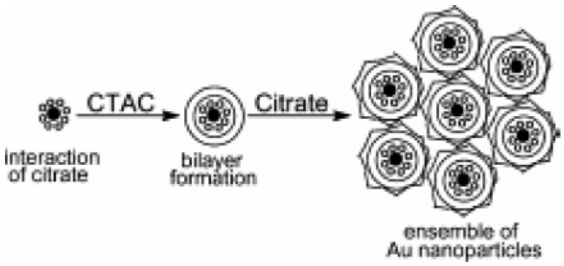

[a] Reprinted with permission from ref 393. Copyright 2004 American Chemical Society.

Interestingly, UV−visible spectrophotometry reveals the absence of any peak near the 520 nm region (characteristic region for dispersed small gold particles); instead a distinct peak appeared at ∼650 nm. The appearance of an absorption maximum at ∼650 nm indicates that the particles are assembled into an aggregate structure. The gradual blue shifting of the absorption maximum with increase in irradiation time is because interparticle spacing decreases with the progress of the reaction. TEM studies of the finally formed stable colloid show that the tiny particles (∼3−5 nm size) are in a closely packed assembly (Figure 31B). Excellent reproducibility of the particle evolution as ensembles of small particles was noticed from UV−vis spectra and also from TEM studies.

The cationic surfactant $C_{16}TAC$ has been introduced for the evolution of the ensemble of small spherical particle aggregates by UV-photoactivation process. The effect of $C_{16}TAC$ concentrations and also the effect of chain lengths of several other homologous cationic surfactants in this gold nanoparticle evolution process have been studied. Tiny spherical particles with tight size distribution were obtained from concentrated CTAC solution as has been reported earlier.[37] A pink sol is produced above and below the prescribed concentration range (0.23−5.0 mM). In the former case, gold particles exhibit a sharp plasmon absorption band (maximum absorbance at a wavelength of 520 nm) as the surfactant acts as a stabilizer only but does not allow the particles to form aggregates.[395] On the other hand, in the latter case, the spectrum is broadened and λ_{max} is red-shifted due to the increase in filling factor in the aggregate at higher surfactant concentration.[133] There exists a threshold concentration of surfactant above which the blue sol is produced for always.

The chain length of cationic surfactants has a profound influence on the evolution of particle geometry and also on aggregation. Surfactants with smaller chain lengths ($C_{10}TAC$ and $C_{12}TAC$) produce smaller particles and impart stability to the particles in the aqueous phase, and hence the particles get precipitated. Surfactants with smaller chain lengths give rise to higher concentrations of micelles with a lower aggregation number,[396] and hence smaller micellar structures encompass a smaller amount of gold ions. Thus, evolution of smaller gold particles is understandable. However, smaller chain lengths of the surfactants are not compatible enough to render stability to the evolved gold particles through hydrophobic repulsion; that is, these surfactants cannot provide steric stability.[397] A surfactant containing a longer chain ($C_{18}TAC$) helps to generate nonspherical particles as is observed in the case of higher $C_{16}TAC$ concentrations. In this case, the number of Au(III) ions per micelle increases, which stimulates the growth of nonspherical particles.[395] However, $C_{14}TAC$ has also been found to be suitable for the purpose and behaves similarly to $C_{16}TAC$. Thus, both $C_{16}TAC$ and $C_{14}TAC$ have been found to serve the purpose of gold particle evolution under the standard procedure.

A bilayer formation mechanism has been proposed for the aggregation of gold nanoparticles. In this experiment, cationic surfactant, CTAC, concentration supersedes citrate concentration, and hence CTAC covers the negatively charged gold surfaces forming a bilayer. Actually, bilayer formation has been recognized when cationic surfactants are adsorbed on solid surfaces.[398] Thus, interparticle interaction becomes pronounced in the citrate case causing the weak aggregation of the gold particles. The stabilization of gold nanoparticle aggregates with cationic surfactant and negatively charged citrate ions has been shown in Scheme 8.

3.1.4.3. Reverse Micelle.

Reverse micelles can be formed by ionic surfactants with double-long alkyl chains alone, such as diethyl sulfosuccinate, or a mixture of ionic and nonionic surfactants with a short oxyethylene chain dissolved in organic solvents. Reverse micelles are usually thermodynamically stable mixtures of four components: surfactant, cosurfactant, organic solvent, and water. The general method of using reverse micelles to synthesize nanoparticles can be divided into two cases. The first case involves the mixing of two reverse micelles. Due to the coalescence of the reverse micelles, exchange of the materials in the water droplet occurs, which causes the reaction between the cores, and thus, nanoparticles are formed in reverse micelles. The

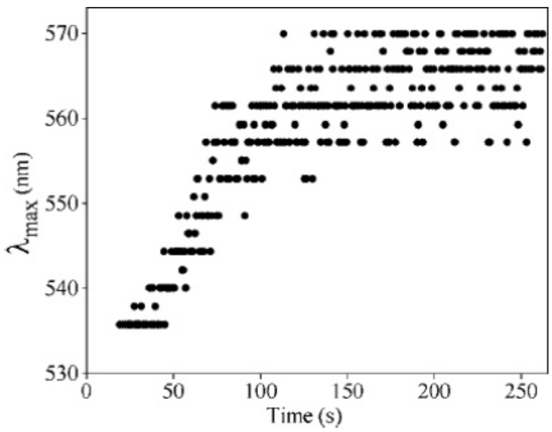

Figure 32. Change in peak extinction wavelength with time for gold nanoparticles synthesized in reverse micelles with $w = 10$ for Au(III) sample concentrations. Reprinted with permission from ref 403. Copyright 2005 IOP Publishing Ltd.

second case involves mixing one reactant that is solubilized in the reversed micelles with another reactant that is dissolved in water. The reaction can take place by coalescence or aqueous phase exchange between the two reverse micelles.

Sodium bis-(2-ethylhexyl) sulfosuccinate (AOT) is one of the most commonly employed surfactants in forming microemulsions;[399−401] its molecular shape allows high water solubilization with the formation of a well-defined aqueous−organic interface. The AOT reverse micelles consist of 23 molecules per aggregate in the form of rounded cylinders.[402] The concentration of entrapped water (defined as water pool, $w = [H_2O]/[AOT]$) is perturbed by the polar headgroups and the counterions of the surfactant. The diameter of the water pool is believed to control the nanoparticle size. The synthesis of gold nanoparticles in reverse micelles with $w = 10$ was performed at a constant temperature at 25 °C.[403] The reduction of gold from an ionic (Au^{3+}) to the atomic state (Au^0) is achieved inside the water droplets according to the chemical reaction

$$2Au^{3+} + 3SO_3^{3-} + 3H_2O \rightarrow 2Au^0 + 3SO_4^{2-} + 6H^+ \tag{51}$$

The product of this reaction quickly changes color from transparent to a deep red or purple color depending on the concentrations of the precursors salt used.

Figure 32 shows the displacement of the maximum absorption wavelength during the reaction. Red shifts from 535 to 570 nm are observed, which indicates that particles are agglomerated, and this affects the absorption spectrum of the sample and invalidates the use of Mie theory to correlate the peak wavelength to particle size. Finally, TEM measurements show gold nanoparticles of 8−10 nm in diameter and evidence of metallic aggregate formation. Such a system would result in multiple scatterings and splitting of the plasmon resonance bands into two peaks due to interaction between the particles. Thus, the time-resolved extinction measurements could be interpreted as resulting from the growth of agglomerates by addition of particles that reach 8−10 nm, resulting in particle−particle interactions and an apparent red shift beyond that due to actual particle growth.

Scheme 9. Structure of Poly(oxypropylene)diamines[a]

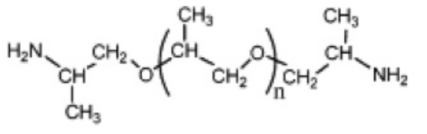

average molecular weight: 230, 400, 2000 and 4000 g/mol

[a] Reprinted with permission from ref 404. Copyright 2005 American Chemical Society.

3.1.5. Polymers as Architectures of Nanoscale Assemblies

The capability of colloidal metal nanocrystals to spontaneously form organized structures has been the subject of recent interest. It has been seen that very often the ligand plays an important part in influencing the ordered packing. The amino group, which has been reported to interact with metal ions as well as with the corresponding reduced metal, can be expected to play a significant role in the formation of self-assemblies, because the molecular configurations and the intermolecular interactions of bifunctional polyoxypropylenated diamines are totally different from those of monofunctional alkyl chains. It would be interesting to know whether any hydrophobic segment other than the alkyl chain could also induce ordered assemblies and how the chain length affects the particle sizes and gaps. A series of poly(oxypropylene)diamines, D230, D400, D2000, and D4000,-were used as ligands to synthesize self-organized gold nanocrystals.[404] The chemical structure of poly(oxypropylene)diamine is shown in Scheme 9, where *n* represents the repeating oxypropylene group on the polymer backbone. The average molecular weights are 230, 400, 2000, and 4000 g/mol for D230, D400, D2000, and D4000, respectively.

Ligand-modified Au nanoparticles were prepared from citrate-stabilized gold nanoparticles.[345,405] Introduction of ethanolic solution of different amines caused an immediate color change from deep red to blue via a ligand-exchange process, except for D2000 and D4000. In this investigation, amine-stabilized gold colloids were prepared using poly(oxypropylene)diamine ligands for two reasons. First, the orientations adopted by the poly(oxypropylene) (POP) structure are likely to be very different from those of the more widely used alkyl chains due to both the flexibility of the $-CH_2CH(CH_3)O-$ group and its intermolecular interactions, and second, the arrangement of POP chains, with different chain lengths, on a confined dimension between two spherical surfaces could be acheived. These changes can be ascribed to the result of an excess of ligand ($[N]/[Au^{3+}] = 100$), which now replaces the citrate as the stabilizing agent. The change of electron density on the nanocrystal's surface, together with the change in the adjacent environment caused by the ligand, decreases the attractive interactions between nanocrystals and serves to keep them apart, resulting in the formation of a 2D monolayer.

In solution phase, the citrate-stabilized nanocrystals displayed an intense surface plasmon absorption band at 524 nm (Figure 33, curve a) and upon addition of poly(oxypropylene)diamine ligands, the color of the colloids changed, with the maximum absorption band eventually shifting toward longer wavelengths. Broad absorption bands centered at 759 and 757 nm, respectively, can be seen for the Au-D230 and Au-D400 colloids accompanying a 524 nm shoulder (Figure 33, curves b and c). For Au-D2000 (curve d), a broad peak was seen at approximately 674 nm

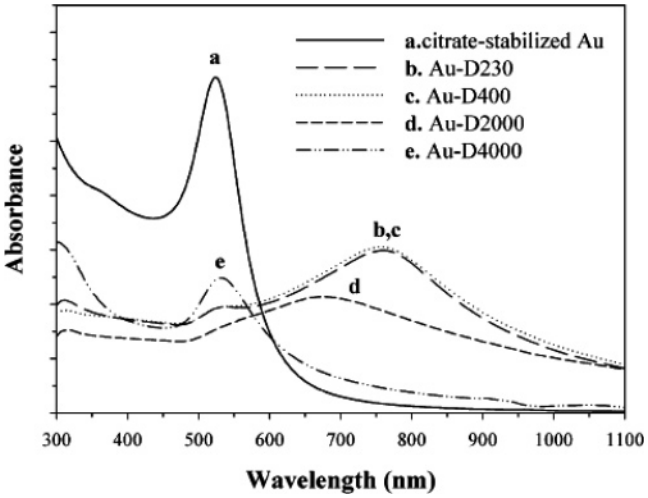

Figure 33. Absorption spectra of the citrate-stabilized gold colloid and those stabilized by different ligands. Reprinted with permission from ref 404. Copyright 2005 American Chemical Society.

accompanying the 524 nm shoulder. Au-D4000 (curve e) reveals only a broad peak at 536 nm, which can be deconvoluted into two bands at 529 and 569 nm. The broad peaks observed for Au-D230, Au-D400, and Au-D2000 illustrates the fact that the particles are forming aggregates in the solution phase.[118,406,407] When gold nanoparticles assemble into 3D structures, there is an increase in the dielectric constant of the surrounding medium, shifting the plasmon peak to a lower energy.[408] For Au-4000 colloids, the slight shift to 569 nm indicates that the gold particles form a loosely compact structure in the solution phase.

To explore the dependence of Au nanocrystal arrangement on the POP chain length, the solutions capped with D230, D400, D2000, and D4000 ($[N]/[Au^{3+}] = 100$) were immediately deposited on a flat carbon-coated copper grid, and TEM images of the resultant nanocrystals were recorded as soon as possible (Figure 34). These images reveal that the colloids capped with D230 show the formation of densely packed 3D structures (Figure 34a), with some minor 2D layers being apparent, indicating that the formation of supracrystal domains occurs quickly in solution. These results coincide with those obtained by absorption spectroscopy.

It is also interesting to note the coherence in the packing order as observed for Au-D4000 colloids (Figure 35). It is clear from the literature that the amines may not be firmly attached to the gold surface, thereby allowing more rapid exchange.[409] As previously noted, the orientation of the POP chains is not well-defined due to the existence of flexible ether linkages and pedant methyl groups; therefore, there is less of a tendency for the POP chains to form highly ordered close-packed monolayers. This situation could lead to the formation of multilayers of these ligands on a gold crystal surface, with some ligands not being directly attached to the particle's surface. Evidence for this is shown by the particle gaps (ξ) of these nanoparticles (Table 2). The D230-capped gold nanocrystals (chain length ≈ 0.8 nm) are separated from each other by about 2.7 nm, and for D400-capped nanocrystals, which have a chain length of about 1.5 nm, the separation is 2.3 nm, suggesting an interdigitation of POP chains on adjacent amine-ligated particles. The theoretical chain lengths of D2000 (77 nm) and D4000 (160 nm) are much longer than the observed particle gaps of 5 and 7.3 nm, respectively, suggesting a more twisted or folded structure on the particle surface.

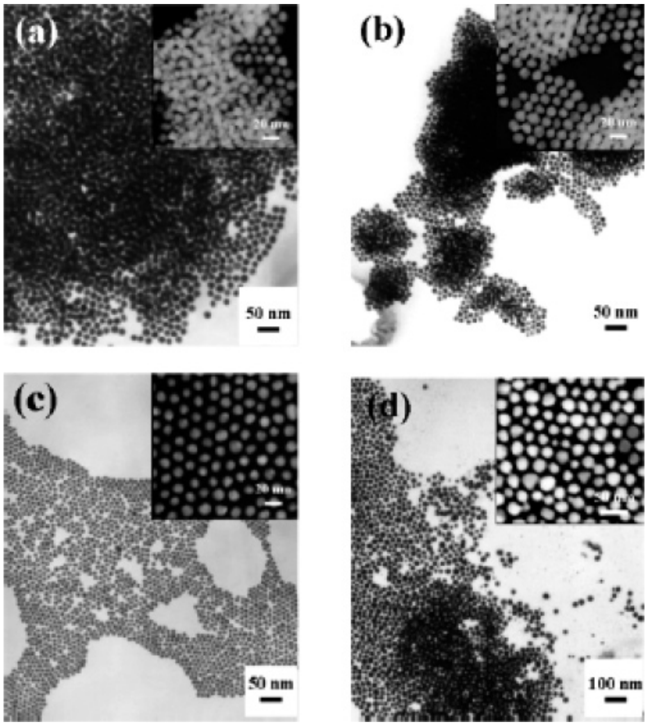

Figure 34. TEM images of the gold nanocrystals modified with different ligands: (a) Au-D230; (b) Au-D400; (c) Au-D2000; (d) Au-D4000. Reprinted with permission from ref 404. Copyright 2005 American Chemical Society.

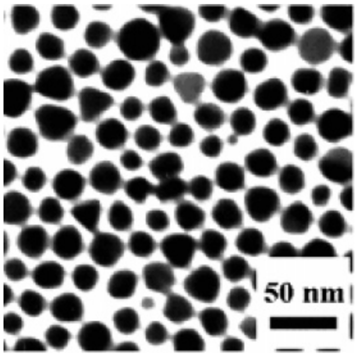

Figure 35. Highlighted image of the same D4000-capped Au colloids seen in Figure 35d showing the existence of ligands (the gray region) between two adjacent particles. Reprinted with permission from ref 404. Copyright 2005 American Chemical Society.

Table 2. Size, Particle Gap, and Potential Energy Analysis of the Gold Nanocrystals before and after the Ligand Exchange[a]

sample	particle size d (nm)	particle gap ζ (nm)	ligand thickness (nm)	chain length (nm)	E_{vdw} (eV)
citrate-stabilized	14.2 ± 1.5		2.9		
Au-D230	13.9 ± 1.2	2.7 ± 0.7	0.7	0.9	1.990
Au-D400	12.0 ± 0.9	2.3 ± 0.8	2.7	1.5	1.050
Au-D2000	10.5 ± 0.8	5.3 ± 1.5	3.6	7.7	0.011
Au-D4000	17.6 ± 3.4	7.3 ± 1.3	4.8	16.0	0.018

[a] Reference 404.

In Figure 36a, the particle gaps and the wavelength of the maximum absorbance bands are plotted against the molecular weight of the poly(oxypropylene)diamines. By fitting these data, it is found that the absorption bands of ligand-modified gold colloids shift linearly toward the high-energy region

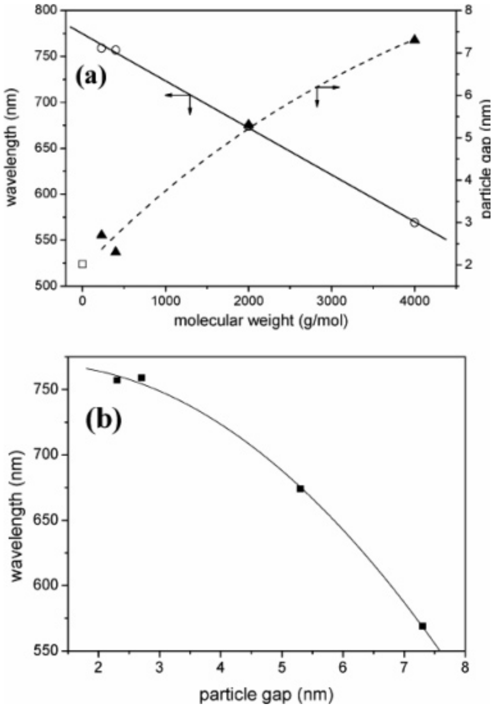

Figure 36. (a) Absorption band (○) and particle gap (▲) of Au colloids change as a function of ligand molecular weight. The absorption band of citrate-stabilized Au nanocrystals (□) is also shown. (b) Gap dependence of the optical absorption of ligand-capped Au nanocrystals. Reprinted with permission from ref 404. Copyright 2005 American Chemical Society.

with increasing poly(oxypropylene)diamine molecular weights. The particle gap is also found to increase as a function of increasing molecular weight, indicating that the interparticle separation is not proportional to the chain length. The POP chains thus either distort somewhat upon solvent evaporation or tend to interdigitate in the confined space. In Figure 37b, the exponential decrease in the absorption band wavelength with increasing particle gaps is shown. It is now well-documented that the optical properties of gold colloids are highly dependent on the level of particle separation. This band in the low-energy region was theoretically predicted by Quinten[410] on the basis that retardation effects and electromagnetic dipolar interactions between different particles would give rise to an additional absorbance at these wavelengths.

3.2. Induced Aggregation among the Already Formed Gold Particles

3.2.1. Electrolyte-Induced Aggregation

The color of the colloidal solution of metallic nanoparticles can be influenced by the addition of salt. The role of the salt is to induce aggregation in the suspension of colloidal nanoparticles. A newly discovered aggregation phenomenon of DNA-functionalized gold nanoparticles induced by hybridization of target DNA has been developed that does not cross-link the nanoparticles.[411] Aggregation of DNA-functionalized poly(*N*-isopropylacrylamide) (PNIPAAm) nanoparticles without the cross-linking mechanism has also been reported by the group.[412] In this system, only one kind of single-stranded probe DNA is grafted on PNIPAAm, which spontaneously forms nanoparticles above 40 °C. When the target DNA is perfectly complementary to the probe in sequence as well as in chain length, the nanoparticles aggregate together at considerably higher salt concentration.

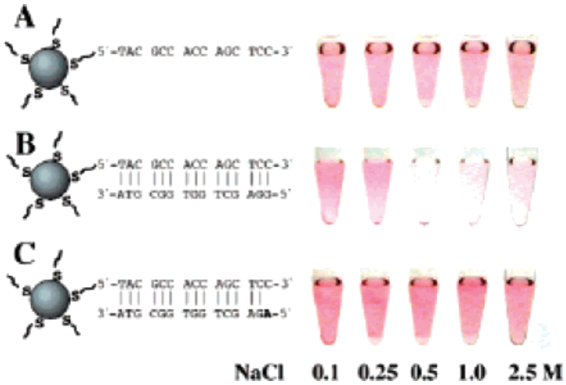

Figure 37. Aggregation behaviors of the DNA−gold nanoparticles at various NaCl concentrations at room temperature: (A) without a target DNA; (B) with the complementary target; (C) with a target containing a single base mismatch at its 5′ terminus. The final concentrations of the particle, the probe DNA, and the targets were 2.3, 500, and 500 nM, respectively. Reprinted with permission from ref 411. Copyright 2003 American Chemical Society.

A colloidal solution containing gold nanoparticles were functionalized with a single-stranded DNA by a procedure similar to that described by Mirkin et al.[413,414] The aggregation behaviors of the gold nanoparticles have been investigated with various concentrations of NaCl by observing the solution colors and monitoring the visible spectra. Bare nanoparticles without probe DNA immediately aggregated at 0.1 M NaCl (data not shown). In contrast, the DNA-functionalized nanoparticles did not exhibit any visible change within the experimental range up to 2.5 M of NaCl (Figure 37A). Next, a target DNA was added with complementary sequence to the probe DNA so that the amounts of the two DNAs should be balanced (Figure 37B). When the NaCl concentration was higher than 0.5 M, a clear colorimetric change to purple, representing the particle aggregation, was immediately observed. The aggregation process of this non-cross-linking system is much more rapid than that of the cross-linking systems, which take several tens of minutes to hours at room temperature.[118] This difference originates from the different aggregation mechanisms. In this non-cross-linking system, the aggregation is driven by the London−van der Waals attractive force between the nanoparticles, when the repulsive interaction is greatly reduced by formation of duplexes on their surfaces. The attractive force works from a distance and leads to rapid aggregation. On the other hand, in the cross-linking system, the kinetics of the aggregation is dominated by random collisions between the nanoparticles with relatively slow Brownian motion. The visible spectra corresponding to Figure 37A,B are shown in Figure 38. In the presence of 0.5 M of NaCl, the extinction peak was shifted from 525 to 560 nm by the addition of the complementary target DNA.

More striking results were derived from experiments for another target DNA with a single-base mismatch at the 5′ terminus. As shown in Figure 37C, addition of this target DNA to the nanoparticle solution did not cause any colorimetric change even at high NaCl concentration. This behavior depends only on the position of the mismatch and not on the combination: two other targets with different terminal mismatches, C−C and T−C, were also confirmed to keep the dispersion. In contrast, a single-base mismatch at the middle of the target DNA brought a colorimetric change

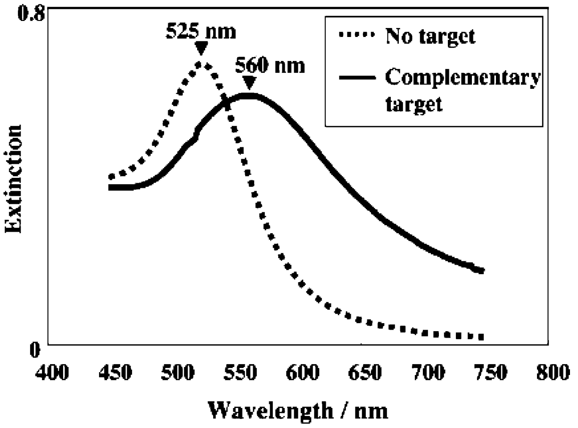

Figure 38. Visible spectra corresponding to Figure 38A (dotted line, no target) and 38B (solid line, complementary target) at 0.5 M NaCl. Reprinted with permission from ref 411. Copyright 2003 American Chemical Society.

similar to that in Figure 37B. Although interpretation of this unusual sensitivity for the terminal mismatch is difficult, it can be presumed that even one base works as a single strand to produce a repulsive interaction when it is located at the outermost position of the DNA−nanoparticle conjugate. Thus, it can be concluded that the terminal-mismatch sensitivity is a common property of these non-cross-linking systems.

3.2.2. Ligand-Induced Aggregation

It is now well-known that addition of several ligands induces aggregation of gold nanoparticles in solution by displacement of the charged species left from the reduction reaction or introduced for stabilization. Rouillat et al.[415] described the pyridine-induced aggregation of gold nanoparticles prepared by the method reported by Turkevich.[416] In this case, the Coulombic repulsion between the particles cannot overcome the van der Waals attractive forces between particles.[416−418] From the transmission electron microscopy, it is seen that during the initial stages of the aggregation process, the gold particles form short chains of a few particles before growing into complex patterns (not shown). In the UV−visible absorption spectrum, the new resonance condition is observed as a second absorption band on the red side of the surface plasmon resonance associated with the surface plasmon along the short axis of the ellipsoid. The latter resonance along the short axis is identical to the one corresponding to the initial spheres (Figure 39). This property can be used to study the local field effects in these chains since the geometry of the particles has a dramatic effect on the local field enhancement.[419]

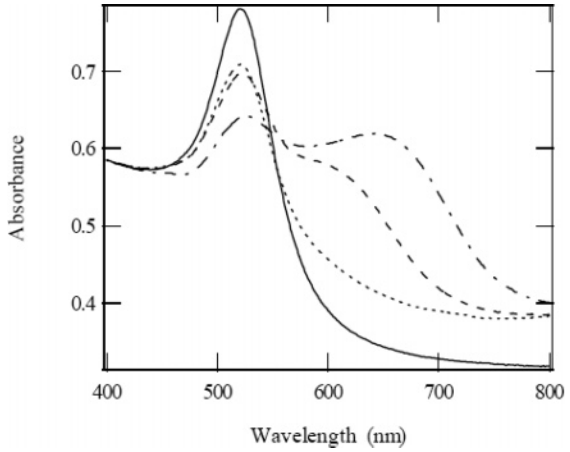

Figure 39. UV−visible absorbance spectra of gold nanoparticles as a function of the pyridine concentration: (—) no pyridine; (···) 0.25 mM; (− − −) 0.30 mM; (− − ·) 0.33 mM. Reprinted with permission from ref 415. Copyright 2001 The Japan Society for Analytical Chemistry.

Scheme 10. Synthetic Scheme for the Preparation of the Dextran-Coated Gold Colloids[a]

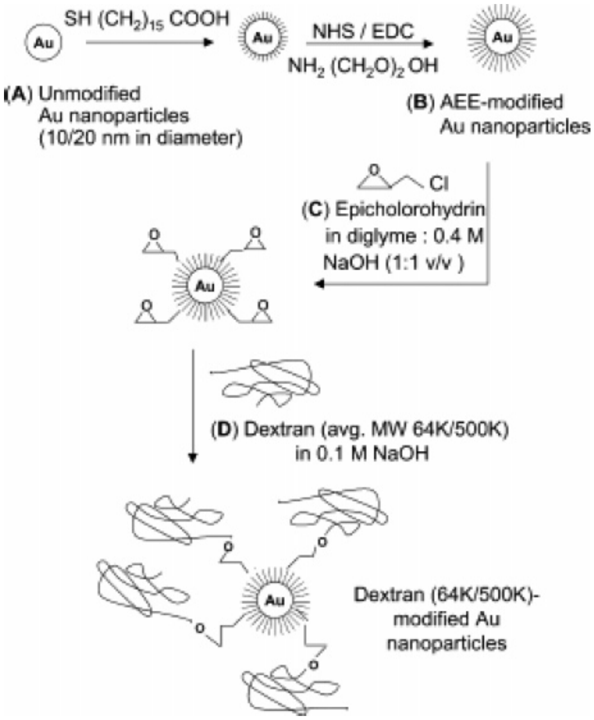

[a] Reprinted with permission from ref 420. Copyright 2004 Elsevier Science.

Dextran-coated gold colloids (10 and 20 nm) can be aggregated with concanavalin A (Con A from *Canavalia ensiformis*) in a controlled fashion in which the change in absorbance at an arbitrary wavelength used to monitor the extent of aggregation can be optimized for sensing.[420] The immobilization of dextran on citrate-stabilized gold nanoparticles (Scheme 10) was performed using the following four steps: chemisorption of a long-chain carboxyl-terminated alkanethiol on gold nanoparticles,[421] the activation of surface hydroxyl groups using *N*-3-(dimethylaminopropyl)-*N*′-ethyl-carbodiimide (EDC) and *N*-hydroxy-2,5-pyrrolidinedione (NHS), activation of hydroxyl groups using epichlorohydrin, and the covalent coupling of dextran. Any glucose present competitively binds with Con A, dissociating the dextran-coated gold colloids, affording the reverse gold plasmon change and hence the determination of glucose concentrations by tuning the extent of aggregation of the gold nanoparticles. Reducing the gold colloid size and dextran molecular weight typically reduces the glucose sensing range (lower [glucose]) but also reduces the long-term stability of the gold aggregate sensors.

To optimize the extent of aggregation and, therefore, the dynamic range for dissociation upon glucose addition, 500K dextran-coated gold colloids (500K, 20 nm gold) were aggregated with different concentration of Con A, which is well-known to competitively bind dextran (Figure 40).[422,423] The normalized spectra show both a broadening and a slight red shift as a function of increased Con A concentration,

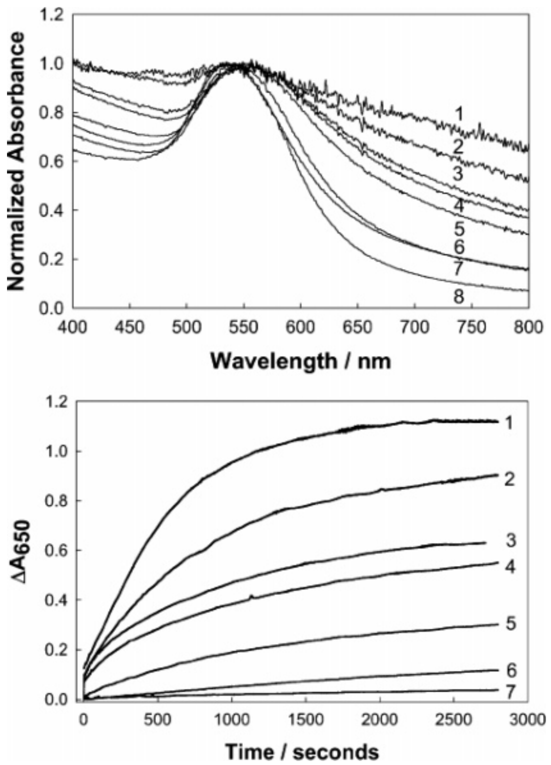

Figure 40. Normalized absorption spectra (top) of 500K dextran-coated 20 nm gold colloids cross-linked with different concentrations, (1) 112, (2) 75, (3) 56, (4) 37.3, (5) 17.4, (6) 8.70, (7) 4.40, and (8) 0 μM, of Con A and the change in absorbance (bottom) at 650 nm after the addition of the respective Con A concentrations. Reprinted with permission from ref 420. Copyright 2004 Elsevier.

simply reflecting the close proximity of increasing aggregated gold colloids and their mutually induced dipole interactions,[424] a function of the affinity of Con A for dextran. The absorbance was measured at a particular wavelength (~650 nm) to monitor the extent of aggregation, and it was seen that there is a significant change in absorbance, ΔA_{650}, between a highly aggregated system (line 1, Figure 40, left) and a slightly aggregated system (line 7). This finding helps to monitor the concentration changes in glucose solution in the millimolar range in a continuous manner. Moreover, the glucose sensing range of the aggregates can be somewhat tuned depending on the size of the gold colloids, the molecular weight of dextran, and the concentration of Con A used to form the sensing aggregate.

Zhong et al.[425] have demonstrated for the first time the ability to control the size of nanoparticle assemblies via a novel mediation template strategy. There are two important forces in controlling this process. The first is the mediation force as a result of the coordination ability of $MeSi(CH_2SMe)_3$ to Au, which can be manipulated by the number of thioether groups on the mediator. Zhong and colleagues have recently demonstrated this viability for forming spherical assemblies of ~60 nm diameter with a tetrathioether.[426] The second is the templating effect exerted by the surfactant reactivity of tetraoctylammonium bromide. Surfactant-based micellar templating effects are well-documented for aqueous solutions,[426] where the shape formation (spheres, rods, etc.) depends on the structure and the concentration of surfactants.

TOAB-capped gold nanoparticles were synthesized according to Schiffrin's protocol[427] and were stored in the toluenic solution. The mixing of TOAB-capped gold and $MeSi(CH_2SMe)_3$ led to the formation of spherical assemblies of gold nanoparticles of relatively high monodispersity (Figure 41). The size of the spherical assemblies is dependent on the relative ratio of mediator to the gold particles (r). The crystallinity of the individual nanocrystals is shown by the HRTEM (insert); the close packed ordering of the assembled nanocrystals can be resolved along the edges of the spheres (Figure 41, right). The formation process of the different spherical sizes involved a gradual color change of the gold nanoparticles from red to purple or blue, as evidenced by the spectral evolution of the surface plasmon resonance (SPR) band (Figure 42). The spectral envelope of the SPR band apparently consists of two overlapping bands. At the lower concentration of the mediator, these two bands are clearly resolved at 520 and 780 nm, and an isosbestic point displayed at 560 nm is indicative of the involvement of two major species in the reaction solution. The final product at low concentrations of the mediator eventually precipitated after 1−2 days, but remained soluble for many weeks when $r \approx 2000$ was used. The number of thioether groups in the mediator was also found to impact the assembly of nanoparticles, including their size and subtle differences in reaction kinetics. There was no indication of any assembly process when a bidentate ligand was used. The

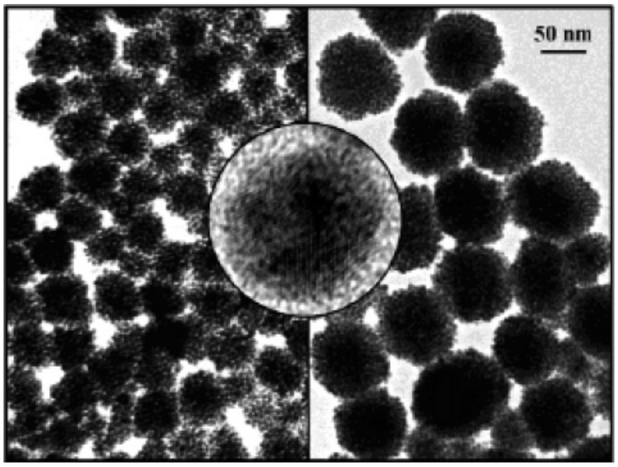

Figure 41. TEM micrographs showing the spherical assemblies obtained from two different [**2**]/[**1**/**Au**] ratios: (left) $r \approx 660$ ([**1**/**Au**] = 0.1 μM, [**2**] = 66 μM). (right) $r \approx 200$ ([**1**/**Au**] = 0.1 μM, [**2**] = 20 μM). Both images have the same scale bar. The inset shows HRTEM of an individual **1**/**Au** nanoparticle. Reprinted with permission from ref 425. Copyright 2003 American Chemical Society.

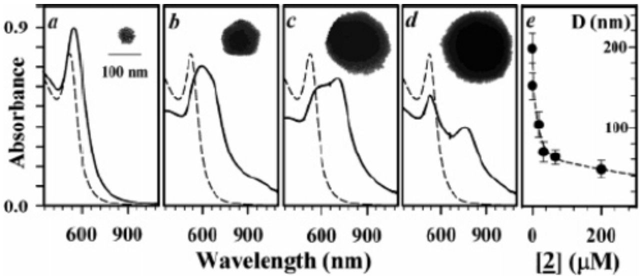

Figure 42. SP band for **1**/**Au** in toluene (0.1 μM, dashed line) and the final spectra upon addition of **2** (200 (a), 20 (b), 0.8 (c), and 0.08 μM (d); $r \approx 2000$ (a), 200 (b), 10 (c), and 1 (d)). TEM micrographs of individual spheres for the corresponding samples are included as insets (all have the same scale bar). A plot of the spherical diameter (D) vs [**2**] is included (d), which can be fitted by $y = a\,e^{-bx} + c\,e^{-dx}$ ($a = 1.13 \times 10^2$, $b = 6.0 \times 10^{-2}$, $c = 6.59 \times 10$, $d = 1.60 \times 10^{-3}$). Reprinted with permission from ref 425. Copyright 2003 American Chemical Society.

Scheme 11. Synthetic Route toward AuMPC 2[a]

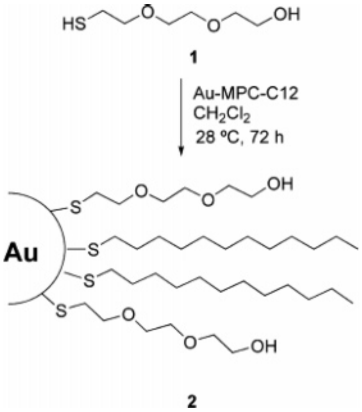

[a] Reprinted with permission from ref 428. Copyright 2002 Elsevier.

use of bulkier thioethers $Me_{4-n}Si(CH_2SBu^t)_n$ ($n = 3$ and 4) did not produce any significant assembly either.

3.2.3. Acid-Induced Aggregation

Pengo et al.[428] described the acid-induced aggregation of the gold nanoparticles protected with tri(ethylene glycol)-functionalized thiolates. Tri(ethylene glycol)-functionalized gold nanoparticles have been prepared by place exchange reaction[429−431] of dodecanethiolate-functionalized gold nanoclusters with 1-mercaptotri(ethylene glycol) (Scheme 11). These gold nanoparticles were obtained as a precipitate from $NaBH_4$ reduction in the presence of an excess thiol.[16,432] The precipitate so obtained was purified by exclusion chromatography on Sephadex LH 60.[433,434] The dark red solution so obtained was exposed to a fixed concentration of added acid, and this leads to a change of color depending on the alcohol employed as the solvent. TEM analysis was carried out in order to assess the nature of the phenomenon associated with the time-dependent shifts of the surface plasmon band toward longer wavelengths upon treatment of the resulting gold nanoparticles with acid solution. The two pictures of the nanoparticles dissolved in methanol before and after completion of the first (fast) kinetic process are shown in Figure 43. The pictures reveal that the addition of acid induces the formation of clusters of the gold nanoparticles without any alteration of their size. The shift of the SP band to longer wavelengths was attributed to the acid-induced clustering of the nanoparticles into aggregates.[435] It is plausible that interdigitation of the protecting monolayer of the clustered gold nanoparticles leads, slowly, to the fusion of gold cores. The interdigitation upon clustering is supported by the fact that the interparticle distance measured in Figure 43b is shorter than that expected on the basis of the length of the polyether and hydrocarbon chains covering the gold surface. The fusion process might be particularly facilitated by the presence of the tri(ethylene glycol) thiolates covering the surface that, compared with hydrocarbons, are much less packed and hence have a much higher degree of conformational freedom. On the other hand, it is likely that the presence of ether units along the protecting chains allows the formation of hydrogen bonds, driven by protonation, between the chains residing on different particles. The extent of the resulting interdigitated cluster (Scheme 12) is also influenced by the hydrophobic interaction between the fractions of hydrocarbon chains still present on the monolayer.

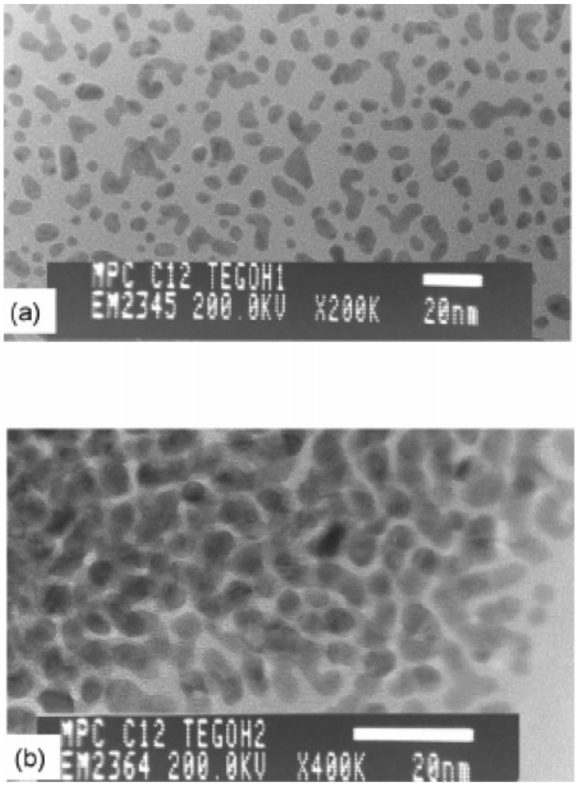

Figure 43. TEM images of AuMPC 2 nanoparticles in methanol before (a) and after (b) treatment with acid. Reprinted with permission from ref 428. Copyright 2002 Elsevier.

Scheme 12. Interdigitation of the Covering Monolayers of Two Nanoparticles upon Protonation[a]

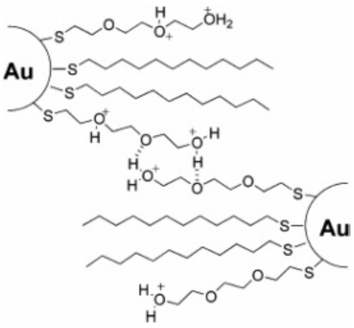

[a] Reprinted with permission from ref 428. Copyright 2002 Elsevier.

Aggregates of gold nanoparticles can also be produced by the surface acid−base reactions of the individual gold nanoparticles. In a very recent article, Kleinermanns et al. showed that from an ensemble of gold nanoparticles[345] modified with an ionizable and pH-sensitive monolayer of thiobarbituric acid (TBA), nanoparticle aggregates can be produced in a controlled fashion by the variation of the pH of the solution.[436] The optical absorption spectra of the gold colloidal solution capped with TBA are shown in Figure 44 at various pH values. For comparison, the spectrum for the uncapped gold colloidal solution is also presented (dotted curve). A successive shift in the surface plasmon resonance from 522 to 531 nm along with a successive reduction in intensity of the plasmon resonance is observed after addition of TBA molecules and adjustment of the solution pH from 12.0 to 7.7, indicating capping of the gold nanoparticles.[437] One notable feature of Figure 44 is that a new absorbance band at around 680 nm evolved gradually, which is more clearly observed when the pH of the solution is decreased

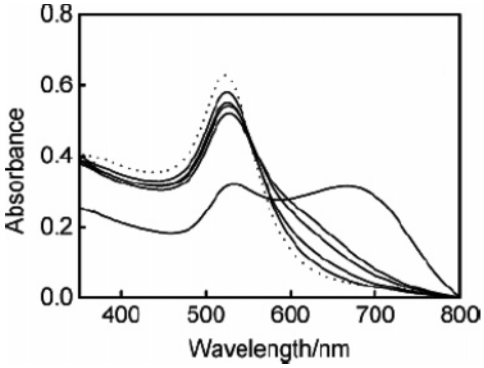

Figure 44. Optical absorbance spectra of Au colloidal solutions before (dotted curve) and after (solid curves) addition of small quantities of TBA as a function of the pH of the solution (from top to bottom pH 12.0, 10.4, 8.6, 7.7, and 6.5). Reprinted with permission from ref 436. Copyright 2005 American Chemical Society.

to 6.5. The colloidal solution at pH 6.5 is stable throughout the measurements. No deposits except a slight decrease in absorbance intensity and red shift of the absorbance of the colloidal solution at around 700 nm have been observed after 24 h. Further lowering of the pH to <6.5 leads to fast aggregation. Deposits can be found at the bottom of the reaction cell, and the solution loses its colloidal properties within several minutes. This is because at higher pH (completely deprotonated TBA) these colloids are stable due to the electrostatic repulsion of the oxyanion groups. Lowering of the pH leads to protonation of the anion group and the formation of the uncharged hydroxy functions, allowing hydrogen bond interactions between the particles, thus leading to aggregation.

Grzybowski et al.[438] made a systematic study of electrostatic interactions[439] of charged metal particles and of the optical properties of aggregates that these interactions give rise to. They have used gold particles covered with HS-$(CH_2)_{10}COOH$ (MUA) ω-functionalized alkanethiols. Formulations of gold nanoparticles were estimated according to the method by Stoeva and co-workers[440] and were $Au_{4100}L_{380}$ (L stands for a thiol ligand) for gold nanoparticles. UV−vis spectrum of solution of gold particles at pH $\approx$ 10 shows λ_{max} at 520 nm with an extinction coefficient of $\epsilon \approx$ 3100, and it was noted that the positions of the maxima depended on pH. Specifically, when the pH was lowered, λ_{max} red-shifted (e.g., from 520 nm for pH 10 to 650 nm at pH 3) due to hydrogen bonding between protonated carboxylic groups on different particles and the ensuing formation of nanoparticle aggregates.

4. Rupturing and Reversible Generation of the Aggregates

The colloidal dispersions of gold nanoparticles show a red color and exhibit a plasmon absorption band at 520 nm. Addition of inorganic salts like NaCl to this red dispersion makes the color change from red to blue. This is usually an irreversible change. Toshima[441] and later on several other authors[288,393,445] reported a reversible color change responsive to pH and stabilizing ligand on gold nanoclusters.

Toshima et al. found that the colloidal dispersions of 3-mercaptopropanoic acid (MPA)-protected gold nanoclusters show a reversible color change between red and blue depending on pH of the solution.[442] The MPA-stabilized gold nanoclusters were prepared by reduction of $HAuCl_4$ with trisodium citrate in the presence of MPA (Figure 45).[443] The as-prepared dispersions (pH $\approx$ 5.9) of the gold nanoclusters showed red color with a plasmon peak at ca. 523 nm. Addition of aqueous HCl to change the pH from 5.9 to 3.8 results in color change from red to purple, having the absorption peak at ca. 532 nm. This large red shift of the plasmon absorption band could be ascribed to a dipole−dipole interaction among the gold nanoclusters forming aggregates as also evident from TEM studies.[444] Addition of aqueous NaOH to this purple solution to change the pH from 3.8 to 5.9 results in color change from purple back to red, having the absorption peak at ca. 524 nm. The TEM photograph of the sample showed that the average diameter of Au nanoclusters is 2.1 ± 0.7 nm, which was quite similar to that of the original. The reversible change of color and TEM photograph of the dispersions of MPA-protected Au nanoclusters could be repeated ten times without any morphological changes. The reversible dispersion−aggregation change could be ascribed to the electronic repulsion between carboxylate anions and to hydrogen bonding between carboxylic acids, respectively, which cover the gold nanoclusters as illustrated in Scheme 13.

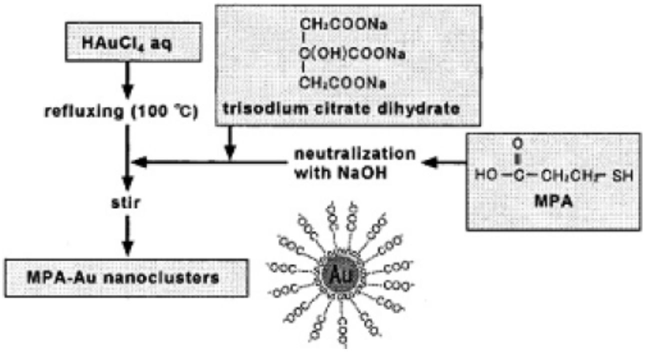

Figure 45. Preparation of MPA (3-mercaptopropionic acid)-protected gold nanoclusters. Reprinted with permission from ref 441. Copyright 2003 International Union of Pure and Applied Chemistry.

Scheme 13. Schematic Illustration of Reversible Color Change of MPA-Protected Gold Nanoclusters Depending on pH[a]

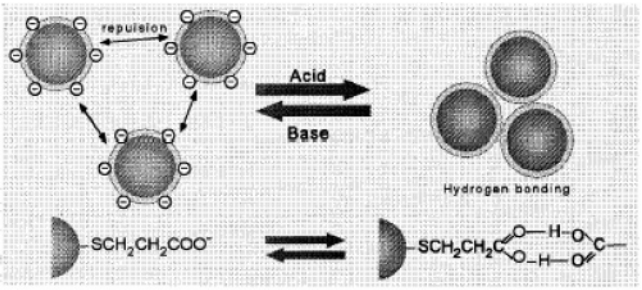

[a] Reprinted with permission from ref 441. Copyright 2003 International Union of Pure and Applied Chemistry.

We have employed sodium citrate in the photoactivation process at room temperature under ambient conditions.[393] It was seen that UV-activation produced a pink ($\lambda_{max} \approx$ 520 nm) sol when citric acid (to see the effect at lower pH) was introduced in lieu of sodium citrate. Higher concentrations of citric acid (i.e., very low pH) corrode the particles as is evident from TEM studies (Figure 46). Sodium citrate and NaOH offer perfect pH (~8) and salt concentrations to render stability to the particle ensembles. Again, after the formation of the blue sol, if it is treated with citric acid to decrease the

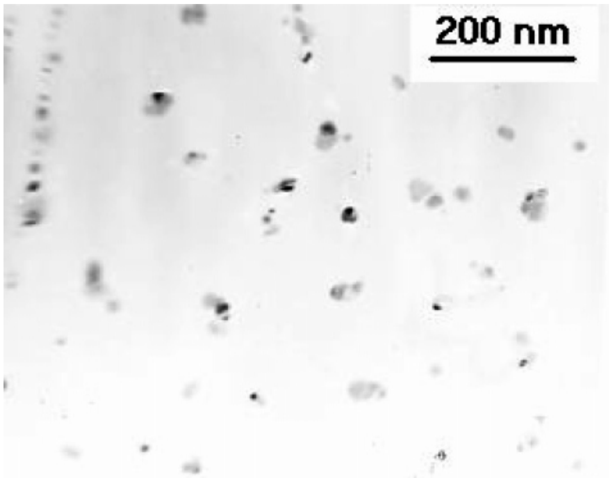

Figure 46. Citric acid induced corrosion of blue gold sol. Conditions: [$HAuCl_4$] = 0.23 mM; [$C_{16}TAC$] = 4.5 mM; [citric acid] = 2.3 mM; irradiation time = 10 min. The irradiation was carried out with a 200 W UV light. Reprinted with permission from ref 393. Copyright 2004 American Chemical Society.

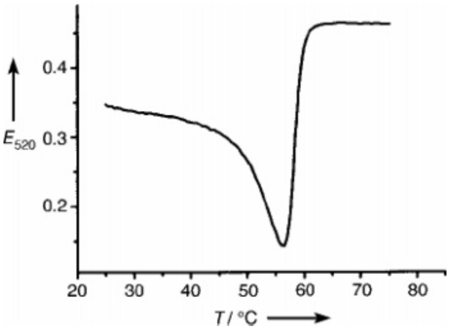

Figure 47. Thermal dissociation curve of the 24-mer DNA linked aggregates consisting of Au nanoparticles and streptavidin. The extinction coefficient at 520 nm was monitored as a function of temperature while the solution was stirred. Reprinted with permission from ref 288. Copyright 2001 Wiley-VCH.

pH to ~6 the blue sol turns pink, and from the TEM measurements, it seems that the particles did not have any particular shape. Again, regeneration of the blue color from the pink solution is possible by the increase of pH and subsequent UV exposure. This authenticates the reversible blue−pink color transformation. From the UV−vis spectra, it is seen that the blue sol does not exhibit any peak at 520 nm; instead a peak appears at the ~650 nm region, but at low pH conditions (with citric acid), the 650 nm band disappears with the evolution of a 520 nm peak. Repetitive UV exposure of the pink sol at higher pH regenerates the peak at 650 nm. This spectral change in this nanoparticle system can be attributed to the reversible formation and dissociation of aggregates.[4] A decrease in the pH of the solution results in the increase in interparticle distances within the aggregate without dispersing the gold nanoparticles in solution, and therefore, the solution shows pink color.

Park et al.[288] performed melting experiments on the streptavidin−nanoparticle aggregates based on UV−vis spectroscopy (Figure 47). Upon heating the aggregates, the extinction coefficient at 520 nm initially decreases, which results in a dip in the melting curve, and then abruptly increases when DNA melting takes place and the particles are dispersed. This dip has been observed in the pure gold nanoparticle system and has been attributed to aggregate growth prior to melting, that is, a type of aggregate “ripening”.[118] After DNA melting has occurred, the gold plasmon resonance is centered at 520 nm, which is characteristic of dispersed 13 nm particles. These experiments further demonstrate that sequence-specific hybridization events, rather than nonspecific interactions, are affecting the particle−protein assembly and that the aggregation process is completely reversible.

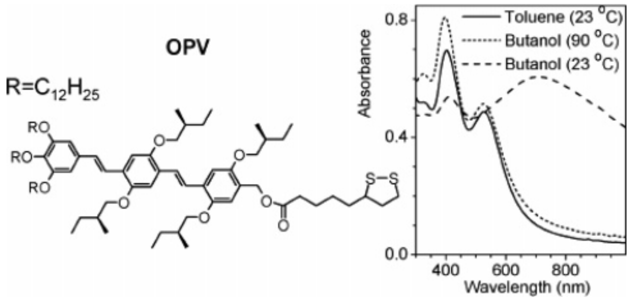

Figure 48. Chemical structure of OPV. UV−vis absorption of OPV-Au (d_{Au} = 4.1 nm, optical path length 1 mm, [OPV-Au] = 0.5 μM) in toluene and butanol. Reprinted with permission from ref 445. Copyright 2006 American Chemical Society.

Schenning et al.[445] have demonstrated a principle for organization of reversible inorganic/π-conjugated nanoparticles involving self-assembly of peripheral π-conjugated ligands and inorganic nanoparticles. Oligo(*p*-phenylene vinylene) OPV, an oligomer with a disulfide moiety, was synthesized in two steps using literature procedures (Figure 48).[446] The OPV-functionalized gold nanoparticles (OPV-Au) with different gold core sizes (diameter $d_{Au} \approx 1.6 \pm 0.3$ and 4.1 ± 0.6 nm) were obtained via standard methods.[16,447] UV−vis absorption studies in toluene show an OPV absorption band at 404 nm and a single isolated species featuring a surface plasmon (SP) absorption band with a maximum at $\lambda \approx 525$ nm indicating the presence of isolated particles. In *n*-butanol, however, it is found that the particles self-organize into larger structures in a reversible manner. Evidence for this comes from the observation of a red-shifted SP band of OPV-Au in butanol with a maximum at $\lambda \approx 720$ nm. When the butanol solution is heated above 80 °C, the SP band shifts back to 525 nm, a spectral position similar to that found for toluene. Upon cooling, the SP band reappears at 720 nm. The red shift could be ascribed to a reversible transition from nonaggregated to aggregated hybrid nanoparticles. The red shift can be interpreted in terms of the Mie scattering theory and results from coupling of the transition dipoles associated with the SP band of metal particles at close distance.[448] This assignment is supported by dynamic light scattering experiments, which reveal the formation of spherical objects with an average diameter of 0.8 μm in butanol that break up at a temperature above 80 °C (Figure 49). Remarkably, the transition from aggregated to isolated hybrid particles takes place in a very narrow temperature window (~10 °C), indicating a cooperative nature for the aggregation process. Therefore, the present examples show that the aggregation event among the gold particles can be controlled reversibly, even up to certain cycles, by suitably monitoring the reaction conditions of the assembling strategy.

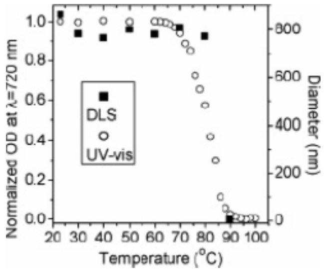

Figure 49. Temperature dependence of the optical density (OD) at $\lambda \approx 720$ nm and diameter of the aggregates from DLS on OPV-Au ($d_{Au} = 4.1$ nm) in *n*-butanol ([OPV-Au] = 0.5 μM).Reprinted with permission from ref 445. Copyright 2006 American Chemical Society.

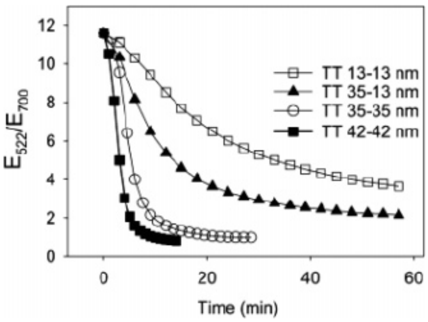

Figure 50. The effect of nanoparticle alignment and size on the rate of color change. Extinction ratios were normalized for comparison. In the figure legends, "TT" denotes "tail-to-tail" alignment. The two numbers following indicate the sizes of nanoparticles used. The experiments were performed with 2 μM 17E at room temperature. The substrate concentration was 160 nM for 13 nm nanoparticles, 120 nM for 13−35 nm mixed nanoparticles, and 3 nM for 35 nm and 42 nm nanoparticles. Time-dependent extinction spectra for the DNAzyme-assembled gold nanoparticles. Reprinted with permission from ref 450. Copyright 2004 American Chemical Society.

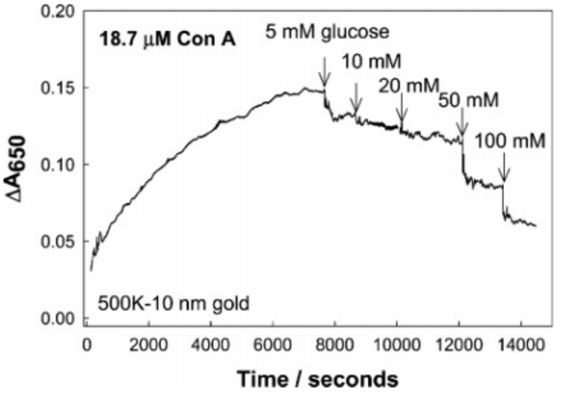

Figure 51. Change in absorbance at 650 nm for 500K dextran-coated 10 nm gold colloids cross-linked by 18.7 μM Con A. Reprinted with permission from ref 420. Copyright 2004 Elsevier.

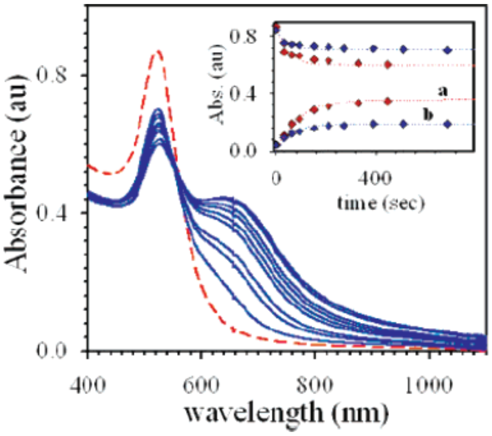

Figure 52. UV−vis for MPF−Au$_{nm}$ assembly at $r \approx 4000$ (blue) (dashed line, Au$_{nm}$). Inset shows kinetic plots for high (a, red) and low *r* (b, blue) for the increase of the Abs$_{680\ nm}$ and decrease of Abs$_{520\ nm}$. Reprinted with permission from ref 337. Copyright 2005 American Chemical Society.

5. Effect of Physical Parameters on Aggregation

5.1. Nanoparticle Size Effect

It has now been investigated that optical properties of a nanoparticle aggregate are dominated by size, instead of the number of nanoparticles in the aggregate.[118,449] Liu et al.[450] developed a colorimetric sensor based on the fundamental understanding of the DNAzyme biochemistry and nanoparticle science for the fast detection of Pb^{2+} at ambient temperature. They have studied the nanoparticle size effect on the process of aggregation and demonstrated that large (42 nm diameter) nanoparticle size is the major determining factor in allowing the fast color change in this sensing event. Figure 50 shows that the rates of color change were progressively faster for larger gold nanoparticles in comparison to the smaller ones. Thus, to accelerate the rate of color change, nanoparticles with larger sizes were employed. Therefore, by using a "tail-to-tail" alignment and larger nanoparticles, a room-temperature aggregation-based sensor was designed. An observation complementary to this was noted by Aslan et al.[420] They investigated the role of smaller gold particles to design a glucose sensor (Figure 51) and explained the complexity when working with smaller nanoparticles.

5.2. Effect of Ligand Concentration

The molar ratio of ligand-to-metal for the synthesis of nanoscale building blocks has a significant effect on the aggregation kinetics. In contrast to the appearance of the surface plasmon resonance band at 520 nm for gold nanoparticles,[451] a new SP band for MPF−gold nanoparticles assemblies in the aqueous solution was found at ∼680 nm (Figure 52). The spectral evolution is indicative of the change in interparticle distance and dielectric medium properties.[452,453] The nanoparticle solution showed a gradual color change from red to purple as a result of the assembly. At $r \approx 4000$ (pH 5), the increase of absorbance for the new band at ∼680 nm was accompanied by a decrease of the 520 nm band. The reactivity is evidenced by the kinetics of the absorbance data for $r \approx 4000$ (a) and ≈ 2000 (b) (inset). Both showed an exponential rise for the 680 nm band and decrease for the 520 nm band, with a clear difference in reaction rate. At the lower *r*, the purplish color of the solution remained for 2 days before precipitation, whereas precipitation occurred within a day for particles with the higher *r*. Importantly, the distinct isosbestic point observed around ∼580 nm indicates the presence of two light-absorbing species at equilibrium (i.e., gold nanoparticle and MPF−Au$_{nm}$ assemblies).

5.3. Effect of pH

The interparticle spacing in Au assembly mediated by MPF was also found to be tunable by pH. On the basis of pK_a values for citric acid (pK_a = 3.1 (a$_1$), 4.8 (a$_2$), and 6.4 (a$_3$))[454] and piperazine (p$K_a \approx 4.2$ (a$_1$) and 8.4 (a$_2$))[455] groups, the

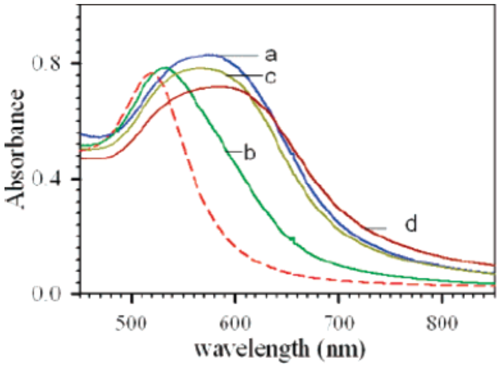

Figure 53. pH-tuning of MPF−Au$_{nm}$ assembly and disassembly. UV−vis spectra for Au$_{nm}$ (dashed line), MPF−Au$_{nm}$ assembly at pH 5 (a), MPF−Au$_{nm}$ upon changing pH to 10 (b), MPF−Au$_{nm}$ upon changing pH to 7 (c), and MPF−Au$_{nm}$ upon changing pH to 2 (d). Each curve was taken after 30 min. Reprinted with permission from ref 337. Copyright 2005 American Chemical Society.

electrostatic interaction involved at least two of the deprotonated -COOH groups in citric acid and one protonated piperazinyl ($-NC_4H_8N^+HCH_3$) of C_{60} at pH ≈ 5. Indeed, when pH is increased to above 8, no apparent spectral evolution was observed. The control of pH was found to tune the assembly and disassembly processes effectively (Figure 53). Upon increase pH from 5 (a) to 10 (b), the SP band shifted from ~580 nm to the wavelength (b) approaching the SP band for Au nanoparticles, indicating the disassembly. This assessment was indeed evidenced by the lack of any nanoparticle clustering feature in the TEM data. As illustrated in Figure 53, the pH-tuned disassembly is due to the absence of electrostatic interactions between MPF and Au nanoparticles because MPF is neutral whereas citrate is negatively charged. This process was reversible as evidenced from the SP band shifting to its original position with the decrease in pH to ~7 (c). At pH ~2 (d), irreversible precipitation and long wavelength broadening of the SP band were observed as a result of instability of the citrate capping on Au nanoparticles at low pH, which was supported by TEM observation of larger aggregates in which individual nanoparticles could hardly be identified. The pH-dependent change in optical properties has implications for controlled release of molecules from the nanoparticle assembly, an area of importance in controlled drug release.

5.4. Solvent Effect

The solvent effect on the position of the surface plasmon band of tri(ethylene glycol)-functionalized gold nanoparticles was investigated by measuring the UV−vis absorbance spectra in the 300−750 nm range in an extended range of alcohols with different polarities.[428] Alcohols were chosen as solvents for specific interactions of the −OH terminus and the oxyethylene chain that could lead to marked effects on the optical properties of gold particles. The time-dependent shift of the SP band to longer wavelengths was attributed to the acid-induced clustering of the nanoparticles into aggregates. The kinetic plot of Figure 54 shows the occurrence of such a transition as a function of the time for trifluoroethanol solution. Similar kinetics could be recorded for the other alcohols. The processes follow first-order kinetics although the final wavelength continues to drift with a much slower kinetic regime. While during the first process the solutions remain limpid, during the second one, large gold colloids are formed that eventually precipitate out of the solution. Furthermore, a careful analysis of the spectra in the SP band region during the kinetic process reveals two distinct behaviors: in the first period of time, there is a shift of the maximum to longer wavelengths without change of the extinction coefficient; at longer times, the extinction coefficient decreases. Recent simulations[118] indicate that such a shift of the λ_{SP} without decrease of the extinction coefficient is associated with a clustering of the nanoparticles resulting in an aggregate.

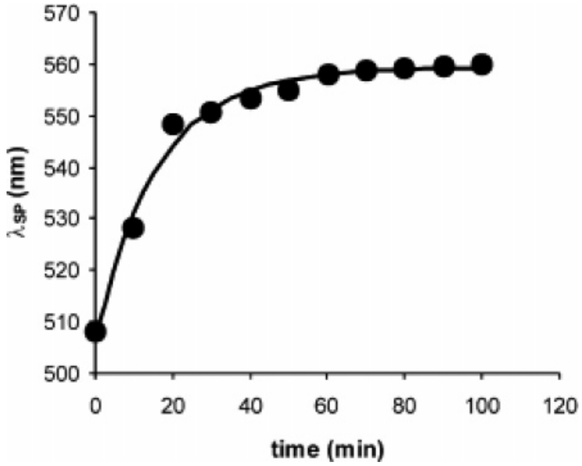

Figure 54. Time dependence of the shift of the maximum of the surface plasmon band for AuMPC 2 in TFE upon addition of HCl (final [HCl] = 37 mM, 25 °C). Reprinted with permission from ref 428. Copyright 2002 Elsevier.

5.5. Temperature Effect

Self-assembly processes are governed by a balance of entropic and enthalpic effects, making them very temperature dependent. Rotello et al.[456] presented a polymer-mediated “bricks and mortar” strategy for the ordering of nanoparticles into structured assemblies. This methodology allows monolayer-protected gold particles to self-assemble into structured aggregates while thermally controlling their size and morphology. Using 2.0 nm gold particles as building blocks, it has been demonstrated that spherical aggregates of size 97 ± 17 nm can be produced at 23 °C (Figure 55a). This temperature dependence is manifested by more efficient recognition processes at lower temperatures,[457] which would be expected to yield larger aggregate structures. Investigations of temperature effects on the preparation of the aggregates yielded results consistent with this prediction. TEM micrographs of the precipitate formed at −20 °C revealed the formation of microscale (0.5 ± 1 μm) discrete spherical particles (Figure 55b), consisting of $(6-50) \times 10^5$ individual thymine−Au units. These microscale particles are among the most complex synthetic self-assembled structures known, demonstrating the thermal control of aggregate size using the “bricks and mortar” methodology. In addition to controlling the size of the aggregates, temperature strongly affects the morphology of the resulting ensembles. At 10 °C, networks were formed (Figure 56c), as opposed to the discrete structures observed at higher and lower temperatures. This suggests that network formation is an intermediate process in the formation of the giant assemblies at −20 °C. The individual assemblies within these networks remained spherical, although their sizes are more highly dispersed. Thus, the degree of ordering and the control of particle size and shape, coupled with the inherent modularity of the “bricks and mortar” colloid−polymer self-assembly process,

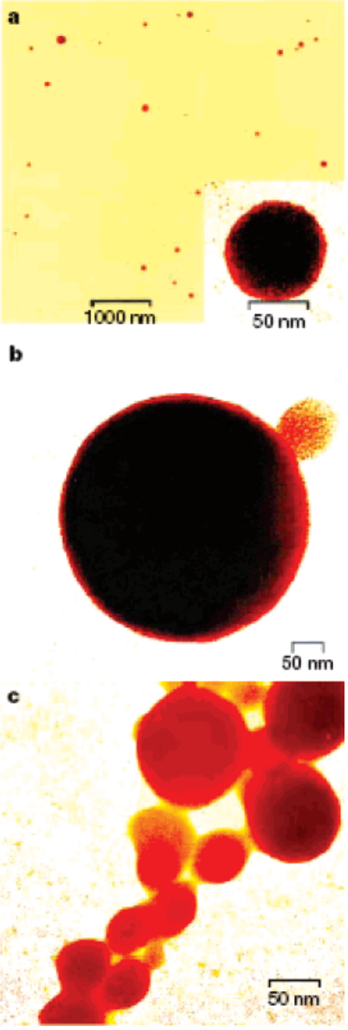

Figure 55. TEM image of polymer 1-Thy-Au aggregates formed at different temperatures: (a) 23 °C (inset shows representative self-assembled microparticle), (b) −20 °C, and (c) 10 °C. Reprinted with permission from ref 356. Copyright 2000 Macmillan Magazines Ltd.

represent a powerful and general strategy for the creation of highly structured multifunctional materials and devices.

5.6. Effect of Reaction Time

In section 3.2.2, it has been reported that dextran-coated gold colloids could be aggregated with concanavalin A in a controlled fashion, and the change in absorbance at an arbitrary wavelength was used to monitor the extent of aggregation.[420] In this experiment, the time to complete the aggregation process was also investigated for the same set of samples (20 nm gold colloids) by monitoring the ΔA_{650} as a function of time (Figure 40). As expected, samples with greater additions of Con A showed a decrease in 90% absorbance (of the final absorbance maximum value) with time, simply reflecting a quicker aggregation rate (Figure 40, right). Therefore, for all subsequent studies, the aggregates were allowed to form well past their 90% ΔA_{650} value before use. Indeed, for glucose additions to the nanoaggregate sensors for sensing, 90% ΔA_{650} values are quoted due to equilibrium between dextran−Con A and glucose.

6. Stabilization of the Nanoscale Aggregates

6.1. Derjaguin–Laudau–Verwey–Overbeck (DLVO) Theory

The classical Derjaguin−Laudau−Verwey−Overbeck (DLVO) theory has been widely employed in colloid science to study particle−particle interactions, colloidal stability, coagulation, sedimentation, filtration, and the behavior of the electrolyte solutions.[458−461] This theory is based on the idea that pairwise interaction forces, which arise from the interplay of attractive van der Waals forces, F_{attr}, and repulsive Coulomb forces, F_{rep}, screened by Debye−Hückel ion clouds, dominate. Obviously, the dispersed colloid is stable for $F_{\mathrm{rep}} \gg F_{\mathrm{attr}}$, whereas the condition of $F_{\mathrm{rep}} \ll F_{\mathrm{attr}}$ leads to aggregation.

The classical DLVO theory states that the total interaction potential between two gold nanoparticles (V_{T}) can be expressed as the sum of electrostatic repulsion (V_{elec}) and the van der Waals attraction (V_{vdw}):[458,459]

$$V_{\mathrm{T}} = V_{\mathrm{elec}} + V_{\mathrm{vdw}} \tag{52}$$

Depending on the particle size and the double layer thickness, the electrostatic repulsion potential, V_{elec}, between two colloidal particles of radii R_1 and R_2 can be expressed in the following two different forms:[460]

$$V_{\mathrm{elec}} = 4\pi\epsilon\psi_0{}^2 \frac{R_1R_2}{R_1+R_2} \ln[1+\exp(-\kappa x)] \qquad \text{(in the case of } \kappa R > 5) \tag{53}$$

$$V_{\mathrm{elec}} = 4\pi\epsilon R_1R_2Y_1Y_2\left(\frac{k_{\mathrm{B}}T}{e}\right)^2 \frac{\exp(-\kappa x)}{x+R_1+R_2} \qquad \text{(in the case of } \kappa R < 5) \tag{54}$$

$$\kappa = \left[\frac{1000e^2N_{\mathrm{A}}(2I)}{\epsilon k_{\mathrm{B}}T}\right]^{1/2} \tag{55}$$

$$Y_i = \frac{8\tanh(e\psi_0/(4k_{\mathrm{B}}T))}{1+\left[1-\dfrac{2\kappa R_i+1}{(\kappa R_i+1)^2}\tanh^2(e\psi_0/(4k_{\mathrm{B}}T))\right]^{1/2}} \tag{56}$$

where ϵ is the permittivity of the medium, ψ_0 the potential at the particle surface, κ the inverse Debye length, x the distance of closest approach between two colloidal particle surfaces, e the electronic charge, k_{B} the Boltzmann's constant, T the temperature, N_{A} the Avogadro number, and I the ionic strength of the solution. The potential at the particle surface can be estimated from the ζ potential measurements.

Assuming the particles to be spherical and the surface potential and the background ionic strength to be constant, the van der Waals attraction potential, V_{vdw}, between the two particles can be calculated as[459−461]

$$V_{\mathrm{vdw}} = -\frac{A_{\mathrm{H}}}{6}\left[\frac{2R_1R_2}{d^2-(R_1+R_2)^2} + \frac{2R_1R_2}{d^2-(R_1-R_2)^2} - \ln\frac{d^2-(R_1+R_2)^2}{d^2-(R_1-R_2)^2}\right] \tag{57}$$

The van der Waals interaction, V_{vdw}, is the dominant attraction and is dependent on the particle radii R_1 and R_2, the center-to-center separation distance, d, and the Hamaker constant, A_H, which plays an important role in the description of attraction energy between the particles.[462,463] The Hamaker constant (A_H) of gold particles from literature[458,464] varies in the range $(1-4) \times 10^{-19}$ J, so the average value, 2.5×10^{-19}, J is used. The Hamaker constant (A_H) can be represented by the equation

$$A_{121} = (\sqrt{A_{11}} - \sqrt{A_{22}})^2 \tag{58}$$

where, the subscript 1 in the Hamaker constant refers to particles of the same material separated by a continuous medium, which is represented through subscript 2. In eq 58, the term A_{11} represents the gold−gold nanoparticle interaction, taken here as 45.3×10^{-20} J[465] and A_{22} corresponds to the solvent interaction.[466] These values of A_{11} and A_{22} can be calculated using the Lifshitz theory for two identical materials interacting across a vacuum.

In the case of metal colloids dispersed in organic solvents, another important effect that can contribute to the total interaction energy is the repulsive forces due to overlapping of the long-chain capping material covering the metal nanoparticles and their interactions with the surrounding solvent molecules. These interactions can be modeled as an osmotic repulsion, V_{osm},[467] which depends on various thermodynamic properties of the system, such as the solubility of the capping molecules in the solvent, and the system temperature.[467,468] Assuming tight size distribution between the particles, that is, $R_1 = R_2 = R$, the osmotic repulsion, V_{osm}, can be presented by

$$V_{osm} = \frac{4\pi R k_B T}{\upsilon_{solv}} \phi^2 \left(\frac{1}{2} - \chi\right)\left(l - \frac{h}{2}\right)^2 \tag{59}$$

where k_B is the Boltzman's constant, υ_{solv} is the molecular volume of the solvent,[469] ϕ is the volume fraction occupied by capping molecules, χ is the Flory−Huggins interaction parameter, l is the chain length of stabilizing molecules, and h represents the interparticle separation distance. The volume fraction and Flory−Huggins interaction parameter can be calculated from

$$\phi = 0.9\left[\frac{3R^2 l}{(R + l)^3 - R^3}\right] \tag{60}$$

$$\chi = \frac{\bar{\nu}_3}{R^{\|} T}(\partial_3 - \partial_2)^2 \tag{61}$$

$$h = d - 2R \tag{62}$$

In eq 61, $\bar{\nu}_3$ represents the molar volume of the solvent,[470] $R^{\|}$ the ideal gas constant, and ∂_i the Hildebrand solubility parameters, in which δ_3 corresponds to solvent solubility[470] and δ_2 is related to the solubility of the capping agent.[471]

6.2. Rationalization of DLVO Theory in the Formation of Gold Aggregates

The phenomena associated with the interactions of colloidal particles have been studied for decades in innumerable ways. The merits of using DLVO theory to assess colloidal phenomena in real systems have also been debated a great deal over the past six decades.[472] In essence, the DLVO theory is a tool that provides a perspective from which we can understand the qualitative characteristics of complex colloidal phenomena engendered by dispersion (Lifshitz−van der Waals) forces and electrostatic interactions.

Table 3. Input Parameters Used for DLVO Calculation and the Stability[a]

sample		Hamaker constant (10^{-19} J)	ionic strength (10^{-4} M)	surface potential (mV)
A	before	2.5	6.10	−52.72
	after	2.5	7.10	−41.38
B	before	2.5	4.16	−43.10
	after	2.5	5.16	−34.86
C	before	2.5	3.66	−41.36
	after	2.5	4.66	−34.71
D	before	2.5	3.26	−32.65
	after	2.5	4.26	−26.48
E	before	2.5	3.08	−29.42
	after	2.5	4.08	−26.17

[a] Reference 473.

The classical DLVO theory is used to rationalize the effect of stabilizing ligand shell on the stability of colloidal nanoparticles. Nanoparticles are stable in solution due to electrostatic repulsion of their charged surface. Lack of sufficient surface charge or stabilizing agent will cause the particles to aggregate or precipitate. Gold reduced by sodium citrate produces nanoparticles with citrate ions adsorbed onto the particle's surface, creating a surface charge that stabilizes the particles.[341] In the citrate-reduced gold nanoparticle system, electrophoretic mobilities and ion conductances are used to estimate the electrokinetic properties and colloidal stability of the particles, and the effect of the citrate concentration on the final particle size could be explained by DLVO theory.[464] It has also been seen that the interparticle interaction of gold nanoparticles can be manipulated to control the final aggregate size.[473] The gold nanoparticles of variable sizes were prepared by the citrate reduction procedure and the interparticle interaction of these particles was manipulated by the addition of benzyl mercaptan ions to replace the citrate ions on the particle surface. The interparticle interaction potentials between two particles can be calculated as a function of their separation from eq 52−57. The input parameters used in the calculation are summarized in Table 3. Figure 56 shows the change in the interaction potential of the gold nanoparticles after the benzyl mercaptan addition. Before the addition of mercaptan ions, the gold particles are colloidally stable since the energy barrier is high enough to prevent aggregation. Upon the addition of the mercaptan ions, the energy barrier is lowered significantly (0 min in Figure 56), leading to destabilization and subsequent aggregation of the particles. The benzyl mercaptan can decrease the energy barrier by both lowering the surface potential of the particles and increasing the ionic strength. As time elapses, the energy barrier increases, suggesting that some of the aggregates could become stable again. Another neutral ligand, pyridine[415] can also be used to disrupt the surface of citrate ions causing particle aggregation. Since there are no species in solution to generate sufficient surface charge on the forming particles, the particles will aggregate. Recent small-angle X-ray scattering on gold particles produced by reduction of $HAuCl_4$ with Na_2S also show clear evidence of aggregates.[341,345]

Several authors have shown that addition of sodium chloride caused aggregation because of screening effect of the electrolyte ions. In many cases, cationic surfactant causes aggregation by neutralizing the negative charge on the

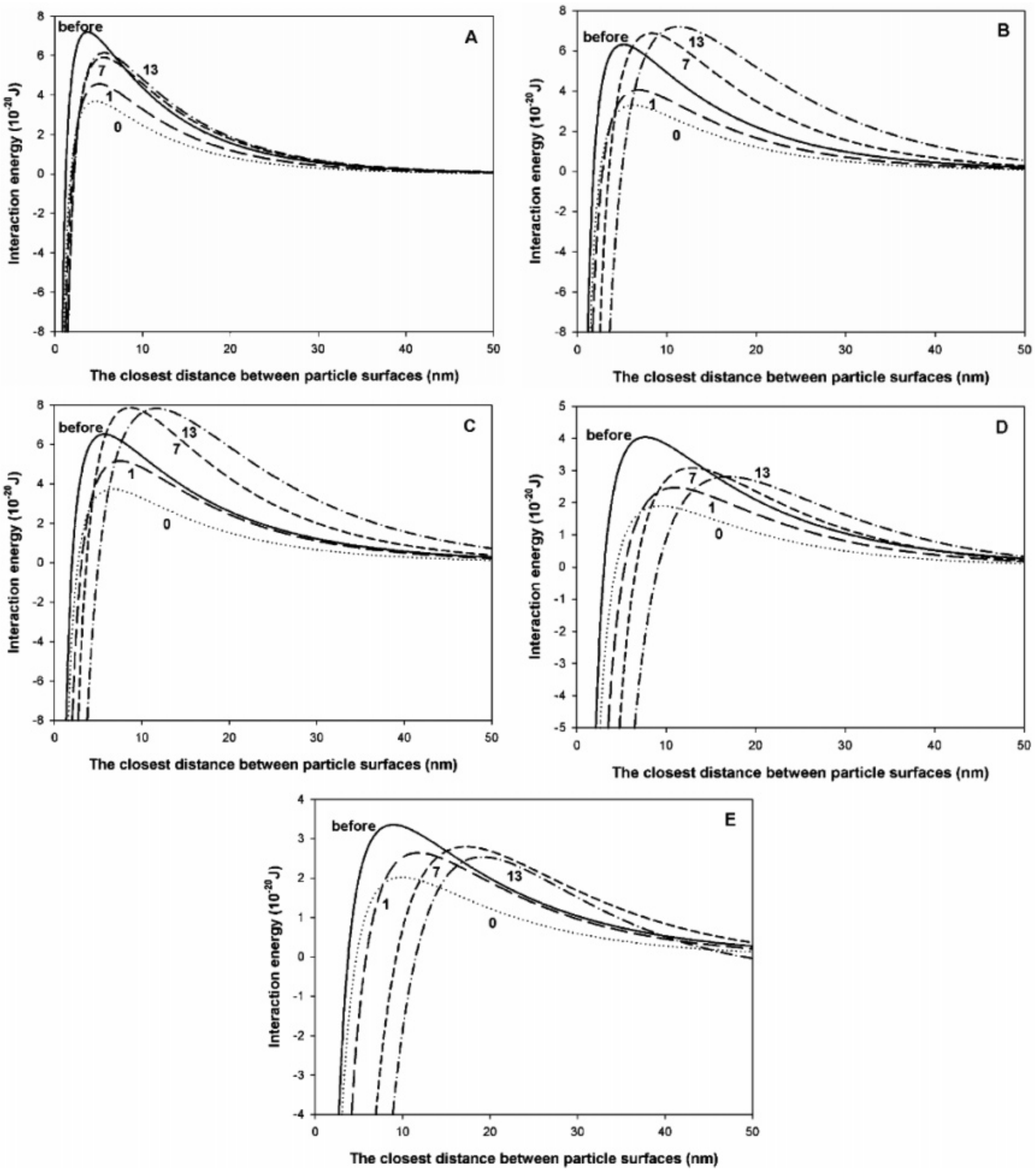

Figure 56. Change in the interparticle interaction potential after the benzyl mercaptan addition (numbers indicate the time in minutes after the benzyl mercaptan addition). Reprinted with permission from ref 473. Copyright 2005 American Chemical Society.

nanoparticle surface. On the other hand, in the case of metallic nanoparticles dispersed in organic solvent stabilized by long-chain cationic surfactants, addition of glutathione (a biomolecule consisting of amino acids, namely, glutamic acid, cystine, and glycine) induces aggregation among the gold particles by replacing the surfactant molecules from the surface of metal particles.[474]

A two-stage assembly strategy uses polyhedral oligomeric silsesquioxane units functionalized with hydrogen-bonding recognition units to assemble gold nanoparticles into discrete aggregates.[475] Diamidopyridine-functionalized POSS units undergo an initial hydrogen bonding interaction with complementary thymine-functionalized gold nanoparticles followed by subsequent aggregation and crystallization of the POSS moieties producing well-defined, spherical, hybrid aggregates of varying size, featuring uniform interparticle spacings.

A symmetry-breaking mechanism has also been proposed to explain the stepwise molecular assembly of small, controlled aggregates of gold nanoparticles.[361] Silica nanoparticles were used as substrates to provide the symmetry-breaking mechanism necessary for colloidal assembly of these small nanoparticle aggregates. The distance between aggregated gold nanoparticles was primarily controlled by a molecular linker, which covalently attached the constituent nanoparticles to each other.[362] The growth scenario for these aggregates is quite different from the recently reported absorption of colloidal aggregates formed in solution onto silica nanoparticle surfaces in certain solvent mixtures.[476] The bifunctional molecule 4-aminobenzenethiol might simply be reducing the surface charge of the gold nanoparticles by replacing citrate ions. The adsorption of gold nanoparticles on planar substrates reduces the electrostatic repulsion between nanoparticles themselves and allows more gold nanoparticles to react with the functionalized surface.

7. Nanoparticle Growth and Aggregation Kinetics

Aggregation processes in colloids have been the subject of numerous experimental, theoretical, and computational studies.[477−482] When any nucleus is formed in a colloidal solution, it may have several possible fates: redissolution, ripening, coagulation, or stabilization.[483] The greatest practical challenge is to prevent coagulation. Even in the absence of van der Waals interactions, Brownian encounters (10^{10} s^{-1}) are frequent enough to cause aggregation between the particles within a few seconds. To prevent rapid and irreversible coalescence and consequent loss of all size-dependent features, the particles must be arrested in the early stages of particle formation. Metal sols are often stabilized in solution by the presence of a charged double layer surrounding each colloidal nanoparticle that produces a Coulomb barrier to aggregation. Sols consisting of metal nanoparticles stabilized against aggregation have been known for the last two centuries. As previously mentioned, a sample of the gold colloid prepared by Michael Farady in the late 18th century is still on display in the Faraday Museum of the Royal Institution.[28] Its purple/violet color is immediate visual proof of the reluctance of the gold colloidal particles to aggregate into a more massive gold sample despite the strong thermodynamic impulse to do so, driven both by the exoergicity of the bulk reaction and by the ensuing reduction of the surface free energy. There are some thermodynamic terms that go the other way, such as the entropic contribution to the structure of water in the neighborhood of the nanoparticles that is increased upon aggregation; but these effects are smaller in magnitude. The stability of most of these sols is largely a kinetic effect due to the large Coulombic repulsive barrier resulting from the localization of the charged particles on or near the nanoparticle's surface,[477−479] making the effective charge on the nanoparticle nonzero. It has been known for sometime that the addition of ionic or neutral species to a stable sol can result in the destabilization of the colloid through one of a number of mechanisms, which may vary according to the concentration of the added material.

A simple treatment[480] of the potential governing two charged colloidal metal particles proceeds as follows.

(1) At very small distances, there would be a short-range repulsive potential (V_1) between two colloidal particles (assuming the particles to be spherical), which is approximately given by

$$V = B/r'^{n} \tag{63}$$

where, r' is the center-to-center distance between the two particles and n an exponent that normally lies in the range of 9−13.

(2) The van der Waals attractive potential between the two particles can be presented by an equation of the form

$$V_2 = C/r'^{6} \tag{64}$$

(3) Finally, if it is assumed that the surface of the colloidal particle accommodates N species each carrying an electronic charge e, there will be a Coulomb repulsion term of the form

$$V_3 = N^2e^2/(\epsilon_0 r') \tag{65}$$

where ϵ_0 is the dielectric constant of the ambient.

Now, the overall potential is given by

$$V = V_1 + V_2 + V_3 = B/r'^{n} + C/r'^{6} + N^2e^2/(\epsilon_0 r') \tag{66}$$

and has the form shown in Figure 57. Since the stability of the colloid results from the potential barrier developed as a result of the competition between van der Waals attraction and Coulomb repulsion, the short-range potential, V_1, term in the above expression could be neglected because it contributes negligibly in the neighborhood of the potential maximum. The height of the barrier, V_{max}, depends approximately on the (average) number, N, of surface charges residing on a nanoparticle as (determining the maximum value of $V_2 + V_3$ using simple calculus)

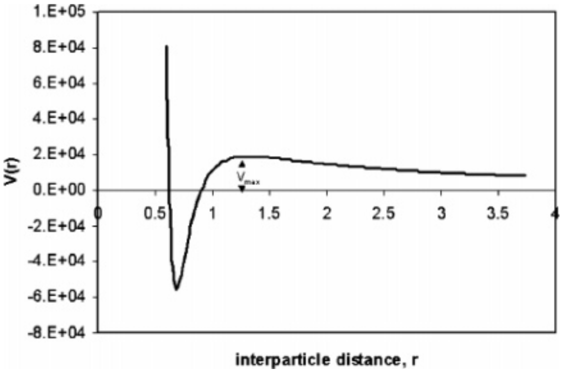

Figure 57. Potential between two charged nanoparticles as a function of the interparticle distance. Both ordinate and abscissa are in arbitrary units. Reprinted with permission from ref 480. Copyright 2005 American Chemical Society.

$$V_{max} = 0.5823C^{-1/5}(N^2e^2/\epsilon_0)^{6/5} \tag{67}$$

Aggregation occurs rapidly when V_{max} is not too large with respect to k_BT. The height of the barrier, V_{max}, can be reduced, and thereby, aggregation can be encouraged, by replacing the charged species on the surface with uncharged species. The number of charges remaining on the nanoparticle surface will be the difference between the numbers of charges originally residing on the nanoparticle's surface less the number of charges displaced by the uncharged adsorbate molecules actually adsorbed at the nanoparticle's surface. Such a displacement will occur if the binding energy of the uncharged adsorbate is greater than that of the charged surface species.[481−485]

Adsorption of ions and molecules on the surfaces of solid particles is a critical step in crystal growth, surface catalysis, and many other physical and chemical phenomena.[486−489] As the dimensions of the particles shrink into the nanometer range, the surface plays an increasingly important role in controlling the overall energy of the particles.[490] The thermodynamic driving force for adsorption at a surface is typically described using the concept of free energy. The overall free energy change for adsorption from solution onto a surface is a function of the chemical composition and structure of the solid, as well as the nature of the solution. For a fixed set of solution parameters, however, the influence of particle size on the adsorption can be described thermodynamically by an adsorption coefficient (K_{ads}), which can be determined experimentally by measuring the extent of surface adsorption as a function of solution concentration. Nanocrystalline materials fall into a regime where classical thermodynamics begins to overlap with atomistic lattice-based theories for understanding physical and chemical behavior. The relationship among K_{ads}, surface free energy, and crystal size can be defined using a classical thermodynamic approach. To describe the influence of particle size on adsorption at particle surfaces, a simple Langmuir-type adsorption isotherm can be employed. In the Langmuir isotherm, the probability of a molecule adsorbing at any surface location is independent of the total surface coverage and dependent only on whether the specific adsorption site is already occupied.[430] For particles of a given size, the Langmuir isotherm is

$$N = N_{\text{max}} \frac{K_{\text{ads}}[\text{I}]}{1 + K_{\text{ads}}[\text{I}]} \tag{68}$$

where [I] presents the activity, that is, the effective concentration of the adsorbate in the solution, N is the number of molecules adsorbed per unit surface area, and N_{max} is the maximum number of molecules per unit area that can be adsorbed, which is limited by the number of available surface sites. The adsorption coefficient, K_{ads}, can be calculated thermodynamically using

$$K_{\text{ads}} = \exp\left(-\frac{\Delta G^{\circ}_{\text{ads}}}{R^{||}T}\right) \tag{69}$$

where $\Delta G^{\circ}_{\text{ads}}$ is the free energy change of adsorption, $R^{||}$ the universal gas constant, and T the absolute temperature. Since at equilibrium the surface coverage by adsorbate is dependent on the concentration of adsorbate molecules in solution through the isotherm, the charge on the nanoparticle's surface will be a function of the concentration of adsorbate in solution.

The number of adsorbed molecules, N_{ads}, at a given equilibrium concentration, m, of adsorbate in solution is given by an equation in which β is a temperature-dependent constant. The number of molecules adsorbed per unit surface area N, which is equal to $N_{\text{max}} - N_{\text{ads}}$, is therefore given by

$$N = \frac{N_{\text{max}}}{1 + \beta m} \tag{70}$$

Substitution into eq 67 produces the equation

$$V_{\text{max}} = \frac{V_0}{(1 + \beta m)^{12/5}} \tag{71}$$

where $V_0 = 0.5823C^{-1/5}N_{\text{max}}{}^{12/5}e^{12/5}\epsilon_0{}^{-6/5}$. The barrier to dimerization of the particles will therefore be a function of the concentration, m, of adsorbate molecules in solution.

Metal sols normally aggregate through two global (nanoparticle-concentration-dependent) mechanisms. First, aggregates can be formed primarily through the addition of single nanoparticles to a growing cluster, that is, cluster−particle aggregation, and second, clusters of all sizes can assimilate into larger clusters, that is, cluster−cluster aggregation.[492] An aggregating colloid can switch from one mechanism to the other depending on the number of depleted nanoparticles in the solution. Whatever the overall process governing aggregation, all aggregation processes begin with the formation of a nanoparticle dimer from two isolated nanoparticles. The rate constant, k, describing the process of dimerization will be related to the aggregation barrier height, V_{max}, as

$$k = k_0\,\mathrm{e}^{-V_{\text{max}}/(k_{\text{B}}T)} = k_0\,\mathrm{e}^{-V_0/(k_{\text{B}}T(1 + \beta m)^{12/5})} \tag{72}$$

Equation 72 predicts very specific adsorbate concentration dependence for the initial rate of aggregation of metal sol by replacing the charged surface species with uncharged adsorbate. These underlying physicochemical approaches have been found to exhibit the observed level of agreement with experiment.

8. Modeling Nanoparticle Aggregation

Aggregation of colloidal dispersions has been a research topic of great relevance in colloidal science because various industrial applications involving colloidal dispersions require a controlled aggregation step to obtain the desired final products.[493] Thus in the last 20 years, a large number of experimental and theoretical studies have been carried out aiming at understanding the physical principles of the aggregation phenomena.[494]

Several experimental techniques, such as light, neutron, and X-ray scattering and electron and confocal microscopy, have been applied to investigate colloidal aggregations. These studies have clarified that there exist two well-defined aggregation regimes under stagnant conditions: the fast or diffusion-limited cluster aggregation (DLCA) regime and the slow or reaction-limited cluster aggregation (RLCA) regime.[493] The two regimes are characterized by structural differences as RLCA regime aggregates are more compact than the DLCA regime aggregates. From the modeling perspective, several approaches, such as Monte Carlo simulations, Brownian dynamic simulations, and the kinetic approach based on the population balance equations, have been applied to describe these aggregation processes. The main objective of using Monte Carlo simulations is to reproduce the fractal structures of the formed clusters rather than to model the time evolution of the cluster mass distribution. Brownian dynamic simulation allows one to investigate the real-time evolution of both structure and mass of the clusters, but it requires an enormous computational time so that only smaller size systems can be dealt with. The kinetic approach based on the population balance equations allows one to investigate the time evolution of the cluster mass distribution without limitations in the size of the aggregating system, although it does not provide any information about the cluster structure.

9. Optical Response of the Aggregates of Gold Nanoparticles

There is abundant literature covering the science and technology of gold nanoparticles, particularly with respect to their optical properties.[74,75] Much of the interest has been focused on plasmon resonances of dilute suspensions of spherical particles, which usually show a violet color. However, when individual gold nanoparticles come into close proximity to each another, the color in transmission becomes blue. The color change that follows from aggregation of gold nanoparticles has found innumerable applications. Thus, metal nanoassemblies offer exciting opportunities for manipulating light at the nanoscale via morphology-controlled resonances associated with surface plasmon modes. When a metal nanostructure is subjected to an external field, the detected signal is determined by a superposition of the driving field with secondary (re-emitted) fields associated with induced SP oscillations. Because of the coherent nature of this superposition, the total field is strongly dependent on the phases of plasmon oscillations. The phase manipulation can be used, in particular, for controlling the spatial distribution of SP modes. Therefore, the properties of the

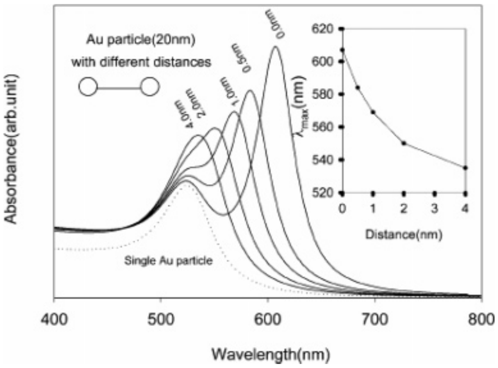

Figure 58. Electrodynamic modeling calculations for gold nanoparticles. Change of extinction spectra for 20 nm diameter particles with interparticle distance (*s*). Inset is the peak shift vs interparticle distance. Reprinted with permission from ref 495. Copyright 2004 American Chemical Society.

aggregates of metal nanoparticles would be explored from theoretical and experimental perspectives.

9.1. Theoretical Calculation

Although, Mie theory has traditionally been developed for the calculation of extinction spectra of single particles of highly symmetric shape and appropriate size range, in reality, a suspension of particles often has an aggregate structure of complex morphology. The complexity of the resulting multiple scattering and interference effects cannot be readily modeled by simple Mie theory. In these calculations, the external plane wave incident on one particle is superimposed by the near-field Mie scattering fields of all neighboring clusters. Therefore, the absorption cross-section of an aggregate of gold nanoparticles was calculated for a range of wavelengths, and a dispersion relation for gold was generated by fitting the real and imaginary parts of the index of refraction. Theoretical calculations reveal that the distance between gold nanoparticles, aggregate size, and the polarization direction has significant influence on the predicted extinction spectra as follows.

The distance between gold nanoparticles, either as discrete particles or as aggregates of varying size, has a significant influence on the absorbance spectra of gold nanoparticles.[495] Figure 58 depicts the calculated absorption spectra for clusters of two spherical gold nanoparticles ($d = 20$ nm) with different separation distance. Highly dispersed gold nanoparticles (effectively considered as single particles) in solution should exhibit only a single peak (Figure 58, dotted line), while linked gold particle pairs (or larger aggregates) show two absorbance maxima. The frequency and intensity of the aggregated system depend on the degree of aggregation as well as orientation of the individual particles within the aggregate. The first peak, located near the resonance peak for single particles, is attributed to the quadrupole plasmon excitation in coupled spheres, while the second peak at a longer wavelength is attributed to the dipole plasmon resonance of the gold nanoparticles.[496] The oscillating electrons in one particle feel the electric field due to the oscillations in a second particle, which can lead to a collective plasmon oscillation of the aggregated system. As the interparticle spacing decreases, the first peak becomes weaker while the second peak intensifies and shifts to longer wavelengths. The maximum peak shift is observed if the interparticle distance approaches zero, at which point the electrodynamic interaction between the nanoparticles is at a maximum. At the other extreme, when the interparticle spacing exceeds about 5 times the particles radius ($d \leq 5R$), classical single-particle Mie theory should apply.

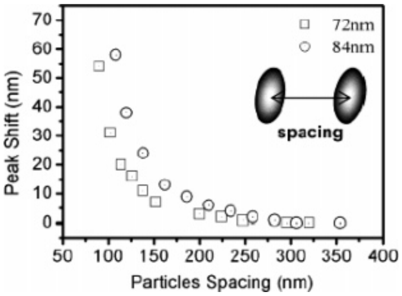

Figure 59. Resonant-peak wavelength as a function of particle center−center spacing for particles with short-axis lengths of 72 and 84 nm. Reprinted with permission from ref 497. Copyright 2003 American Chemical Society.

Su et al.[497] have investigated the coupling between pairs of elliptical metal particles by simulations and experiments. In this investigation, they have focused on the effects of near-field interparticle coupling on the particle plasmon resonances, especially the shift of the plasmon resonant wavelength as a function of particle separation. As expected, the experimental and simulation results indicate that the resonant wavelength of two coupled particles in close proximity is significantly red-shifted from that of the individual particles. Figure 59 shows the resonant wavelength shift as a function of the center−center spacing between two particles for two different particle sizes. The peak shift decays rapidly with increasing particle spacing, reaching zero when the particle spacing exceeds certain distances, indicating the diminishing of the near-field plasmon coupling between these two particles. It is also found that the exponential decay of the peak shift with the particle gap is size-independent because the shift and gap are scaled, respectively, by the peak wavelength and particle sizes. The scaled decay function is particle-shape-dependent in the sense that the decay length depends on particle shapes. These reductions in peak shift drop to zero when the gap between the two particles reaches about 2.5 times the particle size. The enhanced electric fields are confined within only a tiny region of nanometer length scale near the surface of the particles and decay significantly thereafter. This localized field enhancement provides a field gradient that is much greater than that of any far-field optical tweezers; therefore, it may be possible to trap single molecules or other nanoparticles in regions near an elliptical metal nanoparticle or tip[498−500] or between two nanoparticles.[501] The reduction in the peak shift and scattering intensity with particle spacing reflect the decay of the field distribution between the particles, which plays a key role in particle plasmon applications, such as, SERS[100,487,502,503] and nano-optics.[105,504,505]

The plasmon hybridization method has been developed to investigate the plasmon frequencies and optical absorption spectra of nanosphere dimers[506,507] and larger multiparticle aggregates.[508,509] Plasmon hybridization allows us to express the fundamental plasmon modes of these multinanosphere systems as linear combinations of the plasmons of individual nanospheres in a manner analogous to molecular orbital theory. It has been shown that the dimer plasmons can be viewed as bonding and antibonding combinations, that is, hybridization of the individual nanoparticle plasmons. In the plasmon hybridization method, the conduction electrons are modeled as a charged, incompressible liquid sitting on top of a rigid, positive charge representing the ion cores. For large separation distance, *d*, the shifts of the dipolar dimer plasmons essentially follow the interaction energy between two classical dipoles ($1/d^3$). As *d* becomes smaller, the shifts of the dipolar dimer plasmons become much stronger and vary much faster with *d* due to the interaction and mixing with higher multipole oscillations. It has also been shown that calculating the energies of plasmon resonances of complex metallic nanoparticles is equivalent to calculating the electromagnetic interactions between plasmons of nanostructures of simpler geometry. For example, the calculation of plasmonic properties of the symmetric nanosphere trimer and quadrumer has shown that the plasmon modes of each configuration are symmetry-specific linear combinations of plasmons from the individual particles. This leads to higher energy plasmon modes being excitable by light at closer separations, but because the energies lie close to each other, broadening of the peaks will obscure some of these energies. Thus, the plasmons of a complex nanoparticle result from hybridization of the plasmons of individual nanoparticles, and the strength of the hybridization depends on the geometry of the composite particle.

It is now well-established in the literature that the absorption of a single spherical cluster is described as due to a dipole induced by the external electric field. If other clusters are nearby, the total electric field results from superposition of the external incident field and the dipole fields of all other clusters. Electromagnetic coupling of clusters becomes effective for cluster−cluster distances smaller than 5 times the cluster radius and may lead to complicated extinction spectra depending on size and shape of the formed cluster aggregate by a splitting of single cluster resonance. In this case, it can be assumed that the effect of polarization has a great influence on the aggregate formation. Since larger particles are more polarized than the smaller ones, theoretical calculations show that the electrodynamics corrections include the leading terms in the equation below in which the left- and right-hand sides are expanded in powers of $1/\lambda$, and then the result is averaged over the particle volume. The lowest order term is, of course, the electrostatic solution. For spherical particles with polarization *P*, the next higher order corrections involve rewriting the equation as

$$P = \alpha \cdot [\mathbf{E}_{\text{loc}} + \mathbf{E}_{\text{rad}}] \qquad (73)$$

where the radiative correction field, $\mathbf{E}_{\text{rad}}$, is

$$\mathbf{E}_{\text{rad}} = {}^{2}/_{3} ik^3 P + k^2/(RP) \qquad (74)$$

where *R* is the particle radius. The first term in this expression describes radiative damping that arises from spontaneous emission of radiation by the induced dipole. This emission grows rapidly with particle size, eventually reducing the size of the induced dipole and increasing the plasmon line width. The second term comes from depolarization of the radiation across the particle surface due to the finite ratio of particle size to wavelength. This dynamic depolarization term causes red shifting of the plasmon resonance as the particle size is increased. An equivalent theory for other particle shapes has been described by Zeman and Schatz.[510] The net effect of both these terms is to produce a modified polarization, *P*, of the particle multiplied by the following correction factor:

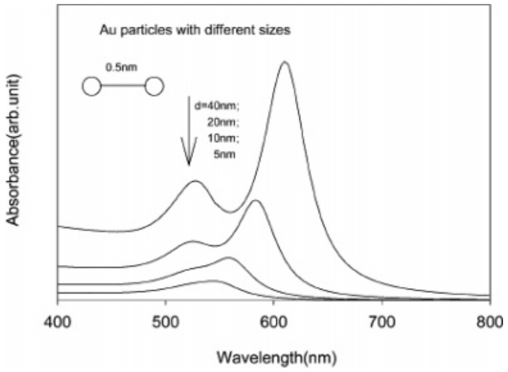

Figure 60. Electrodynamic modeling calculations for Au nanoparticles. Influence of gold nanoparticle diameter (*d*) on the extinction spectra at fixed (0.5 nm) interparticle diameter. Reprinted with permission from ref 495. Copyright 2004 American Chemical Society.

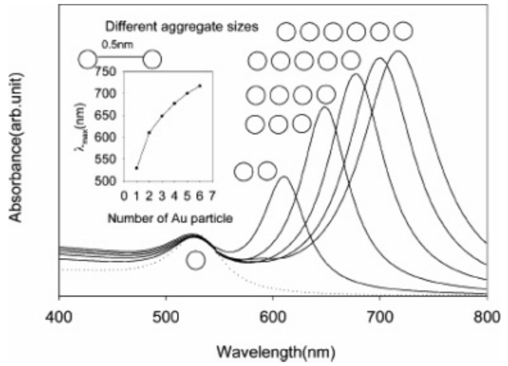

Figure 61. Electrodynamic modeling calculations for gold nanoparticles. Extinction spectra of “line aggregates” of varying number ($d = 40$ nm, $s = 0.5$ nm). Inset is the peak shift against the number of gold particles in the line aggregate. Reprinted with permission from ref 495. Copyright 2004 American Chemical Society.

$$F = (1 - {}^{2}/_{3} ik^3 \alpha - k^2/(R\alpha))^{-1} \qquad (75)$$

It is to be noted that the radiative damping contribution to the correction factor is proportional to the product of the polarizability. The dynamic depolarization term is proportional to α/R (proportional to the particle area) times k^2. Thus, the higher order multipole modes become effective when the particles are in close proximity to each other.

In Figure 60, the interparticle distance is fixed at 0.5 nm for gold nanoparticle pairs (corresponding to the molecular length of the stabilizing ligand, cysteine in the present experiment). With an increase of the particle size from 5 to 40 nm, two distinct peaks develop from a broad single feature of intermediate λ_{max}. The effect of aggregation was simulated using a linear chain or “linear cluster” model.[495] In reality, aggregates of different shape and size are likely to be present in the solution, but as a first approximation, their tendency to aggregate and their scattering characteristics can be simulated and calculated using this model.

Figure 61 shows the calculated absorption spectra for linear aggregates of gold nanoparticles ($d = 40$ nm), where the light polarization direction is oriented parallel. A systematic bathochromic shift in λ_{max} is expected with increasing aggregate size. As the dipole plasmon red shifts, a quadrupole resonance grows in. Because of the rapid variation of the real part of ϵ with wavelength, the quadrupole resonance

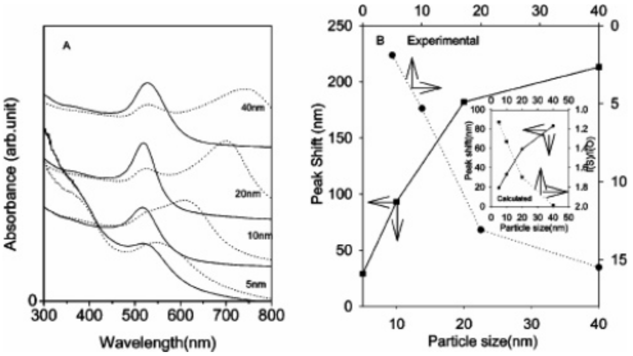

Figure 62. (A) UV−visible peak shift dependence on Au particle size, before (solid line) and after (dotted line) addition of 100 μL of 0.01 M cysteine in 0.01 M HCl and (B) the ratio between the absorbance of the newly developed peak (I_s) after amino acid addition to that of the "reference" peak at ~520 nm (I_o) against Au particle size (dotted line) and the corresponding peak shifts (solid line). The inset is the same plot as predicted theoretically. Reprinted with permission from ref 495. Copyright 2004 American Chemical Society.

also starts at lower wavelength for small particles. The quadrupole resonance also red shifts as the particle size is increased, but the effect is much smaller than that for the dipole resonance.

Although the dielectric constant of the surrounding medium also has an influence on the optical properties of gold nanoparticles (because the interparticle coupling is certainly stronger than the coupling with the surrounding medium), the effect is less pronounced than the above-cited parameters.[511,512] This reveals the trend that large gold particles or aggregates and short separation (or short linker molecules) between particles should give rise to higher optical response (high molar extinction). Because of the idealized model utilized here, it should be noted that the value of such calculations is restricted to prediction of qualitative trends. For more rigorous (quantitative) modeling, various additional physical phenomena must be taken into account, including electrodynamic and material effects, such as electrical charging and tunneling.[513]

9.2. Experimental Observation

In recent years, several authors have investigated the spectroscopic behavior of resonant coupled systems as a function of particle separation[358,514−516] and predicted molecular trapping by the forces associated with the strong field gradient.[517] Direct experimental measurements of electromagnetic fields localized between closely spaced nanostructures are needed to validate theoretical predictions and to develop systems with improved properties.

Amino acids, cysteine and lysine, were chosen to study the effect of gold particle size on the relative optical absorbance change as a basis for molecular recognition and analytical detection.[495] As shown in Figure 62A, the smaller the gold particle size is, the less the peak shift and the lower the relative intensity. In Figure 62B, the peak shift and absorbance ratio of the new peak (I_s) to the reference peak at 520 nm (I_0) after cysteine addition are plotted against the particle size. An almost linear increase in peak displacement (I_s/I_0) against particle size is seen in the range of 5−20 nm, deviating slightly at 40 nm. Thus, the general conclusion for analytical purposes is that larger gold nanoparticles are more sensitive to the target (amino acid) molecules, which is consistent with the theoretical calculation.[518]

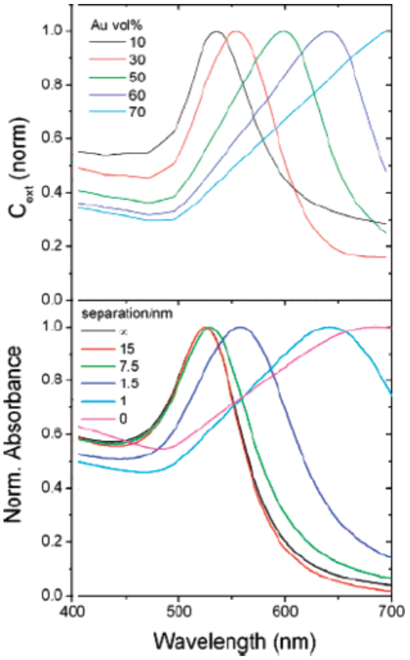

Figure 63. (top) Calculated UV−visible spectra for thin glass films loaded with increasing Au nanoparticle volume fractions and (bottom) experimental spectra of multilayer films of glass-coated Au spheres with varying interparticle distance. Reprinted with permission from ref 519. Copyright 2006 American Chemical Society.

Figure 63 provides an overview of the relative magnitudes of effects of interparticle interactions on the plasmon resonance frequency (both calculated and experimental) of gold nanoparticle systems.[519] As soon as the nanoparticle volume fraction increases above 10%, the single plasmon band of isolated spheres starts to red-shift and broaden, as a result of dipole−dipole interactions. It is important to note that the predictions based on theory have been confirmed experimentally. Thus, it has been briefly shown that the degree of control over the optical response from metallic nanostructures has become extremely sophisticated.

Proteins provide versatile mediators for assembling nanoparticles into organized composites. Verma et al.[520] demonstrated that a single protein spacer (lysozyme) can be used to direct the self-assembly of gold mixed monolayer protected clusters into controlled ensembles with varied functional response. This efficient self-assembly process provides modular collective optical behavior, as examined through UV−visible spectroscopic measurements. The surface plasmon resonance of the solid nanocomposites at various temperatures demonstrates the modulation of dipolar optical interactions as shown in Figure 64. The optical responses of the free nanoparticles in solution (assumed to be free of dipolar coupling) and nanoparticles displaying maximum coupling (spaced only by the monolayer) were monitored. It was observed that the λ_{max} of free nanoparticles in solution was 528 nm, while the nanoparticles spaced only by the monolayer displayed a SPR of 596 nm, due to an increased dipolar coupling. A complementary level of control over the collective optical response was achieved using the assembly formed at higher temperature (50 °C). While the effect of increased refractive index induces a moderate red shift in the SPR of the individual nanoparticles, the collective SPR of the coupled nanoparticles is highly sensitive to the refractive index of the surrounding environment. This has been recently studied by Tsukruk et al., where they have

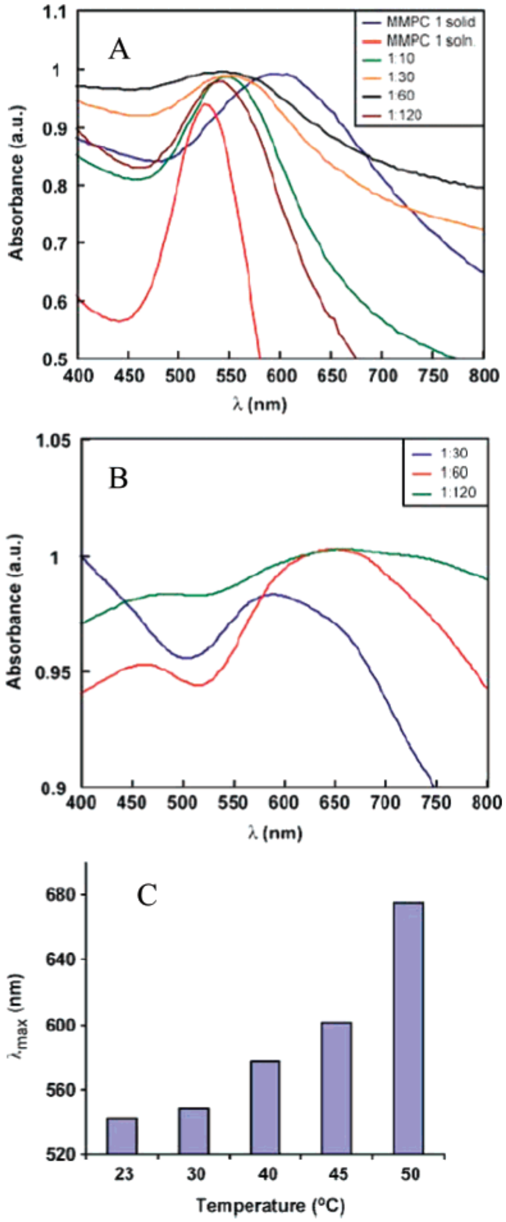

Figure 64. The optical response for the protein−nanocomposite solid films displayed at (A) 23 °C and (B) 50 °C. The ratios indicate MMPC 1/protein stoichiometries and MMPC 1 soln refers to only nanoparticles in water. (C) The 127 nm shift in λ_{max} is obtained through a particle/protein ratio of 1:120, assembled at the different temperatures. Reprinted with permission from ref 520. Copyright 2005 American Chemical Society.

Table 4. Normalized Solvent Polarity Parameter, E_T^N, of the Solvents Studied, Shifts of the Surface Plasmon Band, $\Delta\lambda_{SP}$, upon Acid Treatment (37 mM HCl), and Rate Constants of the Band Shift Processes, log(k_{obs})[a]

solvent	E_T^N	$\Delta\lambda_{SP}$	log(k_{obs})
dioxane	0.164	19.0	−0.66
THF	0.207	8.8	−1.39
i-PrOH	0.546	3.1	−1.37
n-BuOH	0.602	2.6	−1.71
EtOH	0.654	5.4	−1.96
MeOH	0.762	40.4	−1.72
TFE	0.898	51.3	−1.22

[a] Reference 428.

displayed that a few nanometers thick film of polymers coated onto a film of optically coupled gold nanoparticles can red-shift the collective SPR of the assembly by 90 nm.[521] This behavior, combined with the unique gold−protein self-assembly mode at the higher temperature, was exploited to direct the collective response in the hybrid nanocomposites. Samples prepared at 50 °C featured particles spaced by a particular distance, which ensured a constant dipolar coupling for the higher temperature ensembles. However, an increase in the amount of protein around the assembly with increasing nanoparticle/protein ratio is expected to enhance the local refractive index, resulting in a significant red shift of the collective plasmon peak.[437,522] As expected, the collective plasmon peak was found to be dependent on the particle/protein ratio (Figure 64). The absorbance spectra display that the λ_{max} of the protein−nanoparticle composites is red-shifted, even beyond the particles separated only by their monolayer. The collective response of the assembly was found to be dependent on the excess protein used, with the highest ratio shifting the SPR to 675 nm.[523] For the samples assembled at higher temperatures, additional absorbance peaks at ∼460 nm are observed. The origin of these peaks could be due to either local dielectric effects or short-range anisotropy in the assembly process. Additionally, nanoparticle−protein composites (1:120) assembled at various temperatures displayed that the collective plasmon peak can be tuned over a 127 nm range (from 548 to 675 nm) through this efficient self-assembly methodology (Figure 64C). This factor is expected to contribute to the subsequent red shift in the SPR of the assembled nanoparticles by increasing the dipolar coupling between the nanoparticles.

The solvent effect on the surface plasmon band was investigated when tri(ethylene glycol)-functionalized gold nanoparticles were exposed to adventitious traces of acid in a sequence of solvents of different polarities.[428] It was seen that addition of acid leads to a change of color due to aggregation among the gold colloids that occurs in a period of 30 min to 1 h, depending on the solvent. The absorption measurement of the resulting gold colloids shows the variation in λ_{max}, depending on the nature of the solvent. Table 4 shows the change in the maximum of the surface plasmon band ($\Delta\lambda_{SP}$) as a function of E_T^N, the normalized empirical solvent polarity parameter introduced by Dimroth and Reichardt.[524] The plot shows a bimodal behavior with minimum $\Delta\lambda_{SP}$ at $E_T^N = 0.6$ (*n*-BuOH) and linear but opposite dependence from the polarity of the medium below and above this E_T^N value. Thus, it can be concluded that $\Delta\lambda_{SP}$ increases both with the increase and with the decrease of the polarity and the most marked dependence is observed with the most polar solvents. The inverted dependence at lower E_T^N could be explained with a change of the prevailing effect, leading to the formation of the cluster, from the hydrophobic one to the interparticle hydrogen bonds due to the less competitive solvents. The lower solvation of the free nanoparticles in the least polar solvents could also account for their faster clustering rate in these solvents.

The thermal properties of thiol-protected gold nanoparticles are well-documented in the literature.[339] The organic layer of thiol-protected gold nanoparticles (ca. 3 nm in diameter) was cross-linked using ring-opening metathesis polymerization.[310] Upon heating, small nanoparticles aggregate into bigger structures. Maye and Zhong[425] proposed that two consecutive processes are responsible for the size and shape evolution of the particles during heat treatment. The first involves thermally driven desorption of the ligands from the gold surface followed by coalescence of the nanoparticle

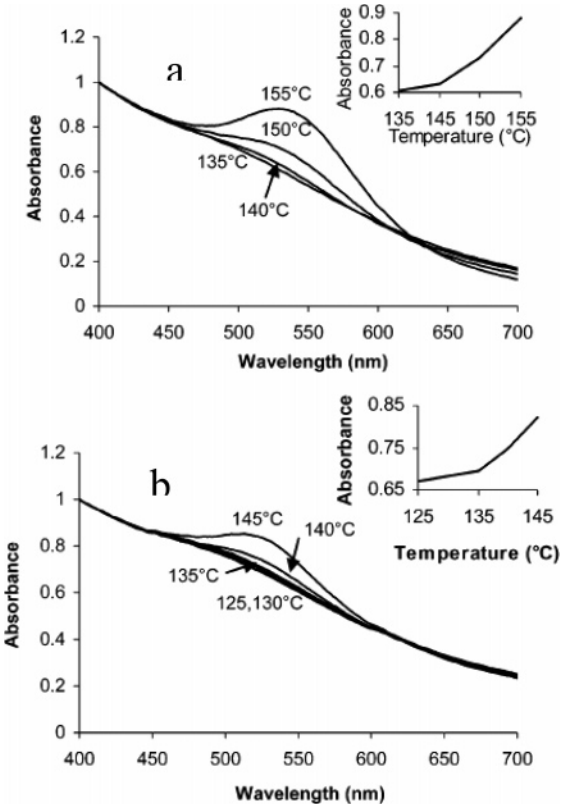

Figure 65. Normalized UV−vis spectra of polyamine cross-linked **7** (a) and parent acrylate-protected Au nanoparticles **3** (b) at different temperatures. The insets show the intensity of the plasmon peak (530 nm) as a function of temperature. Reprinted with permission from ref 310. Copyright 2006 American Chemical Society.

cores. The second implicates the reshaping or resizing that minimizes the chemical potentials followed by competitive re-encapsulation of thiolate shells under the annealing conditions. These ripening properties of gold nanoparticles are often used to manipulate the size and shape of gold nanoparticles. Due to the growth of the particles during thermal treatment, the ripening process is accompanied by color change from dark brown to dark red or purple.[340,525] The temperature at which the color of the solution changed was ascertained using UV−vis spectroscopy. The results are shown in Figure 64. The UV spectra of all samples were nearly constant at low temperatures. However, after a certain threshold, the UV spectra showed substantial changes, consistent with the particle aggregation. The nanoparticle color also visibly changed to red at this temperature. The data in Figure 65 show that polyamine cross-linked nanoparticles undergo changes at temperatures ca. 10 °C higher than the parent non-cross-linked nanoparticles. In this case, the ligand chains have weaker intermolecular interactions, and less energy is required to desorb the ligands from the gold surface. Thus, the temperature of the reaction medium influences the aggregation and thereby the surface plasmon resonance of the colloidal system.

9.3. Survey of Optical Response

The differing features of the resulting optical absorption spectra could be summarized as follows. Theoretical calculation and experimental observation reveal that effect of particle size within the aggregate, interparticle distance, and physical parameters, such as solvent, temperature, and the light polarization direction, has a profound influence on the extinction spectra. The aggregation theories include explicitly the direct electromagnetic multipole coupling among the particles, which causes the single particle plasma peak to split up into several peaks, the splitting energy depending on symmetry and size of the aggregates and particle distances. It is red-shifted and broadened when filling factor is increased. The splitting of the SPR into red and blue components is associated with multipolar electromagnetic interactions arising due to closely spaced nanoparticles in the system.

10. Ultrafast Relaxation of Gold Nanoparticle Aggregates

The ultrafast dynamics of collective oscillation of electrons, known as surface plasmons, give rise to strong interaction with photons. It is of fundamental importance to know how the electron−electron and electron−phonon scattering processes after photoexcitation depend upon size and shape of nanoparticles and how they proceed inside the particle.[526−528] Interaction between metal nanoparticles is a fundamentally intriguing issue. It is critical to understanding the mechanism of self-assembly and formation of superlattices. While it is expected to observe similar electronic (electron−phonon coupling) relaxation times in aggregates as in isolated nanoparticles, coherent vibrational oscillations are not expected. If it is assumed that the aggregates have a broad distribution of sizes and structures that all contribute toward the extended plasmon band (EPB) with similar absorption bandwidth, then no oscillations should be observed, since the differently sized or structured aggregates have different oscillation periods and any oscillations should be averaged out. The electronic relaxation of isolated colloidal gold nanoparticles has been extensively studied and found to be on the time scale of 1−2 ps, similar to that of bulk gold.[527−529] An interesting oscillatory behavior has been observed by both Hartland et al. and Vallee et al. in monitoring the electronic relaxation on longer time scales. These oscillations have been attributed to the excitation of the breathing vibrational modes of the nanoparticles because of energy transfer from the hot electrons into the lattice via electron−phonon coupling.[530−534] The vibrational frequency has been found to be inversely proportional to the radius of the nanoparticles, and the frequency can be calculated quite accurately on the basis of classical mechanics.[535] Similar observations have been recently made on gold nanorods and silver ellipsoids.[536,537]

Several groups[526,531,532] have reported the observation of the ultrafast electronic relaxation and coherent vibrational oscillation of strongly interacting gold nanoparticle aggregates measured by femtosecond laser spectroscopy. Contrary to the previous expectations, it has been observed that there are coherent vibrational oscillations in the transient absorption/bleach measurement of strongly interacting gold nanoparticle aggregates. The oscillation period has been found to be longer at the redder probe wavelengths (55 ps at 850 nm) than at bluer probe wavelengths (37 ps at 720 nm).[526] This suggests that the steady-state electronic absorption of the broad EPB contains contributions from aggregates of different sizes or fractal structures. Previous experimental and theoretical studies on small gold aggregates are consistent with this conclusion.[538−540] The electronic relaxation (1.5 ps) due to electron−phonon coupling is similar to that of isolated, strongly coupled gold nanoparticles[541] as well as bulk gold, as expected. Figure 66 shows the electronic absorption

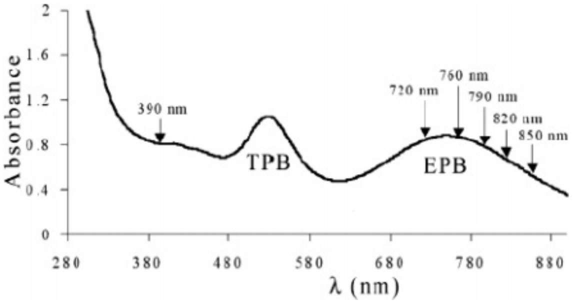

Figure 66. UV−visible absorption spectrum of strongly interacting gold nanoparticle aggregates. The excitation (390 nm) and probe wavelengths used in the dynamics studies are indicated by arrows. Reprinted with permission from ref 526. Copyright 2003 American Chemical Society.

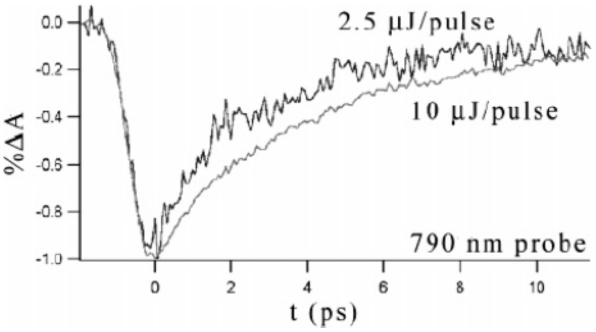

Figure 67. Ultrafast electronic relaxation dynamics of gold nanoparticle aggregates at two very different excitation intensities to illustrate the power dependence of the fast component of the decay. Reprinted with permission from ref 526. Copyright 2003 American Chemical Society.

spectrum of one representative aggregate sample. The peak at ∼540 nm corresponds to the transverse plasmon band (TPB) from individual gold nanoparticles, while the broad near-IR absorption band is assigned to the EPB due solely to nanoparticle aggregates that arises from strong particle−particle interaction.[541] Figure 67 shows the electronic relaxation (transient bleach) of the aggregates probed at 790 nm following excitation at 390 nm for two different excitation intensities (10 and 2.5 μJ/pulse). At high power, the fast component of the relaxation is slower than that at low power, with time constants of ∼2.5 and ∼1.5 ps for high and low power, respectively. On the short time scale (a few picoseconds), the relaxation is dominated by electron−phonon coupling. Energy transfer from the hot electrons to the lattice is dependent upon excitation intensity. This can be accounted for by the two-temperature model.[532,542,543] Higher pump powers produce higher electronic temperatures, which yield longer relaxation times because of the temperature dependence of the electronic heat capacity. Faster relaxation at lower power is consistent with previous observations in isolated gold nanoparticles.[201,530,532] The relaxation is also similar to strongly coupled gold nanoparticle films.[541]

Figure 68 shows the probe wavelength-dependent transient absorption/bleach profiles of gold nanoparticle aggregates. The most striking feature is the periodic oscillations. Since the EPB is due solely to strongly coupled gold nanoparticle aggregates, the oscillations observed must be due to the aggregates, not isolated nanoparticles. Similar measurements on isolated gold nanoparticles alone in the same probe wavelength region show no oscillations. The oscillations are attributed to the coherent vibrations of the aggregates that are excited following the initial hot electron relaxation. The observation of such periodic oscillations in these nanoparticle aggregates is somewhat surprising. If all of the differently sized and/or different structured aggregates contribute to the EPB with the same absorption bandwidth, then each aggregate will vibrate with its own frequency upon excitation. The observed signal would be a sum of all the oscillations with different frequencies or periods that would “wash out” any overall observable oscillation. This is apparently not the case. The oscillations observed suggest that the broad EPB is composed of absorption sub-bands from gold nanoparticle aggregates with different sizes and/or different fractal structures. In other words, the EPB is inhomogeneously broadened by the different aggregate sizes and/or structures. For a given probe wavelength, only a subset of the aggregates with similar size or structure are probed. To use the size analogy, smaller aggregates will likely have an absorption in the bluer part of EPB, while the larger aggregate will absorb in the redder part of the EPB. This conjecture is strongly supported by the probe wavelength dependence of the oscillation period. Thus, it can be concluded that this near-IR absorption is composed of sub-bands from differently sized and/or structured aggregates. This transient absorption technique provides a useful tool for probing the low-frequency vibrational modes of metal nanoparticle aggregates.

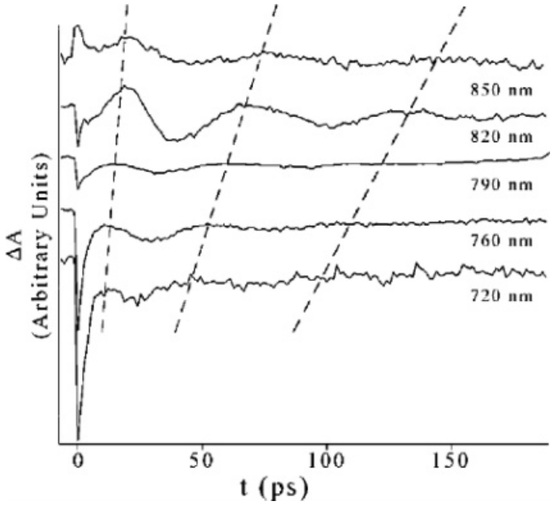

Figure 68. Ultrafast electronic relaxation dynamics of gold nanoparticle aggregates at varying probe wavelengths (shown at right) with excitation at 390 nm at 8 μJ/pulse. Trend lines (dashed) demonstrate an increase in oscillation period and shift of the first peak toward a longer time as probe wavelength is shifted to redder wavelengths. Reprinted with permission from ref 526. Copyright 2003 American Chemical Society.

11. Influence of Intense Pulsed Laser Irradiation on Gold Nanoparticle Aggregates

At the present scenario of the nanoscale research, we are well-aware of the fact that gold nanoparticles show significant photoactivity and undergo morphological changes under laser irradiation.[544−557] Intense pulsed lasers with various pulse widths, energies, and wavelengths have been used to prepare gold nanostructures (sphere, wire and network)[544−553] and to reshape gold nanorods into nanospheres.[554−557] When the plasmon band of well-dispersed gold nanoparticles is excited by an intense pulsed laser, the photon energy absorbed by electrons of the conduction band transfers into the lattice of the nanoparticles as heat (electron−phonon

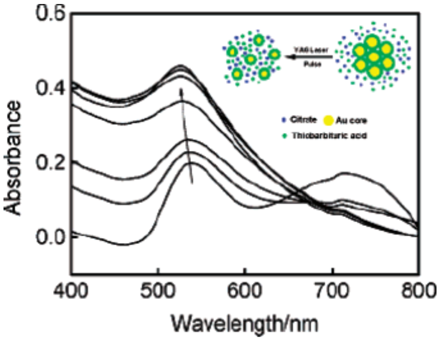

Figure 69. ptical absorption spectra of gold nanoparticle aggregates at different laser irradiation times (from bottom to top: 0, 1, 3, 5, 10, 20, and 30 min). Reprinted with permission from ref 436. Copyright 2005 American Chemical Society.

relaxation) in a few picoseconds.[554,558,559] During a single laser pulse, one parent gold nanoparticle is considered to absorb consecutively more than a thousand photons, and its temperature reaches its boiling point.[554−557] The hot gold nanoparticle releases photofragments and part of the stabilizer molecules which cover the parent nanoparticles. After the laser pulse the heat diffuses into the solution and the temperature of the heated nanoparticle and the photofragments returns to room temperature before the next laser pulse heats the ensemble again. The precise time scale for heat dissipation to the embedding medium depends on the host's heat capacity and thermal conductivity, but in general it is on the order of hundreds of picoseconds.[557] Beside heating, multiple ionization followed by Coulombic explosion similar to an electrospray process may also contribute to fragmentation.[560−562] These information engenders our interest to examine the influence of intense pulsed laser irradiation on gold nanoparticle aggregates.

Studies have been conducted to understand the interaction between an intense pulsed laser and aggregated nanoparticles where the interparticle electronic coupling becomes dominant.[436] The aggregation between the gold nanoparticles in an aqueous medium was induced by the modification of gold nanoparticles with pH-sensitive and ionizable thiols, thiobarbituric acid. Figure 69, bottom curve, shows the optical absorption spectrum of the solution a day after it was prepared by adjusting the pH value of the colloidal solution to 6.5. The other spectra were obtained at different laser irradiation times by using 130 mJ/pulse cm^2 laser energy flux and 532 nm excitation wavelength. There are two notable features in Figure 69. One is the disappearance of the absorbance band near 710 nm corresponding to the coupled resonance absorbance when the irradiation time exceeds 5 min. The intensity of this band is already reduced after a few laser pulses. This observation suggests that the electronic coupling between the nanoparticles becomes very weak after laser irradiation because the mean distance between the particles became too large. The second one is the increase in intensity of the absorbance around 530 nm together with a gradual blue shift of the absorbance maximum from 534 to 524 nm after 5 min of irradiation. The blue shift of the absorbance maximum indicated by an arrow in Figure 69 can be attributed to the decrease of particle size and the change in the complexation of the gold nanoparticles,[563] as they become progressively smaller during fragmentation, which is supported by the results of TEM investigations (Figure 70). It is intriguing why the smaller particles obtained from laser irradiation of the nanoparticle aggregates do not form aggregates again, since the pH value of the solution is the same before and after irradiation. The excess TBA molecules present in the solution stabilize the newly formed fragments and prohibit the fragments from forming large aggregates by steric stabilization, which is more effective for small particles.[564]

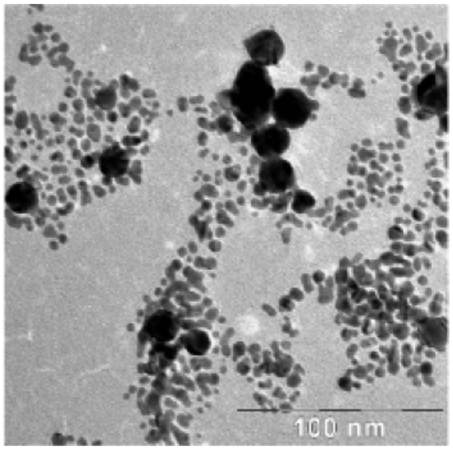

Figure 70. TEM images and size distribution (4.9 ± 2.7 nm) of nanoparticles produced after 532nm pulsed laser irradiation for 30 min. Reprinted with permission from ref 436. Copyright 2005 American Chemical Society.

Concerning the mechanism of the interaction between the intense pulsed laser and gold nanoparticles, Kondow et al.[552] reported that formation of photofragment aggregates depends on the concentration of the stabilizer (sodium dodecyl sulfate, SDS). In dilute SDS solution, parent gold nanoparticles and photofragments are not well stabilized by SDS molecules. As long as they are melted by a laser beam, they grow into network structures by encounter and coagulation. At high concentration of SDS, no aggregate structure but smaller spherical nanoparticles have been observed. So, the aggregation of a gold nanoparticle after each laser pulse is determined by the coverage of the photoproducts by ligand molecules and by the probability of encounters of heated gold nanoparticles or photofragments. In this experiment, the ligand molecules are TBA with a -SH moiety, which has strong affinity to the gold surface, and their number in the solution is large enough to cap all of the photofragments. So, in the presence of TBA, the mechanism of the interaction between gold nanoparticle aggregates and the laser beam can be expressed as (i) the nanoparticles excited by the laser dissociate into photofragments and (ii) subsequently the resulting photofragments are quickly surface capped by TBA molecules. It is the decreased size of the nanoparticles combined with a steric stabilizer of small size present on the particle surface that results in the stability of the products of the laser irradiation.[565]

12. Applications of Interparticle Coupling Effect

Optical properties of noble metal particles have been widely investigated because of fundamental importance in science and industry. Metal nanoparticles have been the subject of extensive research for many years because of their anomalous electromagnetic properties originating from the resonant interaction between light and collective conduction electron oscillations, so-called surface plasmons.[1,21,74,75] When the dimensions of nanoparticles become smaller than the wavelength of the exciting light, energy can be confined in small spatial regions through the local excitation of surface plasmon resonances. The optical properties of metal nanoparticles are strongly influenced by their size, shape, and surrounding environment, such as, the proximity to other particles. These properties, in particular, local electric field enhancements, enable applications, such as single molecule detection using surface-enhanced Raman scattering,[87−99,503,566−571] near-field microscopy,[572,573] nanoscale optical devices[105,574] and a variety of nonlinear scattering measurements[575] (hyperRayleigh,[576−578] hyperRaman,[579] and SHG[580,581]) and time-resolved measurements.[582,583] In addition, resonant energy transfer between closely spaced metal nanoparticles enables transport of electromagnetic energy at length scales below the diffraction limit.[584] Not only the local field enhancement but also the SP mode behaviors in near-field arouse fundamental interests and various applications. Wavelength-dependent characteristics of SP modes on metal nanoparticles are essential for utilizing them as novel optical and electronic materials, and also for constructing molecular systems for nanophotonic applications as well. Utilization of the unique optical properties resulting from the excitation of plasmon resonances in nanosize metallic particles can lead to significant advances in the areas of photocatalysis, information processing, and sensor development. Plasmon resonances, which are collective oscillations of conduction electrons, generate an electromagnetic field, which has absorbing, scattering, and near-field components.[585] This component determines the intensity of local EM field that is enhanced as compared with the incident radiation leading to enhancement of several optical phenomena, such as Raman scattering,[586] fluorescence,[587,588] absorption,[589] photoinduced electron transfer,[590] second and third harmonic generation,[580,581] and four-wave mixing,[591] for molecules in close proximity to the particle surface.

12.1. Spectroscopic Applications

12.1.1. Absorption

The ability to assemble nanoparticles of controllable sizes and shapes is increasingly important because many frontier areas of research, such as sensors, catalysis, medical diagnostics, information storage, and quantum computation, require the precise control of nanomaterial architecture and component miniaturization. In nanotechnology, the assembly of metal nanoparticles has resulted in novel materials with interesting properties.[592−594] The extremely high extinction coefficients and the strongly distance-dependent optical properties of gold nanoparticles allow the nanoparticles to be utilized as ideal color reporting groups. For example, the extinction coefficients of 13 and 50 nm gold particles are 2.7×10^8 and 1.5×10^{10} M^{-1} cm^{-1} (at ∼520 nm), respectively,[595] which are 3−5 orders of magnitude more than those of traditional organic compounds. As a result, nanoparticles at nanomolar concentration can be clearly observed by naked eye, allowing sensitive detection with minimal consumption of materials. When gold nanoparticles approach each other and aggregate, the color of the nanoparticles changes from red to blue because of the shift of the surface plasmon band to longer wavelengths. Thus, absorption studies produce quite a lot of information.

12.1.2. Fluorescence

The manipulation of the surface of a particle to alter its physical properties, either through chemical modification of the surface functionalities or by surface adsorption of molecules, has emerged as a powerful strategy in colloid science. It has been seen that the emission properties of the fluorescent molecules under the influence of an enhanced field are changed dramatically. Fluorescing molecules have often been used as local probes to measure the surface plasmon fields. In the vicinity of a metal, the fluorescent rate of molecules becomes a function of the distance between the molecule and the metal surface.[596] In the presence of an electromagnetic field of aggregated metal clusters, the radiative decay rates and quantum yields of weakly fluorescent species can increase significantly. The fluorescence of molecules in direct contact with the metal is completely quenched. Thus, methods can be formulated for the characterization of locally enhanced fields at laser-irradiated metal nanostructures. Even, multiphoton absorptions and fluorescence excitations have been shown to be possible.[597,598] Recently, several authors have investigated the spectroscopic behavior of the resonant coupled systems as a function of particle separation and polarization direction[358,514−516] and predicted molecular trapping by the forces associated with the strong field enhancement.[517] Direct experimental measurements of electromagnetic fields localized between closely spaced nanostructures are needed to validate theoretical predictions and to develop systems with improved fluorescence properties.

12.1.3. Surface-Enhanced Raman Scattering (SERS)

The recent discovery of single-molecule sensitivity of Raman scattering enhanced by resonantly excited metal nanoparticles has brought a renewed interest in surface-enhanced Raman scattering and its application to molecular detection.[100,502,503] Noble metal nanoparticles, usually of Ag and Au, are well-known for their strong interactions with visible light through the resonant excitations of the collective oscillations of the conduction electrons within the particles. Since its discovery in 1974, the mechanism for SERS has been a matter of considerable debate.[487,599−607] It has been widely accepted that there are two mechanisms for the observed, and at times huge, enhancement in SERS: electromagnetic (EM) and chemical enhancement (CE) mechanisms. The EM mechanism is based on the interaction of the electric field of the surface plasmons with the transition moment of the adsorbed molecule, whereas the CE is based on the idea that mixing of molecular and metal states occur. Although the two are not mutually exclusive, the use of roughened geometries such as island films,[608−617] roughened electrodes,[601,618] encapsulated particles,[619−622] and particularly aggregated nanoparticle clusters[523,526,623−637] have tended to substantiate that the EM mechanism plays a pivotal role[638] to which the chemical effect may provide an additional enhancement. The chemical mechanism may arise from mixing of metal orbitals with orbitals on a molecule, providing charge transfer that states a resonant Raman mechanism at much lower energies than those available in the free molecule. Both mechanisms and even others may contribute simultaneously to the SERS enhancement to a certain extent, which is dependent on the experimental conditions, the nature and morphology of the metallic nanoparticles, the nature of the particular sample, etc.

The EM mechanism is based on the hypothesis that the superposition of incident and scattered fields interacts with the transition moment of a molecule near the surface.[487,605] Surface selection rules determine that the polarization is required for the enhancement. Local field effect near the surface of a conducting sphere provides a means for amplification of EM fields near the surface. The resonance Raman scattering cross section, σ_R, can be expressed as[639]

$$\sigma_R = \frac{8\pi\omega_s^{3}\omega_0 M_{if}^{4}}{9\hbar^2 c^4}\left(\int_0^\infty \langle f|i(t)\rangle \exp\{i(\omega_i + \omega_0)t - \Gamma t\}\, dt\right)^2 \tag{76}$$

where M_{if} is the transition moment of the molecule, ω_0 the frequency of the incident radiation, ω_s the frequency of the scattered radiation, ω_i the vibrational frequency in the ground state, and Γ the damping constant. The absorption cross section, σ_A is related to the resonance Raman cross section as[639]

$$\sigma_A = \frac{2\pi\omega_0 M_{if}^{2}}{3\hbar c}\left(\int_{-\infty}^\infty \langle i|i(t)\rangle \exp\{i(\omega_i + \omega_0)t - \Gamma t\}\, dt\right) \tag{77}$$

although the absorption line shape and Raman excitation profile differ because of the difference in their correlation functions of the prefactors dependent on M_{if}^2 and M_{if}^4, respectively. Despite this well-known difference in the dependence on the transition moment, the probability of both processes, absorption and resonant Raman, depends linearly on the intensity of the incident radiation and, in turn, on the square of the incident radiation field. The intensity can be expressed as $I = {}^1/_2\epsilon_0 c E_0^2$, where E_0 is the electric field amplitude of incident radiation. For a spherical metallic nanoparticle, the tangential and radial field can be expressed as[603]

$$E_t^{\,2} \propto 2E_0^{\,2}[1 - g]^2 \tag{78}$$

$$E_r^{\,2} \propto 2E_0^{\,2}[1 + g]^2 \tag{79}$$

$$g = (\epsilon - \epsilon_0)/(\epsilon + 2\epsilon_0) \tag{80}$$

where g is a factor related to the hyperpolarizability of the metal sphere with a dielectric function ϵ in a medium with dielectric constant ϵ_0. Near the surface plasmon resonance maximum, ϵ approaches $-2\epsilon_0$ and g becomes very large providing a resonance condition.[640] Particle dimension and geometry play a large role in determining the enhancement factor in plasmon resonance spectroscopy. This has mainly to do with the coupling of electromagnetic radiation into the electronic structure of metal. A spherical monomer can be viewed as the smallest entity capable of enhancement.[607] Aggregates of metal particles offer a strong influence on SERS because rough or fractal surfaces can give rise to a stronger coupling of the electric field. As a result, local electromagnetic fields near the particle can be many orders of magnitude higher than the incident fields, and the incident light around the resonant-peak wavelength is scattered very strongly. This local-field enhancement and strong scattering have been proven to be very unique for biomolecular manipulation, labeling, and detection.[641,642]

It is important to mention two recently developed theoretical approaches for SERS that are capable of describing SERS effect involving nanoparticles in a more quantitative fashion. Johansson et al.[643] have presented a general model study of surface-enhanced resonant Raman scattering focusing on the interplay between electromagnetic effects and the molecular dynamics as treated by a density matrix calculation.[644] The model molecule has two electronic levels, which are affected by both radiative and nonradiative damping mechanisms, and a Franck−Condon mechanism yields electron−vibration coupling. The coupling between the molecule and the electromagnetic field is enhanced by placing the molecule between two silver nanoparticles. The results show that the Raman scattering cross section can, for realistic parameter values, increase by some 10 orders of magnitude (to ∼10−14 cm^2) compared with that of the free space.

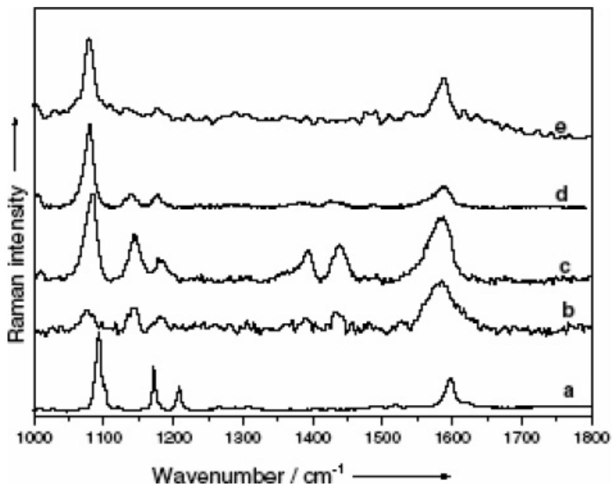

Figure 71. The normal Raman spectrum of solid *p*-ATP recorded with 633 nm laser line (a) and the SERS spectra of *p*-ATP adsorbed on self-assembled gold colloidal nanoparticles recorded with different laser lines: (b) 532 nm, (c) 633 nm, (d) 830 nm, and (e) 1064 nm. Reprinted with permission from ref 654. Copyright 2006 Elsevier.

In typical SERS experiments, a collection of colloidal particles of various sizes are induced to aggregate, and those aggregates that happen to be resonantly excited by the illuminating laser are called “hot spots”. It is seen that when a cluster of metal nanoparticles are placed in close proximity to one another, the coupling between particles becomes very important.[503,645−647] It has been seen that SERS enhancement is small or absent for monomer colloids, that is, well-isolated nanoparticles, and is only observed when salt is added to induce aggregation.[648−653] Therefore, from a practical point of view, it is very important to be able to fabricate optimally designed plasmon configurations of interacting nanoparticles. The experiments performed on these substrates mostly tried to provide key information to validate the EM mechanism of SERS and to find the optimal conditions for the single molecule detection. Gold colloids can be prepared by standard chemical procedures and subsequently self-assembled to exhibit strong electromagnetic coupling between individual nanoparticles and can support a large variety of surface plasmon modes. They were always reported as an ideal substrate for SERS studies, owing to their uniformity and controllability.[650−653] Figure 71 shows the SERS spectra of the *para*-aminothiophenol (*p*-ATP) molecule adsorbed on the gold nanoparticles recorded by using the 532, 633, 830, and 1064 nm laser lines.[654] The interest is focused on correlating the morphology and electronic absorption spectra with the different enhancement patterns observed in the SERS spectra. The absorption spectrum of the test molecule is closely related to that of the parent benzene molecule and presents two bands around 256 and 297 nm. The plasmon resonance absorption shows two bands centered at ∼520 nm and a broad, asymmetric peak centered at ∼615 nm. While the first one located at shorter wavelength is due to the localized plasmon resonance absorption of the individual gold nanoparticles, the second one is due to the aggregation among the individual nanoparticles. The second peak is broad because its position is dependent on both the number of coupled nanoparticles and their relative position with respect to each other and to the incident light. The adsorption of the test molecules on the SERS substrate caused a shift to longer wavelengths and a broadening of the absorption band of the pure substrate (spectrum not shown). Due to high affinity of *p*-ATP for gold, it is expected that *p*-ATP molecules are bound not only on the open surface of nanoparticles but also on sites located in gaps and junctions created between neighboring nanoparticles. As a result of the change induced by the molecular layer in the environment dielectric constant, the molecules inside of interstitial regions play more effectively on the interparticle coupling and the appearance of the absorption spectrum.

From Figure 71, one can see that the SERS spectra are dominated by the bands around 1083 and 1587 cm^{-1} attributed to C−S and C−C stretching vibrations, respectively (a_1 vibrational modes). In the SERS spectra recorded with visible excitations can be also observed the apparent enhancement of the bands around 1439, 1394, and 1143 cm^{-1} (b_2 vibrational modes). The apparent enhancement of the b_2 modes, which are closely related to the thiol group vibrations, has been ascribed to the charge transfer (CT) from the metal to the adsorbed molecules. Thus, the spectral characteristics of the SERS spectra, that is, shifts to lower wavenumbers in comparison with the corresponding Raman bands and changes in relative intensities, demonstrate that the *p*-ATP molecules are adsorbed onto the gold nanoparticles through their sulfur atoms and are standing-up relative to the substrate surface.

The SERS spectrum recorded with the 532 nm line is similar to that obtained with 633 nm excitation relative to the conventional Raman spectrum, excepting the slight enhancement of most of the bands. Two factors could be considered responsible for this behavior. It is known that for a perfectly spherical particle in the Rayleigh limit, only the dipole surface plasmon resonance contributes to the enhancement process. However, for isolated gold nanospheres, the plasmon excitation at 532 nm competes with interband transitions, leading to a low electromagnetic enhancement factor in SERS.[46] Higher factors are obviously expected for nanoparticle clusters due to a red shift of the resonance away from the interband transition edge. This decreasing of electromagnetic effect corroborated with low density of individual nanoparticles is indeed confirmed by the weak intensity of the EM band at 1077 cm^{-1} relative to that of the CT band at 1435 cm^{-1}, in comparison to its behavior at other excitation laser lines. Thus, these results clearly indicate that the as-prepared self-assembled gold nanoparticles turn out to be not only a model for gaining further understanding of SERS mechanisms but a promising substrate for other SERS-based measurements in near-infrared. The possibility of getting good SERS spectra with near-infrared excitations opens up promising perspectives for the investigations of biological samples.

The importance of nanoparticle dimers in the context of surface-enhanced Raman spectroscopy was recognized long ago.[107] Since then, a large number of theoretical and experimental studies of the nanoparticle dimer system have been performed.[358,503,655,656] Although nanoparticle dimers clearly are not the optimal substrate structure for SERS, they serve as a simple prototypical model system for the study of the important physical factors underlying the electromagnetic field enhancements. Talley et al.[657] have explicitly demonstrated that nanoparticle dimers are more efficient as SERS substrates than the individual nanoparticles. The strong field enhancements in the dimer junction result from the opposite alignment of the individual nanoparticle plasmons and from the mixing of individual nanoparticle plasmons of higher angular momentum into the dimer plasmons. Thus, the two major factors for the strong field enhancement are the interaction of localized plasmons and the interference of the electromagnetic fields generated by these plasmons.

Fromm et al.[658] have produced isolated Au bowtie antennas with 75 nm triangle lengths on transparent substrates using electron-beam lithography. It has been observed that bowties excited with polarization along their long axes have plasmon resonances that strongly blue-shift with increasing gap size until the center-to-center particle spacing is ∼2 times the length of an individual triangle, at which time the spectra red-shift with increasing gap size. This coupling effect remains noticeable even when particles are spaced by 7 times the particle length, and FDTD simulations agree quite well with experimental observations, suggesting their utility in predicting the behavior of other coupled nanoparticle systems.[659] Bowties, pumped perpendicular to their long axes, show a gradual decrease in their total scattering intensity and may exhibit a modest red shift in their plasmon resonance with increasing gap spacing. In the microwave regime, it has been shown that a “bowtie” shaped antenna, where two metallic triangles facing tip-to-tip are separated by a small gap, produces a large electric field confined to the area near the gap.[660] Small gaps between two nanometer-scale particles have also been implicated in producing electromagnetically enhanced “hot spots”, enabling the detection of surface-enhanced Raman scattering out of a single molecule.[661]

12.1.4. Photoinduced Electron Transfer (PET)

Noble metals in the bulk are photoactive only to a small extent.[662−664] The nanoparticles of noble metals, on the other hand, exhibit increased photochemical activity because of their high surface/volume ratio and unusual electronic properties. The size- and shape-dependent optical and electronic properties of metal nanoparticles make an interesting case for photochemists and photobiologists to exploit their role in light-induced chemical reactions. It is now realized that the appeal of fluorescence is because it is a highly sensitive method of detection. Unlike many phenomena in chemistry, molecular fluorescence can be easily eliminated or enhanced by chemical command giving rise to the ON−OFF state. Operation of many fluorescent sensors is based on the photoinduced electron transfer (PET) mechanism and employs the fluorophore−receptor design.[665,666] The fluorophore is the site of all photochemical transitions. The receptor is a site tailored specifically for the metal of interest and is responsible for complexation. If PET is to control the sensory action, the molecule employed does not fluoresce in the absence of the metal due to an efficient PET process by an electron-donating group in the molecule. When this electron donation is hindered due to interaction of the group with the guest molecule, PET is quenched and fluorescence is turned on (Figure 72). Herein, lies the power of the PET mechanism; given the appropriate conditions, almost any receptor synthetically available for a given metal can be employed as a sensor.

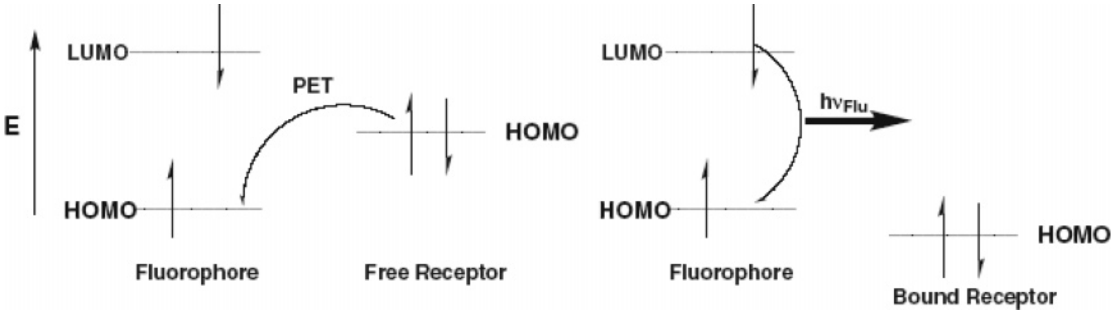

Figure 72. Frontier molecular orbital diagram illustrating the PET phenomenon.

Basic understanding of the optical properties of metal colloids, morphological changes under light irradiation, and excited-state interaction with photoactive molecules are also important for developing nanoassemblies for light-energy-harvesting and optoelectronic applications. Binding a photoactive molecule (e.g., aminopyrene) to a metal nanoparticle enhances the photochemical activity and renders such organic−inorganic hybrid nanoassemblies. The nature of charge-transfer interaction of the fluorophore with the gold surface dictates the pathways with which the excited state deactivates. Surface charge neutralization, which accompanies the binding of a thio or amine group to gold nanoparticles, induces aggregation and shifts the plasmon absorption to the infrared.[361,667−669] This demonstrates the feasibility of achieving desired interparticle distance by controlling the nature as well as size of the alkyl/aryl groups in the capping agent. For example, the purple-colored gold colloidal solution turns blue with addition of small amounts of thionicotinamide (TNA). Upon laser pulse (532 nm) irradiation of a TNA-capped gold nanoparticle suspension for a few minutes, the ruby-red color is restored as the aggregates fuse to form larger segregated spherical particles.

Vectorial electron transfer (ET) is a central feature of many biological transformations such as the photosynthetic apparatus or the biocatalytic oxygen assimilation. A different approach to accomplish photoinduced vectorial ET involves the organization of layered Au nanoparticle arrays cross-linked by the oligocationic bis-bipyridinium-Zn(II)-protoporphyrin IX, acting as a photosensitizer−electron-acceptor dyad. Photoinduced ET assembly leads to the transport of electrons through the conductive Au nanoparticle array and to the generation of a photocurrent. A further approach to stimulate photoactivated vectorial ET involves the use of a photoisomerizable monolayer associated with an electrode as a command interface for the photochemical activation and deactivation of the electrical contact between cytochrome *c* (cyt *c*) and the electrode. A photoisomerizable monolayer consisting of pyridine and nitrospiropyran units is used to control the electrical contact between cyt *c* and the electrode. The electrically contacted cyt *c* activates the biocatalyzed reduction of O_2 by cytochrome oxidase (CO_x). The integrated system, consisting of the photoisomerizable monolayer-functionalized electrode and the cyt $c/CO_x/O_2$ components, provides a system for the amplified electrical transduction of photonic signals recorded by the monolayer interface. This system, thus, duplicates functions of the vision process.

12.2. Nonlinear Optics (NLO)

Nonlinear optical phenomena form the basis for all optical devices like optically bistable switches and nonlinear directional couplers. The suitability of a material for these device applications requires a large magnitude of the third-order nonlinear optical susceptibility, $\chi^{(3)}$. Thus, finding nonlinear optical phenomena with large $\chi^{(3)}$ is up to now a challenge.[670−674] Graded materials are those whose properties vary gradually as a function of position. This gradation may occur naturally or may be a product of manufacturing processes. It has been reported[671,672,675,676] that graded (inhomogeneous) materials can show stronger nonlinear optical responses than the corresponding homogeneous ones. Colloidal-based optical sensors[677] and photonic band gap materials based on opaline structures[678] have been made possible by a class of colloidal-crystal-based nonlinear optical materials, which are made of metallodielectric nanoparticles (namely, a metallodielectric core plus a dielectric shell) suspended in a host fluid. If there is nonlinearity of the host metal or in molecules adsorbed on the surface, the existence of these zones of high-intensity EM fields leads to enhancement of local and average nonlinear optical responses, as was predicted theoretically[679−684] and observed experimentally.[685−690]

12.2.1. Second and Third Harmonic Generation (SHG and THG)

Second and third harmonic generation are processes whereby two or three photons at the fundamental frequency ω are converted into one photon at the harmonic frequency $\Omega = 2\omega$ or $\Omega = 3\omega$, respectively. The technique has been extensively used so far to investigate the surfaces and interfaces since it is inherently surface sensitive. Indeed, nonlinear optical processes of even order are vanishing in media with inversion symmetry in the electric dipole approximation.[691,692] As a result, all kind of interfaces have been investigated, for instance, solid−vacuum, solid−liquid, air−liquid, or liquid−liquid interfaces.[693−695] For geometrical arrangement reasons, planar interfaces have almost extensively investigated, whereas spherical interfaces have received considerably less attention.[696]

In the case of nanoparticles with a diameter much smaller than the wavelength of light, the origin of the second harmonic signal is, therefore, of electric quadrupole origin and is thus expected to be rather weak.[697] However, it is possible to enhance this nonlinear optical response through local field resonances corresponding to the surface plasmon excitations of the particles.[698] Thus, it has attracted wide interest to measure the absolute magnitude of the quadratic hyperpolarizability of gold nanoparticles and to evaluate the local field effects through shape modification of these nanoparticles by aggregation. This aggregation process has been induced by addition of analyte to the solution and led to large ensembles of nonlinear processes. Since in a solution of nanoparticles, no phase relationship exists between the particles, no coherent signal can be collected and the

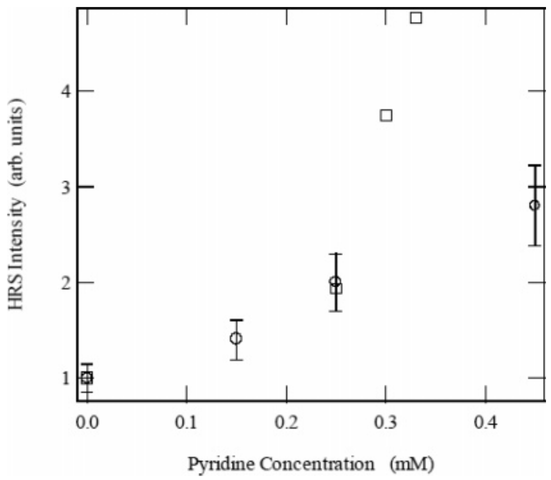

Figure 73. RS intensity normalized to the signal obtained in absence of pyridine as a function of the pyridine concentration (○) and HRS intensity calculated with the effect of the local fields only (□). Reprinted with permission from ref 415. Copyright 2001 The Japan Society for Analytical Chemistry.

incoherent harmonic signal, known as the hyper-Rayleigh signal, scattered by the solution in all direction has been detected from a monodisperse solution of nanoparticles.

It is known that pyridine induces the aggregation of the gold nanoparticles in solution by displacement of the charged species left from the reduction reaction or introduced for stabilization.[699] The aggregation between the particles can be used to study the local field effects in the formed linear chains since the geometry of the particles has a dramatic effect on the local field enhancement.[700] In order to investigate the local field effects on the nonlinear process, the HRS signal was recorded as a function of pyridine concentration (Figure 73). The HRS intensity was increased by a factor of nearly three with the pyridine concentration, and at 0.45 mM of pyridine, the HRS signal reached a saturation regime. It is possible to calculate the contribution of the local field to the HRS intensity. The field enhancement factors at the fundamental or harmonic frequencies are given by[701,702]

$$f(\omega) = \frac{4\pi}{V}\sum w_i \frac{\mathrm{Im}(\alpha li(\omega) + \alpha ti(\omega))}{\mathrm{Im}(\epsilon(\omega))} \qquad (81)$$

$$f(2\omega) = \frac{4\pi}{V}\sum w_i \frac{\mathrm{Im}(\alpha li(2\omega) + \alpha ti(2\omega))}{\mathrm{Im}(\epsilon(2\omega))} \qquad (82)$$

where w_i is the weight of the distribution.

The ratio η can, then, be evaluated as

$$\eta = \left|\frac{f_{\mathrm{agg}}(\omega)^2 f_{\mathrm{agg}}(2\omega)}{f_{\mathrm{sph}}(\omega)^2 f_{\mathrm{sph}}(2\omega)}\right|^2 \qquad (83)$$

and is reported in Figure 73. Experimentally, this ratio is just the HRS intensity normalized to the intensity detected in the absence of any aggregation. It is observed that the HRS intensity during the initial stages of the aggregation process is well described in this model. The fourth power of the field enhancement factor at the fundamental frequency is the dominant contribution to the overall increase as a result of the new plasmon resonance arising at longer wavelengths. The field factor at the harmonic frequency decreases following the absorption cross section at this frequency. Since it only appeared squared in the overall HRS enhancement factor, its effect is not the dominant one. For these small particles and as long as the aggregates are smaller than the wavelength of light, the electric field approximation is still a valid approximation.

12.2.2. Four-Wave Mixing (FWM)

The optical properties of rough nanometer-structured metallic surfaces with fractal geometry recently attracted much attention.[703−708] The strong enhancement of local electromagnetic fields near the rough nanometer-structured metallic surfaces in a wide spectral range can lead to the possibility of performing linear and nonlinear spectroscopic measurements. The enhancement of nonlinear optical responses near rough self-affine metal surfaces of individual nanoparticles has been studied in detail. Experiments have revealed that the enhancement of the degenerate four-wave mixing can reach the value of 10^{22} with wavelength up to 10 μm in the far-infrared spectral region.[591,709,710] In these experiments, the clusters are usually comprised of $N \approx 5000$ elementary units, and it is assumed that individual nanoparticles are first allowed to aggregate in the solution to form fractal clusters (cluster−cluster aggregates).[710] The results are, then, averaged over a large number of samples.

To obtain the optical properties, the coupled dipole method[681] is used with intersections of the neighboring spheres.[709,710] The coupled-dipole equations that couple the linear and nonlinear dipole moments, $d_i(\omega)$ and $d_i^{\mathrm{NL}}(\omega_{\mathrm{g}})$ of the ith monomer to the incident wave have the form

$$d_i(\omega) = \alpha(\omega)[E_i^{(0)} + \sum \hat{W}_{ij}(\omega) + d_j(\omega)] \qquad (84)$$

$$d_i^{\mathrm{NL}}(\omega_{\mathrm{g}}) = \alpha(\omega_{\mathrm{g}})[F_i + \sum \hat{W}_{ij}(\omega_{\mathrm{g}}) + d_j^{\mathrm{NL}}(\omega)] \qquad (85)$$

where ω and ω_{g} are the frequencies of the linear and generated signals, $E_i^{(0)} = E^{(0)} \exp(i\mathbf{k}\cdot r_i)$ is the amplitude of the incident plane wave at the location of the ith monomer, $\alpha(\omega)$ is the frequency-dependent polarizability of a monomer, and $\hat{W}_{ij}(\omega)$ is the fully retarded dipole radiation field produced by a dipole at the jth site oscillating with frequency ω at the ith site. The physical meaning of eqs 84 and 85 is transparent. The first equation couples the linear dipole moments to each other and to the incident wave. The local fields at the incident frequency ω induce nonlinear dipole moments that oscillate at the generated frequency ω_{g} and are further coupled to each other via dipole radiation fields by eq 78. The generated signal frequency ω_{g} and the free term for the equation coupling the nonlinear dipoles to each other, F_i, depend on specific nonlinear processes. In general, F_i can be expressed in terms of linear dipole moments $d_i(\omega)$ or the corresponding local electric fields $E_i(\omega) = \alpha^{-1}(\omega)d_i(\omega)$. For degenerate four-wave mixing, $\omega = \omega_{\mathrm{g}}$, and therefore,

$$F_i = a(E_i\cdot E_i^*)E_i + b(E_i\cdot E_i)E_i^* \qquad (86)$$

Here, a and b are constants related to nonlinear susceptibilities. The term F_i plays the role of the incident field for the nonlinear dipoles and is oscillating at the generated frequency, ω_{g}. In the case of a degenerate nonlinear process of eq 86, both linear and nonlinear dipoles interact at the same frequency and the coupling constants in both eq 84 and eq 85 are the same: $\alpha(\omega) = \alpha(\omega_{\mathrm{g}})$; therefore, the interaction of nonlinear dipoles cannot be disregarded in the spectral region where the interaction of linear dipoles is known to

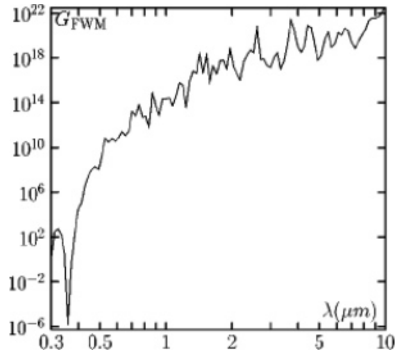

Figure 74. Average enhancement factors for the degenerate four-wave mixing as functions of the wavelength. Reprinted with permission from ref 591. Copyright 1999 The American Physical Society.

be strong. The general formula for an enhancement factor G is[710]

$$G = \left| \frac{\langle \sum_i d_i^{\mathrm{NL}}(\omega_{\mathrm{g}}) \cdot E_i^{(0)*}(\omega_{\mathrm{g}}) \rangle_{\text{on the surface}}}{\langle \sum_i d_i^{\mathrm{NL}}(\omega_{\mathrm{g}}) \cdot E_i^{(0)*}(\omega_{\mathrm{g}}) \rangle_{\text{in dilute solution}}} \right| \qquad (87)$$

This definition for the nonlinear enhancement factor utilizes the idea of work that would be done by a weak probe field oscillating at the generated frequency ω_{g} on the nonlinear dipoles. This definition is convenient because it allows one to express the enhancement factors in terms of linear local fields only. Figure 74 illustrates the wavelength dependence of the averaged enhancement factor G for the degenerate four-wave mixing. Apart from random fluctuations, which are associated with numerical averaging and are not expected to be seen experimentally, the general trend is the increase of enhancement with the wavelength. In the case of a degenerate process, $\omega = \omega_{\mathrm{g}}$ and the linear local fields are first enhanced by eq 84, and then the nonlinear fields are enhanced by eq 85 at the same frequency. The enhancement for the degenerate four-wave mixing is larger than that for the other nonlinear processes, that is, second ($\omega = 2\omega_{\mathrm{g}}$) and third harmonic generation ($\omega = 3\omega_{\mathrm{g}}$). This happens because the higher-order nonlinearities of the local fields are raised to a greater power. Thus, it can be concluded that the enhancement is larger for the degenerate four-wave mixing than for the third harmonic generation, although both are third-order nonlinear processes.

12.2.3. Dye Aggregation

In recent years, considerable research efforts have been undertaken to investigate the photophysical and photochemical aspects of multicomponent nanostructured assemblies consisting of metals and electroactive/photoactive dyes.[4,5,711−714] Association of the electroactive dye molecules onto the surface of metallic nanoparticles very often leads to aggregation effects.[713] Such organic−inorganic hybrid moieties have numerous possible applications in developing efficient light energy conversion systems, optical devices, and sensors. The composites of dye aggregate and metal nanoclusters find applications in biomolecule sensing and imaging applications.[714] Fundamental understanding of such events becomes invaluable guidance for practical applications. Theoretical studies have shown that the nature of molecular orientation of the dye molecules in the aggregate determines the spectral shift in the absorption band.[715] The nature of orientation of the dye molecules governs the type of dye aggregates, which exhibit either a blue shift (H-type) or red shift (J-type) in the extinction spectra. Since the formation of aggregates alters the absorption spectrum and photophysical properties of dyes, the resulting aggregates could emit at a wavelength different from their monomer or show new photosensitizing properties. In addition to their use as photographic sensitizers, the large oscillator strength and fast electronic response of the dye aggregates are of interest for modeling energy transfer in the photosynthetic reaction center antenna, nonlinear optics related to superfluorescence, and solar photochemical energy conversion.[716−718]

During the past few years, significant research interest has been devoted to modifying the surface of metal colloids with organic dyes. Kamat et al.[713] reported efficient capping of gold colloids with H-aggregates of rhodamine 6G and explained the dye aggregation in terms of intermolecular interactions.[716] Gold nanoparticles (with diameter 2.5 nm) are negatively charged due to the adsorption of negatively charged counterions. Addition of cationic dye, rhodamine 6G, results in surface charge neutralization and causes the gold nanoparticles to aggregate. Although the 2.5 nm diameter gold nanoparticles do not have any surface plasmon absorption in the visible, the clustered aggregates can exhibit properties similar to those observed for larger particles (>5 nm). Metal nanoclusters (copper, silver, and gold) embedded in a copper phthalocyanine matrix have been shown to enhance nonlinear optical processes.[719] In a recent communication, we have investigated the spectral characteristics of eosin in the presence of eight different sizes of gold nanoparticles.[5] It has been found that smaller particles of gold stimulate J-aggregation of eosin on the surface of metal particles whereas any kind of aggregation among the dye molecules is not seen in the presence of larger particles. The observed dye aggregation in the presence of smaller particles can be interpreted by considering that dye molecules induce intercluster interactions within the smaller particles and such aggregates, which bring adsorbed dye molecules closer, facilitate dimer formation in the assembly of the dye molecules.[720] Thus, the modification of gold nanoparticles with fluorophores is important for the development of biological traces as well as optoelectronic devices.[717] Adsorbate excited states are also involved in surface photochemical processes,[721] photon- and electron-stimulated desorption,[722] resonance photoemission,[719] and photoluminescence.[723,724] Resonant energy transfer systems consisting of organic dye molecules and noble metal nanoparticles have recently gained considerable interest in biphotonics[636] as well as in material science.[725] The versatile chemistry available for surface functionalization of gold nanoparticles[726] makes the gold nanomaterials especially suitable for possible ligand tethering and therefore applicable for biological sensors and optoelectronic devices.

12.2.4. Optoelectronic Nanodevices

Gold nanoparticles display optical properties that could potentially be exploited in optoelectronic devices.[727−729] Optical responses of metal nanostructures can be manipulated via morphology-controlled resonances associated with surface plasmon modes.[730−732] These SP resonances lead to a significant enhancement of local electric fields, which can result in increased radiative decay,[733] large nonlinear optical responses,[734] and surface-enhanced Raman scattering.[735] Near-field SP-enhanced interactions[736] also provide exciting

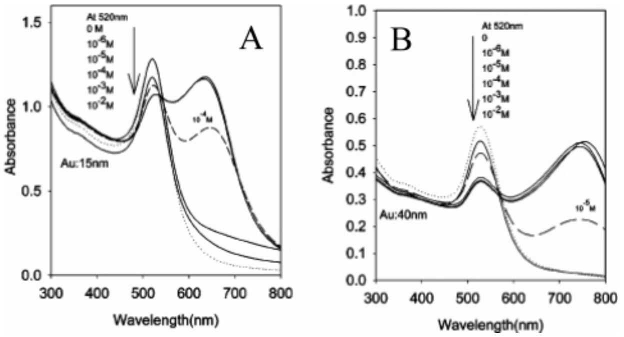

Figure 75. UV−vis spectra of cysteine at various concentrations (in 0.01 M HCl) using 15 and 40 nm diameter Au colloidal particles, respectively. The dashed curve (with concentration marked) represents the detection limit in each case. Reprinted with permission from ref 434. Copyright 2004 American Chemical Society.

opportunities for confining, guiding, and switching light using nanoscale metal-based circuits (SP nanophotonics).[737,738]

12.3. Sensor

The intense colors of noble metal nanoparticles have inspired artists and fascinated scientists for hundreds of years to use them as sensors because of several advantages over conventional electrochemical sensors: resistivity to electromagnetic noise, fire resistance, and the capability of remote control and information transfer through an optical fiber network.[739,740]

12.3.1. Chemical Sensor

The color associated with the nanoparticles is found to be tunable and useful as platforms for chemical sensing of molecules. Several authors have described the refractive index sensing platforms based on the tunability of the surface plasmon resonance of gold nanoparticles.[73,741−745] While the effect of increased refractive index induces a moderate red shift in the SPR of the individual nanoparticles, the collective SPR of the coupled nanoparticles is highly sensitive to the refractive index of the surrounding environment. Gold plasmonic type glucose sensors based on the well-known fact that the nanoparticle solutions display changes in their plasmon absorption spectrum upon aggregation or surface modification have been developed.[420,746,747] The possibility of glucose sensing using the dissociation of Con A-aggregated dextran-coated gold colloids has been explored. It has been found that this approach can readily determine millimolar changes in solution glucose concentrations in a continuous manner. Moreover, the glucose sensing range of the aggregates can be somewhat tuned depending on the size of the gold colloids employed, the molecular weight of the dextran, and the concentration of Con A used to form the sensing aggregate.

Zhong et al.[748] compared the optical response of two different sizes of gold particles (15 and 40 nm) to a wide range of cysteine concentrations as shown in Figure 75. On the basis of the first appearance of a clearly defined new peak at longer wavelength, a detection limit for cysteine with 15 nm gold particles was found to be 10^{-4} M (12 μg/mL), as compared with 10^{-5} M for 40 nm particles. A similar result was obtained for lysine (pH 2), with a detection limit of 14 μg/mL using 15 nm gold particles.

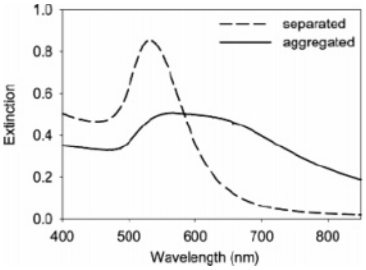

Figure 76. Extinction spectra of separated (dashed curve) and DNAzyme assembled (solid curve) 42-nm gold nanoparticles. The experimental conditions were 3 nM 35 $\mathrm{Sub_{Au}}$, 2 μM 17E, 300 mM NaCl, pH 8.2, and 35 °C. Reprinted with permission from ref 450. Copyright 2004 American Chemical Society.

12.3.2. Biological Sensor

Recent developments in nanotechnology and biology account new methods of designing colorimetric biosensors.[420,749,750] In nanotechnology, the assembly of metallic nanoparticles has resulted in novel materials with interesting properties. Changes in the optical properties of nanoparticles, which depend in part on their spacing within the polymeric aggregate, have been clearly observed. When gold nanoparticles approach each other and aggregate, the color of the nanoparticles changes from red to blue because of the shift of the surface plasmon band to longer wavelength. Surface plasmon resonance biosensors are optical sensors exploiting special electromagnetic waves, surface plasmon polaritons, to probe interactions between an analyte in solution and a biomolecular recognition element immobilized on the SPR sensor surface. Major application areas include detection of biological analytes and analysis of biomolecular interactions where SPR biosensors provide benefits of label-free real-time analytical technology. Recent reports detail the use of proteins to build supramolecular hybrid structures of nanoparticles for applications such as sensing, fabrication of nanoparticle networks, analyte detection, biotemplating, and therapeutic applications.[751] Examples include the use of streptavidin and biotin to form macroscopic gold nanoparticle assemblies[752] and the use of bacterial S-layers to grow nanoparticles in a regular array.[273] This color change can also be applied to highly sensitive detection of target DNA when the gold nanoclusters are modified by the corresponding DNAs.[273,420,592] When gold nanoparticles are functionalized with thiol-modified DNA, the distance between gold nanoparticles can be controlled by a linking DNA that is complementary to DNA attached to nanoparticles.[592] On the basis of this phenomenon, colorimetric biosensors for highly sensitive and selective detection of complementary DNA have been developed.[420,753]

The signaling of the colorimetric biosensor is based on the color change of gold nanoparticles at different assembly states.[450,754] Therefore, it is very important to find a simple yet reliable method to quantify the optical properties of gold nanoparticles. Dispersed 13 nm gold nanoparticles possess a surface plasmon peak at 522 nm. For larger nanoparticles, the peak shifts to longer wavelength (e.g., 532 nm for 42 nm gold nanoparticles). In Figure 76, the extinction spectra of separated (dashed curve) and aggregated (solid curve) 42 nm gold nanoparticles are presented. Upon aggregation, the 532 nm peak decreases in intensity while the extinction in the 700 nm region increases (solid curve), resulting in the red-to-blue color transition.[215] On the basis of previous experiments,[680,681] it was found that quantitative results could be obtained by monitoring the ratio of extinction at the plasmon peak (532 nm) and at 700 nm. A higher ratio was associated with separated nanoparticles of red color, while a lower ratio was associated with aggregated nanoparticles of blue color. Although the extinction ratio differed slightly for nanoparticles of different batches, the trend of the extinction ratio change with respect to the assembly state of nanoparticles was maintained. Therefore, instead of using the change of extinction at a single wavelength, the ratiometric method was used to monitor the assembly state of gold nanoparticles. Ratiometric sensors such as this are suitable for practical applications since they are less vulnerable to fluctuations of sampling and monitoring conditions.

12.4. Catalysis

The field of nanocatalysis has undergone an exponential growth during the past decade. This is because metallic particles in the nanometer size regime inherently provide high surface-to-volume ratio, making them attractive candidates for catalysis. Rotello and co-workers[755,756] have employed the polymer-mediated nanoparticle assembly strategy to obtain highly porous nanoparticle networks as precursors for catalyst fabrication. The final catalyst material was obtained from the porous aggregates through a calcination step, which exposed the catalytically active sites. In making the self-assembly, carboxylic acid-terminated gold and silica nanoparticles were employed together with an amine-functionalized polystyrene random copolymer. In this three component system, assembly was based on acid−base chemistry, resulting in electrostatic attraction between the basic polymer and the acidic nanoparticles upon combination. The inclusion of larger silica nanoparticles in the system enabled the creation of different types of aggregates. For example, well-integrated nanocomposites were obtained when the polymer was added to a mixture of two nanoparticles, while premixing of the silica nanoparticles with the polymer followed by the addition of gold nanoparticles led to segregated clusters, where the gold nanoparticles were highly exposed at the surface of the supporting silica aggregate. The catalytic activity of the calcinated aggregates was investigated in the hydrogenation of 9-decene-1-ol, Heck coupling reaction between the catalytically activated bromoarenes and styrene or methyl acrylate. Catalysts formed by this assembly scheme have been proven to be highly efficient with a very low metal loading and recycled with a small decrease in catalytic activity.

13. Conclusion and Perspectives

In recent years, there has been growing interest among chemists in the preparation of materials that are ordered on the length scales that extend beyond the molecular. Chemistry has occupied the middle ground between physics and biology, and it deals with the organization and reorganization of atoms into the myriad combinations that distinguish one molecule from the next, rather than the fundamental nature of matter (physics) or its animation in time and space (biology). For this reason, the marshalling of atoms by chemists to form new structures and packing arrangements tends to be on the length scale of a few nanometers. Gold nanoparticles, which have been known for 2500 years, are the subject of an exponentially growing number of reports and are full of promises for optical, electronic, magnetic, catalytic, and biomedical applications in the 21st century, using the “bottom-up” approach with the hybrid organic−inorganic and biological−inorganic building blocks derived therefrom. The reason for the present excitement in gold nanoparticle research is due to the stability of gold nanoparticles, the extraordinary diversity of its modes of preparation, its size- and shape-dependent properties, and its role in nanoscience and future nanotechnology.

The synthesis of nanostructured materials with useful and tunable properties is central to development in nanoscale science and technology. In this review, we have highlighted some recent progress toward the development of chemistry of organized matter that opens up new avenues to higher order structures with length scales and architectural complexity that one day might approach those observed in biological systems. These facile syntheses have been shown to be particularly favorable for easy manipulations, such as place-exchange reactions and extensive physical characterizations, formation of superlattices and crystals, and rich molecular chemistry. Bottom-up approaches based on self-assembly and self-organization are especially appealing because of intrinsically low overhead for large scale production. These methods have also been shown to generate network structures, which can serve as precursors to other shapes and sizes of nanoparticle assembly. The degree of ordering and the control of particle size and shape, coupled with the inherent modularity of the “bricks and mortar” self-assembly process, represent a powerful and general strategy for the creation of highly structured multifunctional materials and devices. By these means, it would be possible to obtain parallel assembly of identical multiple copies of nanoparticle-based structures for a wide range of applications. Generally, the integration of biomolecular recognition processes into inorganic systems could lay the foundations for potentially unprecedented advances in our ability to control the material world and offers the prospect of highly efficient and highly sustainable “bottom-up” manufacturing processes in the “Factory of the Future”.

A variety of synthetic possibilities for the gold nanoparticle superstructures reveals that metal sols can be induced to aggregate by replacing the charged surface species with oppositely charged or uncharged adsorbates. The experiments described here revealed several key features of the surface chemistry of gold colloids via their adsorptive interactions with organic/inorganic compounds containing various functional groups. Experiments demonstrate that the surface chemistry of colloidal gold is dominated by electrodynamic factors related to its (negative) surface charge. For several ligands, pH adjustment and judicious intermixing are seen to regulate or “tune” their interactions with gold nanoparticles. The interparticle interaction of gold nanoparticles prepared by citrate reduction or other synthetic strategies can be manipulated to control the size and colloidal stability of nanoparticle aggregates. These approaches have been useful in the self-organization of monolayer-protected metal nanoparticles into 1D, 2D, and 3D architectures, with many of these assemblies demonstrating novel optical and electronic properties as a function of particle size or interparticle spacing. These results are confirmed by calculating the interparticle interaction energy and stability ratio of nanoparticle aggregates from the DLVO theory. These results also offer theoretical insights to a new preparation route of stable nanoparticle aggregates by manipulating the interparticle interaction with different organic/inorganic adsorbates at the nanoparticle surface.

The understanding of the electronic absorption and dynamics in individual nanoparticles is essential before assembling them into devices, which is essentially the future goal of the use of nanostructured systems. The study of a sample with a narrow size and shape distribution is essential in determining the physical and especially the optical properties of individual particles in an assembly. In order to self-assemble nanoparticles, the size distribution needs to be very narrow so that the goals of both preparing a sample and assembling the nanoparticles are very closely related. This, in turn, presents the prospect of observing new optical properties of self-assembled monolayers of metallic nanoparticles as now the electric field connected to the plasmon resonance (enhancement of the incoming and outgoing electric fields when interacting with light) will influence the effective fields around the neighboring particles. Fascinating aspects are the optoelectronic properties of gold nanoparticles related to the surface plasmon absorption, reflecting the collective oscillation of the conducting electrons of the gold core, a feature relevant to the quantum size effect. The theory and experiments presented here indicate that it is now possible to describe many optical properties of gold metal nanoparticles having complex shapes and in complex dielectric environments. Optical properties of noble metal particles have been widely investigated because of their fundamental importance in science and industry. Not only the local field enhancement but also the surface plasmon mode behaviors in near-field arouse fundamental interest and various applications. The ultrafast electronic relaxation and coherent vibrational oscillations of strongly interacting gold nanoparticle aggregates using femtosecond laser spectroscopy have been reported. A model exists for the ensemble-averaged plasmon absorption with experimentally determined gold nanoparticle size and shape as input parameters. Taking into account the refractive index of the matrix, shape anisotropy, and interparticle coupling, the experimental data are quite-well described. Wavelength-dependent characteristics of surface plasmon modes on metal nanoparticles have been found to be essential for utilizing them as novel optical and electronic materials and also for constructing molecular systems for nanophotonic applications as well.

Although bulk gold is well-known for being inert, the reactivity of the gold cores in gold nanoparticles especially when those are assembled into well-defined architectures have been found to be useful in excellent sensory and environmental devices applications and catalysis by tuning the electrochemical characteristics of gold nanoparticles with those of substrates including DNA, sugars, and other biological molecules or systems with absorption, fluorescence, and surface-enhanced Raman scattering spectroscopy. The sensitivity of the plasmon resonance characteristics to adsorbed species is important for their potential applications as chemical and biological sensors. The faster times of nanoparticle sensors should permit kinetic binding studies of macromolecular target analytes that are currently possible. The need for tunable glucose sensing ranges has recently been obviated, which has involved the fabrication of a range of glucose sensing contact lenses for potential use by diabetics. These new aggregate sensors have the opportunity to be incorporated into disposable, plastic contact lenses for the noninvasive and continuous monitoring of tears, and therefore blood glucose, alleviating eye autofluorescence and overexposure of the eye to UV radiation. The review of the optical and dynamic properties of gold nanocrystals in assembly shows that a great deal of understanding has been accomplished. Although the individual metallic nanoparticles and their optical absorption have been studied experimentally and theoretically, in the aggregates those present new properties different from the individual nanoparticles. In most practical situations, particle interactions are important, and sometimes they are dominant. The understanding of the dynamics of the electrons and the lattice of the nanostructured assemblies is of great importance to their potential use in future photonic applications. NLO applications of gold nanoparticles are also rapidly growing. The combination of this photonics discipline with biology and medicine has already been demonstrated by the seminal work on gold nanoparticle−DNA assemblies and is very promising for future biomolecular manipulations and applications, such as labeling, detection, and transfer of drugs, including genetic materials. The calculation of other properties, such as second and third harmonic generation and four-wave mixing, provides new challenges for nanostructured architectures that are an important component of present research.

Finally, this review demonstrates that a wide range of different types of architectures of gold nanoparticles can be synthesized, and it is clear that further investigations will continue to design novel methodologies to enlarge the variety of such compounds available. There is a wealth of detailed information in this review with many useful tables, formulas, equations, graphs, and references. The publication is to be recommended as a reference for all those interested in gold chemistry, both in academia and industrial circles.

14. Abbreviations

SPR	surface plasmon resonance
SERS	surface-enhanced Raman scattering
IB	interband contribution
DDA	discrete dipole approximation
FDTD	finite-difference time-domain
1D	one-dimensional
2D	two-dimensional
3D	three-dimensional
DSBA	disulfide biotin analogue
TEM	transmission electron microscopy
HRTEM	high-resolution transmission electron microscopy
SAXS	small-angle X-ray scattering
STV	streptavidin
PDDF	pair distance distribution function
PA	phenylacetylene
MPF	1-(4-methyl)piperazinyl fullerene
OA-POSS	octa-ammonium polyhedral oligomeric silsesquioxanes
cmc	critical micelle concentration
DPPC	dipalmitoylphosphatidylcholine
CTAB	cetyltrimethylammonium bromide
CTAC	cetyltrimethylammonium chloride
AOT	sodium bis-(2-ethylhexyl) sulfosuccinate
TOAB	tetraoctylammonium bromide
LB	Langmuir−Blodgett
SPP	surface plasmon polariton
UV	ultraviolet
POP	poly(oxypropylene)
PNIPAAm	poly(*N*-isopropylacrylamide)
DNA	deoxyribonucleic acid
Con A	*Canavalia ensiformis*
TBA	thiobarbituric acid
MPA	3-mercaptopropanoic acid
OPV	oligo(*p*-phenylene vinylene)
SP	surface plasmon
DLVO	Derjaguin−Laudau−Verwey−Overbeck
DLCA	diffusion-limited cluster aggregation
RLCA	reaction-limited cluster aggregation
EPB	extended plasmon band
TPB	transverse plasmon band
SDS	sodium dodecyl sulfate

EM	electromagnetic
CE	chemical enhancement
p-ATP	*para*-aminothiophenol
CT	charge transfer
PET	photoinduced electron transfer
TNA	thionicotinamide
ET	electron transfer
NLO	nonlinear optics
SHG	second harmonic generation
THG	third harmonic generation
FWM	four-wave mixing

15. Acknowledgements

S. K. Ghosh is thankful to Dr. Anjali Pal and his labmates for helpful discussions and suggestions and colleagues of Raidighi College for encouragement. We are thankful to all the reviewers for suggestions and constructive comments.

16. References

(1) Kreibig, U.; Vollmer, M. *Optical Properties of Metal Clusters*; Springer: Berlin, 1995.
(2) Schmid, G. *Clusters and Colloids − From Theory to Applications*; VCH: Weinheim, Germany, 1994.
(3) Ghosh, S. K.; Kundu, S.; Mandal, M.; Pal, T. *Langmuir* **2002**, *18*, 8756.
(4) Ghosh, S. K.; Pal, T.; Kundu, S.; Nath, S.; Pal, T. *Chem. Phys. Lett.* **2004**, *395*, 366.
(5) Ghosh, S. K.; Pal, A.; Kundu, S.; Nath, S.; Panigrahi, S.; Pal, T. *Chem. Phys. Lett.* **2005**, *412*, 5.
(6) Kubo, R. *J. Phys. Soc. Jpn.* **1962**, *17*, 975.
(7) Jackson, J. D. *Classical Electrodynamics*; Wiley: New York, 1975; p 98.
(8) Atwater, H. A. *Sci. Am.* **2007**, *296*, 56.
(9) Malinsky, M. D.; Kelly, K. L.; Schatz, G. C.; Van Duyne, R. P. *J. Am. Chem. Soc.* **2001**, *123*, 1471.
(10) Bain, C. D.; Evall, J.; Whitesides, G. M. *J. Am. Chem. Soc.* **1989**, *111*, 7155.
(11) Bain, C. D.; Whitesides, G. M. *J. Am. Chem. Soc.* **1989**, *111*, 7164.
(12) Templeton, A. C.; Pietron, J. J.; Murray, R. W.; Mulvaney, P. *J. Phys. Chem. B* **2000**, *104*, 564.
(13) George Thomas, K.; Zajicek, J.; Kamat, P. V. *Langmiur* **2002**, *18*, 3722.
(14) Zhang, J. Z. *Acc. Chem. Res.* **1997**, *30*, 423.
(15) Brust, M.; Walker, M.; Bethel, D.; Schiffrin, D. J.; Whyman, R. *Chem. Commun.* **1994**, 801.
(16) Brust, M.; Fink, J.; Bethel, D.; Schiffrin, D. J.; Kiely, C. *Chem. Commun.* **1995**, 1655.
(17) Vijay Sarathy, K.; Kulkarni, G. U.; Rao, C. N. R. *Chem. Commun.* **1997**, 537.
(18) Nakao, Y. *Chem. Commun.* **1994**, 2067.
(19) Lin, S. T.; Franklin, M. T.; Klabunde, K. J. *Langmuir* **1986**, *2*, 259.
(20) Esumi, K.; Kameo, A.; Suzuki, A.; Torigoe, K. *Colloids Surf. A* **2001**, *189*, 155.
(21) Bohren, C. F.; Huffman, D. R. *Absorption and Scattering of Light by Small Particles*; Wiely Interscience: New York, 1983.
(22) Cretu, C.; van der Lingen, E. *Gold Bull.* **1999**, *32*, 115.
(23) Quinten, M. *J. Cluster Sci.* **1999**, *10*, 319.
(24) Martin, C. R.; Mitchell, D. T. *Anal. Chem. News Features* **1998**, 1st May, 322A.
(25) Ghosh, S. K.; Nath, S.; Kundu, S.; Esumi, K.; Pal, T. *J. Phys. Chem. B* **2004**, *108*, 13963.
(26) Compton, D.; Comish, L.; van der Lingen, E. *Gold Bull.* **2003**, *36*, 10.
(27) Faraday, M. *Philos. Trans. R. Soc. London, Ser. A* **1857**, *147*, 145.
(28) The Royal Institution's Faraday Museum, The Royal Institution of Great Britain, 21 Albemarle Street, London, U.K.
(29) Mie, G. *Ann. Phys.* **1908**, *25*, 377.
(30) Kerker, M. *The Scattering of Light and other Electromagnetic Radiation*; Academic Press: New York, 1969.
(31) Lazarides, A. A.; Kelly, K.; Schatz, G. C. *Proceedings of the Materials Research Society Meeting*; Boston, 2001; p 635.
(32) Rayleigh, J. W. S. *Proc. R. Soc. London, Ser. A* **1907**, *79*, 399.
(33) Rayleigh, J. W. S. *Philos. Mag.* **1907**, *14*, 70.
(34) Landau, L. M.; Lifshitz, E. M. *Electrodynamics of Continuous Media*; Pergamon: Oxford, 1971. Jackson, J. D. *Classical Electrodynamics*; Wiley: New York, 1975.
(35) Chen, S. W.; Pei, R. J. *J. Am. Chem. Soc.* **2001**, *123*, 10607.
(36) Henglein, A. *J. Phys. Chem. B* **2000**, *104*, 6683.
(37) Henglein, A.; Giersig, M. *J. Phys. Chem. B* **2000**, *104*, 5056.
(38) Park, J. I.; Cheon, J. *J. Am. Chem. Soc.* **2001**, *123*, 5743.
(39) Park, S.; Yang, P. X.; Corredor, P.; Weaver, M. J. *J. Am. Chem. Soc.* **2002**, *124*, 2428.
(40) Wang, Z. L. *J. Phys. Chem. B* **2000**, *104*, 1153.
(41) Krug, J. T.; Wang, G. D.; Emory, S. R.; Nie, S. M. *J. Am. Chem. Soc.* **1999**, *121*, 9208.
(42) Templeton, A. C.; Hostetler, M. J.; Warmoth, E. K.; Chen, S. W.; Hartshorn, C. M.; Krishnamurthy, V. M.; Forbes, M. D. E.; Murray, R. W. *J. Am. Chem. Soc.* **1998**, *120*, 4845.
(43) Pileni, M. P.; Taleb, A.; Petit, C. *J. Dispersion Sci. Technol.* **1998**, *19*, 185.
(44) Alvarez, M. M.; Khoury, J. T.; Schaaff, T. G.; Shafigullin, M. N.; Vezmar, I.; Whetten, R. L. *J. Phys. Chem. B* **1997**, *101*, 3706.
(45) Lyon, L. A.; Pena, D. J.; Natan, M. J. *J. Phys. Chem. B* **1999**, *103*, 5826.
(46) Link, S.; El-Sayed, M. A. *J. Phys. Chem. B* **1999**, *103*, 8410.
(47) Collin, R. *Field Theory of Guided Waves*, 2nd ed.; Wiley: New York, 1990.
(48) Ritchie, R. H. *Phys. Rev.* **1957**, *106*, 874.
(49) Raether, H. *Surface Plasmons*; Springer-Verlag: Berlin, 1988.
(50) Barnes, W. L.; Dereux, A.; Ebbesen, T. W. *Nature* **2003**, *424*, 824.
(51) Moskovits, M. *Rev. Mod. Phys.* **1985**, *57*, 783.
(52) Metiu, H.; Das, P. *Annu. Rev. Phys. Chem.* **1984**, *35*, 507.
(53) Metiu, H. *Prog. Surf. Sci.* **1984**, *17*, 153.
(54) Efrima, S.; Metiu, H. *J. Chem. Phys.* **1979**, *70*, 1602.
(55) Aravind, P. K.; Metiu, H. *Chem. Phys. Lett.* **1980**, *74*, 301.
(56) Gersten, J. I.; Nitzan, A. *J. Chem. Phys.* **1980**, *73*, 3023.
(57) Wang, D.-S.; Chew, H.; Kerker, M. *Appl. Opt.* **1980**, *19*, 2256.
(58) Mirkin, C. A.; Ratner, M. A. *Annu. Rev. Phys. Chem.* **1997**, *101*, 1593.
(59) Rampi, M. A.; Schueller, O. J. A.; Whitesides, G. M. *Appl. Phys. Lett.* **1998**, *72*, 1781.
(60) Klein, D. L.; Roth, R.; Lim, A. K. L.; Alivisatos, A. P.; McEuen, P. L. *Nature* **1997**, *389*, 699.
(61) Bumm, L. A.; Arnold, J. J.; Cygan, M. T.; Dunbar, T. D.; Burgin, T. P.; Jones, L., II; Allara, D. L.; Tour, J. M.; Weiss, P. S. *Science* **1996**, *271*, 1705.
(62) Ghosh, S. K.; Kundu, S.; Mandal, M.; Nath, S.; Pal, T. *J. Nanopart. Res.* **2003**, *5*, 577.
(63) Lazarides, A. A.; Schatz, G. C. *J. Phys. Chem. B* **2000**, *104*, 460.
(64) Lazarides, A. A.; Schatz, G. C. *J. Chem. Phys.* **2000**, *112*, 2987.
(65) Pal, A.; Ghosh, S. K.; Esumi, K.; Pal, T. *Langmuir* **2004**, *20*, 575.
(66) Markel, V. A.; Shalaev, V. M.; Zhang, P.; Huynh, W.; Tay, L.; Haslett, T. L.; Moskovits, M. *Phys. Rev. B* **1999**, *59*, 10903.
(67) Millstone, J. E.; Park, S.; Shuford, K. L.; Qin, L.; Schatz, G. C.; Mirkin, C. A. *J. Am. Chem. Soc.* **2005**, *127*, 5312.
(68) Wokaun, A.; Gordon, J. P.; Liao, P. F. *Phys. Rev. Lett.* **1982**, *48*, 957.
(69) Doremus, R. H.; Pratima, R. *J. Mater. Res.* **1996**, *11*, 2834.
(70) Kreibig, U.; Fragstein, C. v. *Z. Phys.* **1962**, *224*, 307.
(71) Meier, M.; Wokaun, A. *Opt. Lett.* **1983**, *8*, 581.
(72) Lam, C. C.; Leung, P. T.; Young, K. *J. Opt. Soc. Am. B* **1992**, *9*, 1585.
(73) Genzel, L.; Martin, T. P.; Kreibig, U. *Z. Phys. B* **1975**, *21*, 339.
(74) Novotny, L.; Hecht, B. *Principles of Nano-Optics*; Cambridge, U.K., 2006.
(75) Maier, S. A. *Plasmonics: Fundamentals and Applications*; Springer: Berlin, 2007.
(76) Special issue: Nanostructured Materials, *Chem. Mater.* **1996**, *8*, 1569.
(77) Special issue: *Science* **1996**, *271*, 920.
(78) Heath, J. R. *Science* **1995**, *270*, 1315.
(79) Papavassiliou, G. C. *Prog. Solid State Chem.* **1980**, *12*, 185.
(80) Krenn, J. R.; Dereux, A.; Weeber, J. C.; Bourillot, E.; Lacroute, Y.; Coadonnet, J. P. *Phys. Rev. Lett.* **1999**, *82*, 2590.
(81) Pendry, J. B. *Science* **1999**, *285*, 1687.
(82) Storhoff, J. J.; Elghanian, R.; Mucic, R. C.; Mirkin, C. A.; Letsinger, R. L. *J. Am. Chem. Soc.* **1998**, *120*, 1959.
(83) Elghanian, R.; Storhoff, J. J.; Mucic, R. C.; Letsinger, R. L.; Mirkin, C. A. *Science* **1997**, *277*, 1078.
(84) Kreibig, U.; Gartz, M.; Hilger, A. *Ber. Bunsen-Ges. Phys. Chem.* **1997**, *101*, 1593.
(85) Van Duyne, R. P.; Hulteen, J. C.; Treichel, D. A. *J. Chem. Phys.* **1993**, *99*, 2101.
(86) Malinsky, M. D.; Kelly, K. L.; Schatz, G. C.; Van Duyne, R. P. *J. Phys. Chem. B* **2001**, *105*, 2343.
(87) Jeanmaire, D. L.; Van Duyne, R. P. *J. Electroanal. Chem.* **1977**, *84*, 1.
(88) Albrecht, M. G.; Creighton, J. A. *J. Am. Chem. Soc.* **1977**, *99*, 5215.
(89) Moskovits, M. *J. Chem. Phys.* **1978**, *69*, 4159.
(90) Moskovits, M. *Solid State Commun.* **1978**, *32*, 59.

(91) Pettmger, B.; Tadjeddme, A.; Kolb, D. H. *Chem. Phys. Lett.* **1979**, *66*, 544.
(92) Efrima, S.; Metiu, H. *J. Chem. Phys.* **1979**, *70*, 1602.
(93) Otto, A. *Surf. Sci.* **1980**, *110*, 99.
(94) Otto, A. *Appl. Surf. Sci.* **1980**, *6*, 308.
(95) Dornhaus, R.; Benner, R. E.; Chang, R. K.; Chabay, I. *Surf. Sci.* **1980**, *101*, 367.
(96) Aravind, P. K.; Metiu, H. *Chem. Phys. Lett.* **1980**, *74*, 301.
(97) Chen, C. Y.; Burstem, E. *Phys. Rev. Lett.* **1980**, *45*, 1278.
(98) Schatz, G. C. In *Surface Enhanced Raman Scattering*; Chang, R. K., Furtak, T. E., Eds.; Plenum: New York, 1982; p 35.
(99) Shen, Y. R. *The Principles of Nonlinear Optics*; Wiley: New York, 1984.
(100) Nie, S.; Emory, S. R. *Science* **1997**, *275*, 1102.
(101) Betzig, E.; Trautman, J. K.; Harris, T. D.; Weiner, J. S.; Kostelak, R. L. *Science* **1991**, *251*, 1468.
(102) Betzig, E.; Trautman, J. K. *Science* **1992**, *257*, 189.
(103) Buratto, S. K.; Hsu, J. W. P.; Trautman, J. K.; Betzig, J. K.; Bylsma, R. B.; Bahr, C. C.; Cardillo, M. J. *J. Appl. Phys.* **1994**, *76*, 7720.
(104) Grober, R. D.; Harris, T. D.; Trautman, J. K.; Betzig, E.; Wegscheider, W.; Pfeiffer, L.; West, K. *Appl. Phys. Lett.* **1994**, *64*, 1421.
(105) Quinten, M.; Leitner, A.; Krenn, A.; Aussenegg, F. R. *Opt. Lett.* **1998**, *23*, 1331.
(106) Maier, S. A.; Kik, P. G.; Attwater, H. A. *Phys. Rev. B* **2003**, *67*, No. 205402.
(107) Aravind, P. K.; Nitzan, A.; Metiu, H. *Surf. Sci.* **1981**, *110*, 189.
(108) Creighton, J. A.; Blatchford, C. G.; Albrecht, M. G. *J. Chem. Soc., Faraday Trans. II* **1979**, *75*, 790.
(109) von Raben, K. U.; Chang, R. K.; Laube, B. L. *Chem. Phys. Lett.* **1981**, *79*, 465.
(110) Lanqbein, D. *Theory of van der Walls Interactions*; Springer: New York, 1974.
(111) Martin, C. R.; Mitchell, D. T. *Anal. Chem. News Features* **1998**, 1st May, 322A.
(112) Alivisatos, A. P. *Sci. Am.* **2001**, September, 67.
(113) Templeton, A. C.; Wuelfing, W. P.; Murray, R. W. *Acc. Chem. Res.* **2000**, *33*, 27.
(114) Sanchez, C.; Solar-Illia, G. J. A. A.; Ribot, F.; Lalot, T.; Mayer, C. R.; Cabuil, V. *Chem. Mater.* **2001**, *13*, 3061.
(115) Mirkin, C. A.; Letsinger, R. L.; Mucic, R. C.; Storhoff, J. J. *Nature* **1996**, *382*, 607.
(116) Park, S.-J.; Taton, T. A.; Mirkin, C. A. *Science* **2002**, *295*, 1503.
(117) Lazarides, A. A.; Schatz, G. C. *J. Chem. Phys.* **2000**, *112*, 2982.
(118) Storhoff, J. J.; Lazarides, A. A.; Mucic, R. C.; Mirkin, C. A.; Letsinger, R. L.; Schatz, G. C. *J. Am. Chem. Soc.* **2000**, *122*, 4640.
(119) Drukker, K.; Wu, G.; Schatz, G. C. *J. Chem. Phys.* **2001**, *114*, 579.
(120) Compton, D.; Comish, L.; van der Lingen, E. *Gold Bull.* **2003**, *36*, 10.
(121) Pileni, M. P. *J. Phys. Chem.* **1993**, *97*, 6961.
(122) Fendler, J.; Meldrum, F. C. *Adv. Mater.* **1995**, *7*, 607.
(123) Purcell, E. M.; Pennypacker, C. R. *Astrophys. J.* **1973**, *186*, 705.
(124) Solecka-Cermakova, K.; Vlckova, B. *J. Phys. Chem.* **1996**, *100*, 4954.
(125) Badia, A.; Gao. W.; Singh, S.; Demers, L.; Cuccia, L.; Reven, L. *Langmuir* **1996**, *12*, 1262.
(126) Brust, M.; Bethell, D.; Schiffrin, D. J.; Kiely, C. J. *Adv. Mater.* **1995**, *7*, 795.
(127) Spatz, J. P.; Roescher, A.; Moller, M. *Adv. Mater.* **1996**, *8*, 337.
(128) Kimizuka, N.; Kunitake, T. *Adv. Mater.* **1996**, *8*, 89.
(129) Tse, A. S.; Wu, Z.; Asher, S. A. *Macromolecules* **1995**, *28*, 6533.
(130) Asher, S. A.; Holtz, J.; Liu, L.; Wu, Z. *J. Am. Chem. Soc.* **1994**, *116*, 4997.
(131) Chang, S. Y.; Liu, L.; Asher, S. A. *J. Am. Chem. Soc.* **1994**, *116*, 6739.
(132) Motte, L.; Billoudet, F.; Pileni, M. P. *J. Phys. Chem.* **1995**, *99*, 16425.
(133) Maxwell Garnett, J. C. *Philos. Trans. R. Soc.* **1904**, *203*, 805. Maxwell Garnett, J. C. *Philos. Trans. R. Soc.* **1906**, *205*, 237.
(134) Xu, X.; Stevens, M.; Cortie, M. B. *Chem. Mater.* **2004**, *16*, 2259.
(135) Ung, T.; Liz-Marzan, L. M.; Mulvaney, P. *J. Phys. Chem. B* **2001**, *105*, 3441.
(136) Etchegoin, P.; Cohen, L. F.; Hartigan, H.; Brown, R. J. C.; Milton, M. J. T.; Gallop, J. C. *Chem. Phys. Lett.* **2004**, *383*, 577.
(137) Giersig, M.; Mulvaney, P. *Langmuir* **1993**, *9*, 3408.
(138) Yang, T. J.; Lessard, G. A.; Quake, S. R. *Appl. Phys. Lett.* **2000**, *76*, 378.
(139) Hayazawa, N.; Inouye, Y.; Sekkat, Z.; Kawata, S. *Chem. Phys. Lett.* **2001**, *335*, 369.
(140) Hartschuh, A.; Sanchez, J.; Xie, X. S.; Novotny, L. *Phys. Rev. Lett.* **2003**, *90*, No. 095503.
(141) Andres, R. P.; Bielefeld, J. D.; Henderson, J. I.; Janes, D. B.; Kolagunta, V. R.; Kubiak, C. P.; Mahoney, W. J.; Osifchin, R. G. *Science* **1996**, *273*, 1690.
(142) Murray, C. B.; Kagan, C. R.; Bawendi, M. G. *Science* **1995**, *270*, 1335.
(143) Collier, C. P.; Saykally, R. J.; Shiang, J. J.; Henrichs, S. E.; Heath, J. R. *Science* **1997**, *277*, 1978.
(144) Feldstein, M. J.; Keating, C. D.; Liau, Y.-H.; Natan, M. J.; Scherer, N. F. *J. Am. Chem. Soc.* **1997**, *119*, 6638.
(145) Liu, Z.; Wang, H.; Li, H.; Wang, X. *Appl. Phys. Lett.* **1998**, *72*, 1823.
(146) Gaponik, N. P.; Talapin, D. V.; Rogach, A. L. *J. Mater. Chem.* **2000**, *10*, 2163.
(147) Jana, N. R.; Gearhert, L.; Murphy, C. J. *Chem. Commun.* **2001**, 617.
(148) Nam, J. M.; Park, S.-J.; Mirkin, C. A. *J. Am. Chem. Soc.* **2002**, *124*, 3820.
(149) Jana, N. R.; Sau, T. K.; Pal, T. *J. Phys. Chem. B* **1999**, *103*, 115.
(150) Sau, T. K.; Pal, A.; Pal, T. *J. Phys. Chem. B* **2001**, *105*, 9266.
(151) Pradhan, N.; Pal, A.; Pal, T. *Langmuir* **2001**, *17*, 1800.
(152) Henglein, A. *Isr. J. Chem.* **1993**, *33*, 77.
(153) Falkenhagen, D. *Artif. Organs* **1995**, *19*, 792.
(154) Palato, L.; Benedetti, L. M.; Callegaro, L. *J. Drug Targeting* **1994**, *2*, 53.
(155) Drukker, K.; Wu, G.; Schatz, G. C. *J. Chem. Phys.* **2001**, *114*, 579.
(156) Yannouleas, C.; Broglia, R. A. *Ann. Phys.* **1992**, *217*, 105.
(157) Brack, M. *Rev. Mod. Phys.* **1993**, *65*, 677.
(158) Adams, A.; Rendell, R. W.; West, W. P.; Broida, H. P.; Hansma, P. K.; Metiu, H. *Phys. Rev. B* **1980**, *21*, 5565.
(159) Adams, A.; Rendell, R. W.; Garnett, R. W.; Hansma, P. K.; Metiu, H. *Opt. Commun.* **1980**, *34*, 417.
(160) Adams, A.; Moreland, J.; Hansma, P. K. *Surf. Sci.* **1981**, *111*, 351.
(161) Adams, A.; Moreland, J.; Hansma, P. K.; Schlesinger, Z. *Phys. Rev. B* **1982**, *25*, 3457.
(162) Gersten, J. I. *J. Chem. Phys.* **1980**, *72*, 5779.
(163) Kerker, M.; Wang, D. S.; Chew, H. *Appl. Opt.* **1980**, *19*, 3373.
(164) Chen, C. Y.; Burstem, E. *Phys. Rev. Lett.* **1980**, *45*, 1278.
(165) Pettinger, B.; Moerl, L. *J. Electron Spectrosc. Relat. Phenom.* **1983**, *29*, 383.
(166) Pettinger, B.; Wenning, V.; Kolb, C. M. *Ber. Bunsen-Ges. Phys. Chem.* **1979**, *82*, 1326.
(167) Bonacic-Koutecky, V.; Fantucci, P.; Koutecky, J. *Chem. Rev.* **1991**, *91*, 1035.
(168) Charlé, K. P.; Schulze, W. *Ber. Bunsen-Ges. Phys. Chem.* **1984**, *88*, 350.
(169) Hövel, H.; Fritz, S.; Hilger, A.; Kreibig, U.; Vollmer, M. *Phys. Rev. B* **1993**, *48*, 18178.
(170) Persson, B. N. J. *Surf. Sci.* **1993**, *281*, 153.
(171) Chumanov, G.; Sokolov, K.; Gregory, B. W.; Cotton, T. M. *J. Phys. Chem.* **1995**, *99*, 9946.
(172) Jensen, J. R.; Duval, M. L.; Kelly, K. L.; Lazarides, A. A.; Shatz, G. C.; Van, Duyne, R. P. *J. Phys. Chem. B* **1999**, *103*, 9846.
(173) Mochizuki, S.; Ruppin, R. *J. Phys.: Condens. Matter* **1993**, *5*, 135.
(174) Fletcher, P.; Howe, A.; Robinson, B. *J. Chem. Soc., Faraday Trans. I* **1987**, *83*, 985.
(175) Kwok, H. *Electronic Materials*; PWS Publishing Co.: New York, 1997.
(176) Palpant, B.; Pŕevel, B.; Lermé, J., Treilleux, M.; Vialle, J *Phys. Rev.* B **1998**, *5*,1963.
(177) Roldughin, V. *Russ. Chem. Rev.* **2000**, *69*, 821.
(178) Penn, S.; He, L.; Natan, M. *Curr. Opin. Biotechnol.* **2003**, *7*, 1.
(179) Wilcoxon, J.; Williamson, R.; Baughman, R. *J. Chem. Phys.* **1993**, *98*, 9933.
(180) Schmitt, J.; Machtle, P.; Eck, D.; Mohwald, H.; Helm, C. *Langmuir* **1999**, *15*, 3256.
(181) Lin, J.; Zhou, W.; O'Connor, C. *Mater. Lett.* **2001**, *49*, 282.
(182) Evans, D. F.; Wennerstrom, H. *The Colloidal Domain: Where Physics, Chemistry, Biology, and Technology Meet*, 2nd ed.; Wiley: Canada, 1999.
(183) Henglein, A. *J. Phys. Chem.* **1993**, *97*, 8457.
(184) Mulvaney, P. *Langmuir* **1996**, *12*, 788.
(185) Kreibig, U.; Genzel, U. *Surf. Sci.* **1985**, *156*, 678.
(186) Devaty, R. P.; Sievers, A. J. *Phys. Rev.* **1985**, *B32*, 1951.
(187) Fragstein, C. V.; Kreibig, U. *Z. Phys.* **1969**, *224*, 306.
(188) Johnson, P. B.; Christy, R. W. *Phys. Rev.* **1972**, *B6*, 4370.
(189) Alvarez, M. M.; Khoury, J. T.; Schaff, T. G.; Shafigullin, M. M.; Vezmar, I.; Whetten, R. L. *J. Phys. Chem. B* **1997**, *101*, 3706.
(190) Creighton, J. A.; Eadon, D. G. *J. Chem. Soc., Faraday Trans.* **1991**, *87*, 3881.
(191) Perenboom, J. A. A. J.; Wyder, P.; Meier, P. *Phys. Rep.* **1981**, *78*, 173.
(192) Nozik, A. J.; Memming, R. *J. Phys. Chem.* **1996**, *100*, 13061.
(193) Schaaff, T. G.; Knight, G.; Shafigullin, M. N.; Borkman, R. F.; Whetten, R. L. *J. Phys. Chem. B* **1998**, *102*, 10643.
(194) Schaaff, T. G.; Shafigullin, M. N.; Khoury, J. T.; Vezmer, I.; Whetten, R. L.; Cullen, W. G.; First, P. N.; Gutierrez-Wing, C.; Ascensio, J.; Jose-Yacaman, M. J. *J. Phys. Chem. B* **1997**, *101*, 1593.
(195) van der Zande, B.; Bohmer, M. R.; Fokkink, L. G. J.; Schonenberger, C. *J. Phys. Chem. B* **1997**, *101*, 852.

(196) van der Zande, B. M. I.; Koper, G. J. M.; Lekkerkerker, N. W. *J. Phys. Chem. B* **1999**, *103*, 5754.

(197) van der Zande, B. M. I.; Pages, L.; Hikmet, R. A. M.; van Blaaderen, A. *J. Phys. Chem. B* **1999**, *103*, 5761.

(198) Link, S.; Mohamed, M. B.; El-Sayed, M. A. *J. Phys. Chem. B* **1999**, *103*, 3073.

(199) Yu, Y.; Chang, S.; Lee, C.; Wang, C. R. *J. Phys. Chem. B* **1997**, *101*, 6661.

(200) Draine, B. T.; Flatau, P. J. *J. Opt. Am. A* **1994**, *11*, 1491.

(201) Draine, B. T.; Goodman, J. J. *Astrophys. J.* **1993**, *405*, 685.

(202) Kelly, K. L.; Coronado, E.; Zhao, L. L.; Schatz, G. C. *J. Phys. Chem. B* **2003**, *107*, 668.

(203) Orendorff, C. J.; Sau, T. K.; Murphy, C. J. *Small* **2006**, *2*, 636.

(204) Wang, H.; Brandl, D. W.; Nordlander, P.; Halas, N. J. *Acc. Chem. Res.* **2007**, *40*, 53.

(205) Prodan, E.; Radloff, C.; Halas, N. J.; Nordlander, P. *Science* **2003**, *302*, 419.

(206) Prodan, E.; Nordlander, P. *J. Chem. Phys.* **2004**, *120*, 5444.

(207) Chen, J.; Wiley, B.; Li, Z.-Y.; Campbell, D.; Saeki, F.; Cang, H.; Au, L.; Lee, J.; Li, X.; Xia, Y. *Adv. Mater.* **2005**, *17*, 2255.

(208) Hu, M.; Chen, J.; Li, Z.-Y.; Au, L.; Hartland, G. V.; Li, X.; Marquez, M.; Xia, Y. *Chem. Soc. Rev.* **2006**, *35*, 1084.

(209) Jin, R.; Cao, Y.; Mirkin, C. A.; Kelly, K. L.; Schatz, G. C.; Zheng, J. G. *Science* **2001**, *294*, 1901.

(210) Arnold, G. W.; Borders, J. A. *J. Appl. Phys.* **1997**, *48*, 1488.

(211) Kubo, M.; Nakamura, S. *Bull. Chem. Soc. Jpn.* **1953**, *26*, 318.

(212) Maniv, T.; Metiu, H. *J. Chem. Phys.* **1980**, *72*, 1996.

(213) Maniv, T.; Metiu, H. *Phys. Rev. B* **1980**, *22*, 4731.

(214) Maniv, T.; Metiu, H. *J. Chem. Phys.* **1982**, *76*, 2697.

(215) Maniv, T.; Metiu, H. *J. Chem. Phys.* **1982**, *76*, 696.

(216) Maniv, T.; Metiu, H. *Chem. Phys. Lett.* **1981**, *79*, 79.

(217) Daniel, M.-C.; Astruc, D. *Chem. Rev.* **2004**, *104*, 293.

(218) Barbar, P. W.; Chang, R. K.; Massoudi, H. *Phys. Rev. B* **1983**, *27*, 7251.

(219) Hutter, E.; Fendler, J. H. *Adv. Mater.* **2004**, *16*, 1685.

(220) Liz-Marzan, L. M. *Mater. Today* **2004**, January, 26.

(221) Quinten, M.; Kreibig, U. *Appl. Opt.* **1993**, *32*, 6173.

(222) Kreibig, U.; Althoff, A.; Pressmann, H. *Surf. Sci.* **1991**, *106*, 308.

(223) Quinten, M.; Kreibig, U. *Surf. Sci*. **1986**, *172*, 557.

(224) Quinten, M.; Schoenauer, D.; Kreibig, U. *Surf. Sci*. **1986**, *172*, 557.

(225) Turkevich, J. *Gold Bull.* **1985**, *18*, 86.

(226) Genzel, L.; Martin, T. P. *Surf. Sci.* **1973**, *34*, 33.

(227) Ung, T.; Liz-Marzán, L. M.; Mulvaney, P. *Colloids Surf. A* **2002**, *202*, 119.

(228) Norman, T. J.; Grant, C. D.; Magana, D.; Zhang, J. Z.; Liu, J.; Cao, D.; Bridges, F.; van Buuren, A. *J. Phys. Chem. B* **2002**, *106*, 7005.

(229) Gerárdy, J. M.; Ausloos, M. *Phys. Rev. B* **1983**, *27*, 6446.

(230) Shipway, A. N.; Lahav, M.; Gabai, R.; Willner, I. *Langmuir* **2000**, *16*, 8789.

(231) Dimon, P.; Sinha, S. K.; Weitz, D. A.; Safinya, C. R.; Smith, G. S.; Varady, W. A.; Lindsay, H. M. *Phys. Rev. Lett.* **1986**, *57*, 595.

(232) Shih, W. Y.; Liu, J.; Shih, W. H.; Aksay, I. A. *J. Stat. Phys*. **1991**, *62*, 961.

(233) Mayya, K. S.; Patil, V.; Sastry, M. *Bull. Chem. Soc. Jpn.* **2000**, *73*, 1757.

(234) Schatz, G. C. *J. Mol. Struct. (THEOCHEM)* **2001**, *573*, 73.

(235) Blatchford, C. G.; Campbell, J. R.; Creighton, J. A. *Surf. Sci.* **1982**, *120*, 435.

(236) Wilcoxon, J. P.; Martin, J. E.; Schaefer, D. W. *Phys. Rev. A* **1989**, *39*, 2675.

(237) Hornyak, G. L.; Patrissi, C. J.; Martin, C. R. *J. Phys. Chem. B* **1997**, *101*, 1458.

(238) Foss, C. A., Jr.; Hornyak, G. L.; Stockert, J. A.; Martin, C. R. *J. Phys. Chem. B* **1992**, *96*, 7497.

(239) Foss, C. A., Jr.; Hornyak, G. L.; Stockert, J. A.; Martin, C. R *J. Phys. Chem.* **1994**, *98*, 2963.

(240) Belloni, J.; Mostafavi, M.; Remita, H.; Marignier, J. L.; Delcourt, M. O. *New J. Chem.* **1998**, *22*, 1239.

(241) Moskovits, M.; Hulse, J. E. *J. Chem. Phys.* **1977**, *66*, 3988.

(242) Foss, C. A., Jr.; Tierney, M. J.; Martin, C. R. *J. Phys. Chem.* **1992**, *96*, 9001.

(243) Lazarides, A. A.; Kelly, K. L.; Schatz, George C. *Mater. Res. Soc. Symp. Proc.* **2001**, *635*, C6.5/1−10.

(244) Yee, K. *IEEE Trans.* **1966**, *14*, 302.

(245) Taflove, A. *IEEE Trans.* **1980**, *22*, 191.

(246) Kunz, K. S.; Luebbers, R. J. *The Finite Difference Time Domain Method for Electromagnetics*; CRC Press: Boca Raton, FL, 1993; p 8657.

(247) Novak, J. P.; Feldheim, D. L. *J. Am. Chem. Soc.* **2000**, *122*, 3979.

(248) Chandrasekharan, N.; Kamat, P. V. *Nano Lett.* **2001**, *1*, 67.

(249) Hassenkam, T.; Nørgaard, K.; Iversen, L.; Kiely, C. J.; Brust, M.; Bjørnholm, T. *Adv. Mater.* **2002**, *14*, 1126.

(250) Park, S. J.; Taton, T. A.; Mirkin, C. A. *Science* **2002**, *295*, 1503.

(251) Quinten, M.; Leitner, A.; Krenn, J. R.; Aussenegg, F. R. *Opt. Lett.* **1998**, *23*, 1331.

(252) Panoiu, N.-C.; Osgood, R. M., Jr. *Nano Lett.* **2004**, *4*, 2427.

(253) Xu, X.; Stevens, M.; Cortie, M. B. *Chem. Mater.* **2004**, *16*, 2259.

(254) Etchegoin, P.; Cohen, L. F.; Hartigan, H.; Brown, R. J. C.; Milton, M. J. T.; Gallop, J. C. *Chem. Phys. Lett.* **2004**, *383*, 577.

(255) Hainfield, J.; Powell, R. *J. Histochem. Cytochem.* **2000**, *48*, 471.

(256) Feldheim, D.; Foss, C. *Metal Nanoparticles: Synthesis, Characterization and Applications*; Marcel Dekker Inc.: New York, 2002; pp 135−150.

(257) Zhou, Q.; Swager, T. M. *J. Am. Chem. Soc.* **1995**, *117*, 12593.

(258) Walt, D. R. *Acc. Chem. Res.* **1998**, *31*, 267.

(259) Bissell, R. A.; Cordova, E.; Kaifer, A. E.; Stoddart, J. F. *Nature* **1994**, *369*, 133.

(260) Feldheim, D. L.; Keating, C. D. *Chem. Soc. Rev.* **1997**, 27.

(261) Brousseau, L. C., III; Zhao, Q.; Shultz, D. A.; Feldheim, D. L. *J. Am. Chem. Soc.* **1998**, *120*, 7645.

(262) Chumanov, G.; Sokolov, K.; Gregory, B.; Cotton, T. M. *J. Phys. Chem.* **1995**, *99*, 9466.

(263) Feilchenfeld, H.; Chumanov, G.; Cotton, T. M. *J. Phys. Chem.* **1996**, *100*, 4937.

(264) Andres, R. P.; Bein, T.; Dorogi, M.; Feng, S.; Henderson, J. I.; Kubiak, C. P.; Mahoney, W.; Osifchin, R. G.; Reifenberger, R. *Science* **1996**, *272*, 1323.

(265) Peschel, S.; Schmid, G. *Angew. Chem., Int. Ed. Engl.* **1995**, *34*, 1442.

(266) Colvin, V. L.; Goldstein, A. N.; Alivisatos, A. P. *J. Am. Chem. Soc.* **1992**, *114*, 5221.

(267) Liu, J.; Alvarez, J.; Kaifer, A. E. *Adv. Mater.* **2000**, *12*, 1381.

(268) Kim, B.; Tripp, S. L.; Wei, A. *J. Am. Chem. Soc.* **2001**, *123*, 7955.

(269) Frankamp, B. L.; Uzun, O.; Ilhan, F.; Boal, A. K.; Rotello, V. M. *J. Am. Chem. Soc.* **2002**, *124*, 892.

(270) Andres, R. P.; Bein, T.; Dorogi, M.; Feng, S.; Henderson, J. I.; Kubiak, C. P.; Mahoney, W.; Osifchin, R. G.; Reifenberger, R. *Science* **1996**, *272*, 1323.

(271) Freeman, R. G.; Grabar, K. C.; Allison, K. J.; Bright, R. M.; Davis, J. A.; Guthrie, A. P.; Hommer, M. B.; Jackson, M. A.; Smith, P. C.; Walter, D. G.; Natan, M. J. *Science* **1995**, *267*, 1629.

(272) Zamborini, F. P.; Hicks, J. F.; Murray, R. W. *J. Am. Chem. Soc*. **2000**, *122*, 4514.

(273) Elghanian, R.; Storhoff, J. J.; Mucic, R. C.; Letsinger, R. L.; Mirkin, C. A. *Science* **1997**, *277*, 1078.

(274) Alivisatos, A. P.; Johnsson, K. P.; Peng, X. G.; Wilson, T. E.; Loweth, C. J.; Bruchez, M. P.; Schultz, P. G. *Nature* **1996**, *382*, 609.

(275) Hostetler, M. J.; Green, S. J.; Stokes, J. J.; Murray, R. W. *J. Am. Chem. Soc.* **1996**, *118*, 4212.

(276) Murray, C. B.; Kagan, C. R.; Bawendi, M. G. *Science* **1995**, *270*, 1335.

(277) Kagan, C. R.; Murray, C. B.; Nirmal, M.; Bawendi, M. G. *Phys. Rev. Lett.* **1996**, *76*, 1517.

(278) Mann, S.; Shenton, W.; Li, M.; Connolly, S.; Fitzmaurice, D. *Adv. Mater.* **2000**, *12*, 147.

(279) Mucic, R. C.; Storhoff, J. J.; Mirkin, C. A.; Letsinger, R. L. *J. Am. Chem. Soc.* **1998**, *120*, 12674.

(280) Mitchell, G. P.; Mirkin, C. A.; Letsinger, R. L. *J. Am. Chem. Soc.* **1999**, *121*, 8122.

(281) Taton, T. A.; Mucic, R. C.; Mirkin, C. A.; Letsinger, R. L. *J. Am. Chem. Soc.* **2000**, *122*, 6305.

(282) Park, S.-J.; Lazarides, A. A.; Mirkin, C. A.; Brazis, P. W.; Kannewurf, C. R.; Letsinger, R. L. *Angew. Chem.* **2000**, *112*, 4003; *Angew. Chem., Int. Ed.* **2000**, *39*, 3845.

(283) Taton, T. A.; Mirkin, C. A.; Letsinger, R. L. *Science* **2000**, *289*, 1757.

(284) Niemeyer, C. M.; Burger, W.; Peplies, J. *Angew. Chem.* **1998**, *110*, 2391; *Angew. Chem., Int. Ed.* **1998**, *37*, 2265.

(285) Shenton, W.; Davis, S. A.; Mann, S. *Adv. Mater.* **1999**, *11*, 449.

(286) Connolly, S.; Fitzmaurice, D. *Adv. Mater.* **1999**, *11*, 1202.

(287) Li, M.; Wong, K. W.; Mann, S. *Chem. Mater.* **1999**, *11*, 23.

(288) Park, S.-J.; Lazarides, A. A.; Mirkin, C. A.; Letsinger, R. L. *Angew. Chem., Int. Ed.* **2001**, *40*, 2909.

(289) Guinier, A.; Fournet, A. *Small Angle Scattering of X-rays*; Wiley: New York, 1955.

(290) Korgel, B. A.; Fitzmaurice, D. *Phys. Rev. B* **1999**, *59*, 14191.

(291) Demers, L. M.; Mirkin, C. A.; Mucic, R. C.; Reynolds, R. A.; Letsinger, R. L.; Elghanian, R.; Viswanadham, G. *Anal. Chem.* **2000**, *72*, 5535.

(292) Hayat, M. A. *Colloidal Gold: Principles, Methods, and Applications*; Academic Press: San Diego, CA, 1991.

(293) Brust, M.; Walker, M.; Bethell, D.; Schiffrin, D. J.; Whyman, R. *Chem. Commun.* **1994**, 801.

(294) Shon, Y. S.; Mazzitelli, C.; Murray, R. W. *Langmuir* **2001**, *17*, 7735.

(295) Li, X. M.; de Jong, M. R.; Inoue, K.; Shinkai, S.; Huskens, J.; Reinhoudt, D. N. *J. Mater. Chem.* **2001**, *11*, 1919.

(296) Boal, A. K.; Ilhan, F.; DeRouchey, J. E.; Thurn-Albrecht, T.; Russell, T. P.; Rotello, V. M. *Nature* **2000**, *404*, 746.

(297) Brousseau, L. C.; Novak, J. P.; Marinakos, S. M.; Feldheim, D. L. *Adv. Mater.* **1999**, *11*, 447.
(298) Jana, N.; Gearheart, L.; Murphy, C. J. *Langmuir* **2001**, *17*, 6782.
(299) Schmid, G.; Simon, U. *Chem. Commun.* **2005**, 697.
(300) Tang, Z.; Kotov, N. *Adv. Mater.* **2005**, *17*, 951.
(301) Werts, M. H. V.; Lambert, M.; Bourgoin, J.-P.; Brust, M. *Nano Lett.* **2002**, *2*, 43.
(302) Corbierre, M. K.; Beerens, J.; Lennox, R. B. *Chem. Mater.* **2005**, *17*, 5774.
(303) Alivisatos, A. P.; Johnsson, K. P.; Peng, X.; Wilson, T. E.; Loweth, C. J.; Bruchez, M. P., Jr.; Schultz, P. G. *Nature* **1996**, *382*, 609.
(304) Nakao, H.; Shiigi, H.; Yamamoto, Y.; Tokonami, S.; Nagaoka, T.; Sugiyama, S.; Ohtani, T. *Nano Lett.* **2003**, *3*, 1391.
(305) Spatz, J. P.; Chan, V. Z.-H.; Mössmer, S.; Kamm, F.-M.; Plettl, A.; Ziemann, P.; Möller, M. *Adv. Mater.* **2002**, *14*, 1827.
(306) Liu, S.; Maoz, R.; Sagiv, J. *Nano Lett.* **2004**, *4*, 845.
(307) Fresco, Z. M.; Frèchet, J. M. J. *J. Am. Chem. Soc.* **2005**, *127*, 8302.
(308) Corbierre, M. K.; Beerens, J.; Beauvais, J.; Lennox, R. B. *Chem. Mater.* **2006**, *18*, 2628.
(309) Al-Sáady, A. K.; McAuliffe, C. A.; Parish, R. V.; Sandbank, J. A. A. *Inorg. Synth.* **1985**, *23*, 191.
(310) Koenig, S.; Chechik, V. *Langmuir* **2006**, *22*, 5168.
(311) Watson, K. J.; Zhu, J.; Nguyen, S. T.; Mirkin, C. A. *J. Am. Chem. Soc.* **1999**, *121*, 462.
(312) Koenig, S.; Chechik, V. *Langmuir* **2003**, *19*, 9511.
(313) Li, X.-M.; Huskens, J.; Reinhoudt, D. N. *Nanotechnology* **2003**, *14*, 1064.
(314) Choi, T.-L.; Grubbs, R. H. *Angew. Chem., Int. Ed.* **2003**, *42*, 1743.
(315) Marinakos, S. M.; Brousseau, L. C., III; Jones, A.; Feldheim, D. L. *Chem. Mater.* **1998**, *10*, 1214.
(316) Hornyak, G. L.; Kroll, M.; Pugin, R.; Sawitowski, T.; Schmid, G.; Bovin, J.-O.; Karsson, G.; Hofmeister, H.; Hopfe, S. *Chem.—Eur. J.* **1997**, *3*, 1951.
(317) Peng, X.; Wilson, T. E.; Alivisatos, A. P.; Schultz, P. G. *Angew. Chem., Int. Ed. Engl.* **1997**, *36*, 145.
(318) Alivisatos, A. P.; Johnsson, K. P.; Peng, X.; Wilson, T. E.; Loweth, C. J.; Bruchez, M. P., Jr.; Schultz, P. G. *Nature* **1996**, *382*, 609.
(319) Brousseau, L. C., III; Novak, J. P.; Marinakos, S. M.; Feldheim, D. L. *Adv. Mater.* **1999**, *11*, 447.
(320) Grabar, K. C.; Smith, P. C.; Musick, M. D.; Davis, J. A.; Walter, D. G.; Jackson, M. A.; Guthrie, A. P.; Natan, M. J. *J. Am. Chem. Soc.* **1996**, *118*, 1148.
(321) Freeman, R. G.; Grabar, K. C.; Allison, K. J.; Bright, R. M.; Davis, J. A.; Guthrie, A. P.; Hommer, M. B.; Jackson, M. A.; Smith, P. C.; Walter, D. G.; Natan, M. J. *Science* **1995**, *267*, 1629.
(322) Innocenzi, P.; Brusatin, G. *Chem. Mater.* **2001**, *13*, 3216.
(323) Mirkin, C. A.; Caldwell, W. B. *Tetrahedron* **1996**, *52*, 5113.
(324) Shi, X.; Caldwell, W. B.; Chen, K.; Mirkin, C. A. *J. Am. Chem. Soc.* **1994**, *116*, 11598.
(325) Bianco, A.; Gasparrini, F.; Maggini, M.; Misiti, D.; Polese, M.; Prato, G.; Scorrano, C.; Toniolo, C.; Villani, C. *J. Am. Chem. Soc.* **1997**, *119*, 7550.
(326) Mbindyo, J. K. N.; Reiss, B. D.; Martin, B. R.; Keating, C. D.; Natan, M. J.; Mallouk, T. E. *Adv. Mater.* **2001**, *13*, 249.
(327) Zheng, W. X.; Maye, M. M.; Leibowitz, F. L.; Zhong, C. J. *Anal. Chem.* **2000**, *72*, 2190.
(328) Imahori, H.; Azuma, T.; Ozawa, S.; Yamada, H.; Ushica, K.; Ajavakom, A.; Norieda, H.; Sakata, Y. *Chem. Commun.* **1999**, 557.
(329) Brust, M.; Kiely, C.; Bethel, D.; Schiffrin, D. J. *J. Am. Chem. Soc.* **1998**, *120*, 1655.
(330) Hou, J. G.; Wang, Y.; Xu, W.; Zhang, Y.; Jian, Z.; Zhang, Y. H. *Appl. Phys. Lett.* **1997**, *70*, 3110.
(331) Liu, J.; Alvarez, J.; Ong, W.; Kaifer, A. E. *Nano Lett.* **2001**, *1*, 57.
(332) Fujihara, H.; Nakai, H. *Langmuir* **2001**, *17*, 6393.
(333) Shon, Y.-S.; Choo, H. *Chem. Commum.* **2002**, 2560.
(334) Hostetler, M. J.; Templeton, A. C.; Murray, R. W. *Langmuir* **1999**, *15*, 3782.
(335) Shih, S.-M.; Su, W.-F.; Lin, Y.-J.; Wu, C.-S.; Chen, C.-D. *Langmuir* **2002**, *18*, 3332.
(336) Choi, S. Y.; Lee, Y.-J.; Park, Y. S.; Ha, K.; Yoon, K. B. *J. Am. Chem. Soc.* **2000**, *122*, 5201.
(337) Lim, I. S.; Ouyang, J.; Luo, J.; Wang, L.; Zhou, S.; Zhong, C. J. *Chem. Mater.* **2005**, *17*, 6528.
(338) Yim, H. W.; Tran, L. M.; Dobbin, E. D.; Rabinovich, D.; Liable-Sands, L. M.; Incarvito, C. D.; Lam, K.-C.; Rheingold, A. L. *Inorg. Chem.* **1999**, *38*, 2211.
(339) Israelachvilli, J. N.; Mitchell, D. J.; Ninham, B. W. *J. Chem. Soc., Faraday Trans. II* **1976**, *72*, 1525.
(340) Liu, T. *J. Am. Chem. Soc.* **2003**, *125*, 312.
(341) Norman, T. J., Jr.; Grant, C. D.; Magana, D.; Zhang, J. Z.; Liu, J.; Cao, D.; Bridges, F.; Van Buuren, A. *J. Phys. Chem. B* **2002**, *106*, 7005.
(342) Zhou, H. S.; Honma, I.; Komiyama, H.; Haus, J. W. *Phys. Rev. B* **1994**, *50*, 12052.
(343) Oldenburg, S. J.; Averitt, R. D.; Westcott, S. L.; Halas, N. J. *Chem. Phys. Lett.* **1998**, *288*, 243.
(344) Morris, T.; Copeland, H.; Szulczewski, G. *Langmuir* **2002**, *18*, 535.
(345) Turkevich, J.; Stevenson, P. C.; Hillier, J. *J. Discuss. Faraday Soc.* **1951**, *11*, 55.
(346) Lichtenhan, J. D. In *Polymeric Materials Encyclopedia*; Salamone, J. C., Ed.; CRC Press: Boca Raton, FL, 1996; p 7768.
(347) Feher, F. J.; Newman, D. A.; Walzer, J. F. *J. Am. Chem. Soc.* **1989**, *111*, 1741.
(348) Brown, J. F.; Vogt, L. H. *J. Am. Chem. Soc.* **1965**, *87*, 4313.
(349) Zheng, L.; Kasi, R. M.; Farris, R. J.; Coughlin, E. B. *J. Polym. Sci., Part A: Polym. Chem.* **2002**, *40*, 885.
(350) Zheng, L.; Farris, R. J.; Coughlin, E. B. *Macromolecules* **2001**, *34*, 8034.
(351) Xu, H.; Kuo, S. W.; Lee, J. S.; Chang, F. C. *Macromolecules* **2002**, *35*, 8788.
(352) Zheng, L.; Waddon, A. J.; Farris, R. J.; Coughlin, E. B. *Macromolecules* **2002**, *35*, 2375.
(353) Carroll, J. B.; Waddon, A. J.; Nakade, H.; Rotello, V. M. *Macromolecules* **2003**, *36*, 6289.
(354) Jeoung, E.; Carroll, J. B.; Rotello, V. M. *Chem. Commun.* **2002**, 1510.
(355) Cassagneau, T.; Caruso, F. *J. Am. Chem. Soc.* **2002**, *124*, 8172.
(356) Carroll, J. B.; Frankamp, B. L.; Srivastava, S.; Rotello, V. M. *J. Mater. Chem.* **2004**, *14*, 690.
(357) Ingram, R. S.; Hostetler, M. J.; Murray, R. W. *J. Am. Chem. Soc.* **1997**, *119*, 9175.
(358) Rechberger, W.; Hohenau, A.; Leitner, A.; Krenn, J. R.; Lamprecht, B.; Aussenegg, F. R. *Opt. Commun.* **2003**, *220*, 137.
(359) Teranishi, T.; Hasegawa, S.; Shimizu, T.; Miyake, M. *Adv. Mater.* **2001**, *13*, 1699.
(360) Carroll, J. B.; Waddon, A. J.; Nakade, H.; Rotello, V. M. *Macromolecules* **2003**, *36*, 6289.
(361) Westcott, S. L.; Oldenburg, S. J.; Randall Lee, T.; Halas, N. J. *Chem. Phys. Lett.* **1999**, *300*, 651.
(362) Sato, T.; Ahmed, H.; Brown, D.; Johnson, B. F. G. *J. Appl. Phys.* **1997**, *82*, 696.
(363) Stöber, W.; Fink, A.; Bohn, E. *J. Colloid Interface Sci.* **1968**, *26*, 62.
(364) van Blaaderen, A.; Vrij, A. *J. Colloid Interface Sci.* **1993**, *156*, 1.
(365) Grabar, K. C.; Allison, K. J.; Baker, B. E.; Bright, R. M.; Brown, K. R.; Freeman, R. G.; Fox, A. P.; Keating, C. D.; Musick, M. D.; Natan, M. J. *Langmuir* **1996**, *12*, 2353.
(366) Oldenburg, S. J.; Averitt, R. D.; Westcott, S. L.; Halas, N. J. *Chem. Phys. Lett.* **1998**, *288*, 243.
(367) Fendler, J. H. *Membrane Mimetic Chemistry*; New York-Chichester-Brisbane-Toronto-Singapore, 1982.
(368) Hassenkam, T.; Nrgaard, K.; Iversen, L.; Kiely, C. J.; Brust, M.; Bjrnholm, T. *Adv. Mater.* **2002**, *14*, 1126.
(369) Chung, S.-W.; Markovich, G.; Heath, J. R. *J. Phys. Chem.* **1998**, *102*, 8685.
(370) Kiely, C. J.; Fink, J.; Brust, M.; Bethel, D.; Schiffrin, D. J. *Nature* **1998**, *396*, 444.
(371) Wang, Z. H.; Moskovits, M.; Shalaev, V. M.; Suh, J. S.; Botet, R. *Phys. Rev. Lett.* **1994**, *72*, 4149.
(372) Wenseleers, W.; Stellacci, F.; Meyer-Friedrichsen, T.; Mangel, T.; Bauer, C. A.; Pond, S. J. K.; Marder, S. R.; Perry, J. W. *J. Phys. Chem. B* **2002**, *106*, 6853.
(373) Tsai, D. P.; Kovacs, J.; Safonov, V. P.; Shalaev, V. M.; Markel, V. A.; Danilova, Y. E.; Lepeshkin, N. N.; Kim, W.; Rautian, S. G.; Armstrong, R. L. *Phys. Rev. Lett.* **1998**, *80*, 1102.
(374) Stockman, M. I.; Shalaev, V. M.; Moskovits, M.; Botet, R.; George, T. F. *Phys. Rev. B* **1992**, *46*, 2821.
(375) Moskovits, M.; Suh, J. S. *J. Phys. Chem.* **1984**, *88*, 5526.
(376) Feilchenfeld, H.; Siiman, O. *J. Phys. Chem.* **1986**, *90*, 4590.
(377) Siiman, O.; Feilchenfeld, H. *J. Phys. Chem.* **1988**, *92*, 453.
(378) Zhang, H. G.; Liu, F. Z.; He, T. J.; Xin, H. W. *Sci. China, Ser. B: Chem.* **1994**, *37*, 395.
(379) Yamaguchi, Y.; Weldon, M. K.; Morris, M. D. *Appl. Spectrosc.* **1999**, *53*, 127.
(380) Cheng, W.; Dong, S.; Wang, E. *J. Phys. Chem. B* **2005**, *109*, 19213.
(381) Meguro, K.; Torizuka, M.; Esumi, K. *Bull. Chem. Soc. Jpn.* **1988**, *61*, 341.
(382) Meguro, K.; Tano, T.; Torigoe, K.; Nakamura, H.; Esumi, K. *Colloids Surf.* **1989**, *34*, 381.
(383) Wilcoxon, J. P.; Williamson, R. L.; Baughman, R. *J. Chem. Phys.* **1993**, *98*, 9933.
(384) Rabani, E.; Reichman, D. R.; Geissler, P. L.; Brus, L. E. *Nature* **2003**, *426*, 271.
(385) Rabani, E.; Egorov, S. A. *Nano Lett.* **2002**, *2*, 69.
(386) Rabani, E.; Egorov, S. A. *J. Chem. Phys.* **2001**, *115*, 3437.

(387) Heath, J. R.; Knobler, C. M.; Leff, D. V. *J. Phys. Chem. B* **1997**, *101*, 189.
(388) Zhou, X. H.; Liu, C. Y.; Jiang, L.; Li, J. R. *Colloids Interfaces A* **2004**, *248*, 43.
(389) Lu, Y.; Liu, G. L.; Lee, L. P. *Nano Lett.* **2005**, *5*, 5.
(390) Tang, Z. Y.; Kotov, N. A.; Giersig, M. *Science* **2002**, *297*, 237.
(391) Special Issue for Diffusion-Limited Aggregation and Dendritic Growth. *Phys. Rev. A* **1992**, *45*, 1018.
(392) Maier, S. A.; Kik, P. G.; Atwater, H. A.; Meltzer, S.; Harel, E.; Koel, B.; Requicha, A. G. *Nat. Mater.* **2003**, *2*, 229.
(393) Pal, A.; Ghosh, S. K.; Esumi, K.; Pal, T. *Langmuir* **2004**, *20*, 575.
(394) Frens, G. *Nature* **1973**, *241*, 20.
(395) Mandal, M.; Ghosh, S. K.; Kundu, S.; Esumi, K.; Pal, T. *Langmuir* **2002**, *18*, 7792.
(396) Kameo, A.; Suzuki, A.; Torigoe, K.; Esumi, K. *J. Colloid Interface Sci.* **2001**, *241*, 289.
(397) Dorrance, R. C.; Hunter, T. F. *J. Chem. Soc., Faraday Trans. 1* **1974**, *70*, 1572.
(398) Esumi, K. In *Structure-Performance Relationship in Surfactants*, 2nd ed.; Esumi, K., Ueno, M., Eds.; Marcel Dekker: New York, 2003; Chapter 17.
(399) Kotlarchyk, M.; Huang, J.; Chen, S. *J. Phys. Chem.* **1985**, *89*, 4382.
(400) Cassin, G.; Badiali, J.; Pileni, M. *J. Phys. Chem.* **1995**, *99*, 12941.
(401) Nazário, L. M. M.; Hatton, T. A.; Crespo, J. P. S. G. *Langmuir* **1996**, *12*, 6326.
(402) Wong, M.; Thomas, J. K.; Grätzel *J. Am. Chem. Soc.* **1976**, 98, 2391.
(403) Herrera, A. P.; Resto, O.; Briano, J. G.; Rinaldi, C. *Nanotechnology* **2005**, *16*, S618.
(404) Huang, H.-Y.; Chen, W.-F.; Kuo, P.-L. *J. Phys. Chem. B* **2005**, *109*, 24288.
(405) Mayya, S. K.; Caruso, F. *Langmuir* **2003**, *19*, 6987.
(406) Sawyer, L. C.; Grubb, D. T. *Polymer Microscopy*, 2nd ed.; Chapman & Hall: New York, 1996.
(407) Mayya, K. S.; Sastry, M. *Langmuir* **1999**, *15*, 1902.
(408) Galletto, P.; Brevet, P. F.; Girault, H. H.; Antoine, R.; Broyer, M. *J. Phys. Chem. B* **1999**, *103*, 8706.
(409) Ulman, A. *Chem. Rev.* **1996**, *96*, 1533.
(410) Quinten, M.; Kreibig, U. *Surf. Sci.* **1986**, *172*, 557.
(411) Sato, K.; Hosokawa, K.; Maeda, M. *J. Am. Chem. Soc.* **2003**, *125*, 8102.
(412) Mori, T.; Maeda, M. *Polym. J.* **2002**, *34*, 624.
(413) Storhoff, J. J.; Elghanian, R.; Mucic, R. C.; Mirkin, C. A.; Letsinger, R. L. *J. Am. Chem. Soc.* **1998**, *120*, 1959.
(414) Demers, L. M.; Mirkin, C. A.; Mucic, R. C.; Reynolds, R. A.; Letsinger, R. L.; Elghanian, R.; Viswanadham, G. *Anal. Chem.* **2000**, *72*, 5535.
(415) Rouillat, M. H.; Russier-Antoine, I.; Benichou, E.; Brevet, P. F. *Anal. Sci.* **2001**, *17*, i235.
(416) Creighton, J. A.; Alvarez, M. S.; Weitz, D. A.; Kim, M. W. *J. Phys. Chem.* **1983**, *87*, 4793.
(417) Blatchford, C. G.; Campbell, J. R.; Creighton, J. A. *Surf. Sci.* **1982**, *120*, 435.
(418) Weitz, D. A.; Oliveria, M. *Phys. Rev. Lett.* **1984**, *52*, 1433.
(419) Felidj, N.; Levy, G.; Pantigny, J.; Aubard, J. *New J. Chem.* **1998**, 725.
(420) Aslan, K.; Lakowicz, J. R.; Geddes, C. D. *Anal. Chim. Acta* **2004**, *517*, 139.
(421) Aslan, K.; Pérez-Luna, V. H. *Langmuir* **2002**, *18*, 6059.
(422) Ballerstadt, R.; Schultz, J. S. *Anal. Chem.* **2000**, *72*, 4185.
(423) Yoshizumi, A.; Kanayama, N.; Maehara, Y.; Ide, M.; Kitano, H. *Langmuir* **1999**, *15*, 482.
(424) Mirkin, C. A.; Storhoff, J. J. *Chem. Rev.* **1999**, *99*, 1849.
(425) Maye, M. M.; Luo, J.; Lim, I-Im S.; Han, L.; Kariuki, N. N.; Rabinovich, D.; Liu, T.; Zhong, C.-J. *J. Am. Chem. Soc.* **2003**, *125*, 9906.
(426) Maye, M. M.; Chun, S. C.; Han, L.; Rabinovich, D.; Zhong, C. J. *J. Am. Chem. Soc.* **2002**, *124*, 4958.
(427) Fink, J.; Kiely, C. J.; Bethell, D.; Schiffrin, D. J. *Chem. Mater.* **1998**, *10*, 922.
(428) Pengo, P.; Pasquato, L.; Scrimin, P. *J. Supramol. Chem.* **2002**, *2*, 305.
(429) Templeton, A. C.; Cliffel, D. E.; Murray, R. W. *J. Am. Chem. Soc.* **1999**, *121*, 7081.
(430) Templeton, A. C.; Chen, S.; Gross, S. M.; Murray, R. W. *Langmuir* **1999**, *15*, 66.
(431) Warner, M. G.; Reed, S. M.; Hutchison, J. E. *Chem. Mater.* **2000**, *12*, 3316.
(432) Hostetler, M. J.; Wingate, J. E.; Zhong, C.-J.; Harris, J. E.; Vachet, R. W.; Clark, M. R.; Londono, J. D.; Green, S. J.; Stokes, J. J.; Wignall, G. D.; Glish, G. L.; Porter, M. D.; Evans, N. D.; Murray, R. W. *Langmuir* **1998**, *14*, 17.
(433) Brust, M.; Walker, M.; Bethell, D.; Schiffrin, D. J.; Whyman, R. *J. Chem. Soc., Chem. Commun.* **1994**, 801.
(434) Lang, H.; Duschl, C.; Vogel, H. *Langmuir* **1994**, *10*, 197.
(435) Pasquato, L.; Rancan, F.; Scrimin, P.; Mancin, F.; Frigeri, C. *Chem. Commun.* **2000**, 2253.
(436) Peng, Z.; Walther, T.; Kleinermanns, K. *Langmuir* **2005**, *21*, 4249.
(437) Mulvaney, P. *Langmuir* **1996**, *12*, 788.
(438) Kalsin, A. M.; Pinchuk, A. O.; Smoukov, S. K.; Paszewski, M.; Schatz, G. C.; Grzybowski, B. A. *Nano Lett.* **2006**, *6*, 1896.
(439) Kalsin, A. M.; Fialkowski, M.; Paszewski, M.; Smoukov, S. K.; Bishop, K. J. M.; Grzybowski, B. A. *Science* **2006**, *312*, 420.
(440) Stoeva, S.; Klabunde, K. J.; Sorensen, C. M.; Dragieva, I., *J. Am. Chem. Soc.* **2002**, *124*, 2305.
(441) Toshima, N. *Macromol. Symp.* **2003**, *204*, 219.
(442) Shiraishi, Y.; Arakawa, D.; Toshima, N. *Eur. Phys. J., E* **2002**, *8*, 377.
(443) Yonezawa, T.; Kunitake, T. *Colloids Surf. A* **1999**, *149*, 193.
(444) Satoh, N.; Hasegawa, H.; Tsujii, K.; Kimura, K. *Colloids Surf. A* **1997**, *127*, 221.
(445) van Herrikhuyzen, J.; Janssen, R. A. J.; Meijer, E. W.; Meskers, S. C. J.; Schenning, A. P. H. J. *J. Am. Chem. Soc.* **2006**, *128*, 686.
(446) Schenning, A. P. H. J.; Jonkheijm, P.; Peeters, E.; Meijer, E. W. *J. Am. Chem. Soc.* **2001**, *123*, 409.
(447) George, Thomas, K.; Kamat, P. V. *J. Am. Chem. Soc.* **2000**, *122*, 2655.
(448) Hoeben, F. J. M.; Jonkheijm, P.; Meijer, E. W.; Schenning, A. P. H. J. *Chem. Rev.* **2005**, *105*, 1491.
(449) Reynolds, R. A., III; Mirkin, C. A.; Letsinger, R. L. *J. Am. Chem. Soc.* **2000**, *122*, 3795.
(450) Liu, J.; Lu, Y. *J. Am. Chem. Soc.* **2004**, *126*, 12298.
(451) Maye, M. M.; Han, L.; Kariuki, N. N.; Ly, N. K.; Chan, W.-B.; Luo, J.; Zhong, C. J. *Anal. Chim. Acta* **2003**, *496*, 17.
(452) Maye, M. M.; Chun, S. C.; Han, L.; Rabinovich, D.; Zhong, C. J. *J. Am. Chem. Soc.* **2002**, *124*, 4958.
(453) Maye, M. M.; Lim, I.-I. S.; Luo, J.; Rab, Z.; Rabinovich, D.; Liu, T.; Zhong, C. J. *J. Am. Chem. Soc.* **2005**, *127*, 1519.
(454) Dean, J. A. *Lange's Handbook of Chemistry*; McGraw-Hill: New York, 1972.
(455) Santos, M. A.; Esteves, M. A.; Vaz, M. C.; Frausto da Silva, J. J. R.; Noszal, B.; Farkas, E. *J. Chem. Soc., Perkin Trans.* **1997**, *2*, 1977.
(456) Boal, A. K.; Ilhan, F.; DeRouchey, J. E.; Thurn-Albrecht, T.; Russell, T. P.; Rotello, V. M. *Nature* **2000**, *404*, 746.
(457) Deans, R.; Ilhan, F.; Rotello, V. M. *Macromolecules* **1999**, *32*, 4956.
(458) Yang, W.-H.; Schatz, G. C.; Van, Duyne, R. P. *J. Chem. Phys.* **1995**, *103*, 869.
(459) Wang, T.; Zhang, D.; Xu, W.; Li, S.; Zhu, D. *Langmuir* **2002**, *18*, 8655.
(460) Hunter, R. J. *Foundations of Colloid Science*; Clarendon Press: Oxford, U.K., 1992.
(461) Verwey, E. J. W.; Overbeek, J. Th. G. *Theory of the Stability of Lyophobic Colloids*; Dover: Mineola, New York, 2000.
(462) Lee, K.; Sathyagal, A. N.; Mc Cormick, A. V. *Colloids Surf.* **1998**, *144*, 115.
(463) Lee, T. G.; Kim, K.; Kim, M. S. *J. Raman. Spectrosc.* **1991**, *22*, 339.
(464) Evans, D. F.; Wennerstrom, H. *The Colloidal Domain: Where Physics, Chemistry, Biology, and Technology Meet*, 2nd ed., Wiley: Canada, 1999.
(465) Kwok, H. *Electronic Materials*; PWS Publishing Co.: New York, 1997.
(466) Chow, M. K.; Zukoski, C. F. *J. Colloid Interface Sci.* **1994**, *165*, 97.
(467) Bargeman, D.; Vader, F. V. V. *J. Electroanal. Chem. Interfacial Electrochem.* **1972**, *37*, 45.
(468) Israelachvili, J. *Intermolecular& Surface Forces*, 2nd ed.; Academic Press: San Diego, CA, 1991.
(469) Hiemenz, P.; Rajagopalan, R. *Principles of Colloid and Surface Chemistry*, 3rd ed.; Marcel Dekker: New York, 1997.
(470) Kitchens, C.; Chandler, M.; Roberts, C. *J. Phys. Chem.* **2003**, *107*, 11331.
(471) Sedivec, V.; Flek, J. *Handbook of Analysis of Organic Solvents*; E. H. Limited: London, 1976.
(472) Ninham, B. W. *Adv. Colloid Interface Sci.* **1999**, *83*, 1.
(473) Kim, T.; Lee, K.; Gong, M.; Joo, S.-W. *Langmuir* **2005**, *21*, 9524.
(474) Basu, S.; Panigrahi, S.; Praharaj, S.; Ghosh, S. K.; Pande, S.; Jana, S.; Pal, T. *New J. Chem.* **2006**, *30*, 1333; *J. Colloids Interface Sci.* **2007**, in press.
(475) Carroll, J. B.; Frankamp, B. L.; Rotello, V. M. *Chem. Commun.* **2002**, 1892.
(476) Westcott, S. L.; Oldenburg, S. J.; Lee, T. R.; Halas, N. J. *Langmuir* **1998**, *14*, 5396.
(477) Myers, D. *Surfaces, Interfaces and Colloids*; Wiley-VCH: New York, 1999; Chapters 4, 5, and 10.
(478) Bradley, J. S. In *Clusters and Colloids*; Schmid, G., Ed.; VCH: Weinheim, Germany, 1994; p 465.

(479) Creighton, J. A. In *Surface Enhanced Raman Scattering*; Chang, R. K., Furtak, T. E., Eds.; Plenum: New York, 1982; p 315.

(480) Moskovits, M.; Vlčkova, B. *J. Phys. Chem. B* **2005**, *109*, 14755.

(481) Meakin, P. In *The Fractal Approach to Heterogeneous Chemistry*; Avnir, D., Ed.; Wiley: New York, 1989; p 131.

(482) Matsushita, M. In *The Fractal Approach to Heterogeneous Chemistry*; Avnir, D., Ed.; Wiley: New York, 1989; p 161.

(483) Mulvaney, P.; Liz-Marzan, L. M.; Giersig, M.; Ung, T. *J. Mater. Chem.* **2000**, *10*, 1259.

(484) Creighton, J. A.; Blatchford, C. G.; Albrecht, M. G. *J. Chem. Soc., Faraday Trans. II* **1979**, *75*, 790.

(485) Heard, S. M.; Grieser, F.; Barraclough, C. G. *J. Colloid Interface Sci.* **1983**, *93*, 545.

(486) Vlĉková, B.; Tsai, D.; Gu, X.; Moskovits, M. *J. Phys. Chem.* **1996**, *100*, 3169.

(487) Moskovits, M. *Rev. Mod. Phys.* **1985**, *57*, 783.

(488) Zhang, H.; Penn, R. L.; Hamers, R. J.; Banfield, J. F. *J. Phys. Chem. B* **1999**, *103*, 4656.

(489) Sverjensky, D. A. *Nature* **1993**, *364*, 776.

(490) Alivisatos, A. P. *Science* **1996**, *271*, 933.

(491) Langmuir, I. *J. Am. Chem. Soc.* **1916**, *38*, 2221.

(492) Weitz, D. A.; Oliveria, M. *Phys. Rev. Lett.* **1984**, *52*, 1433.

(493) Lattuada, M.; Wu, H.; Sefcik, J.; Morbidelli, M. *J. Phys. Chem. B* **2006**, *110*, 6574 and references therein.

(494) von Smoluchowski, M. *Z. Phys. Chem.* **1917**, *92*, 129.

(495) Zhong, Z.; Patskovskyy, S.; Bouvrette, P.; Luong, J. H. T.; Gedanken, A. *J. Phys. Chem. B* **2004**, *108*, 4046.

(496) Jensen, T.; Lelly, L.; Lazarides, A.; Schatz, G. C. *J. Cluster Sci.* **1999**, *10*, 295.

(497) Su, K.-H.; Wei, Q.-H.; Zhang, X.; Mock, J. J.; Smith, D. R.; Schultz, S. *Nano Lett.* **2003**, *3*, 1087.

(498) Novotony, L.; Bian, R. X.; Xie, X. S. *Phys. Rev. Lett.* **1997**, *79*, 645.

(499) Calander, N.; Willander, M. *Phys. Rev. Lett.* **2002**, *89*, 143603.

(500) Chaumet, P. C.; Rahmani, A.; Nieto-Vesperinas, M. *Phys. Rev. Lett.* **2002**, *88*, 13601.

(501) Xu, H. X.; Käll, M. *Phys. Rev. Lett.* **2002**, *89*, 24802.

(502) Kneipp, K.; Wang, Y.; Kneipp, H.; Perelman, L. T.; Itzkan, I.; Dasari, R.; Feld, M. S. *Phys. Rev. Lett.* **1997**, *19*, 1667.

(503) Xu, H.; Bjerneld, E. J.; Käll, M.; Börjesson, L. *Phys. Rev. Lett.* **1999**, *83*, 4357.

(504) Maier, S. A.; Kik, P. G.; Atwater, H. A. *Appl. Phys. Lett.* **2002**, *81*, 1714.

(505) Kottmann, J. P.; Martin, O. J. F.; Smith, D. R.; Schultz, S. *J. Microsc.* **2001**, *202*, 60.

(506) Nordlander, P.; Oubre, C.; Prodan, E.; Li, K.; Stockman, M. I. *Nano Lett.* **2004**, *4*, 899.

(507) Nordlander, P.; Oubre, C. *J. Phys. Chem. B* **2005**, *109*, 10042.

(508) Brandl, D. W.; Mirin, N. A.; Nordlander, P. *J. Phys. Chem. B* **2006**, *110*, 12302.

(509) Brandl, D. W.; Oubre, C.; Nordlander, P. *J. Chem. Phys.* **2005**, *123*, 024701.

(510) Zeman, E. J.; Schatz, G. C. In *Dynamics of Surfaces, Proceedings of the 17th Jersusalem Symposium*; Pullman, B., Jortner, J., Gerber, B., Nitzan, A., Eds.; Reidel: Dordrecht, The Netherlands, 1984; p 413.

(511) Hayat, M. A. *Colloidal Gold: Principles, Methods, and Applications*; Academic Press: San Diego, CA, 1989.

(512) Schmitt, J.; Machtle. P.; Eck, D.; Mohwald, H.; Helm, C. A. *Langmuir* **1999**, *15*, 3256.

(513) Kreibig, U.; Hilger, A.; Hovel, M. In *Large Clusters of Atoms and Molecules*; Martin, T. P., Ed.; Kluwer: Norwell, MA, 1996; pp 475−494.

(514) Bouhelier, A.; Beverluis, M. R.; Novotny, L. *Appl. Phys. Lett.* **2003**, *83*, 5041.

(515) Kottmann, J. P.; Martin, O. J. F. *Opt. Express* **2001**, *18*, 655.

(516) Tamaru, H.; Kuwata, H.; Miyazaki, H. T.; Miyano, K. *Appl. Phys. Lett.* **2002**, *80*, 1826.

(517) Rechberger, W.; Hohenau, A.; Leitner, A.; Krenn, J. R.; Lamprecht, B.; Aussenegg, R. *Opt. Commun.* **2003**, *200*, 137.

(518) Xu, H.; Käll, M. *Phys. Rev. Lett.* **2002**, *89*, 246802.

(519) Liz-Marzán, L. M. *Langmuir* **2006**, *22*, 32.

(520) Verma, A.; Srivastava, S.; Rotello, V. M. *Chem. Mater.* **2005**, *17*, 6317.

(521) Jiang, C.; Markutsya, S.; Tsukruk, V. V. *Langmuir* **2004**, *20*, 882.

(522) Yonzon, C. R.; Jeoung, E.; Zou, S.; Schatz, G. C.; Mrksich, M.; Van Duyne, R. P. *J. Am. Chem. Soc.* **2004**, *126*, 12669.

(523) Saponjic, Z. V.; Csencsits, R.; Rajh, T.; Dimitrijevic, N. M. *Chem. Mater.* **2003**, *15*, 4521.

(524) Reichard, C. *Solvents and Solvent Effects in Organic Chemistry*; VCH: Weinheim, Germany, 1988.

(525) Fink, J.; Kiely, C. J.; Bethell, D.; Schiffrin, D. *J. Chem. Mater.* **1998**, *10*, 922.

(526) Grant, C. D.; Schwartzberg, A. M.; Norman, T. J., Jr.; Zhang, J. Z. *J. Am. Chem. Soc.* **2003**, *125*, 549.

(527) Faulhaber, A. E.; Smith, B. A.; Andersen, J. K.; Zhang, J. Z. *Mol. Cryst. Liq. Cryst. Sci. Technol.* **1996**, *283*, 25.

(528) Ahmadi, T. S.; Logunov, S. L.; Elsayed, M. A. *J. Phys. Chem.* **1996**, *100*, 8053.

(529) Hodak, J.; Martini, I.; Hartland, G. V. *Chem. Phys. Lett.* **1998**, *284*, 135.

(530) Hodak, J. H.; Martini, I.; Hartland, G. V. *J. Phys. Chem. B* **1998**, *102*, 6958.

(531) Hodak, J. H.; Henglein, A.; Hartland, G. V. *J. Chem. Phys.* **1999**, *111*, 8613.

(532) Jain, P. K.; Qian, W.; El-Sayed, M. A. *J. Phys. Chem. B* **2006**, *110*, 136.

(533) Voisin, C.; Christofilos, D.; Del Fatti, N.; Vallee, F. *Physica B* **2002**, *316*, 89.

(534) Hodak, J. H.; Henglein, A.; Hartland, G. V. *J. Phys. Chem. B* **2000**, *104*, 9954.

(535) Perner, M.; Gresillon, S.; Marz, J.; von Plessen, G.; Feldmann, J.; Porstendorfer, J.; Berg, K. J.; Berg, G. *Phys. Rev. Lett.* **2000**, *85*, 792.

(536) Hartland, G. V.; Hu, M.; Wilson, O.; Mulvaney, P.; Sader, J. E. *J. Phys. Chem. B* **2002**, *106*, 743.

(537) Quinten, M. *Appl. Phys. B* **2001**, *B73*, 317.

(538) Schonauer, D.; Quinten, M.; Kreibig, U. *Phys. Rev. Lett.* **1989**, 527.

(539) Quinten, M.; Schonauer, D.; Kreibig, U. *Z. Phys. D* **1989**, 521.

(540) Feldstein, M. J.; Keating, C. D.; Liau, Y. H.; Natan, M. J.; Scherer, N. F. *J. Am. Chem. Soc.* **1997**, *119*, 6638.

(541) Schoenlein, R. W.; Lin, W. Z.; Fujimoto, J. G.; Easley, G. L. *Phys. Rev. Lett.* **1987**, *58*, 1680.

(542) Sun, C. K.; Vallee, F.; Acioli, L.; Ippen, E. P.; Fujimoto, J. G. *Phys. Rev. B* **1993**, *48*, 12365.

(543) Fojtik, A.; Henglein, A. *Ber. Bunsen-Ges. Phys. Chem.* **1993**, *97*, 252.

(544) Sibbald, M. S.; Chumanov, G.; Cotton, T. M. *J. Phys. Chem.* **1996**, *100*, 4672.

(545) Kurita, H.; Takami, A.; Koda, S. *Appl. Phys. Lett.* **1998**, *72*, 789.

(546) Takami, A.; Kurita, H.; Koda, S. *J. Phys. Chem. B* **1999**, *103*, 1226.

(547) Yeh, M. S.; Yang, Y. S.; Lee, Y. P.; Lee, H. F.; Yeh, Y. H.; Yeh, C. S. *J. Phys. Chem. B* **1999**, *103*, 6851.

(548) Mafuné, F.; Kohno, J.; Takeda, Y.; Kondow, T. *J. Phys. Chem. B* **2001**, *105*, 9050.

(549) Mafuné, F.; Kohno, J.; Takeda, Y.; Kondow, T. *J. Phys. Chem. B* **2002**, *106*, 7575.

(550) Mafuné, F.; Kohno, J.; Takeda, Y.; Kondow, T.; Sawabe, H. *J. Phys. Chem. B* **2002**, *106*, 8555.

(551) Brause, R.; Möltgen, H.; Kleinermanns, K. *Appl. Phys. B* **2002**, *75*, 711.

(552) Mafuné, F.; Kohno, J.; Takeda, Y.; Kondow, T. *J. Phys. Chem. B* **2003**, *107*, 12589.

(553) El-Sayed, M. A. *Acc. Chem. Res.* **2001**, *34*, 257.

(554) Link, S.; Wang, Z. L.; El-Sayed, M. A. *J. Phys. Chem. B* **2000**, *104*, 7867.

(555) Link, S.; Burda, C.; Nikoobakht, B.; El-Sayed, M. A. *Chem. Phys. Lett.* **1999**, *315*, 12.

(556) Link, S.; Hathcock, D. J.; Nikoobakht, B.; El-Sayed, M. A. *Adv. Mater.* **2003**, *15*, 5.

(557) Del Fatti, N.; Voisin, C.; Achermann, M.; Tzortzakis, S.; Christofilos, D.; Vallee, F. *Phys. Rev. B* **2000**, *61*, 16956.

(558) Klar, T.; Perner, M.; Grosse, S.; von Plessen, G.; Spirkl, W.; Feldmann, J. *Phys. Rev. Lett.* **1998**, *80*, 4249.

(559) Näher, U.; Bjornholm, S.; Fraundorf, S.; Gracias, F.; Guet, C. *Phys. Rep.* **1997**, *285*, 245.

(560) Last, I.; Schek, I.; Jortner. J. *J. Chem. Phys.* **1997**, *107*, 6685.

(561) Last, I.; Jortner, J. *Phys. Rev. Lett.* **2001**, *87*, No. 033401.

(562) George Thomas, K.; Zajicek, J.; Kamat, P. V. *Langmuir* **2002**, *18*, 3722.

(563) Mulvaney, P. In *Nanoscale Materials in Chemistry*; Klabunde, K. J., Ed.; John Wiley & Sons: New York, 2001; Chapter 5.

(564) Kneipp, K.; Wang. Y.; Kneipp, H.; Perelman, L. T.; Itzkan, I.; Dasari, R. R.; Feld, M. S. *Phys. Rev. Lett.* **1997**, *78*, 1667.

(565) Van Duyne, R. P.; Hulteen, J. C.; Treichel, D. A. J. *Chem. Phys.* **1993**, *99*, 2101.

(566) Hulteen, J. C.; Van Duyne, R. P. *J. Vac. Sci. Technol.* **1995**, *A13*, 1553.

(567) Adrian, F. *Chem. Phys. Lett.* **1981**, *78*, 45.

(568) Wang, D. S.; Kerker, M. *Phys. Rev. B* **1981**, *24*, 1777.

(569) Schatz, G. C. *Acc. Chem. Res.* **1984**, *17*, 370.

(570) Kerker, M. *Acc. Chem. Res.* **1984**, *17*, 271.

(571) Knoll, B.; Keilmann, F. *Nature* **1999**, *399*, 134.

(572) Hartschuh, A.; Sanchez, E. J.; Xie, X. S.; Novotny, L. *Phys. Rev. Lett.* **2003**, *90*, No. 095503.

(573) Maier, S. A.; Kik, P. G.; Atwater, H. A. *Phys. Rev. B* **2003**, *67*, No. 205402.
(574) Ricard, D.; Roussignol, P.; Flytzanis, C. *Opt. Lett.* **1985**, *10*, 511.
(575) Dadap, J. I.; Shan, J.; Eisenthal, K. B.; Heinz, T. F. *Phys. Rev. Lett.* **1999**, *83*, 4045.
(576) Johnson, R. C.; Li, J.-T.; Hupp, J. T.; Schatz, G. C. *Chem. Phys. Lett*. **2002**, *356*, 534.
(577) Novak, J. P.; Brousseau, L. C., III; Vance, F. W.; Johnson, R. C.; Lemon, B. I.; Hupp, J. T.; Feldheim, D. L. *J. Am. Chem. Soc*. **2000**, *122*, 12029.
(578) Yang, W. H.; Hulteen, J.; Schatz, G. C.; Van Duyne, R. *J. Chem. Phys.* **1996**, *104*, 4313.
(579) Chen, C. K.; de Castro, A. R. B.; Shen, Y. R. *Phys. Rev. Lett.* **1981**, *46*, 145.
(580) Boyd, C. T.; Rasing, T.; Leite, J. R. R.; Shen, Y. R. *Phys. Rev.* **1984**, *B30*, 519.
(581) Hartland, G. V. J. *Chem. Phys.* **2002**, *116*, 8048.
(582) Link, S.; El-Sayed, M. A.; Schaaf, G. T.; Whetten, R. L. *Chem. Phys. Lett.* **2002**, *356*, 246.
(583) Maier, S. A.; Kik, P. G.; Atwater, H. A.; Meltzer, S.; Harel, E.; Koel, B. E.; Requicha, A. A. G. *Nat. Mater.* **2003**, *2*, 229.
(584) Messinger, B. J.; von Raben, K. U.; Chang, R. K.; Barber, P. W. *Phys. Rev. B* **1981**, *24*, 649.
(585) Kneipp, K.; Kneipp, H.; Itzkan, I.; Dasari, D. R.; Feld, M. S. *Chem. Rev.* **1999**, *99*, 2957.
(586) Sokolov, K.; Chumanov, G.; Cotton, T. M. *Anal. Chem.* **1998**, *70*, 3898.
(587) Geddes, C. D.; Cao, H.; Gryczynski, I.; Gryczynski, Z.; Fang, J.; Lakowicz, J. R. *J. Phys. Chem. A* **2003**, *107*, 3443.
(588) Nishikawa, Y.; Nagasawa, T.; Fujiwara, K.; Osawa, M. *Vib. Spectrosc.* **1993**, *6*, 43.
(589) Zheng, J. W.; Lu, H.; Cotton, T. M.; Chumanov, G. *J. Electroanal. Chem.* **2002**, *518*, 6.
(590) Poliakov, E.; Shalaev, V. M.; Shubin, V.; Markel, V. A. *Phys. Rev. B* **1999**, *60*, 10739.
(591) Mirkin, C. A.; Letsinger, R. L.; Mucic, R. C.; Storhoff, J. J. *Nature* **1996**, *382*, 607.
(592) Alivisatos, A. P.; Johnsson, K. P.; Peng, X.; Wilson, T. E.; Loweth, C. J.; Bruchez, M. P., Jr.; Schultz, P. G. *Nature* **1996**, *382*, 609.
(593) Chen, S. *Adv. Mater.* **2000**, *12*, 186.
(594) Jin, R.; Wu, G.; Li, Z.; Mirkin, C. A.; Schatz, G. C. *J. Am. Chem. Soc.* **2003**, *125*, 1643.
(595) Ditlbacher, H.; Krenn, J. R.; Felidj, N.; Lamprecht, B.; Schider, G.; Salerno, M.; Leitner, A.; Aussenegg, F. R. *Appl. Phys. Lett.* **2002**, *80*, 404.
(596) Wenseleers, W.; Stellacci, F.; Meyer-Friedrichsen, T.; Mangel, T.; Bauer, C. A.; Pond, S. J. K.; Marder, S. R.; Perry, J. W. *J. Phys. Chem. B* **2002**, *106*, 6853.
(597) Yin, X.; Fang, N.; Zhang, X.; Martini, I. B.; Schwartz, B. J. *Appl. Phys. Lett.* **2002**, *81*, 3663.
(598) Tully, J. C. *Annu. Rev. Phys. Chem.* **2000**, *51*, 153.
(599) Weitz, D. A.; Garoff, S.; Gersten, J. I.; Nitzan, A. *J. Phys. Chem.* **1983**, *78*, 5324.
(600) Philpott, M. R. *J. Chem. Phys.* **1975**, *62*, 1812.
(601) Moskovits, M.; Suh, J. S. *J. Chem. Phys.* **1984**, *88*, 5526.
(602) Creighton, J. A. *Surf. Sci.* **1983**, *124*, 209.
(603) Campion, A.; Kambhampati, P. *Chem. Soc. Rev.* **1998**, *27*, 241.
(604) Keller, O.; Liu, A.; Zayats, A. *Opt. Commun.* **1994**, *110*, 604.
(605) Voisin, C.; Fatti, N. D.; Christofilos, D.; Vallee, F. *J. Phys. Chem. B* **2001**, *105*, 2264.
(606) Kerker, M. *Selected Papers on Surface-Enhanced Raman Scattering*; The International Society for Optical Engineering: Bellingham, MA, 1990; Vol. MS 10.
(607) Pan, D.; Philips, D. L. *Chem. Phys. Lett.* **1997**, *275*, 227.
(608) Kurokawa, Y.; Imai, Y.; Tamai, Y. *Analyst* **1997**, *122*, 941.
(609) Zeisel, D.; Deckert, V.; Zenobi, R.; Vo-Dinh, T. *Chem. Phys. Lett.* **1998**, *283*, 381.
(610) DiLella, D. P.; Gohin, A.; Lipson, R. H.; McBreen, P.; Moskovits, M. *J. Chem. Phys.* **1980**, *73*, 4282.
(611) Moskovits, M.; McBreen, P. *J. Chem. Phys.* **1978**, *68*, 4992.
(612) Cai, W.; Wan, L.; Noda, H.; Hibino, Y.; Ataka, K.; Osawa, M. *Langmuir* **1998**, *14*, 6992.
(613) Garoff, S.; Weitz, D. A.; Gramila, T. J.; Hanson, C. D. *Opt. Lett.* **1981**, *6*, 245.
(614) Greenler, R. G. *J. Chem. Phys*. **1965**, *44*, 310.
(615) Zhang, Z.; Imae, T. *J. Colloid Interface Sci.* **2001**, *233*, 99.
(616) Zhang, Z.; Imae, T. *J. Colloid Interface Sci.* **2001**, *233*, 107.
(617) Fleischmann, M.; Hendra, P. J.; McQuillan, A. J. *Chem. Phys. Lett.* **1974**, *26*, 163.
(618) Clark, H. A.; Campagnola, P. J.; Wuskell, J. P.; Lewis, A.; Loew, L. M. *J. Am. Chem. Soc.* **2000**, *122*, 10234.
(619) Small, J. R.; Foster, N. S.; Amonette, J. E.; Autrey, T. *Appl. Spectrosc.* **2000**, *54*, 1142.
(620) Lettinga, M. P.; Zuilhof, H.; Zandvoort, M. A. M. J. *Phys. Chem. Chem. Phys.* **2000**, *2*, 3697.
(621) Makarova, O. V.; Ostafin, A. E.; Miyoshi, H.; J R Norris, J. *J. Phys. Chem. B* **1999**, *105*, 9080.
(622) Ahmadi, T. S.; Lognov, S. L.; El-Sayed, M. A. *J. Phys. Chem.* **1996**, *100*, 8053.
(623) Chun-ping, Z.; Feng-qi, Y.; Guang-yin, Z. *J. Raman. Spectrosc*. **1989**, *20*, 431.
(624) Prochazka, M.; Hanzlikova, J.; Stepanek, J.; Baumruk, V. *J. Mol. Struct.* **1997**, *410*−*411*, 77.
(625) Sbrana, G.; Neto, N.; Muniz-Miranda, M.; Nicentini, M. *J. Phys. Chem.* **1990**, *94*, 3706.
(626) Kim, M.; Itol, K. *J. Phys. Chem.* **1987**, *91*, 126.
(627) Vlckova, B.; Matejka, P.; Simonova, J.; Cermakova, K.; Pancoska, P.; Baumruk, V. *J. Phys. Chem.* **1993**, *97*, 9719.
(628) Marchi, M. C.; Blimes, S. A.; Blimes, G. M. *J. Colloid Interface Sci.* **1999**, *218*, 112.
(629) Weitz, D. A.; Lin, M. Y.; Sandroff, C. J. *Surf. Sci*. **1985**, *158*, 147.
(630) Ahera, A. M.; Garrell, R. L. *Anal. Chem.* **1987**, *59*, 2813.
(631) Herne, T. M.; Garrell, R. L. *Anal. Chem.* **1991**, *62*, 2290.
(632) Neddersen, J.; Chumanov, G.; Cotton, T. M. *Appl. Spectrosc.* **1993**, *47*, 1993.
(633) Srnova, I.; Prochazka, M.; Vlckova, B.; Stepanek, J.; Maly, P. *Langmuir* **1998**, *14*, 4666.
(634) Prochazka, M.; Mojzes, P.; Stepanek, J.; Vlckova, B.; Turpin, P. *Anal. Chem.* **1997**, *69*, 5103.
(635) Templeton, A. C.; Wuelfing, W. P.; Murray, R. W. *Acc. Chem. Res*. **2000**, *33*, 27.
(636) Kang, S. Y.; Jeon, I. C.; Kim, K. *Appl. Spectrosc.* **1998**, *52*, 278.
(637) Litorja, M.; Haynes, C. L.; Haes, A. J.; Jensen, T. R.; Duyne, R. P. V. *J. Phys. Chem. B* **2001**, *105*, 6907.
(638) Myers, A. B. In *Biological Applications of Raman Spectroscopy*; Mathies, R. A., Eds.; Wiley: New York, 1988; Vol. 1.
(639) Fowles, G. R. *Introduction to Modern Optics*, 2nd ed.; Holt, Rinehart and Winston: New York, 1975.
(640) Schultz, S.; Smith, D. R.; Mock, J. J.; Schultz, D. A. *Proc. Natl. Acad. Sci. U.S.A.* **2000**, *97*, 996.
(641) Cao, Y. W. C.; Jin, R. C.; Mirkin, C. A. *Science* **2002**, *297*, 1536.
(642) Kottmann, J. P.; Martin Oliver, J. F. *Opt. Lett.* **2001**, *26*, 1096.
(643) Johansson, P.; Xu, H.; Käll, M. *Phys. Rev. B* **2005**, *72*, No. 035427.
(644) Gibson, J. W.; Johnson, B. R. *J. Chem. Phys.* **2006**, *124*, No. 064701.
(645) Kelly, K. L.; Coronado, E.; Zhao, L. L.; Schatz, G. C. *J. Phys. Chem. B* **2003**, *107*, 668.
(646) Jensen, T.; Kelly, L.; Lazarides, A.; Schatz, G. *Cluster Sci.* **1999**, *10*, 295.
(647) Srnova, I.; Prochazka, M.; Vlckova, B.; Stepanek, J.; Maly, P. *Langmuir* **1998**, *14*, 4666.
(648) Song, O. K.; Pauley, M. A.; Wang, C. H.; Jen, A. K. Y. *J. Raman Spectrosc.* **1996**, *27*, 685.
(649) Michaels, A. M.; Jiang, J.; Brus, L. *J. Phys. Chem. B* **2000**, *104*, 11965.
(650) Lecomte, S.; Moreau, N. J.; Manfait, M.; Aubard, J.; Baron, M. H. *Biospectroscopy* **1995**, *1*, 423.
(651) Picorel, R.; Chumanov, G.; Cotton, T. M.; Montoya, G.; Toon, S.; Seibert, M. *J. Phys. Chem.* **1994**, *98*, 6017.
(652) Jensen, T.; Kelly, L.; Lazarides, A.; Schatz, G. C. *J. Cluster Sci.* **1999**, *10*, 295.
(653) Kamat, P. V. *J. Phys. Chem. B* **2002**, *106*, 7729.
(654) Baia, M.; Toderas, F.; Baia, L.; Popp, J.; Astilean, S. *Chem. Phys. Lett.* **2006**, *422*, 127.
(655) Schmeits, M.; Dambly, L. *Phys. Rev. B* **1991**, *44*, 12706.
(656) Moskovits, M.; Jeong, D. H. *Chem. Phys. Lett.* **2004**, *397*, 91.
(657) Talley, C. E.; Jackson, J. B.; Oubre, C.; Grady, N. K.; Hollars, C. W.; Lane, S. M.; Huser, T. R.; Nordlander, P.; Halas, N. J. *Nano Lett.* **2005**, *5*, 1569.
(658) Fromm, D. P.; Sundaramurthy, A.; James, Schuck, P.; Kino, G.; Moerner, W. E. *Nano Lett.* **2004**, *4*, 957.
(659) Fromm, D. P.; Sundaramurthy, A.; Kinkhabwala, A.; James Schuck, P. *J. Chem. Phys.* **2006**, *124*, No. 061101.
(660) Grober, R. D.; Schoelkopf, R. J.; Prober, D. E. *Appl. Phys. Lett.* **1997**, *70*, 1354.
(661) Michaels, A. M.; Jiang, J.; Brus, L. *J. Phys. Chem. B* **2000**, *104*, 11965.
(662) Barazzouk, S.; Kamat, P. V.; Hotchandani, S. *J. Phys. Chem. B* **2005**, *109*, 716.
(663) Sass, J. K.; Sen, R. K.; Meyer, E.; Gerischer, H. *Surf. Sci.* **1974**, *44*, 515.
(664) Harrop, T. C.; Mascharak, P. K. *Chemtracts: Inorg. Chem.* **2001**, *14*, 442.
(665) de Silva, A. P.; Gunaratne, H. Q. N.; Gunnlaugsson, T.; Huxley, A. J. M.; McCoy, C. P.; Rademacher, J. T.; Rice, T. E. *Chem. Rev.* **1997**, *97*, 1515.

(666) Fujiwara, H.; Yanagida, S.; Kamat, P. V. *J. Phys. Chem. B* **1999**, *103*, 2589.
(667) Porter, L. A.; Ji, D.; Westcott, S. L.; Graupe, M.; Czernuszewicz, R. S.; Halas, N. J. *Langmuir* **1998**, *14*, 7378.
(668) Brust, M.; Kiely, C. J.; Bethell, D.; Schiffrin, D. J. *J. Am. Chem. Soc.* **1998**, *120*, 12367.
(669) Rodenberger, D. C.; Heflin, J. R.; Garito, A. F. *Nature* **1992**, *359*, 309.
(670) Fischer, G. L.; Boyd, R. W.; Gehr, R. J.; Jenekhe, S. A.; Osaheni, J. A.; Sipe, J. E.; Weller-Brophy, L. A. *Phys. Rev. Lett.* **1995**, *74*, 1871.
(671) Bennink, R. S.; Yoon, Y.-K.; Boyd, R. W.; Sipe, J. E. *Opt. Lett.* **1999**, *24*, 1416.
(672) Sekikawa, T.; Kosuge, A.; Kanai, T.; Watanabe, S. *Nature* **2004**, *432*, 605.
(673) Huang, J. P.; Yu, K. W. *Appl. Phys. Lett.* **2005**, *86*, No. 041905.
(674) Huang, J. P.; Yu, K. W. *Appl. Phys. Lett.* **2004**, *85*, 94.
(675) Huang, J. P.; Yu, K. W. *Opt. Lett.* **2005**, *30*, 275.
(676) Holtz, J. H.; Asher, S. A. *Nature* **1997**, *389*, 829.
(677) Vlasov, Y. A.; Bo, X. Z.; Strum, J. C.; Norris, D. J. *Nature* **2001**, *414*, 289.
(678) Shalaev, V. M.; Stockman, M. I. *Zh. Eksp. Teor. Fiz.* **1987**, *92*, 509.
(679) Butenko, A. V.; Shalaev, V. M.; Stockman, M. I. *Zh. Eksp. Teor. Fiz.* **1988**, *94*, 107.
(680) Markel, V. A.; Muratov, L. S.; Stockman, M. I.; George, T. F. *Phys. Rev. B* **1991**, *43*, 8183.
(681) Shalaev, V. M.; Stockman, M. I.; Botet, R. *Physica A* **1992**, *185*, 181.
(682) Stockman, M. I.; Shalaev, V. M.; Moskovits, M.; Botet, R.; George, T. F. *Phys. Rev. B* **1992**, *46*, 2821.
(683) Shalaev, V. M.; Poliakov, E. Y.; Markel, V. A. *Phys. Rev. B* **1996**, *53*, 2437.
(684) Rautian, S. G.; Safonov, V. P.; Chubakov, P. A.; Shalaev, V. M.; Stockman, M. I. *Pis'ma Zh. Eksp. Teor. Fiz.* **1988**, *47*, 200.
(685) Butenko, A. V.; Chubakov, P. A.; Danilova, Y. E.; Karpov, S. V.; Popov, A. K.; Rautian, S. G.; Safonov, V. P.; Slabko, V. V.; Shalaev, V. M.; Stockman, M. I. *Z. Phys. D* **1990**, *17*, 283.
(686) Danilova, Y. E.; Rautian, S. G.; Safonov, V. P. *Bull. Russ. Acad. Sci. Phys.* **1996**, *60*, 374.
(687) Danilova, Y. E.; Drachev, V. P.; Perminov, S. V.; Safonov, V. P. *Bull. Russ. Acad. Sci. Phys.* **1996**, *60*, 342.
(688) Danilova, Y. E.; Lepeshkin, N. N.; Rautian, S. G.; Safonov, V. P. *Physica A* **1997**, *241*, 231.
(689) Drachev, V. P.; Perminov, S. V.; Rautian, S. G.; Safonov, V. P. *Pis'ma Zh. Eksp. Teor. Fiz.* **1998**, *68*, 618.
(690) Shen, Y. R. *Principles of Nonlinear Optics*; Wiley: New York, 1984.
(691) Brevet, P. F. *Surface Second Harmonic Generation*; Presses Polytechniques Universitaires Romandes: Lausanne, 1997.
(692) Corn, R. M.; Higgins, D. A. *Chem. Rev.* **1994**, *94*, 107.
(693) Eisenthal, K. B. *Chem. Rev.* **1996**, *96*, 1343.
(694) Brevet, P. F. In *Liquid Interfaces in Chemical Biological and Pharmaceutical Applications*; Volkov, A. G. Ed., Surfactant Science Series, Marcel Dekker: New York, 2000; Vol. 95.
(695) Dadap, J. I.; Shan, J.; Eisenthal, K. B.; Heinz, T. F. *Phys. Rev. Lett.* **1999**, *83*, 4045.
(696) Agarwal, G. S.; Jha, S. S. *Solid State Commun.* **1982**, *42*, 499.
(697) Galletto, P.; Brevet, P. F.; Girault, H. H.; Antoine, R.; Broyer, M. *Chem. Commun.* **1999**, 581.
(698) Creighton, J. A.; Alvarez, M. S.; Weitz, D. A.; Kim, M. W. *J. Phys. Chem.* **1983**, *87*, 4793.
(699) Felidj, N.; Levy, G.; Pantigny, J.; Aubard, J. *New J. Chem.* **1998**, 725.
(700) Leitner, A. *Mol. Phys.* **1990**, *70*, 197.
(701) Galletto, P.; Brevet, P. F.; Girault, H. H.; Antoine, R.; Broyer, M. *J. Phys. Chem. B* **1999**, *103*, 8706.
(702) Bozhevolnyi, S. I.; Vohnsen, B.; Zayats, A. V.; Smolyaninov, I. I. *Surf. Sci.* **1996**, *356*, 268.
(703) Bozhevolnyi, S. I. *Phys. Rev. B* **1996**, *54*, 8177.
(704) Bozhevolnyi, S. I.; Markel, V. A.; Coello, V.; Kim, W.; Shalaev, V. M. *Phys. Rev. B* **1998**, *58*, 11 441.
(705) Kneipp, K.; Kneipp, H.; Kartha, V. B.; Manoharan, R.; Deinum, G.; Itzkan, I.; Dasari, R. R.; Feld, M. S. *Phys. Rev. E* **1998**, *57*, R6281.
(706) Kneipp, K.; Kneipp, H.; Kartha, V. B.; Manoharan, R.; Deinum, G.; Itzkan, I.; Dasari, R. R.; Feld, M. S. *Appl. Spectrosc.* **1998**, *52*, 1493.
(707) Markel, V. A.; Shalaev, V. M.; Zhang, P.; Huyanh, W.; Tay, L.; Haslett, T. L.; Moskovits, M. *Phys. Rev. B* **1999**, *59*, 10903.
(708) Markel, V. A.; Shalaev, V. M.; Stechel, E. B.; Kim, W.; Armstrong, R. L. *Phys. Rev. B* **1996**, *53*, 2425.
(709) Markel, V. A.; Shalaev, V. M. In *Computational Studies of New Materials*; Jelski, D. A., George T. F., Eds., World Scientific: Singapore, 1999; pp 210−243.
(710) Poliakov, E. Y.; Markel, V. A.; Shalaev, V. M.; Botet, R. *Phys. Rev. B* **1998**, *57*, 14901.
(711) Kawasaki, M.; Sato, T.; Yoshimoto, Y. *Langmuir* **2000**, *16*, 5409.
(712) Shinozaki, R.; Nakato, T. *Langmuir* **2004**, *20*, 7583.
(713) Nasr, C. P.; Liu, D.; Hotchandani, S.; Kamat, P. V. *J. Phys. Chem.* **1996**, *100*, 11054.
(714) Xu, P.; Yanagi, H. *Chem. Mater.* **1999**, *11*, 2626.
(715) McRae, E. G.; Kasha, M. In *Physical Processes in Radiation Biology*; Augenstein, L., Mason, R., Rosenberg, B., Eds.; Academic Press: New York, 1964; p 23.
(716) Chandrasekharan, N.; Hu, J.; Jones, G., II; Kamat, P. V. *J. Phys. Chem. B* **2000**, *104*, 11103.
(717) Stenzel, O.; Stendal, A.; Voigtsberger, A. C. *Sol. Energy Mater. Sol. Cells* **1995**, *37*, 337.
(718) Fan, C.; Wang, S.; Hong, J. W.; Bazan, G. C.; Plaxco, K. W.; Heeger, A. J. *Appl. Phys. Sci.* **2003**, *100*, 6297.
(719) Hranisavljevic, J.; Dimitrijevic, N. M.; Wurtz, G. A.; Wiederrecht, G. P. *J. Am. Chem. Soc.* **2002**, *124*, 4536.
(720) Lee, P. C.; Meisel, D. *J. Phys. Chem.* **1982**, *86*, 3391.
(721) Kerker, M. *J. Colloid Interface Sci.* **1985**, *105*, 297.
(722) Kometani, N.; Tsubonishi, M.; Fujita, T.; Asami, K.; Yonezawa, Y. *Langmuir* **2001**, *17*, 578.
(723) Goerge Thomas, K.; Kamat, P. V. *J. Am. Chem. Soc.* **2000**, *122*, 2655.
(724) Makarova, O. V.; Ostafin, A. E.; Miyoshi, H.; Norris, J. R.; Miesel, D. *J. Phys. Chem. B* **1999**, *103*, 9080.
(725) Su, G.-J.; Yin, S.-X.; Wan, L.-J.; Zhao, J.-C.; Bai, C.-L. *Chem. Phys. Lett.* **2003**, *370*, 268.
(726) Higgins, D. A.; Reid, P. J.; Barbara, P. F. *J. Phys. Chem.* **1996**, *100*, 1174.
(727) Meriaudeau, F.; Downey, T.; Wig, A.; Passian, A.; Buncick, M.; Ferrell, T. L. *Sens. Actuators B* **1999**, *54*, 106.
(728) Sun, S. H.; Murray, C. B.; Weller, D.; Folks, L.; Moser, A. *Science* **2000**, *287*, 1989.
(729) Wang, J. F.; Gudiksen, M. S.; Duan, X. F.; Cui, Y.; Lieber, C. M. *Science* **2001**, *293*, 1455.
(730) Mikhailovsky, A. A.; Petruska, M. A.; Li, K.; Stockman, M. I.; Klimov, V. I. *Phys. Rev. B* **2004**, *69*, No. 085401.
(731) Raether, H. *Surface Plasmons*; Springer-Verlag: Berlin, 1998.
(732) Stockman, M. I.; Faleev, S. V.; Bergman, D. J. *Phys. Rev. Lett.* **2001**, *87*, No. 167401.
(733) Glass, A. M.; Liao, P. F.; Bergman, J. G.; Olson, D. H. *Opt. Lett.* **1980**, *5*, 368.
(734) Neuendorf, R.; Quinten, M.; Kreibig, U. *J. Chem. Phys.* **1996**, *104*, 6348.
(735) Stockman, M. I.; Shalaev, V. M.; Moskovits, M.; Botet, R.; George, T. F. *Phys. Rev. B* **1992**, *46*, 2821.
(736) Krenn, J. R.; Dereux, A.; Weeber, J. C.; Bourillot, E.; Lacroute, Y.; Goudonnet, J. P. *Phys. Rev. Lett.* **1999**, *82*, 2590.
(737) Balistreri, M. L. M.; Korterik, J. P.; Kuipers, L.; van Hulst, N. F. *Phys. Rev. Lett.* **2000**, *85*, 294.
(738) Bozhevolnyi, S. I.; Volkov, V. S.; Leosson, K. *Phys. Rev. Lett.* **2002**, *89*, No. 186801.
(739) Ando, M.; Kobayashi, T.; Haru, M. J. *J. Chem. Soc., Faraday Trans.* **1994**, *90*, 1011.
(740) Eguchi, K. In *Gas Sensors*; Sberveglieri, G., Eds., Kluwer: Dordrecht, The Netherlands, 1992; p 307.
(741) Jensen, T. R.; Schatz, G. C.; Van Duyne, R. P. *J. Phys. Chem B* **1999**, *103*, 2394.
(742) Bauer, L. A.; Birenbaum, N. S.; Meyer, G. J. *J. Mater. Chem.* **2004**, *14*, 517.
(743) Bruchez, M.; Moronne, M.; Gin, P.; Weiss, S.; Alivisatos, A. P. *Science* **1998**, *281*, 2013.
(744) Nam, J. M.; Thaxton, C. S.; Mirkin, C. A. *Science* **2003**, *301*, 1884.
(745) Han, M. Y.; Gao, X. H.; Su, J. Z.; Nie, S. *Nat. Biotechnol.* **2001**, *19*, 631.
(746) Henglein, A. *J. Phys. Chem.* **1993**, *97*, 5457.

(747) Belloni, J. *Curr. Opin. Colloid Interface Sci.* **1996**, *1*, 184.

(748) Lim, I.-I.; Ouyang, J.; Luo, J.; Wang, L.; Zhou, S.; Zhong, C.-J. *Chem. Mater.* **2005**, *17*, 6528.

(749) Liu, J.; Lu, Y. *J. Am. Chem. Soc.* **2003**, *125*, 6642.

(750) Liu, J.; Lu, Y. *Anal. Chem.* **2004**, *76*, 1627.

(751) Kreibig, U.; Genzel, L. *Surf. Sci.* **1985**, *156*, 678.

(752) Yang, W. H.; Schatz, G. C.; Van Duyne, R. P. *J. Chem. Phys.* **1995**, *103*, 869.

(753) Chakrabarti, R.; Klibanov, A. M. *J. Am. Chem. Soc.* **2003**, *125*, 12531.

(754) Liu, J.; Lu, Y. *Chem. Mater.* **2004**, *16*, 3231.

(755) Shenhar, R.; Norsten, T. B.; Rotello, V. M. *Adv. Mater.* **2005**, *17*, 657.

(756) Boal, A. K.; Galow, T. H.; Ilhan, F.; Rotello, V. M. *Adv. Funct. Mater.* **2001**, *11*, 461.

CR0680282